Fermilab Library
0 1160 0077715 5

E-821

NEUTRON RADIATION FIELDS OUTSIDE SHIELDING AT THE FERMILAB TEVATRON

by

Márcia Maria Campos Torres

A dissertation submitted in partial fulfillment
of the requirements for the degree of
Doctor of Philisophy
(Environmental Health Sciences)
in The University of Michigan
1996

Doctoral Committee:

Associate Professor James E. Martin, Co- Chair
Alexander J. Elwyn, Applied Scientist, Fermilab, Co-Chair
Assistant Professor David M. Hamby
Professor Glenn F. Knoll
Professor Robert Tickle
Jack D. Cossairt, Applied Scientist, Fermilab

FERMILAB
LIBRARY

LIBOFFICE
FERMILAB
THESIS

Abstract

Neutron Radiation Fields Outside Shielding at the Fermilab Tevatron

by

Márcia Maria Campos Torres

Co-Chairs: James E. Martin, Alexander J. Elwyn

The present measurements characterize the neutron radiation fields outside shielding in two different experimental areas at Fermilab, the Neutrino West (NWA) and the Proton Center (PC-4) beam lines. At NWA, a beam stop, constructed out of a series of iron slabs, was used as absorbing material for the incident beam. The particles incident on this beam stop were negative pions with energies between 25 and 150 GeV. Neutron spectra were obtained with a Bonner Sphere Spectrometer at ten depths in the forward direction and at one depth laterally. Based on the forward direction studies, the shape of the spectrum for the neutrons that leak through Fe is roughly independent of beam energy, E, and absorber thickness. The lateral measurements are consistent with attenuation through Fe with a mean free path that is in agreement with that from other studies. In the longitudinal direction both fluence and dose equivalent can be represented by the product of build up and attenuation terms, with a dependence on beam energy that scales as $E^{0.8}$. The source strength or conversion factor from dose equivalent to fluence, is very closely the same for both lateral and longitudinal shielding directions. The agreement of the spectral data with the predictions of a Monte Carlo (FLUKA) simulation is generally excellent, particularly at neutron energies below 5-10 MeV. At PC-4, neutron spectra, also measured with a Bonner Sphere Spectrometer, were determined at four locations outside of the shielding. At

FERMILAB LIBRARY

FERMILAB LIBRARY

AAE4623

least 50 % of the dose equivalent was found to arise from neutrons with energies above 0.1 MeV, in spite of the fact that over 60 % of the fluence is from neutrons with lower energies. These results, as well as the Quality Factors determined from the data, are in agreement with previous studies, and suggest that PC-4 is fairly typical of neutron radiation areas generated at high energy accelerators.

ACKNOWLEDGMENTS

First of all, I would like to thank my advisor Assistant Professor James E. Martin, for allowing me the freedom of choosing the research of my interest, and not necessarily his.

Secondly, Dr. Alex Elwyn, for being my co-advisor at Fermilab in this endeavour. I appreciate your patience with all the delays that I brought into this research, especially for putting up with me during my pregnancy. Working with you has been one of the best experiences that I have had in America. I will dearly miss our weekly discussions; it is going to be sad to see the end of this partnership. I owe so much of this work to Alex's dedication and fine touches, always pushing me ahead which made me think that there is still light at the end of the tunnel.

Dr. Don Cossairt, Section Head-ESH at Fermilab, first for giving me the opportunity of working at your facility, secondly for reading the manuscript and making such insightful comments. Being one of the world's leading experts in this subject, your comments meant a lot to me.

Professor Ken Johns, University of Arizona, for allowing me to take the lead in the analysis of the data of E-821. Your confidence and trust are highly appreciated. Also, thanks for running shifts on Christmas Eve with me. All my collaborators at E-821, Eric James, David Fein, David Ciampa, Bill Davis and Ed Mierkiewicz; it would have been impossible to take all the data without your help. I can't thank all of you enough.

Dr. Alfredo Ferrari at Milano, one of the "fathers" of FLUKA for allowing me to use the code when the version used was still in "draft " form. Although we never

met each other, your help through e-mail in instructing me to set up the code was very important for my research.

Dr. Alberto Fasso at CERN, for your patience and dedication in teaching me how to run FLUKA, this work would never have had an end if it weren't for your guidance. Mr. Panini in Bologna, for being so kind and permitting this Brazilian to use your cross sections.

Mac Louis J. Robinet, Section Head ESH-HP at Argonne National Laboratory. Your understanding of the time needed to conduct my research was very important to me, especially the time you allowed for work at Fermilab.

Dr. Robert Wynveen, Division Director of ESH at Argonne, for encouraging and supporting me during this work. I really appreciate you and Mac giving me the freedom to pursue my degree.

The Brazilian Government-CNPQ, for the financial support during my years as a student at Michigan.

Special thanks to Fermilab where this research was done and to Argonne for employing me during the last four years.

To all my family in Brazil, especially to my mother who has been following me around the world and has never complained, your love was needed.

Last but not least, my husband Dr. William Cobau, for helping me to put this work together; your knowledge of PageMaker made my life a lot easier. Also for taking care of Nilo, our son, during the weekends, and allowing me the free time to finish up this dissertation.

Table of Contents

Acknowledgments ii

List of Tables v

List of Figures vi

List of Appendices x

Introduction, Objectives and Background 1
- 1.1 Introduction 1
- 1.2 Objectives 3
- 1.3 Background 4

Experimental Setup and Measurements 10
- 2.1 Fermilab 10
- 2.2 The NWA Measurements 12
- 2.3 The Proton Center Measurements (PC-4) 12
- 2.4 The Detectors 16

Data Analysis 25
- 3.1 Normalization of NWA Data 25
- 3.2 Normalization of Proton Center PC-4 Data 28
- 3.3 Spectral Unfolding 28
- 3.4 Calibration of Bonner Sphere Spectrometer (BSS) 30

Results and Discussions 34
- 4.1 NWA and PC-4 Results 34
- 4.2 NWA Results at Longitudinal and Lateral Directions 34
- 4.3 Lateral (Transverse) Shielding at NWA 47
- 4.4 Forward (Longitudinal) Shielding at NWA 53
- 4.5 FLUKA Monte Carlo Calculations 61
- 4.6 Proton Center PC-4 Results 75
  - 4.6.1 The Roofs 75
  - 4.6.2 Downstream Hyperon Extension Enclosure 75
  - 4.6.3 Upstream Hyperon Extension Enclosure 81
- 4.7 Monte Carlo Calculations at PC-4 84

Conclusions 86
- 5.1 Dependence on Shielding Thickness 86
- 5.2 Dependence on Energy 87
- 5.3 Conversion Factor 87
- 5.4 Comparison with Monte Carlo Calculations 89
- 5.5 Properties of the Neutron Fields 90

Appendices 91

References 160

List of Tables

Table 4.1. Summary of Results on Lateral Shielding. 52
Table 4.2. Summary of Fits of Fluence and Dose Equivalent as a Function of Incident Pion Energy for the Longitudinal Shielding. 57
Table 4.3. Summary of Fits of Fluence as a Function of Incident Pion Energy for the Longitudinal Shielding Generated by FLUKA. 71
Table 4.4. Summary of Results for the On-Axis Longitudinal Shielding. 74
Table 4.5. PC-4 Fluence in Specific Energy Bins for Unfolded Neutron Spectra. 78
Table 4.6. PC-4 Dose Equivalent in Specific Energy Bins for Unfolded Neutron Spectra. 79
Table 4.7. PC-4 Comparison of the Unfolded Data by use of BUNKI and LOUHI. 83
Table 4.8. PC-4 Comparison of Dose Equivalent Unfolded from the Data by BUNKI with CASIM Simulations. 85
Table A.1. Depth 40.6 cm of Fe Data Taken at NWA 93
Table A.2. Depth 61 cm of Fe Data Taken at NWA 94
Table A.3. Depth 81.3 cm of Fe Data Taken at NWA 95
Table A.4. Depth 121.9 cm of Fe Data Taken at NWA 96
Table A.5. Depth 142.2 cm of Fe Data Taken at NWA 97
Table A.6. Depth 162.6 cm of Fe Data Taken at NWA 98
Table A.7. Depth 182.9 cm of Fe Data Taken at NWA 99
Table A.8. Depth 243.8 cm of Fe Data Taken at NWA 100
Table A.9. Depth 264.2 cm of Fe Data Taken at NWA 101
Table A.10. Depth 60.9 cm of Fe Data Taken at NWA in the Lateral Direction ... 102

List of Figures

Figure 1.1. Hadronic Cascade 2
Figure 1.2. Neutron Spectra at Proton Accelerators Around The World 6
Figure 2.1. Fermi National Accelerator Laboratory Accelerator Complex 11
Figure 2.2. Top View of a Beam Dump at NWA. 13
Figure 2.3. Front View of a Beam Dump at NWA 14
Figure 2.4. PC-4 Area Elevation View in the Plane of the Beam 15
Figure 2.5. Bonner Sphere Schematic. 18
Figure 2.6. Bonner Sphere Spectrometer Set-up 19
Figure 2.7. ^{6}LiI(Eu) Pulse Height Spectrum 20
Figure 2.8. Bonner Sphere Neutron Signal 21
Figure 2.9. Response Functions for a 12.7 mm by 12.7 mm ^{6}LiI(Eu) Scintillator 22
Figure 3.1. Bonner Sphere Layout 26
Figure 3.2. Beam Profile Study at 100 GeV 27
Figure 3.3. Unfolded Neutron Spectra for Incident Pions at 121.9 cm of Iron. 31
Figure 3.4. Unfolded Neutron Spectrum for Am-Be Source 33
Figure 4.1. Unfolded Neutron Spectra For Incident Pions on 40.6 cm of Iron. 35
Figure 4.2. Unfolded Neutron Spectra For Incident Pions on 162.6 cm of Iron 36
Figure 4.3. Unfolded Neutron Spectra For Incident Pions on 243.8 cm of Iron 37
Figure 4.4. Unfolded Neutron Spectra for Incident Pions on 162.6 cm of Iron 39
Figure 4.5. Unfolded Neutron Spectra for Incident Pions on 162.6 cm of Iron 41
Figure 4.6. Unfolded Neutron Spectra for Incident Pions at 40.6 cm of Iron 42
Figure 4.7. Unfolded Neutron Spectra for Incident Pions at 264.2 cm of Iron. 43
Figure 4.8. Unfolded Neutron Spectra for Incident Pions on 243.8 cm of Iron 45
Figure 4.9. Unfolded Neutron Spectra for Incident Pions at 60.9cm of Iron 46
Figure 4.10. Fluence and Dose Equivalent vs. Thickness of Iron 48
Figure 4.11. Fluence and Dose Equivalent vs. Incident Pion Energy 49
Figure 4.12. Fits to Fluence and Dose Equivalent vs Pion Energy 51
Figure 4.13. Neutron Fluence at 100 GeV 55
Figure 4.14. Dose Equivalent at 100 GeV 56
Figure 4.15. Exponents from the Fits 59
Figure 4.16. Energy Dependence Fit 60

Figure 4.17. Neutron Spectra for Incident Pions on 40.6 cm of Iron 63
Figure 4.18. Neutron Spectra for Incident Pions on 61 cm of Iron. 64
Figure 4.19. Unfolded Neutron Spectra for Incident Pions on 142.2 cm of Iron 65
Figure 4.20. Thickness Dependence Comparison Between FLUKA and BUNKI at 25 GeV 67
Figure 4.21. Thickness Dependence Comparison Between FLUKA and BUNKI at 50 and 75 GeV. 68
Figure 4.22. Thickness Dependence Comparison Between FLUKA and BUNKI at 100 and 150 GeV. 69
Figure 4.23. Calculations of Neutron Fluence at 100 GeV (FLUKA) 70
Figure 4.24. Energy Dependence Fit (FLUKA) 73
Figure 4.25 PC-4 First Roof Neutron Spectrum 76
Figure 4.26 PC-4 Fourth Roof Neutron Spectra 77
Figure 4.27. PC-4 Downstream and Upstream of the Hyperon Extension Enclosures Neutron Spectra 80
Figure 4.28. PC-4 Downstream Hyperon Extension Enclosure Neutron Spectra at 3 Milliradians 82
Figure 5.1. Average Quality Factor at NWA 88
Figure B.1. Unfolded Neutron Spectra for Incident Pions on 40.6 cm of Iron 104
Figure B.2. Unfolded Neutron Spectra for Incident Pions on 61 cm of Iron 105
Figure B.3. Unfolded Neutron Spectra for Incident Pions on 81.3 cm of Iron 106
Figure B.4. Unfolded Neutron Spectra for Incident Pions on 121.9 cm of Iron 107
Figure B.5. Unfolded Neutron Spectra for Incident Pions on 142.2 cm of Iron 108
Figure B.6. Unfolded Neutron Spectra for Incident Pions on 162.6 cm of Iron 109
Figure B.7. Unfolded Neutron Spectra for Incident Pions on 182.9 cm of Iron 110
Figure B.8. Unfolded Neutron Spectra for Incident Pions on 243.8 cm of Iron 111
Figure B.9. Unfolded Neutron Spectra for Incident Pions on 243.8 cm of Iron 112
Figure B.10 Unfolded Neutron Spectra for Incident Pions on 264.2 cm of Iron 113
Figure C.1. Unfolded Neutron Spectra for Incident Pions on 40.6 cm of Iron 115
Figure C.2. Unfolded Neutron Spectra for Incident Pions on 40.6 cm cm of Iron 116
Figure C.3. Unfolded Neutron Spectra for Incident Pions on 40.6 cm of Iron 117
Figure C.4. Unfolded Neutron Spectra for Incident Pions on 40.6 cm of Iron 118
Figure C.5. Unfolded Neutron Spectra for Incident Pions on 40.6 cm of Iron 119
Figure C.6. Unfolded Neutron Spectra for Incident Pions on 61 cm of Iron 120
Figure C.7. Unfolded Neutron Spectra for Incident Pions on 61 cm of Iron 121
Figure C.8. Unfolded Neutron Spectra for Incident Pions on

61 cm of Iron 122
Figure C.9. Unfolded Neutron Spectra for Incident Pions on 61 cm of Iron 123
Figure C.10. Unfolded Neutron Spectra for Incident Pions on 61 cm of Iron 124
Figure C.11. Unfolded Neutron Spectra for Incident Pions on 81.3 cm of Iron 125
Figure C.12. Unfolded Neutron Spectra for Incident Pions on 81.3 cm of Iron 126
Figure C.13. Unfolded Neutron Spectra for Incident Pions on 81.3 cm of Iron 127
Figure C.14. Unfolded Neutron Spectra for Incident Pions on 81.3 cm of Iron 128
Figure C.15. Unfolded Neutron Spectra for Incident Pions on 121.9 cm of Iron 129
Figure C.16. Unfolded Neutron Spectra for Incident Pions on 121.9 cm of Iron 130
Figure C.17. Unfolded Neutron Spectra for Incident Pions on 121.9 cm of Iron 131
Figure C.18. Unfolded Neutron Spectra for Incident Pions on 121.9 cm of Iron 132
Figure C.19. Unfolded Neutron Spectra for Incident Pions on 121.9 cm of Iron 133
Figure C.20. Unfolded Neutron Spectra for Incident Pions on 121.9 cm of Iron 134
Figure C.21. Unfolded Neutron Spectra for Incident Pions on 121.9 cm of Iron 135
Figure C.22. Unfolded Neutron Spectra for Incident Pions on 142.2 cm of Iron 136
Figure C.23. Unfolded Neutron Spectra for Incident Pions on 142.2 cm of Iron 137
Figure C.24. Unfolded Neutron Spectra for Incident Pions on 142.2 cm of Iron 138
Figure C.25. Unfolded Neutron Spectra for Incident Pions on 142.2 cm of Iron 139
Figure C.26. Unfolded Neutron Spectra for Incident Pions on 142.2 cm of Iron 140
Figure C.27. Unfolded Neutron Spectra for Incident Pions on 162.6 cm of Iron 141
Figure C.28. Unfolded Neutron Spectra for Incident Pions on 162.6 cm of Iron 142
Figure C.29. Unfolded Neutron Spectra for Incident Pions on 162.6 cm of Iron 143
Figure C.30. Unfolded Neutron Spectra for Incident Pions on 162.6 cm of Iron 144
Figure C.31. Unfolded Neutron Spectra for Incident Pions on 162.6 cm of Iron 145
Figure C.32. Unfolded Neutron Spectra for Incident Pions on 182.9 cm of Iron 146
Figure C.33. Unfolded Neutron Spectra for Incident Pions on 182.9 cm of Iron 147
Figure C.34. Unfolded Neutron Spectra for Incident Pions on 182.9 cm of Iron 148
Figure C.35. Unfolded Neutron Spectra for Incident Pions on

243.8 cm of Iron 149
Figure C.36. Unfolded Neutron Spectra for Incident Pions on 243.8 cm of Iron 150
Figure C.37. Unfolded Neutron Spectra for Incident Pions on 243.8 cm of Iron 151
Figure C.38. Unfolded Neutron Spectra for Incident Pions on 243.8 cm of Iron 152
Figure C.39. Unfolded Neutron Spectra for Incident Pions on 243.8 cm of Iron 153
Figure C.40. Unfolded Neutron Spectra for Incident Pions on 243.8 cm of Iron 154
Figure C.41. Unfolded Neutron Spectra for Incident Pions on 243.8 cm of Iron 155
Figure C.42. Unfolded Neutron Spectra for Incident Pions on 243.8 cm of Iron 156
Figure C.43. Unfolded Neutron Spectra for Incident Pions on 264.2 cm of Iron 157
Figure C.44. Unfolded Neutron Spectra for Incident Pions on 264.2 cm of Iron 158
Figure C.45. Unfolded Neutron Spectra for Incident Pions on 264.2 cm of Iron 159

List of Appendices

Appendix A 92
Appendix B 103
Appendix C 114

Chapter 1

Introduction, Objectives and Background

1.1 Introduction

Neutron dosimetry–a concept that encompasses the entire process of radiation field characterization and interpretation in terms of quantities used in radiological protection–around medium and high energy particle accelerators is a difficult problem. Although neutrons dominate the radiation field outside of shielding, other kinds of ionizing radiation are often present. Furthermore, since the neutron component of the field is propagated through the shielding by the high energy component of the extranuclear cascade [Fig. 1.1, ICRU 28], neutron energies can extend as high as the primary beam energy. In any event, neutrons must be measured over a wide range of energies; in fact, from energies as low as thermal up to the high energy region. These conditions therefore require the use of a number of techniques [Cossairt et al. 1988; Thorngate et al. 1985; Thomas et al. 1985] to determine the radiation environment, and then to provide the appropriate radiation protection to workers around high energy accelerators who may be subject to potential whole body exposure from neutrons.

Knowledge of the radiation environment around high energy accelerators, particularly the spectra of the neutrons which escape the shielding as well as those that exist within enclosures and around equipment, is essential to appropriate radiation protection. It is important to the development of instrumentation to be used for neutron detection, to the interpretation of dosimeter intercomparison studies, and in the design of shielding. Determination, experimentally, of fluence to dose equivalent conversion factors for neutrons outside the shielding at high energy

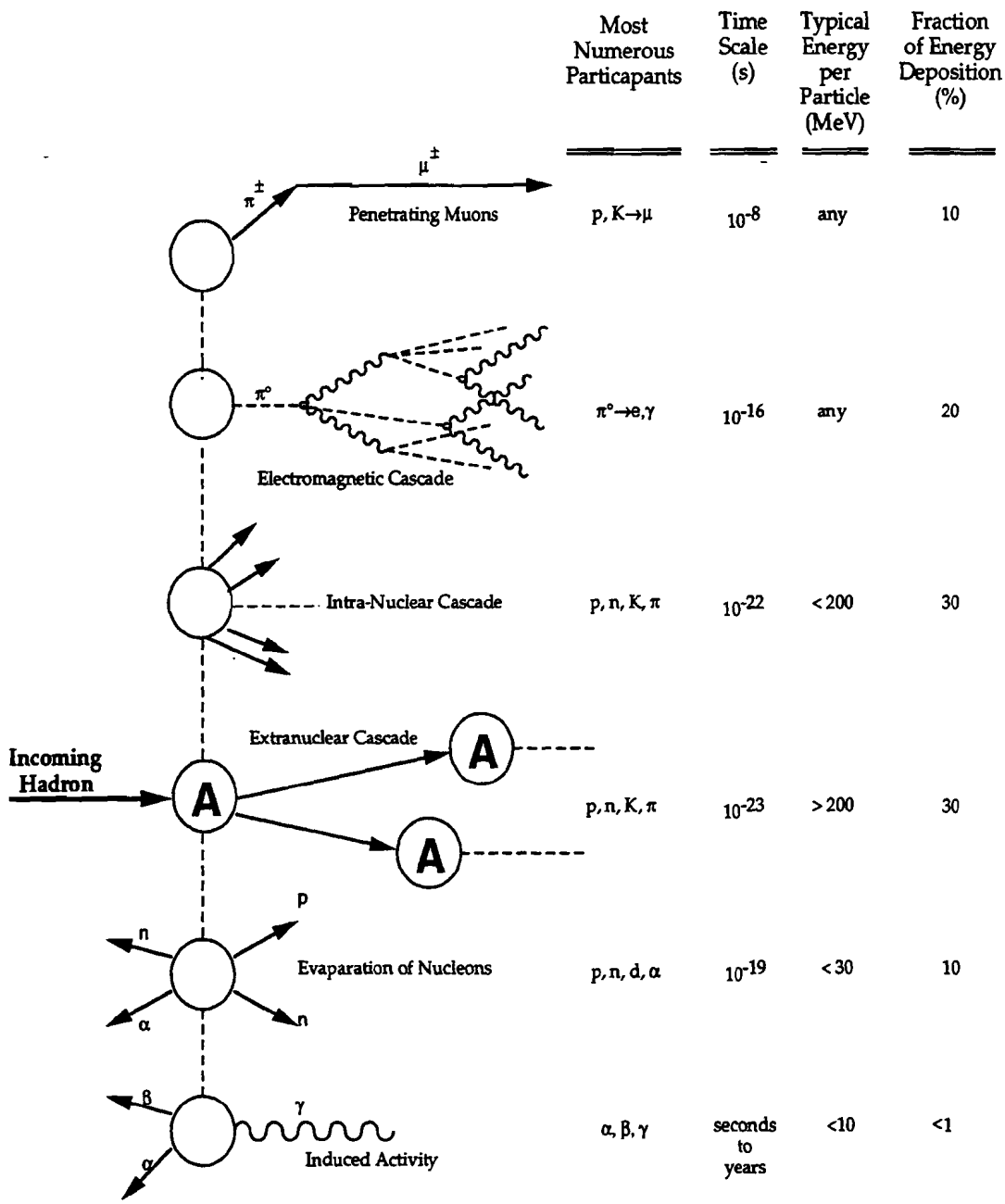

Figure 1.1. Hadronic Cascade. The six levels of the hadronic cascade; the incoming hadron strikes the nucleus and the cascade is formed. Note that 30% of the energy is deposited by the extra nuclear cascade. After ICRU Report 28.

accelerators, can lead to a more appropriate design of shielding for future accelerator upgrade projects.

This study was conducted in two experimental areas at Fermi National Accelerator Laboratoty (Fermilab): The first is called NWA where a beam stop was constructed of movable iron slabs in order to study the spectra of neutrons that arise from hadronic showers in high energy pion interactions in iron. This beam stop is representative of a typical particle detector frequently used at high energy accelerators called a calorimeter. The second location was in an enclosure called PC-4 where measurements were done on the top of a roof and at locations further downstream, outside of a beamline target area, in an attempt to characterize the neutron radiation field outside of typical shielding at an high energy proton accelerator.

For the purposes of this dissertation, high energy neutrons are defined to be those with energies of about 20 MeV and higher. This limit is chosen because it corresponds approximately to the upper limit of response of moderated thermal neutron instruments, and more importantly it is the threshold of the $^{12}C(n,2n)^{11}C$ reaction, frequently used as an activation detector [McCaslin 1959; Stevenson 1984] to explore this high energy region. The extent to which the neutron field outside of shielding contains neutrons of such energies is one of the questions that this study had hoped to answer through the measurements discussed here. As it turned out, however, this determination was addressed only partially. This point will be discussed in more detail in the following chapters.

1.2 Objectives

The objectives of this experimental study from the accelerator health physics point of view are given below:

1) To measure the energy spectra of neutrons produced by hadronic cascades or showers in an iron shield of variable thickness in or-

der to characterize this neutron field by a determination of fluence, dose equivalent, and quality factor as a function of incident beam energy and depth in the shield.

2) To develop a quantitative understanding of the dependence on both energy and depth of neutron fluence and dose equivalent, in both lateral and forward iron shielding.

3) To measure the energy spectra of neutrons outside of a "typical" shielded beam line enclosure in an attempt to characterize the neutron field by a determination of fluence, dose equivalent and quality factor.

4) To use systematic data on the fluence and energy spectra of neutrons arising from hadronic showers as a benchmark to test hadronic shower and neutron transport Monte Carlo codes. Upon verification, the Monte Carlo prediction would be of great use in the design and construction of detector elements and shielding at high energy particle accelerators.

1.3 Background

Even though the first particle accelerators were in operation in the early 1930s, it was not until twenty years later that the character of the radiation field around accelerators was investigated. The first scientific investigation that described the radiation environment around accelerators was published in 1957 [Solon 1957]. In the mid-fifties researchers [Thomas et al. 1985] identified neutrons outside of roof shielding near the AERE 110-inch synchrocyclotron. As investigations were performed in the 1950s at the 184-inch Synchrocyclotron at Berkeley and at other proton accelerators, the characteristics of the radiation environment outside of thick shielding were delineated. A rule of thumb [Thomas et al. 1988] was derived from those measurements:

> Neutrons between 0.1 and 10 MeV contribute more than 50% to the dose equivalent; gamma rays and very low energy neutrons contribute about 20%, and neutrons with energy greater than 10 MeV contribute the rest.

Patterson et al. [1959] suggested that the spectrum obtained outside shielding at a high energy proton accelerator must be similar to the cosmic ray neutron spectrum. He concluded that neutrons between 0.1 and 30 MeV gave the largest

contribution to the dose equivalent in the radiation field outside shielding. By the early 1960s there was sufficient data from high energy accelerators at Berkeley, Rutherford Laboratory, and Saclay to confirm Patterson's predictions. However in 1965 and 1966 some results from measurements performed at CERN indicated that Patterson's predictions were not quite true. These results showed that high energy neutrons (E_n>20 MeV) can contribute between 50 to 90% to the dose equivalent depending on the kind of shielding used at the accelerator [Thomas et al. 1988]. Measurements taken outside of an earth shield indicated a large contribution to dose equivalent from high energy neutrons and the data taken outside the concrete shielding confirmed that the neutron spectrum was quite similar to that produced by cosmic rays.

In Figure 1.2 typical neutron spectra obtained at proton accelerators around the world in these early years are shown [Shaw et al. 1969]. The definitions of these symbols are as following:

RT is a neutron spectrum determined at the CERN 28 GeV proton synchrotron (CPS) above earth shielding with a target intercepting the beam as a primary radiation source.

PSB is a spectrum measured at the CPS above concrete shielding, again with a target acting as the primary source.

BEV is a spectrum measured at the University of California Radiation Laboratory (now Lawrence Berkeley National Laboratory) 6.3 Gev proton synchrotron.

X2 is a spectrum measured at the 7 Gev proton synchrotron of the Rutherford Laboratory, outside concrete shielding.

P1 is a spectrum measured as for X2 but outside steel shielding.

PLA is the ambient neutron spectrum around the 50 MeV proton linac of the Rutherford Laboratory.

CR is the Hess cosmic ray neutron spectrum [Hess et al. 1959].

For ease of interpretation, these data are plotted as energy E times neutron fluence $\phi(E)$, not just $\phi(E)$ alone. The reasons for this representation will be discussed more fully in later chapters. For the top part of this figure a combination of

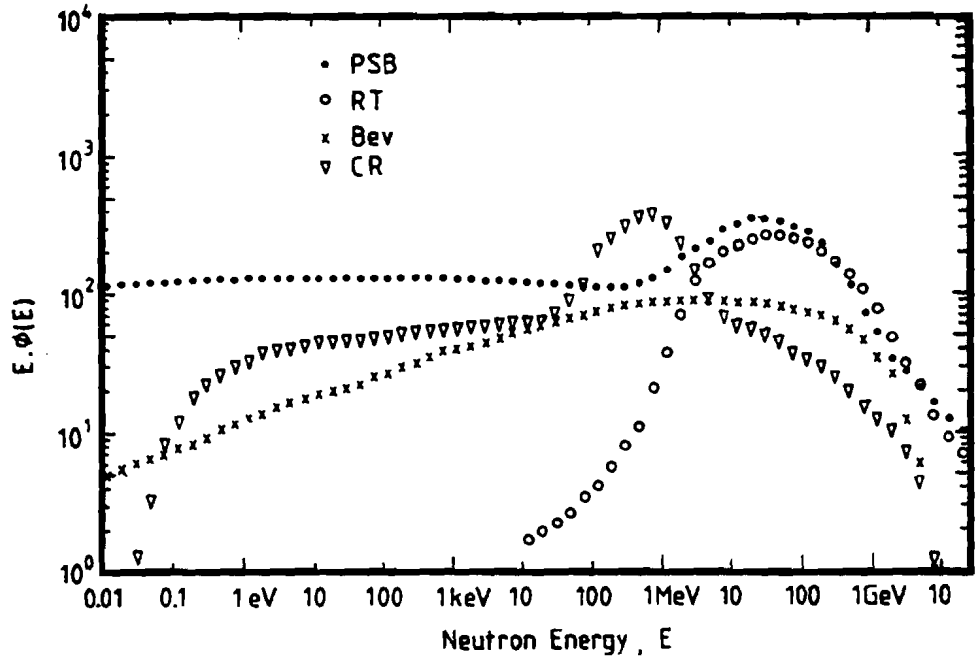

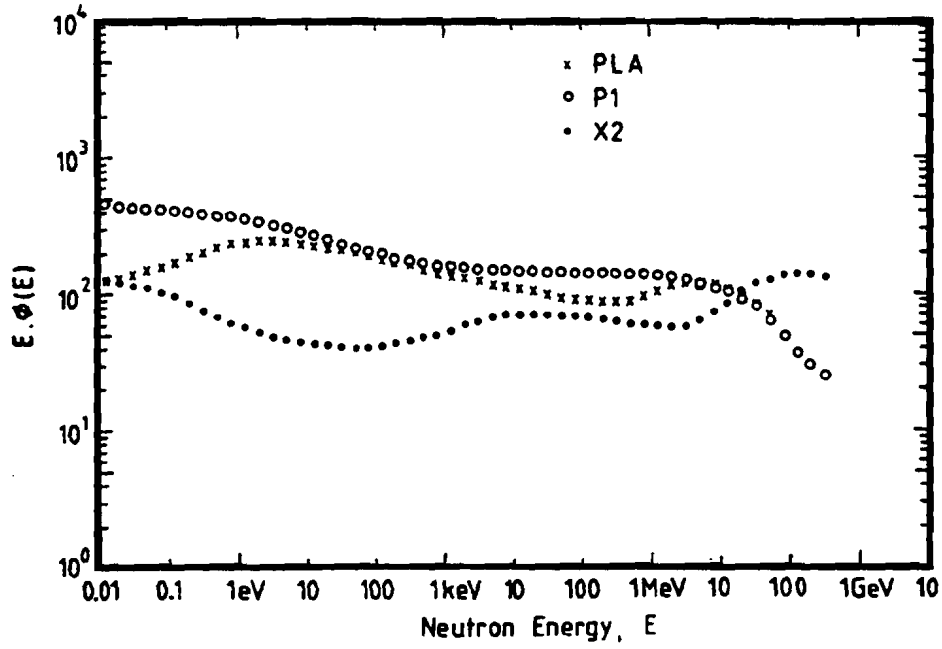

Figure 1.2. Neutron Spectra at Proton Accelerators Around The World. The upper plot was a measurement performed by the Health Physics Group of LBL in the mid-1960s. The lower plot was measured at the 7-GeV proton synchrotron (Nimrod) of the Rutherford Laboratory using Bonner spheres. Note that these spectra are relatively flat reflecting an approximate 1/E differential energy spectrum. See text for explanation of the legends. [From Swanson and Thomas 1990]

four detectors were used to perform the measurements in the mid 1960s: A BF_3 tube in a cylindrical moderator, two activation detectors based on $^{12}C(n,2n)^{11}C$ and $^{27}Al(n,\alpha)^{24}Na$ reactions, and a bismuth ionization chamber. These spectra are well defined in the energy range between 0.1 and 100 MeV, but are not very accurate outside this range. The PSB and RT spectra were both measured above a target area outside shielding; the main difference between them is in the type and amount of shielding material. It can be seen from Figure 1.2 upper plot, that the RT spectrum is much harder (that is, more energetic) than that of the PSB probably due to the amount of moisture in the earth shielding, which absorbed most of the thermal neutrons. Both spectra present a well defined peak in the region between 10 and 100 MeV, and their shape agrees very well within that energy range. The BEV spectrum does not show a well defined peak in the 1 to 100 MeV energy interval. The CR spectrum shows a well defined peak between 100 keV and 1 MeV, and drops off around 10 MeV.

The lower plot in Figure 1.2 shows the three spectra (PLA, P1, X2) measured outside shielding at Rutherford Laboratory utilizing a Bonner Sphere Spectrometer with a ^{6}LiI scintillator. Those curves are relatively flat, when plotted as indicated, reflecting the existence of an approximate 1/E differential energy spectrum. The PLA spectrum was taken near the 50 MeV proton linac and is due mainly to skyshine. The X2 and P1 were both taken outside shielding at a 7 GeV proton synchrotron, the main difference again is in the shielding material; the X2 had concrete as shielding whereas the P1 was measured outside steel shielding. In addition the X2 spectrum is somewhat harder than the P1 spectrum which had the outer shield made of iron, and also there was a contribution coming from neutrons scattered by neighboring concrete blocks.

A comparison of the radiation environment outside the shielding of the 6.3 GeV Bevatron proton accelerator at Lawrence Berkeley Laboratory (LBL) and the

20 GeV Electron Accelerator at Stanford (SLAC) was published in the mid-seventies [McCaslin et al 1977]. Even though the total dose equivalent rate measured by three participants groups at SLAC were in reasonable agreement, there were large differences in the neutron and photon dose equivalent rates determined by use of the different techniques employed by LBL and SLAC.

More recently, results of measurements describing the leakage of neutrons through an iron shield were reported [Elwyn et al.1986]. These measurements showed that a large fluence of neutrons with energies between 5 keV and 1 MeV, escaped from the iron because of the very low inelastic cross section of ^{56}Fe at these energies. The authors showed, furthermore, that with the addition of 0.9 m of concrete shielding external to the iron blocks, these neutrons were eliminated from the field outside of the shield. Also, the quality factor of the radiation environment was reduced by a factor of two when the concrete shielding was added.

Another series of investigations [Cossairt et al.1988] to detect neutrons by use of Bonner multispheres, both with $^{6}LiI(Eu)$ scintillators and $^{6,7}LiF$ TLD's, have been reported. These measurements were done in enclosures and outside of shielding at Fermilab. Some of the spectra indicated that high energy neutrons (E_n>25 MeV) contributed more than 30% to the dose equivalent.

Moritz et al. [1989, 1990] have performed measurements at a 500 MeV proton accelerator at TRIUMF and at a 12 GeV proton accelerator at KEK (Japan). Those measurements were done using a set of multispheres along with a passive activation detector based on the $^{12}C(n,2n)^{11}C$ to better characterize the high energy neutron region. At KEK, it was found that neutrons with energy greater than 50 MeV contributed about 50% to the dose equivalent. At TRIUMF, for the "hardest" (that is, most energetic) spectrum, more than 70% of the dose equivalent came from neutrons with energy higher than 20 MeV.

The importance of measuring neutron spectra around high energy accelera-

tors is well recognized for the reasons outlined in this chapter, but except for the measurements mentioned above little experimental work has been done recently. The current experiment represents an attempt to quantify neutron radiation field measurements more completely in some specific cases, and, insofar as possible to benchmark this data to an appropriate hadronic transport code.

Chapter 2

Experimental Setup and Measurements

2.1 Fermilab

Fermilab is an high energy accelerator laboratory funded by the Department of Energy located on a 6800 acre site about 40 miles west of Chicago. The accelerator actually consists of a series of five accelerators in series:

a) A Cockcroft-Walton machine, in which negative hydrogen ions are accelerated up to 750keV.

b) A linear accelerator (Linac), where the ions are accelerated through a distance of approximately 200 meters up to 200MeV (recently the energy was upgraded to 400 MeV), and then pass through a stripping foil that removes the electrons leaving only the protons for the next stage of acceleration.

c)The Booster, a synchrotron 170 meters in diameter, where the protons are accelerated to an energy of 8 GeV for injection into the Main Ring, the next stage of acceleration.

d) The Main Ring, a proton synchrotron which is 6.3 kilometer in circumference and accelerates the protons up to 150 GeV at which energy the particles are loaded into the last stage of acceleration, the Tevatron.

e) The Tevatron is a proton synchrotron with superconducting magnets, and has the ability to accelerate the protons to almost 1 TeV.

During the fixed-target running period the beam is extracted from the Tevatron once every minute delivering a 23 second spill. The extracted beam is split and sent to three experimental areas where as many as fifteen experiments can be performed simultaneously.

The present measurements to characterize the neutron radiation field outside shielding were made in two different experimental areas at Fermilab, the Neutrino West (NWA) and the Proton Center (PC-4) beam lines. These are shown schematically in Figure 2.1.

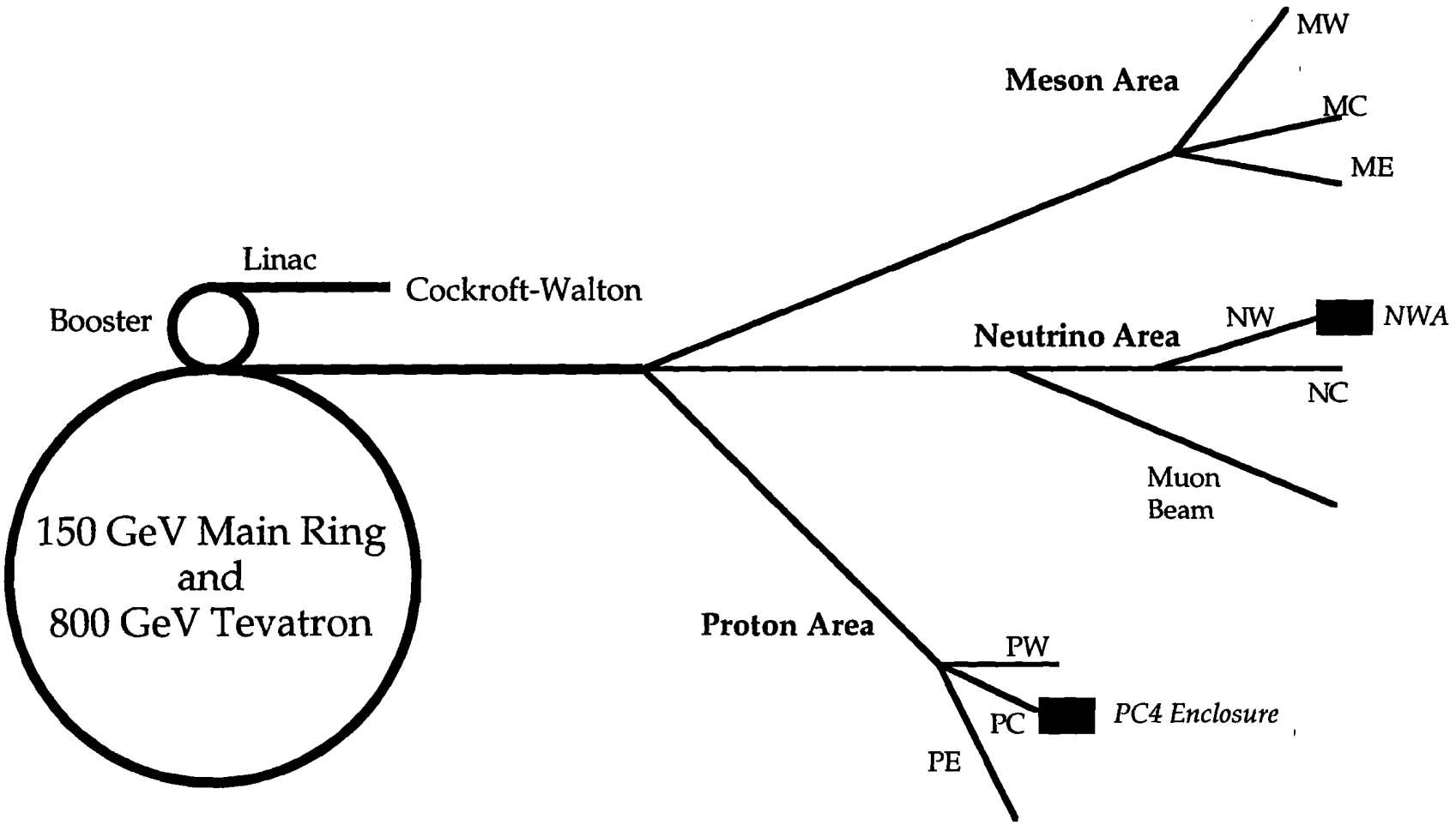

Figure 2.1. Fermi National Accelerator Laboratory Accelerator Complex. Shown schematically are the Fermilab accelerator complex and the "fixed target" beamlines. Also noted are the locations of enclosures NWA and PC-4.

2.2 The NWA Measurements

The first measurements discussed in this study were made during the 1991-1992 fixed target run at Fermilab, in the NWA enclosure at the NW beam line. The beam stop (Fig. 2.2, 2.3) which was constructed out of a series of iron slabs was used as absorbing material for the incident beam. A gap was left in the iron region to accommodate the insertion of the detectors, and the movement of the individual iron slabs from front to back permitted measurements at different depths in iron. In addition, the iron was surrounded on three sides by large blocks of concrete, which helped to shield the detectors from background due to adjacent beam lines.

The particles incident on this beam stop were negative pions with energies between 25 and 150 GeV measured to within an accuracy of about one percent. The beam impinged on iron shield blocks of transverse dimensions 95 cm by 183 cm and a total thickness of 264 cm. Neutron spectra were obtained with a Bonner Sphere Spectrometer using seven spheres, described in this Chapter (Section 2.4), at ten depths in the forward direction from 40.6 cm (2.4 λ) to 264 cm (15.7 λ) in intervals of approximately 20.3 cm, and at one depth laterally 60.9 cm (3.6 λ). The interaction mean free path, λ, in Fe for high energy hadrons was taken as 17 cm. As will be seen, λ is useful as it sets the distance scale of the shielding.

2.3 The Proton Center Measurements (PC-4)

The second set of measurements were performed to characterize the neutron field outside of a representative shielded enclosure at Fermilab. The location was outside the PC-4 enclosure at the PC beam line. The radiation field at this location includes neutrons that emerge from the target and beam dump, and the shield consists of iron as well as concrete. Figure 2.4 shows an elevation view of the area with the respective positions at which measurements were made. A beam of 800 GeV protons strikes a Cu target 15 cm long just before entering the large electromagnet (hyperon magnet). The protons that do not interact with the target are

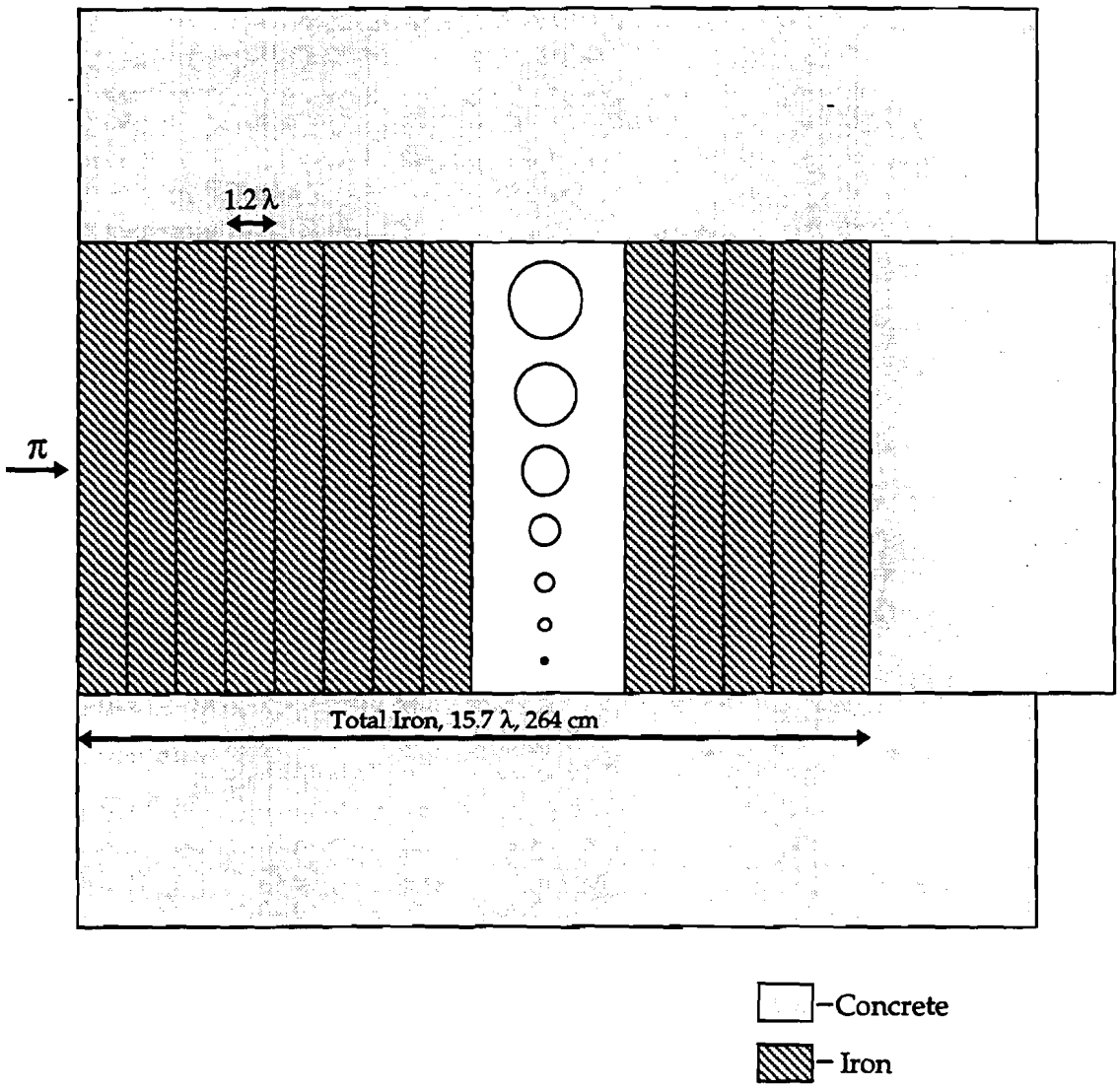

Figure 2.2. Top View of a Beam Dump at NWA. This drawing shows the configuration of the iron beam dump at NWA where data were taken at nine depths (2.4 λ to 15.7 λ), using a Bonner Sphere Spectrometer, shown as the circles in the figure.

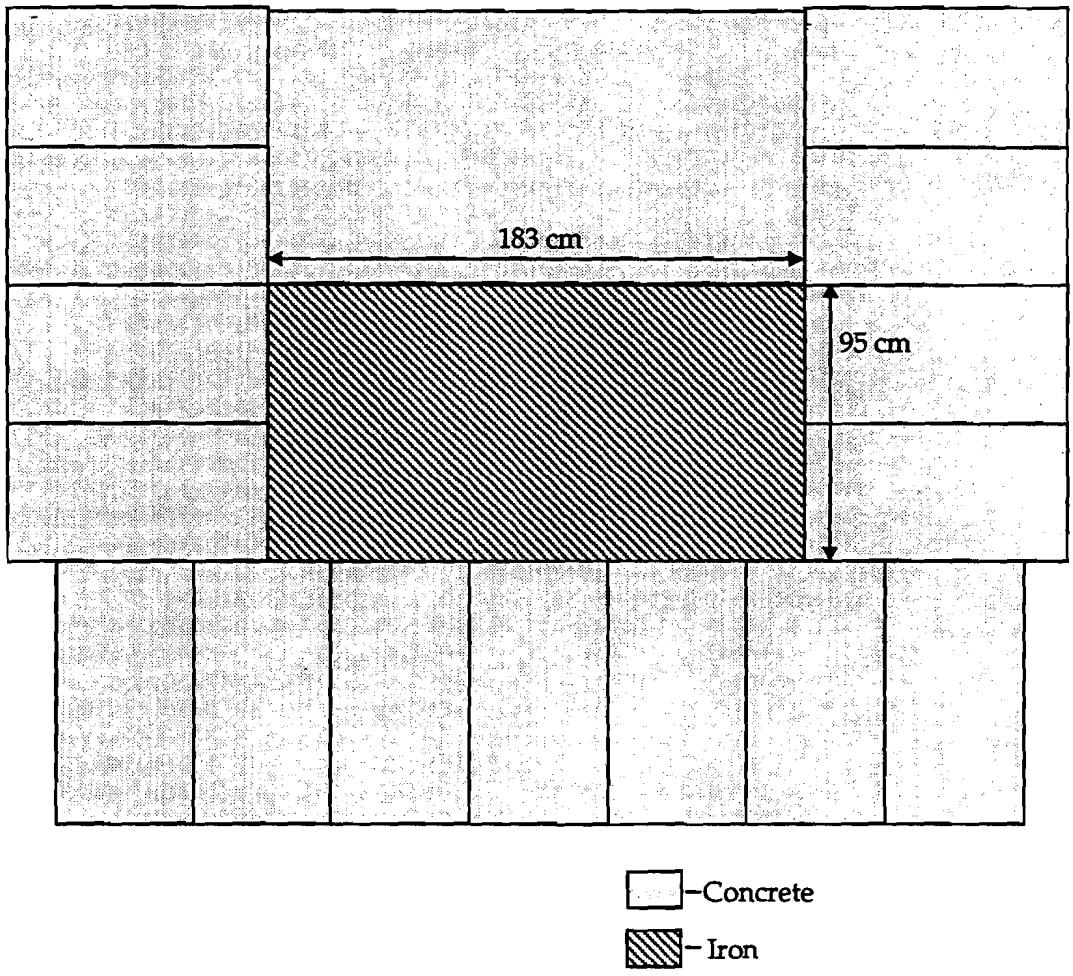

Figure 2.3. Front View of a Beam Dump at NWA. This drawing showing the configuration and dimensions of the iron beam dump built at NWA where data were taken at nine depths (2.4 λ to 15.7 λ), using a Bonner Sphere Spectrometer.

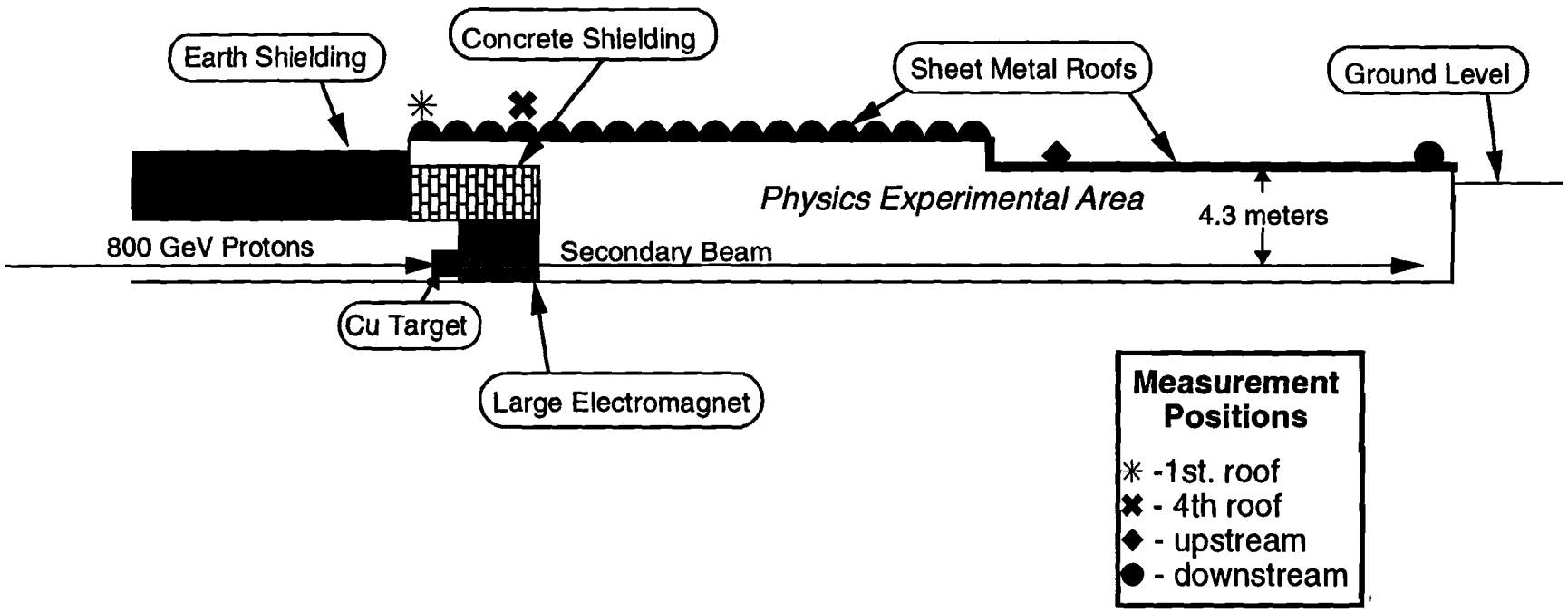

Figure 2.4. PC-4 Area Elevation View in the Plane of the Beam. This drawing shows the configuration of the PC-4 beam line, as well as the four positions where measurements were performed.

dumped in the entrance of the magnet which is composed of tungsten and iron. Those that interact in the target produce hyperons that are extracted at the end of the magnet; the dimensions of the magnet are 7 m long by 2.07 m high by 2.97 m wide.

Measurements of the neutron spectra were made at four locations as shown in Figure 2.4. Two of the measurements were performed on the first and fourth roof over the hyperon magnet enclosure and the other two were done downstream on the hyperon enclosure extension. All measurements, except the one at the "first roof", were done at three different beam targeting angles of 0, +3 and –3 milliradians. The neutron spectra were obtained as were the measurements at NWA by the use of a Bonner Sphere Spectrometer, but in this case a full set of eight spheres were used.

It is known [Cossairt et al. 1987] that the radiation field at locations around the PC-4 enclosure contains a sizeable contribution from muons produced in hadronic cascades in the target and shielding. These muons are essentially minimum ionizing particles, and would (ideally) produce a peak in the spectrum of pulse heights for each detector at a pulse height considerably larger than that associated with neutrons [Mc Caslin et al. 1986]. Although this peak would be quite broad it would still be well separated from neutrons. There is no evidence seen in the pulse height spectrum (see Section 2.4) of any contribution from muons in the vicinity of the neutron peak in the ^{6}LiI(Eu) scintillator.

2.4 The Detectors

To carry out these measurements a Bonner Sphere Spectrometer (BSS) [Bramblett et al. 1960] was used as the principal neutron detector. This device consists of a set of spheres, made of polyethylene with diameters of 5.1 cm (2"), 7.6 cm (3"), 12.7 cm (5"), 20.3 cm (8"), 25.4 cm (10"), 30.5 cm (12") and 45.7 (18") cm (although the largest one was not used for the NWA measurements because of space

limitations) at the center of which are placed 12.7 mm diameter by 12.7 mm long cylindrical ^{6}LiI(Eu) scintillators (Fig. 2.5, 2.6) which respond mainly to thermal neutrons via the ^{6}Li(n,α)^{3}H reaction. A bare (unmoderated) detector was also used.

Figures 2.7 and 2.8 show a typical pulse height spectrum from the ^{6}LiI(Eu) scintillator. The neutron peak is well separated from contributions due to gamma rays and background (and, as mentioned in the previous section, from any minimum ionizing muons). The peak arises from the capture of thermal neutrons leading to the ^{6}Li(n,α)^{3}H reaction which is exothermic with a Q-value of 4.78 MeV, and the area under the curve represents the detector response. The dimensions of the crystal itself are chosen to limit the light output from electrons or other external charged particles crossing it. About 80% of incident thermal neutrons are absorbed in 1 mm of ^{6}Li so detection of thermal neutrons is essentially a surface effect, whereas the detection of gamma rays and fast neutrons is roughly proportional to the volume of the crystal. In addition to reducing the number of gamma ray pulses, the small size of the crystals limits the maximum size pulse due to gamma rays and good gamma ray discrimination is obtained. Li is an extremely hygroscopic substance and even well sealed crystals tend to degrade in time. The degradation is evident by a change in crystal color and an increase in the width of the (n,α) peak.

By placing the scintillators in the center of moderating polyethylene spheres (ρ = 0.95 g/cm^3) of different diameters, the detector becomes sensitive to neutrons in a very broad energy range [Awschalom et al. 1985, Bramblett et al. 1960] because of the moderating properties of polyethylene. The energy response of each detector is shown in Figure 2.9. The absolute neutron detection efficiency is typically 0.1%-0.2%. These data (Fig. 2.9) are based on the calculations of Sanna [1973], and are referred to as response functions.

One can see from Figure 2.9 that the bare unmoderated detector responds mainly to thermal neutrons. The 2" and 3" spheres respond almost equally to neu-

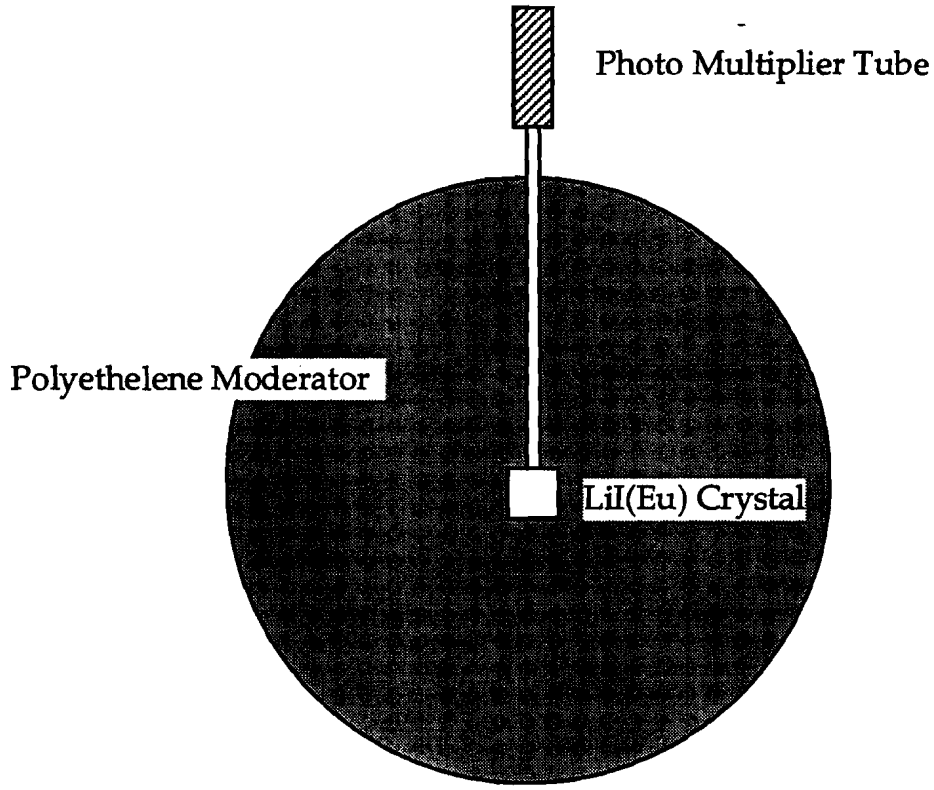

Figure 2.5. Bonner Sphere Schematic. A Bonner Sphere detector that uses polyethylene as moderator, and with a LiI(Eu) scintillator inserted in the center of the sphere and connected to a photomultiplier through a light pipe is shown.

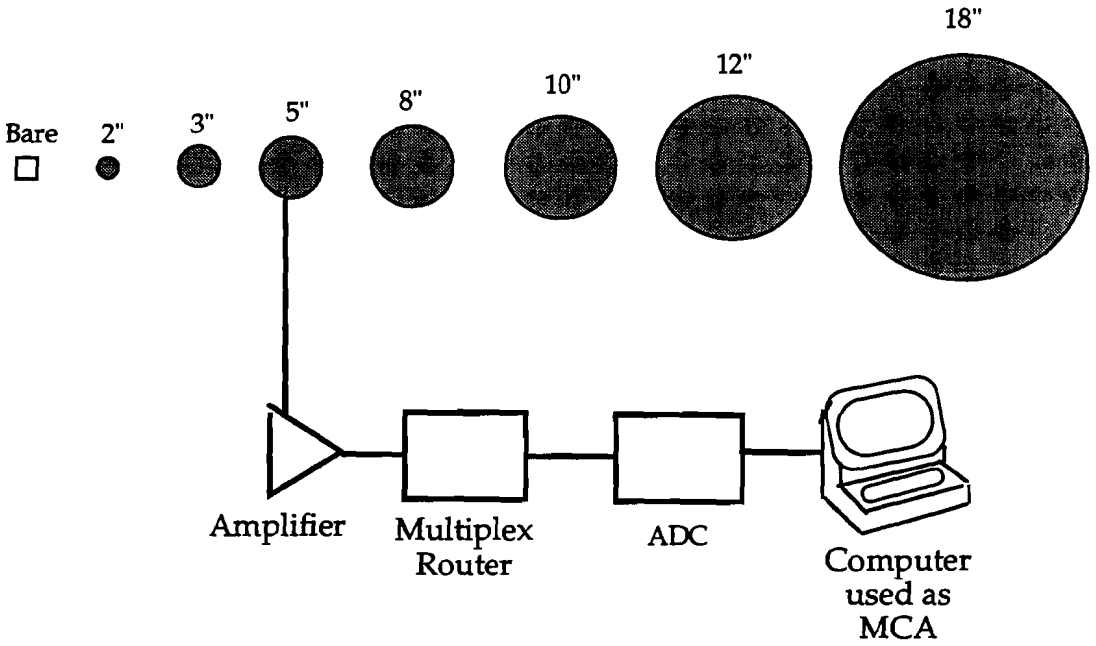

Figure 2.6. Bonner Sphere Spectrometer Set-up. A set of polyethylene moderated spheres of various diameters along with a bare (unmoderated) detector was used simultaneously to collect data at PC-4 and NWA. Each sphere had a ^{6}LiI(Eu) scintillator inserted at its center and connected to an amplifier through a light pipe. The signal from the scintillator was recorded in the computer which was used as a MCA.

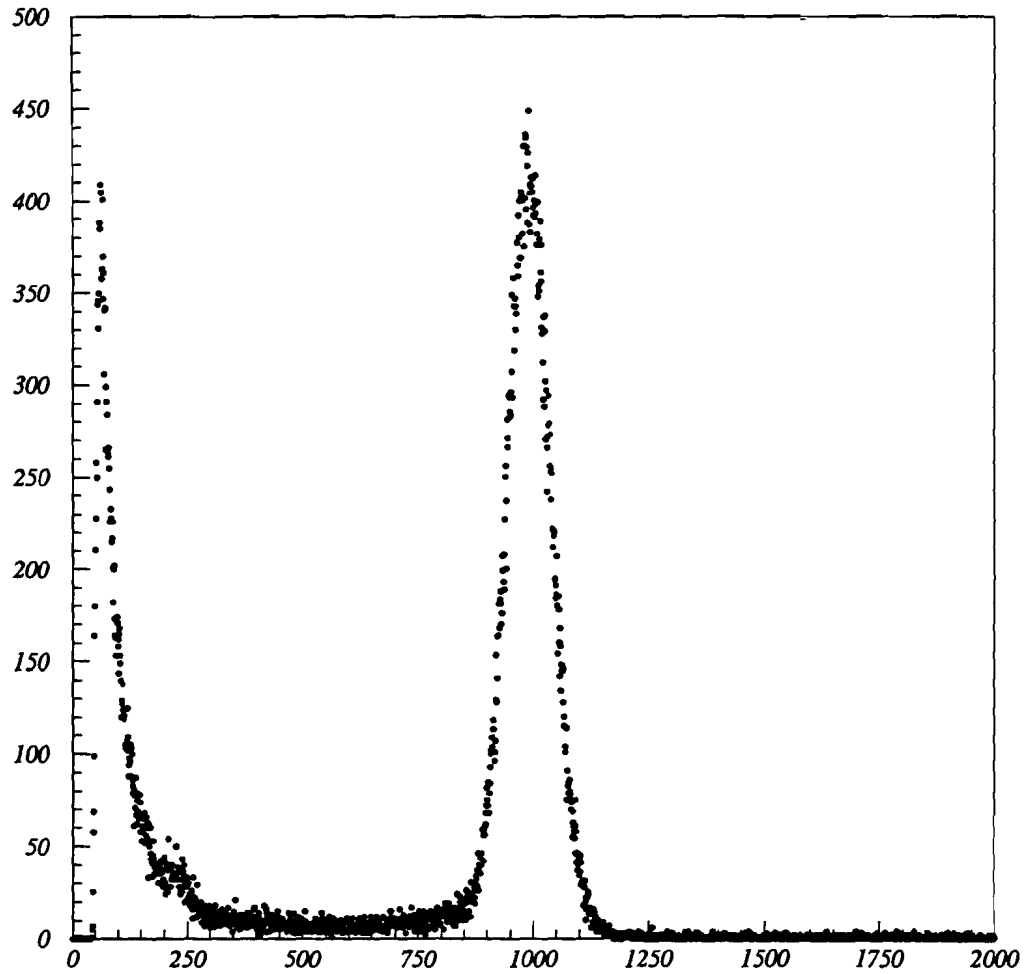

Figure 2.7. ^{6}LiI(Eu) Pulse Height Spectrum. Shown is a typical pulse height spectrum from an individual Bonner Sphere recorded by the multi-channel analyzer. Note that the neutron signal peaks at approximately channel 1000. The low pulse height peak is due to photons and noise.

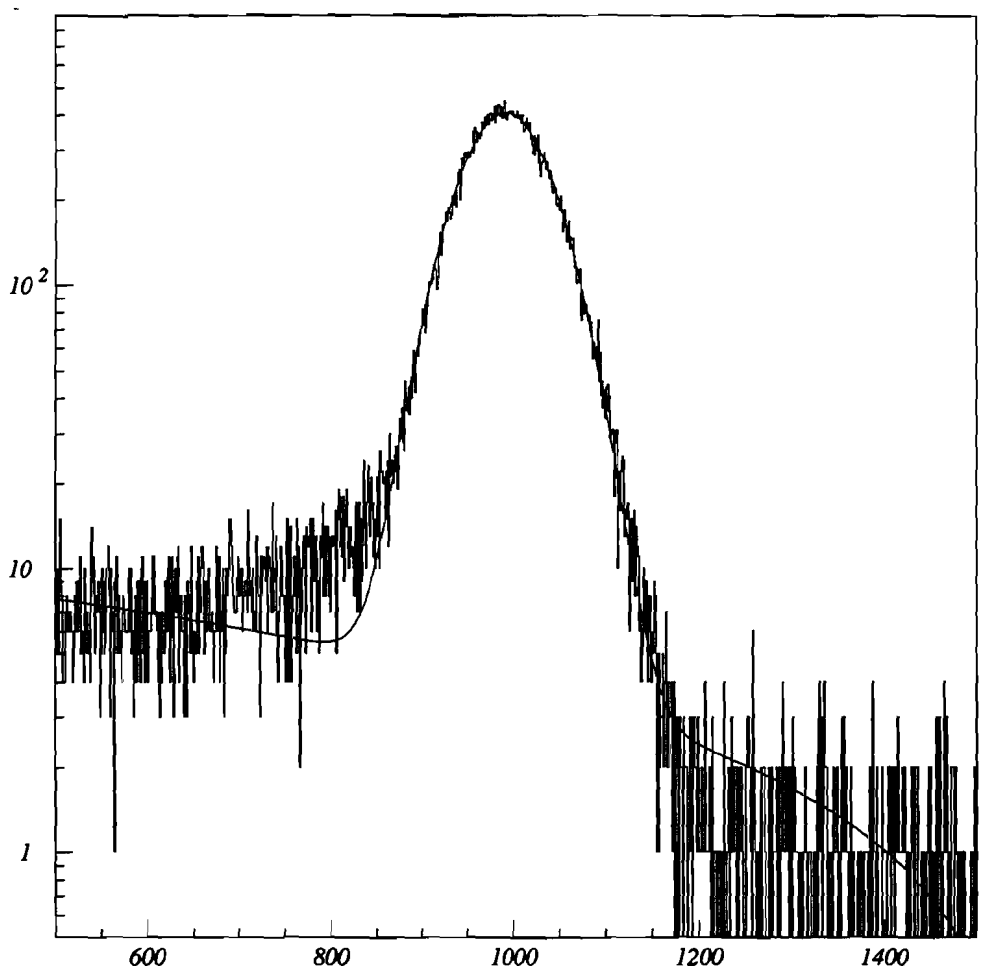

Figure 2.8. Bonner Sphere Neutron Signal. Shown is the neutron signal region of the pulse height spectrum of Figure 2.7. The spectrum has been plotted logarithmically and the data fit to a Gaussian (for the signal) and a second order polynominal for the background. Note that the signal is well represented by a Gaussian while the background is adequately parameterized by the polynominal.

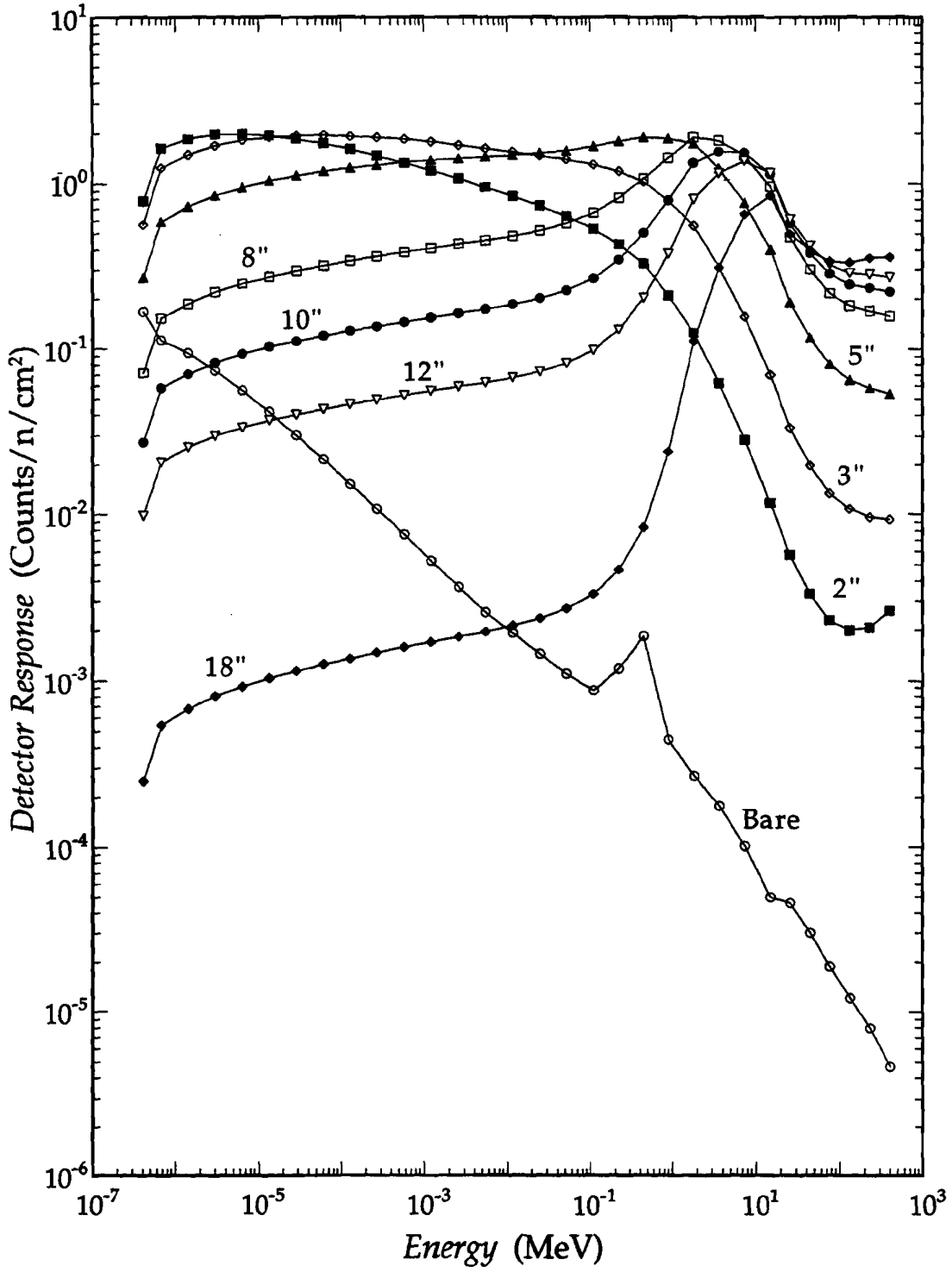

Figure 2.9. Response Functions for a 12.7 mm by 12.7 mm ^{6}LiI(Eu) Scintillator. Plotted are Sanna's response functions for a 12.7 mm by 12.7 mm Li scintillator for the 2" (■), 3" (◇), 5" (▲), 8" (□), 10" (●), 12" (▽), 18" (◆) and a bare (○) detectors. Note that the bare detector responds mainly to thermal neutrons.

trons up to about 10^{-2} to 10^{-1} MeV, and then drop off beyond 1 MeV. The 8",10" and 12" spheres respond maximally to neutrons with energy between 1 and 10 MeV. The response of the 18" sphere is similar to that of the 12" sphere but slightly larger at energies above 10 MeV. Even though the Bonner Sphere Spectrometer may not be very sensitive to neutrons of energies higher than 20 MeV the response functions have been calculated up to a few hundred MeV.

Figure 2.6 shows, schematically, ^{6}LiI(Eu) detectors placed at the center of each sphere connected to photomultipliers tubes. These spherical detectors are then placed simultaneously into the neutron radiation field, and the signal from each photomultiplier is transmitted through an amplifier (one for each detector) to a multiplex router and an ADC, and finally into a PC. Software developed by Canberra [1988] allowed the use of the computer as a multichannel pulse height analyzer.

The main advantage of a BSS is that it covers a very broad energy range. The major disadvantage is its low energy resolution. If one uses multiple detectors, one for each moderator, and makes simultaneous exposure of the entire system in the radiation field of interest, two concerns can be identified: The first addresses the issue of whether the spectral shape is the same at all points along the total length of the detector array. The second is about the spatial variation of the neutron field and the need to correct for non uniformity of the neutron flux along the length of the detector array, since data analysis requires that the same neutron flux must be incident on each detector. These issues will be discussed further in Chapters 3 and 4.

The measured neutron counting rate from each Bonner sphere (along with that from the bare detector as well) are related to neutron fluence by the so called Fredholm equation:

$$B_j = \int_0^\infty N(E) R_j(E) dE \quad , \qquad 2.1$$

with $j = 1, 2, ..., r$.

Here:

r = number of detectors

B_j = is the response for the j-th detector in the array.

$N(E)$ = dN/dE is the neutron fluence in units such as n/cm^2-MeV

and

$R_j(E)$ = is the absolute response for the j-th detector as function of neutron energy, in neutron counts per unit of fluence.

These response functions $R_j(E)$ have been calculated by a number of authors. As mentioned above the response funtions of Sanna [1973] were used in the present work.

Given the values of $R_j(E)$ and the measured neutron counts in each sphere B_j, the determination of the fluence as function of energy can be obtained by the use of unfolding techniques. Spectral unfolding will be discussed in more detail in the next chapter.

For the NWA measurements, a second neutron detection scheme based on the use of an organic liquid scintillator was employed in order to extend the neutron response to energies well above 20 MeV. Unfortunately, attempts to calibrate these devices failed, and no useable information could be obtained. A preliminary measurements based on the radioactivation [McCaslin 1959] of ^{11}C through the $^{12}C(n,2n)^{11}C$ reaction, with a threshold of 20.4 MeV, was also tried. Initial studies suggested that the total number of neutrons with energies higher than 20 MeV was quite small. Unfortunately, because of the untimely conclusion of the fixed target run at the Tevatron, the technique could not be developed sufficiently for a quantitative assessment, so that no hard experimental information on the neutron spectrum at energies much greater than 20 MeV could be obtained.

Chapter 3

Data Analysis

3.1 Normalization of NWA Data

Data was taken simultaneously with a set of six Bonner spheres (the 45.7 cm diameter sphere was not used) plus a bare detector with the spheres deployed as indicated in Figure 3.1 They were set onto a platform such that their centers were 82.5 cm above the floor; the pion beam on the other hand was centered at a position 57 cm above the floor. The profile of the neutron beam at the detector position was determined by moving the 5" (12.7 cm) diameter sphere to the location of the 3", 8", 10" and 12" diameter spheres, and at four depths 40.6 cm, 121.9 cm, 162.6 cm and 243.8 cm and two pion energies (except for the 162.6 cm case where data was taken at only one incident pion energy). (It is conventional to refer to the spheres in terms of the English units. The metric equivalent is defined in Section 2.4.) Figure 3.2 shows an illustration of the beam profile spectrum taken at a depth of 40.6 cm and 100 GeV. It was observed from plots of all these data that the shape of the neutron profile was independent of both incident beam energy and thickness of iron. Therefore, it was concluded that no further data at other depths and energies were needed to define the shape of the neutron beam after the incident pion beam had struck the iron shield. As a result of these observations the beam profile peaks near the 8" detector location. In reference to Figure 3.1, a cartesian coordinate system (x,y) can be defined such that the beam position at the longitudinal coordinate z that corresponds to the position of the detectors is (0,0) and the coordinates of the 8 " sphere are (0,25.4)(in cm). The distance to each sphere i from the beam center (0,0) is defined as $r_i^2=x_i^2+(25.4)^2$. Data from all spheres, at each energy and thick-

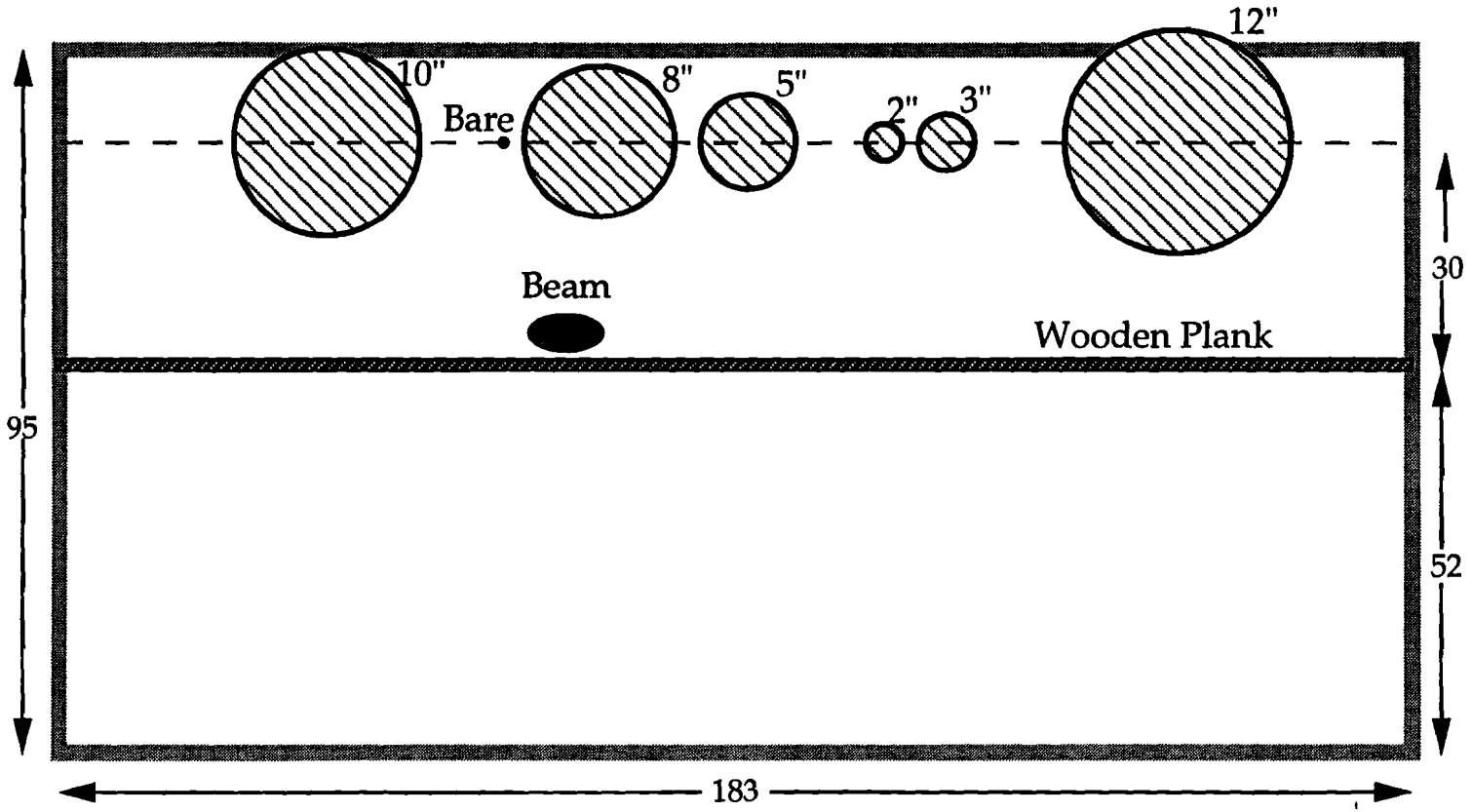

Figure 3.1. Bonner Sphere Layout. Shown is the layout of the Bonner sphere spectrometer used at NWA. The pion beam is traveling into the page. The extent of the iron plate shielding is indicated by the gray outline. The positions of the spheres, beam and the wooden plank support structure are shown. The dimensions indicated are in centimeters. The origin of the coordinate system is at the center of the beam position.

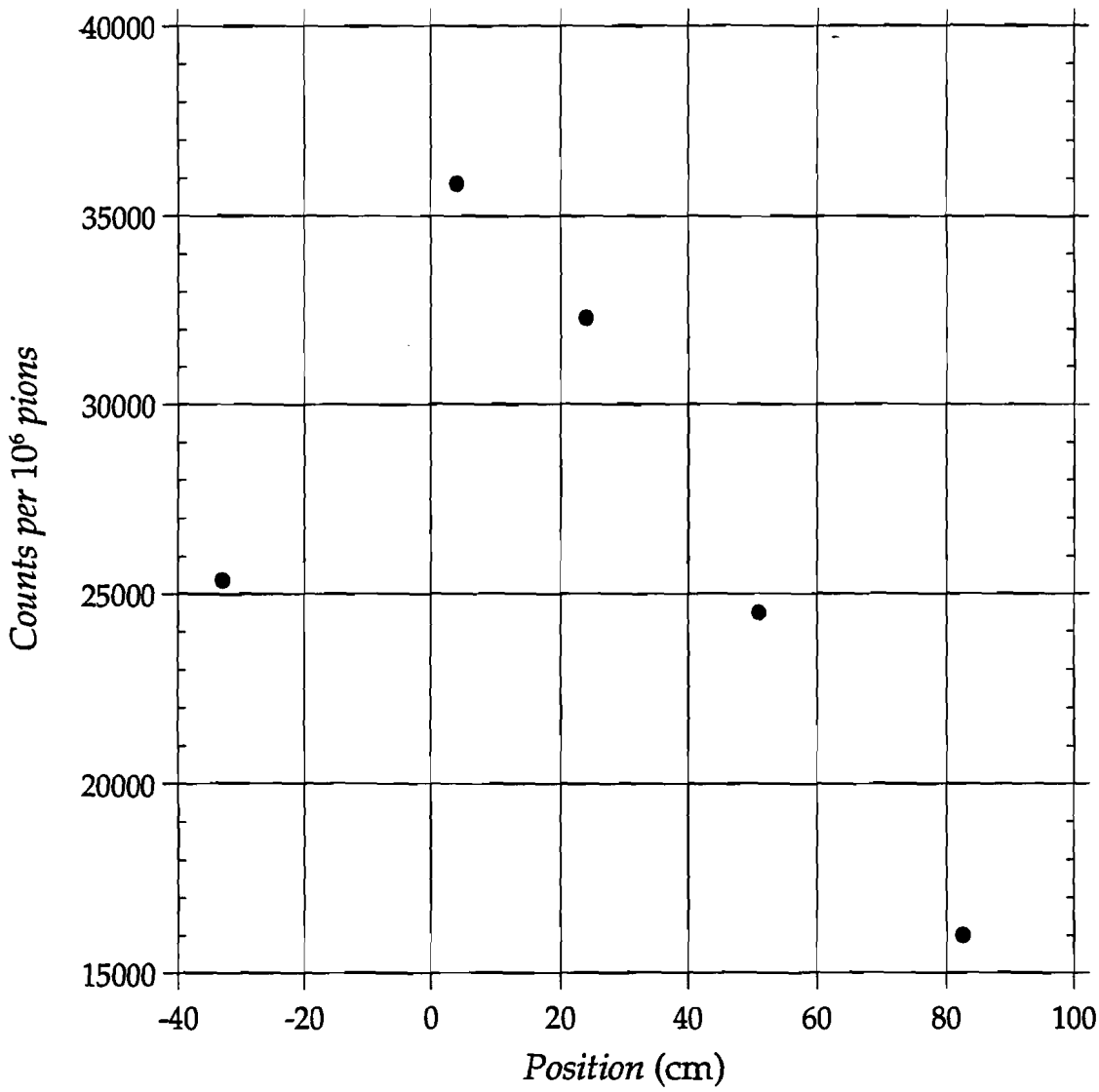

Figure 3.2. Beam Profile Study at 100 GeV. Measurement taken with a 5" Bonner sphere at 40.6 cm depth.

ness, were first normalized to the neutron fluence at the 8" sphere position by dividing the measured sphere responses by normalized factors defined as the ratios of the counts in the 5" sphere at each sphere location along the array to that in the 5" sphere at the position of the 8" sphere, (0,25.4). The data were then renormalized to the beam position (0,0) by multiplying these normalized responses in each sphere by the y-intercept in a linear fit to the normalization factors plotted as a function of r.

This procedure, as mentioned in Chapter 2, assumes that the shape of the spectrum does not change with transverse location along the detector array in back of the iron shield. The validity of this assumption will be discussed in Chapter 4.

The number of pions delivered during the 23 second beam spill that occurs every 60 seconds was determined by use of a pair of plastic scintillators in coincidence placed to intercept the pion beam approximately 40 meters up stream of the iron blocks. The total neutron counts obtained by each detector was divided by the total number of pions for that specific run, to obtain the final neutron responses in each detector per incident pion.

3.2 Normalization of Proton Center PC-4 Data

During the fixed target run of August 1990 a set of 7 Bonner spheres with their detectors plus a bare detector were deployed simultaneously to collect data over four different locations at PC-4 (see Fig. 2.4). Two tissue equivalent ion chambers (Fermilab- designed Chipmunks) [Awschalom 1972] were deployed at both ends of the detector array. The response (counting rate) of each sphere was normalized to the same incident neutron fluence by linear interpolation between the counting rates in these two tissue equivalent chambers. The data were further normalized to the total number of protons incident on the PC-4 beam line.

3.3 Spectral Unfolding

The normalized neutron response of each detector is related to the neutron

spectrum as indicated by Equation 2.1 in Section 2.4. If the response functions $R_j(E)$ are known analytically or can be calculated, the neutron spectrum N(E) can in principle be unfolded from the data [Gollon 1983]. In the present case, response functions calculated by Sanna for 12.7 mm by 12.7 mm ^{6}Li detectors were used as a good approximation of the ^{6}LiI(Eu) scintillator responses. Since these are not analytic functions, standard mathematical unfolding techniques can not be used, and other procedures have been developed.

In general, to solve this problem, Equation 2.1 is replaced by a discrete summation:

$$B_j = \sum_{g=1}^{N} N_g R_{jg} \Delta E_g \qquad 3.1$$

where the index j=1,2...r, with r the number of neutron detectors, and g = 1, 2....N the numbers of discrete energy intervals into which the energy region is divided. The unfolding problem then is to solve a system of "r" linear equations (the number of neutron detectors) in "N" unknowns (the number of energy intervals). Since the number of detectors is in general less than the number of energy intervals used to describe the spectrum, no unique solution exists for Equation 3.1. However a number of computer programs [Lowry et al. 1984, Routti et al. 1980] have been developed to yield approximate solutions by quadrature methods. From the set of approximate solutions, those having physically acceptable characteristics such as smoothness and non-negativity are chosen to yield "appropriate solutions". The quadrature method involves the solution of Equation 3.1 by linear estimation, least squares, or a combination. The BUNKI [Lowry et al. 1984] and LOUHI [Routti et al. 1980] computer codes used in the present studies belong to such categories. It is useful to use two independent codes to gain confidence in the results of the unfolding because of the inherent mathematical difficulties of the unfolding problem. With only eight detectors and, in our case, thirty-one energy groups, one is left with the need to solve eight equations for thirty-one unknowns. The two computer pro-

grams mentioned above apply various constraints on the possible solutions that give acceptable final results.

BUNKI is based on an iterative recursion method and LOUHI on a least square method with user controlled constraints. With BUNKI, a choice between two initial spectra can be made. In the former, the neutron fluence spectrum is assumed to vary with energy as 1/E. In the latter, it can be approximated instead by a spectrum that has a high energy peak (in the form of a Maxwellian distribution) and a thermal peak connected by a 1/E type spectrum. This algorithm in BUNKI is called Maxiet.

In LOUHI, a priori information is implemented by transforming the group of linear equations into a minimization problem. A non-negative condition is implemented by expressing the unknown fluxes as the squares of real numbers. This evolves into a non-linear minimization problem that is solved by an iterative algorithm. Various user-supplied constraints can be imposed to obtain reasonably acceptable solutions.

An example of a neutron fluence spectrum unfolded from measured sphere responses is shown in Fig. 3.3. It is seen that the ordinate on the left plot is N(E) and the ordinate on the plot to the right is EN(E) not N(E) itself. This can be shown to be equivalent to neutron fluence per unit logarithmic energy (or, per unit lethargy), dN/d(LogE), and essentially suppresses the approximate "1/E" dependence of the spectrum to show more clearly any structural details. The neutron spectra obtained in these studies (shown in the next chapter) have been displayed in this manner. As discussed by Rohrig [1983], with this kind of representation the energy dependence is suppressed and spectral details are enhanced. Furthermore, the area under the curve for each energy bin is proportional to the neutron fluence within that bin.

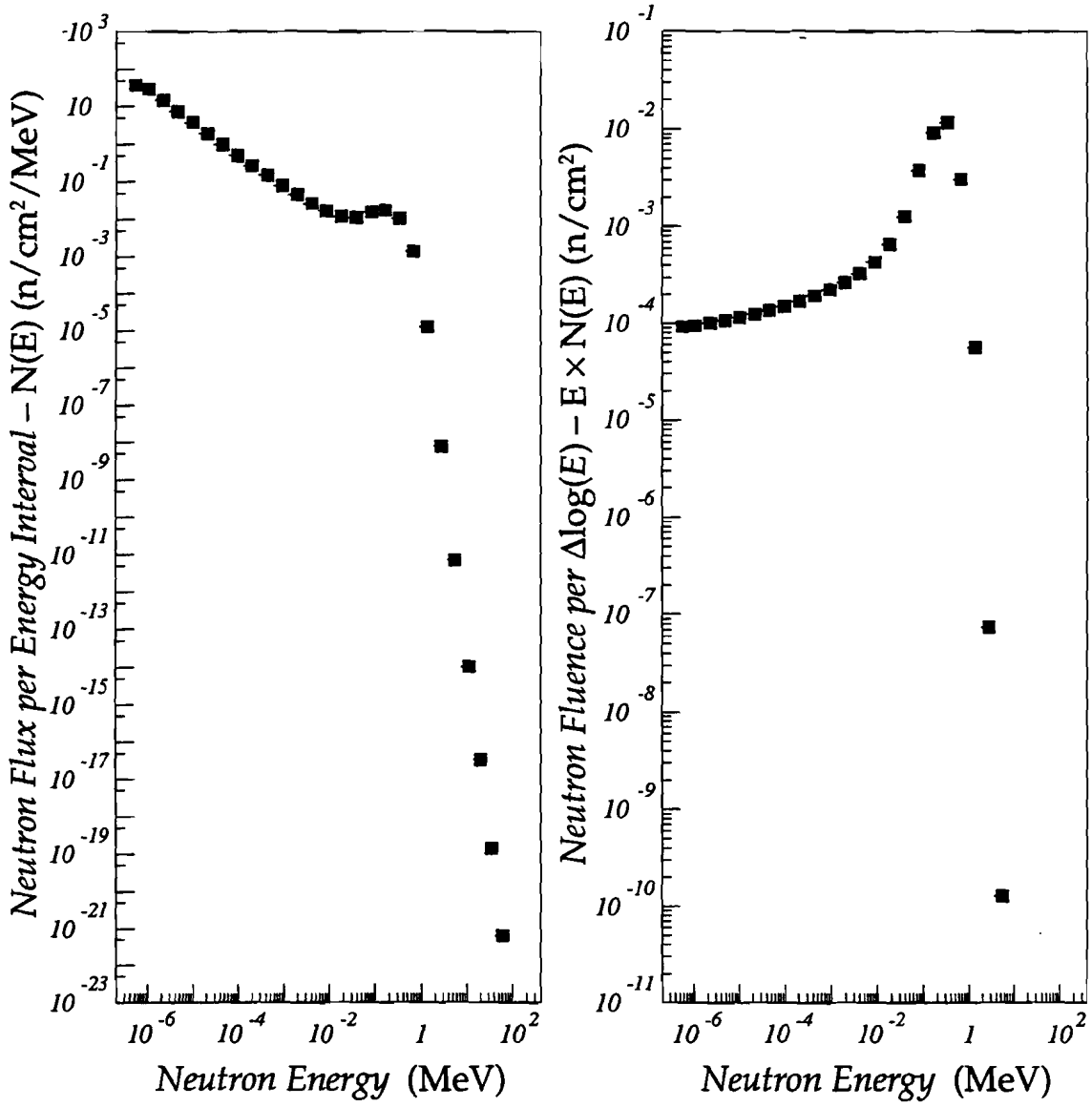

Figure 3.3. Unfolded Neutron Spectra for Incident Pions at 121.9 cm of Iron. Shown are the neutron spectra obtained by using the BUNKI unfolding code, for incident pions at 100 GeV on 121.9 cm (48 in, 7.3 λ) of iron. On the left plot the ordinate is N(E) and on the right plot is E x N(E) or dN/d(logE).

3 .4 Calibration of Bonner Sphere Spectrometer (BSS)

In order to check that the response matrices calculated by Sanna used in the spectral unfolding are reasonable, a set of 6 Bonner Sphere detectors (all except the 45.7 cm diameter sphere) plus an unmoderated (bare) detector were used to measure the neutron spectrum from an Am-Be neutron source. A neutron source can be used to verify that the response matrices used in the unfolding lead to the same spectral shape, fluence, quality factor and dose conversion factors as those that are known from a source with a given source strength (neutrons/sec). The detectors were exposed to the source at three different distances 100, 150 and 200 cm, in a large room at the Fermilab Radiation Physics Calibration Facility, and the responses corrected for room scattering. The source was covered with a 3 mm thick lead cap to cut off the 60 keV gamma radiation from ^{241}Am. Except for the ladder supporting the source and the detectors, all scattering objects were more than 2 m away. After unfolding, the measured fluence differed from that calculated from the known source strength by only 5 %; the average energy determined from the unfolding procedure was 4.1 MeV, in excellent agreement (within 10 %) with the known properties of Am-Be neutron sources. Also the conversion factor from dose equivalent to fluence agrees within 5 %, and the quality factor within 1 %, with the known properties of such neutron sources. Figure 3.4 shows the flux per unit lethargy as a function of energy for the Am-Be source at a distance of 100 cm from the detectors. A comparison is made with the measured results of Kluge et al. [1982], as presented in the IAEA [1990] compilation, and the agreement in spectral shape is excellent. The agreement establishes the " validity" of both the response functions and the BUNKI unfolding procedure at least at those energies appropriate to the Am-Be source neutrons.

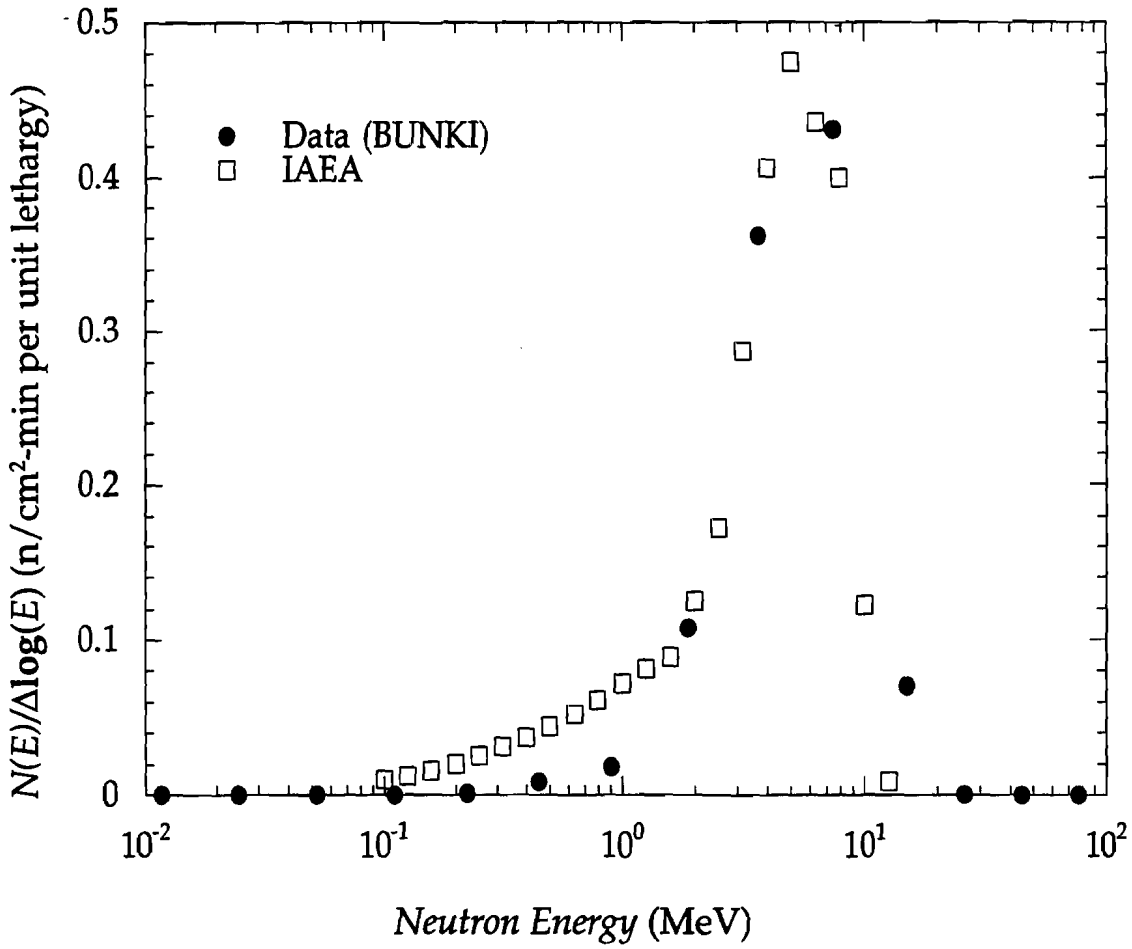

Figure 3.4. Unfolded Neutron Spectrum for Am-Be Source. A set of six Bonner spheres plus an unmoderated detector was used to acquire the data. This spectrum was unfolded by use of BUNKI. The source was positioned at 100 cm from the detectors. Also for purposes of comparison the spectrum from IAEA [1990] was plotted in the same figure.

Chapter 4

Results and Discussions

4.1 NWA and PC-4 Results

This chapter will describe the results and analyses of the measurements taken at NWA in the lateral and longitudinal directions as well as the attempt to model the shielding in both directions. Comparison with Monte Carlo calculations (FLUKA) will be shown for the longitudinal direction only. The results of measurements taken at Proton Center (PC-4) and comparison with CASIM, a Monte Carlo code, will also be discussed.

4.2 NWA Results at Longitudinal and Lateral Directions

Figures 4.1, 4.2 and 4.3 show the neutron spectra unfolded from the forward-direction (longitudinal) data using BUNKI for pions incident on 40.6 cm (2.4 λ), 162.6 cm (9.7 λ) and 243.8 cm (14.5 λ) of Fe. The ordinate is fluence per unit lethargy in order to display the spectral details more clearly, as discussed in Chapter 3. It is worth noting that the energy spectra peak at energies in the hundreds of keV range, and are sharply cut off at a few MeV; these are typical spectra of neutron leakage through Fe [Elwyn et al. 1986]. Very generally, one can say that the spectral shape is roughly independent of incident beam momentum and absorber (Fe) thickness although there are differences in the low neutron energy region where the fluence is, in any case, small. Total fluence increases with the energy for a given thickness. In all cases, there is little evidence of the existence of neutrons with energies higher than 10 MeV. This might be because of the poor response of the Bonner Sphere Spectrometer to such neutrons. However, a preliminary measurement that utilized

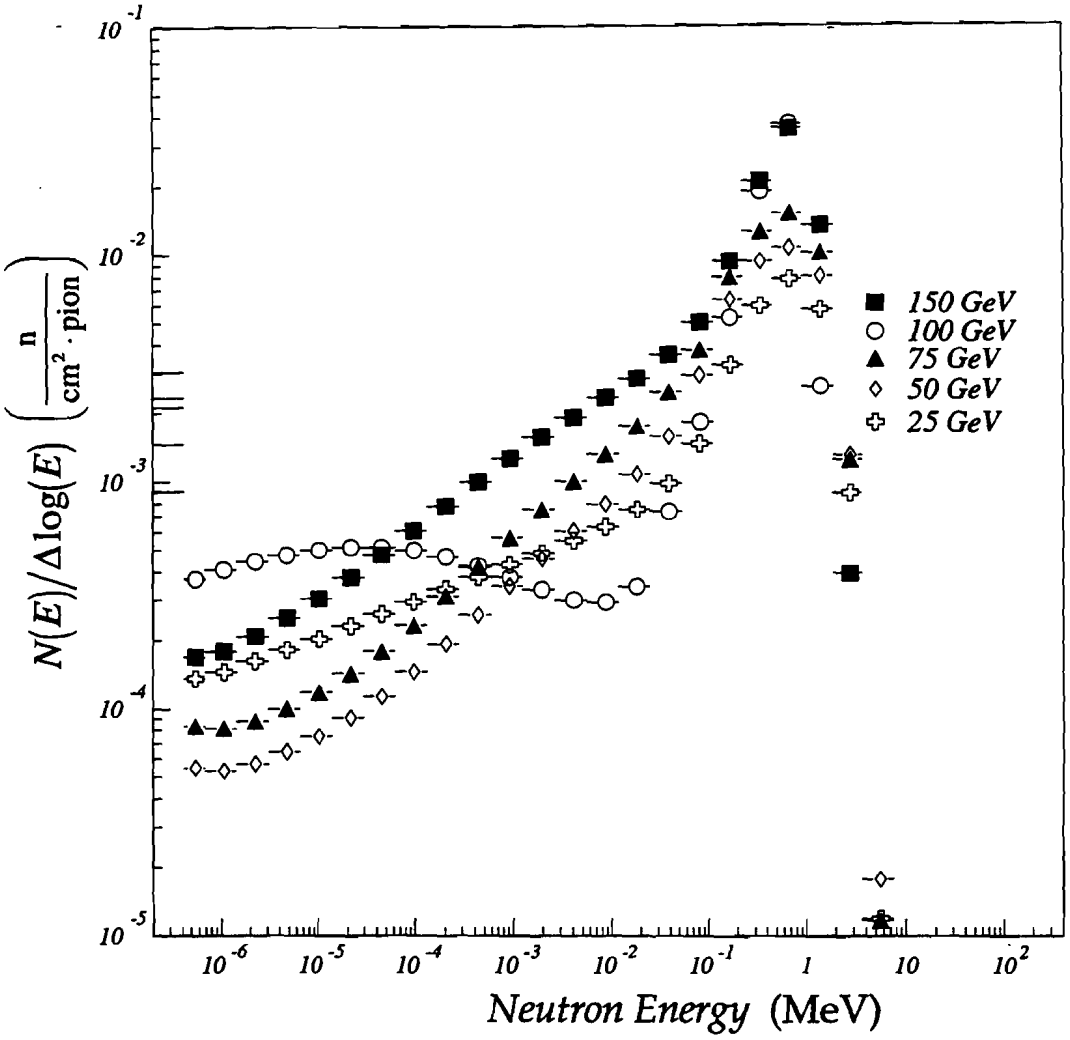

Figure 4.1. Unfolded Neutron Spectra For Incident Pions on 40.6 cm of Iron. Shown are the neutron spectra obtained using BUNKI for pions at 5 different energies incident on 40.6 cm (16 in, 2.4 λ) of iron. For each energy, the fluence per unit lethargy per pion is plotted as a function of neutron energy.

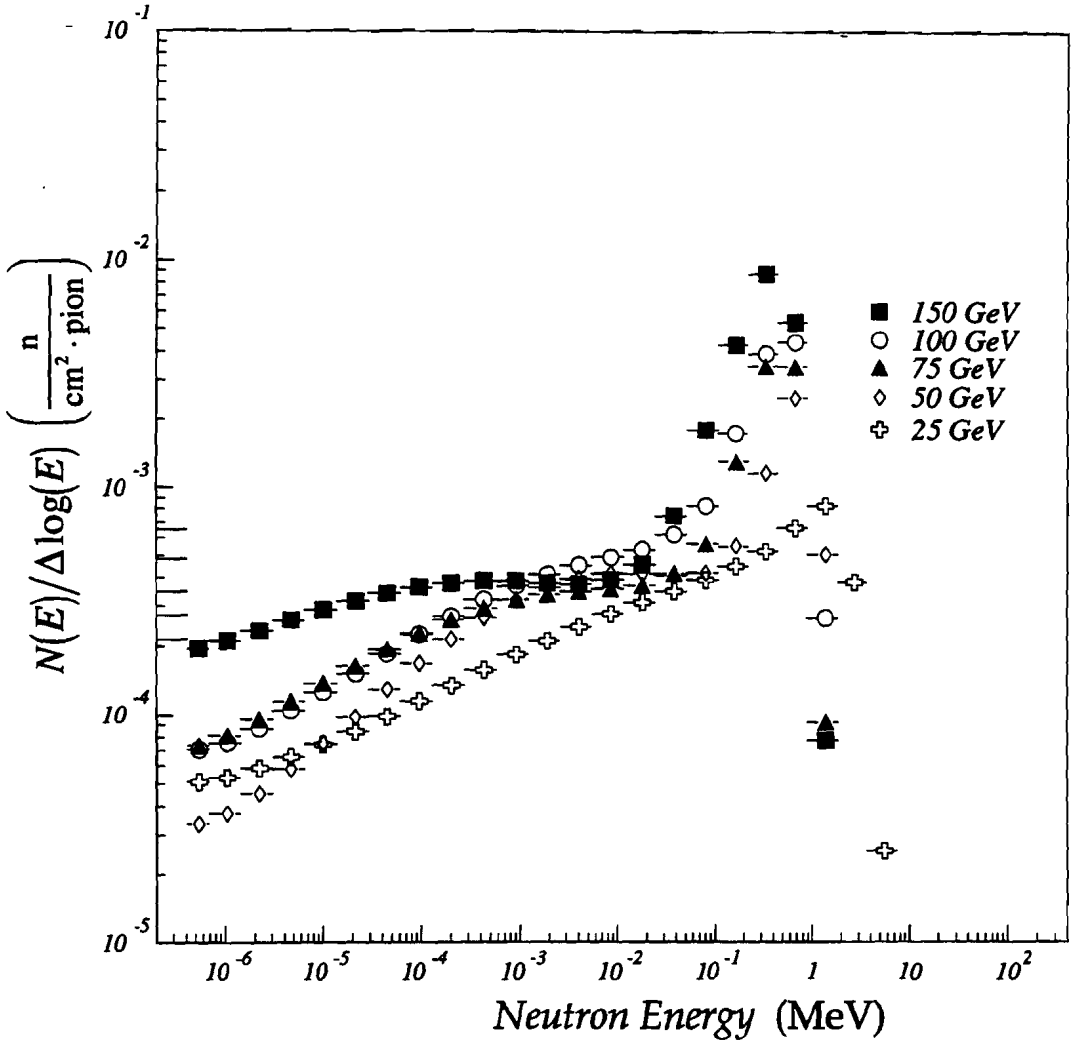

Figure 4.2. Unfolded Neutron Spectra For Incident Pions on 162.6 cm of Iron. Shown are the neutron spectra obtained using BUNKI for pions at 5 different energies incident on 162.6 cm (64 in, 9.7 λ) of iron. For each energy, the fluence per unit lethargy per pion is plotted as a function of neutron energy.

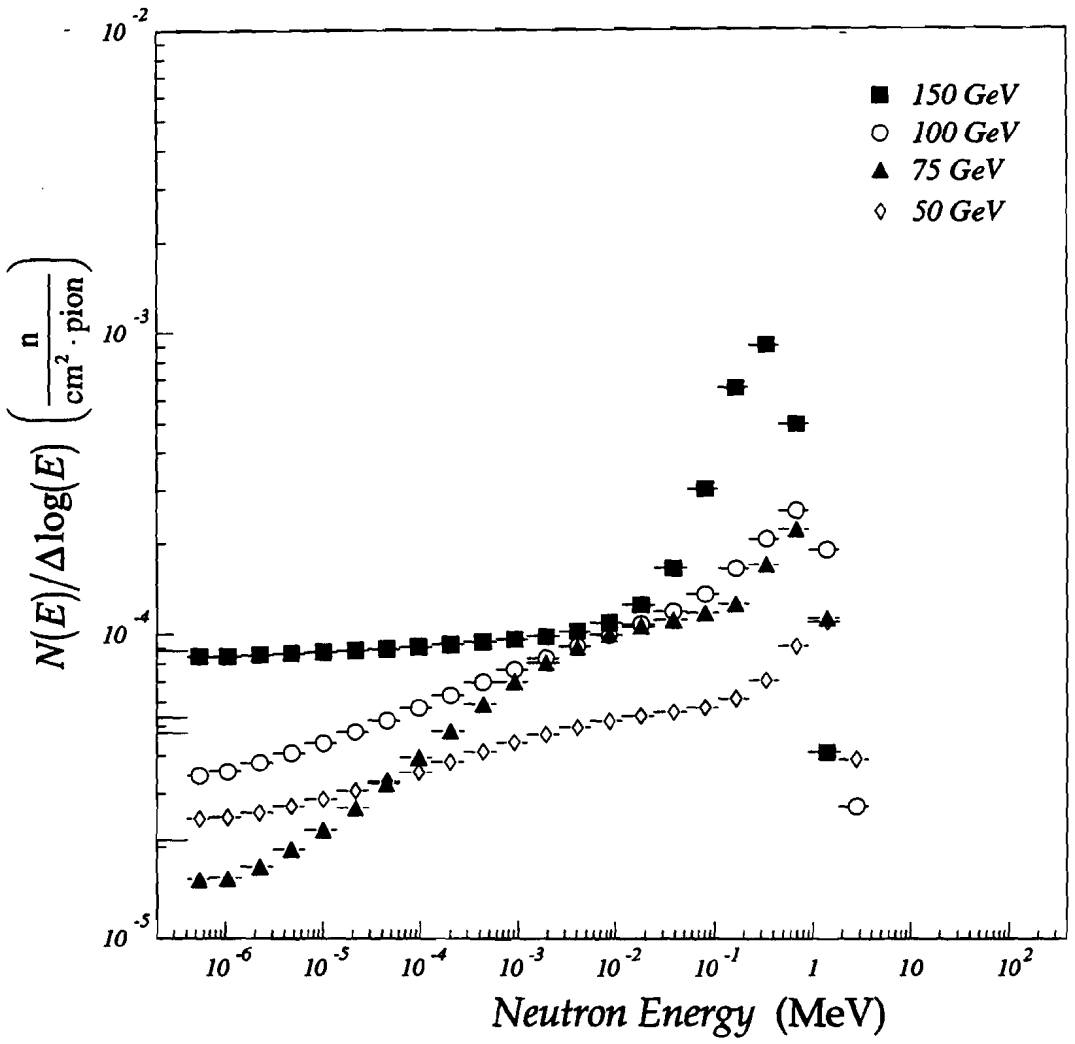

Figure 4.3. Unfolded Neutron Spectra For Incident Pions on 243.8 cm of Iron. Shown are the neutron spectra obtained using BUNKI for pions at 4 different energies incident on 243.8 cm (96 in, 14.5 λ) of iron. For each energy, the fluence per unit lethargy per pion is plotted as a function of neutron energy.

^{11}C activation (with a threshold near 20 MeV) did not provide any definitive information on the neutron spectrum in the high energy region, as was discussed in Chapter 2.

As mentioned in Chapter 3, making the measurements with all the spheres simultaneously implicitly assumes that the spectral shape does not change with the transverse position along the detector array in back of the iron shield.This assumption is supported by the fact that the shape of the spectrum is nearly independent of the depth z in iron. Thus, the shape should also be rather independent of transverse coordinate x at a given value of z because for each value of x the amount of iron between the locations of interest and the point of initial beam interaction is slightly different. In fact, the actual depth in iron is $d^2= x^2+y^2+z^2$, where y=25.4 cm is the difference in height between the beam position and that of the detector array. The dependence of the spectral shape on angle ($\tan^{-1}(x/z)$ or $\tan^{-1}(y/z)$) is not expected to be significant due to the numerous scattering events involved in the hadronic cascade process.

To address this assumption more quantitatively measurements were performed - at one thickness (162.6 cm) and one pion energy (100 GeV)- by placing each spherical detector one at a time at the position of the 8" diameter sphere (see e.g., Fig. 3.1), and comparing the results to that from a simultaneous measurements. The spectra unfolded from the sphere responses for the two cases are shown in Figure 4.4. As observed, the spectral shapes are essentially identical; thus, any differences in shape with position along the array in back of the iron shield must be small, and the assumption is shown to be reasonable. The similarity in spectral shape also indicates that any contribution to each sphere response from "crosstalk" because of the existence of the other spheres in the simultaneous measurements must be small.

The effect of backscattering on the measured neutron spectrum was investi-

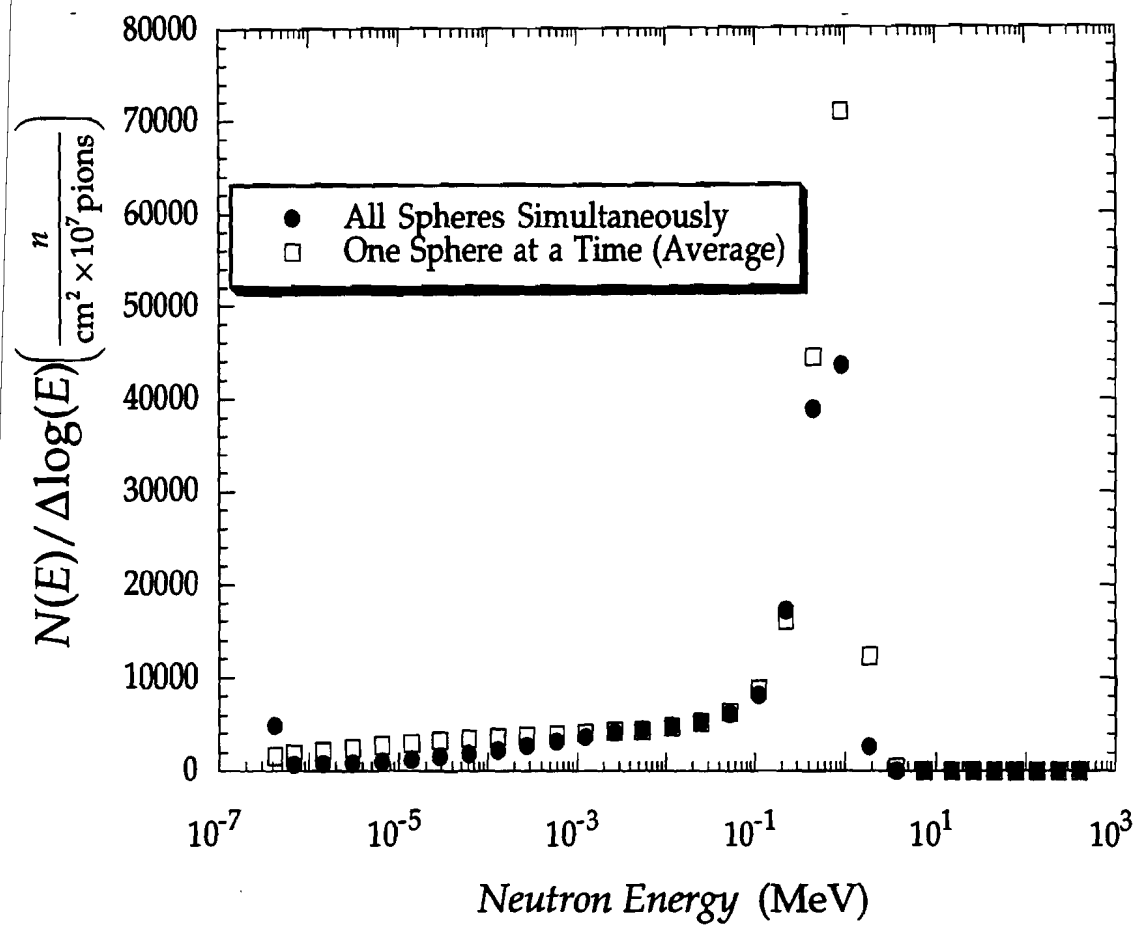

Figure 4.4 Unfolded Neutron Spectra For Incident Pions on 162.6 cm of Iron. Shown are the neutron spectra obtained using BUNKI for pions at 100 GeV incident on 162.6 cm (64 in, 9.7 λ) of iron. Comparison is between the case when all spheres are deployed simultaneously and that when one sphere at a time is in place. For each energy, the fluence per unit lethargy per 10^7 pions is plotted as a function of neutron energy.

gated. A 10 cm thick sheet of polyethylene was placed in front of the iron blocks situated in back of the Bonner sphere spectrometer (See Fig.2.2). Measurements were performed, at the same thickness and energy described above, and compared with measurements performed without the presence of plastic. Again the spherical detectors were deployed one at a time at the position of the 8" diameter sphere. Spectral shapes unfolded from the data are compared in Figure 4.5. As observed, with the polyethylene sheet in place the peak fluence is reduced while that at a somewhat lower energy (between 0.01 and 0.1 MeV) is enhanced compared with the results of the measurements with no cover. Such a shift to lower energies would be expected because of the moderating properties of polyethylene. When the polyethylene sheet is replaced by one containing 5 cm of borated polyethylene the spectral shape remains the same as with polyethylene alone. (See Fig. 4.5). Thus, there are, apparently, few thermal neutrons backscattered from the iron into the detector or thermalized in the polyethylene as these would be removed because of the high thermal capture cross section of boron.

Even though there are small shifts toward lower neutron energies in the unfolded neutron spectra with polyethylene and boron sheets in place, both the total fluence and dose equivalent are the same, and agree within 12 % with the no cover case. Furthermore, the overall quality factor is the same within 4 %. It can be concluded therefore that the number of neutrons backscattered into the detectors from the iron blocks is fairly small and backscattering contributes little to the overall properties of the neutron radiation field at the detector position.

Figures 4.6 and 4.7 show neutron spectra for 25 and 150 GeV incident pions striking 40.6 and 264.2 cm of Fe respectively, unfolded from the data by using both the BUNKI and LOUHI unfolding codes. It can be seen from the plots that the agreement in terms of gross features between the two codes is quite good; the fluence and dose equivalent extracted from both codes agree within 1 % and 17 % respec-

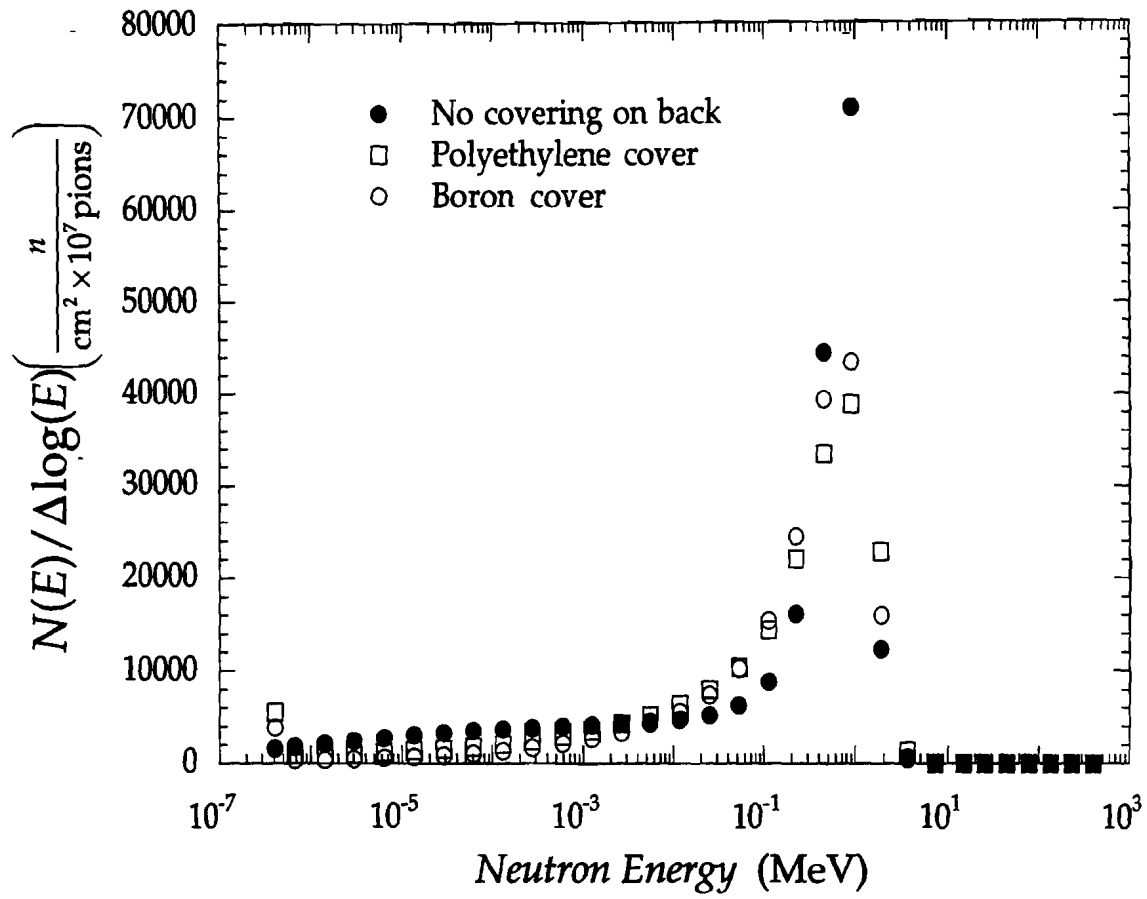

Figure 4.5 Unfolded Neutron Spectra For Incident Pions on 162.6 cm of Iron. Shown are the neutron spectra obtained using BUNKI for pions at 100 GeV incident on 162.6 cm (64 in, 9.7 λ) of iron. Comparison is between the case when there is no covering in the back of detectors and that when there are boron and polyethylene cover sheets in place. For each energy, the fluence per unit lethargy per 10^7 pions is plotted as a function of neutron energy.

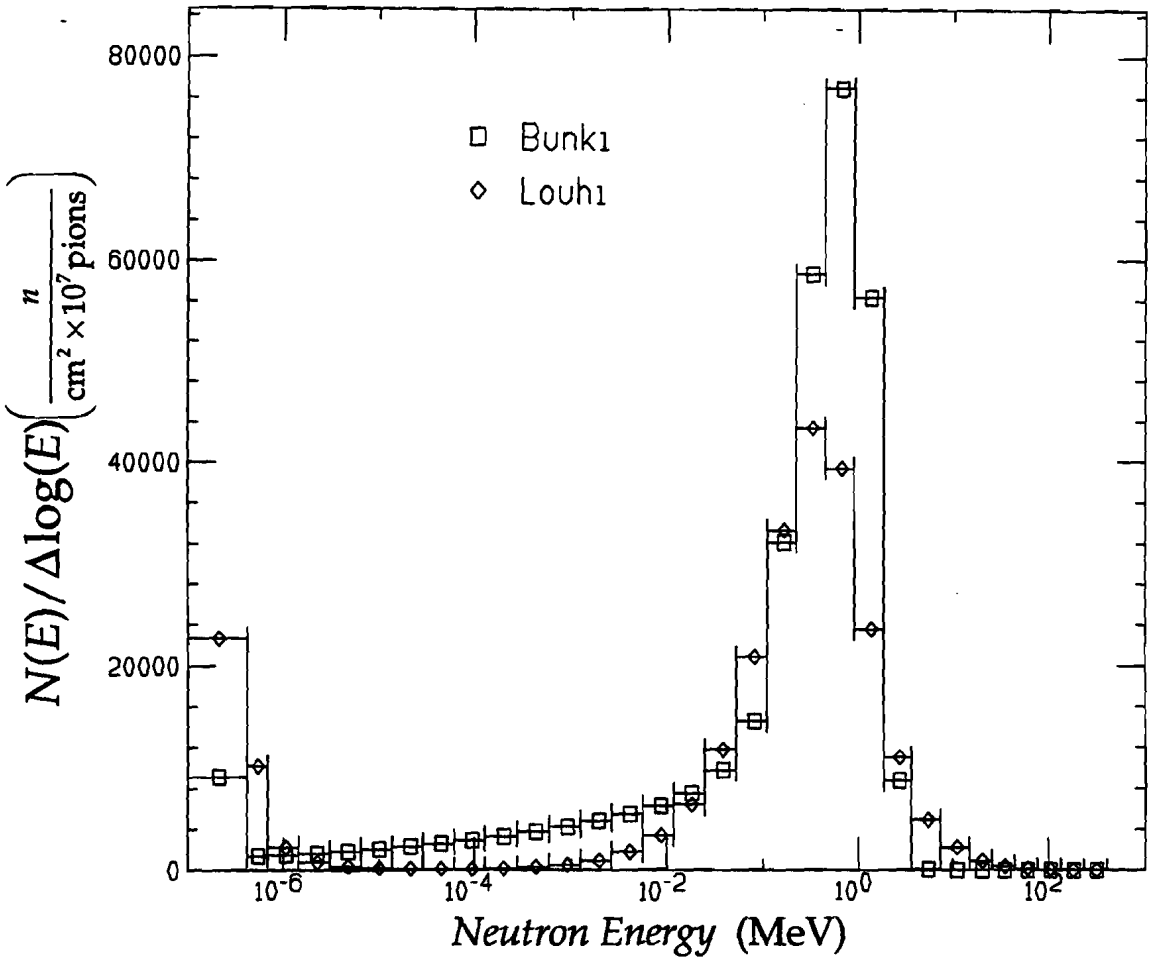

Figure 4.6. Unfolded Neutron Spectra for Incident Pions at 40.6 cm of Iron. Shown are the neutron spectra obtained by using BUNKI and LOUHI unfolding codes, for incident pions at 25 GeV on 40.6 cm (16 in, 2.4 λ) of iron. The fluence per unit lethargy is plotted as function of neutron energy.

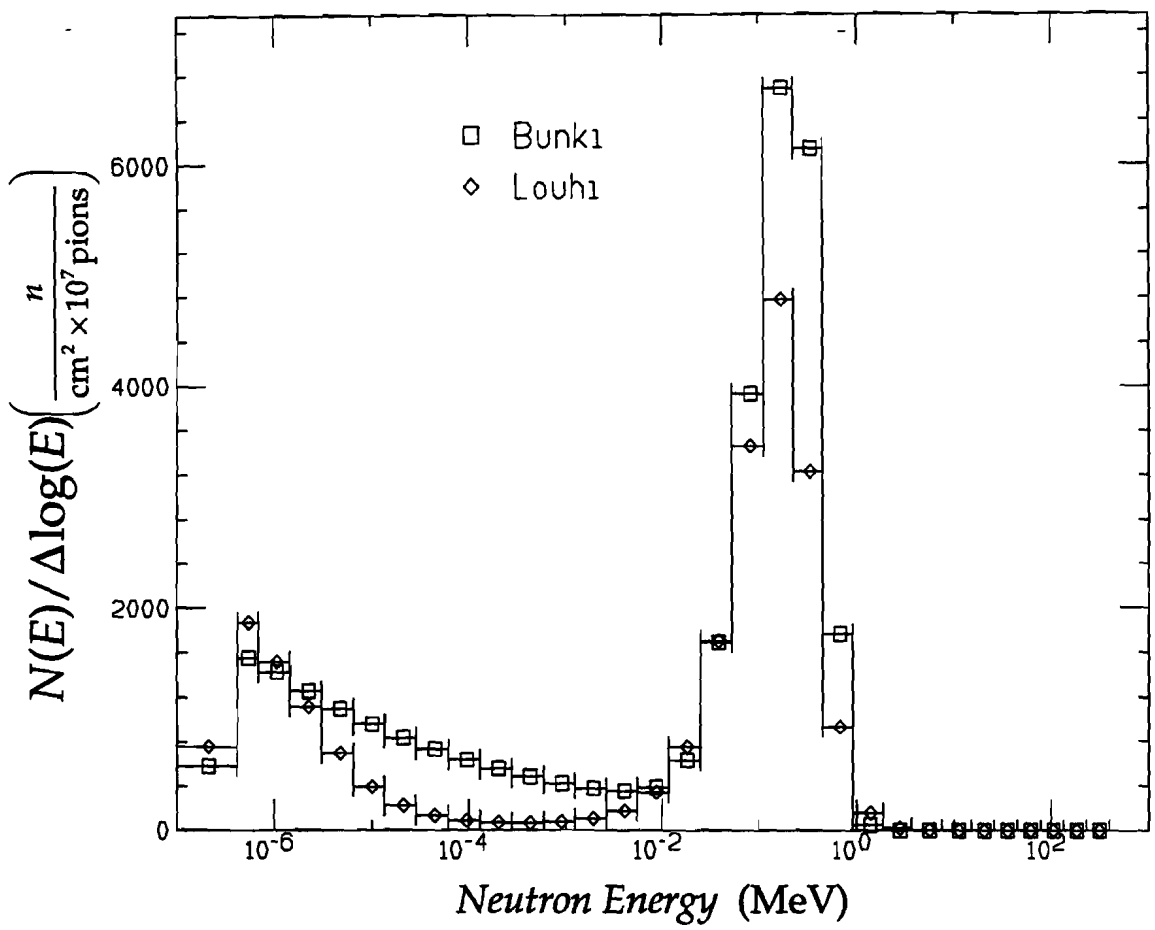

Figure 4.7. Unfolded Neutron Spectra for Incident Pions at 264.2 cm of Iron. Shown are the neutron spectra obtained by using BUNKI and LOUHI unfolding codes, for incident pions at 150 GeV on 264.2 cm (104 in, 15.7 λ) of iron. The fluence per unit lethargy is plotted as function of neutron energy.

tively. Based on the results of the unfolding, the quality factor for the neutron field was found to be essentially constant with incident pion energy at each depth in Fe (see Appendix A). In Appendix A, a complete set of the data including fluence, dose equivalent and quality factors (among other parameters) are presented for the unfolded results from both codes for all thicknesses and energies.

As mentioned in Chapter 3, all the results based on spectrum unfolding presented in this work arise from the use of sphere response functions calculated by Sanna [1973]. To investigate the sensitivity of the unfolding to any particular set of such functions, results were compared with calculations based on the widely used Universty of Texas (UTA) sphere response functions [Hertel et al. 1985]. Figure 4.8 shows a comparison of an unfolded neutron spectra at 100 GeV incident pions on 243.8 cm of iron, by use of BUNKI with two different response funtions, Sanna's and UTA. Except at low neutron energies where the fluence is very small both sets of responses give identical spectral shapes. The total fluence, fluence to dose equivalent conversion factors, and quality factors obtained from the unfolded spectra are the same within 10 %. Thus, at least for these two widely-utilized sets of response functions, the results are relatively independent of which set is used.

Spectral measurements in the lateral shielding direction (transverse to the incident beam) at NWA were performed at a single radial depth of 60.9 cm in Fe and at three pion energies by placing the Bonner Sphere detectors one at a time on top of the Fe blocks. Figure 4.9 shows a comparison of the neutron spectrum in the lateral direction with a measurement at approximately the same depth in the longitudinal direction. Even though the main neutron peak is at the same energy, the height of the peak in the lateral shield measurement is lower by a factor of 3.3 and the spectral shape is different at lower energies. The quality factors extracted from the unfolding codes for the lateral and forward measurements are the same within 5%.

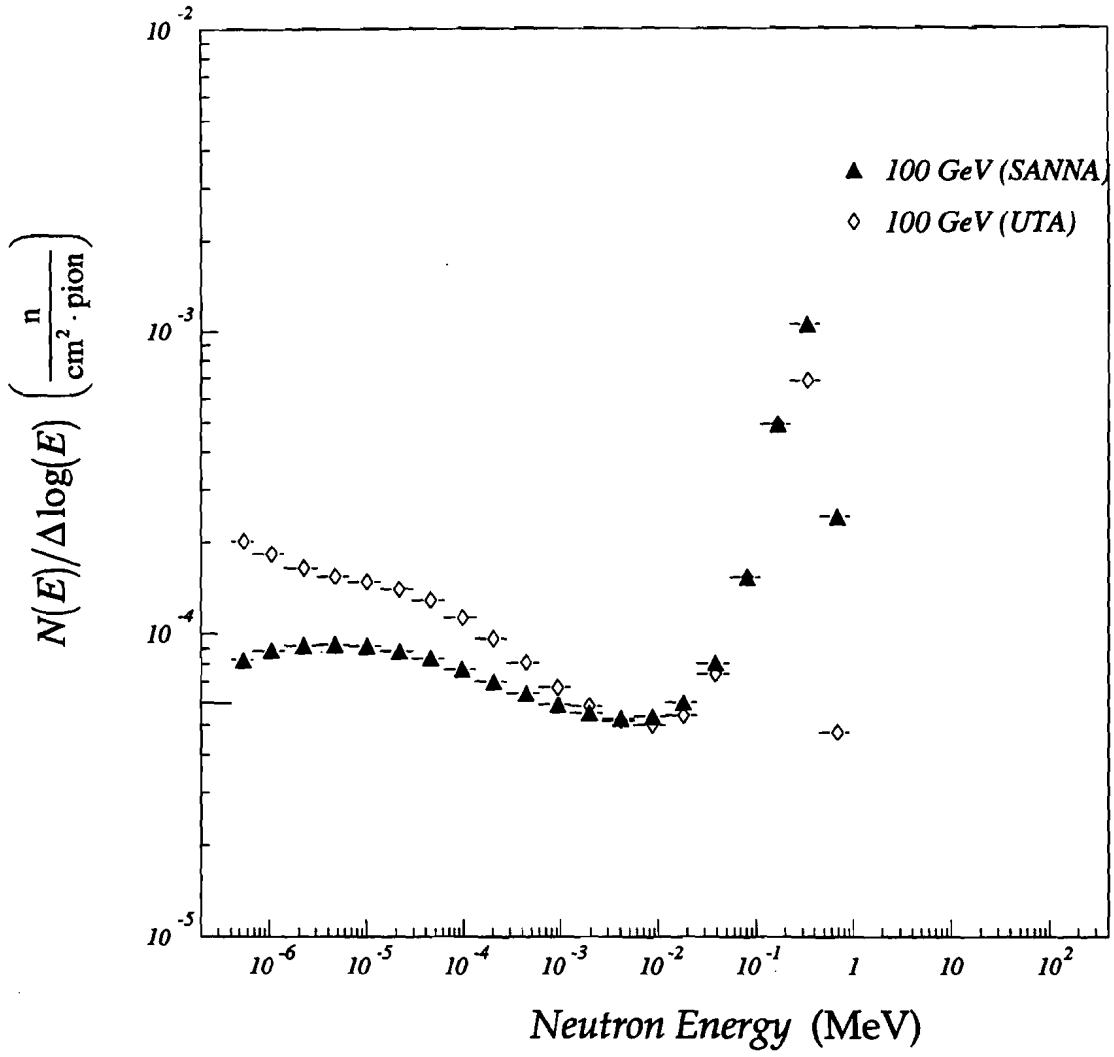

Figure 4.8. Unfolded Neutron Spectra For Incident Pions on 243.8 cm of Iron. Shown are the neutron spectra obtained using BUNKI for pions at 100 GeV incident on 243.8 cm (96 in, 14.5 λ) of iron, for two different response functions. For each energy, the fluence per unit lethargy per pion is plotted as a function of neutron energy.

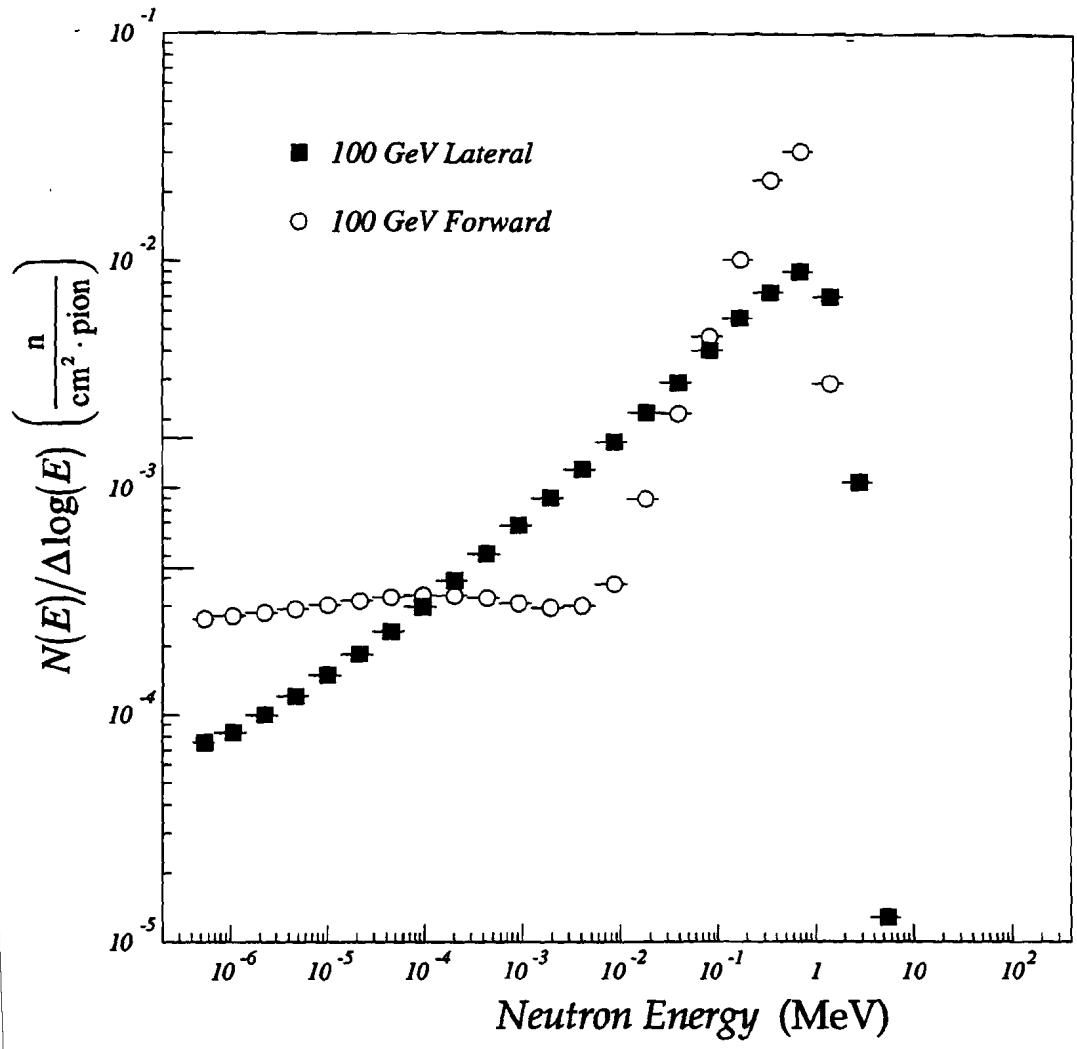

Figure 4.9. Unfolded Neutron Spectra for Incident Pions at 60.9cm of Iron. Shown is a comparison of the neutron spectra obtained for the lateral and longitudinal (forward) directions by using BUNKI for incident pions at 100 GeV on 60.9 cm (24 in, 3.6 λ) of iron. The fluence per unit lethargy per pion is plotted as function of neutron energy.

Figure 4.10 shows the dependence of neutron fluence and dose equivalent on thickness in the longitudinal (forward) direction. The fluence and dose equivalent decrease as a function of thickness at each energy. Figure 4.11 shows the dependence of these quantities (neutron fluence and dose equivalent) on energy in the longitudinal direction. It can be seen from this figure that both quantities increase approximately as the incident energy at each thickness. Based on these systematic studies an attempt was made to develop an empirical understanding of both depth and energy dependence.

4.3 Lateral (Transverse) Shielding at NWA

Stevenson [1986], and others, have analyzed lateral shielding measurements and performed Monte Carlo calculations for incident hadrons at energies between 10 GeV and 10 TeV. On the basis of such studies, it has been suggested [Stevenson 1986] that the dose equivalent can be empirically represented by the expression:

$$H = \frac{H_o(E)e^{-r/\lambda}}{r^2} \qquad 4.1$$

with

$$H_o = H_o' E^m$$

Here H is the measured dose equivalent, H_o (the so called source term) is the extrapolated dose equivalent at zero depth, r is the distance from the source to shield surface or other point of interest outside the shielding, λ is the effective interaction length in iron, and E is the energy of the incident particle. Furthermore, it is reasonable to expect that the fluence can be represented by an expression identical to Equation 4.1 above. That is, for fluence

$$\Phi = \frac{\Phi_o(E)e^{-r/\lambda}}{r^2} \qquad 4.2$$

with,

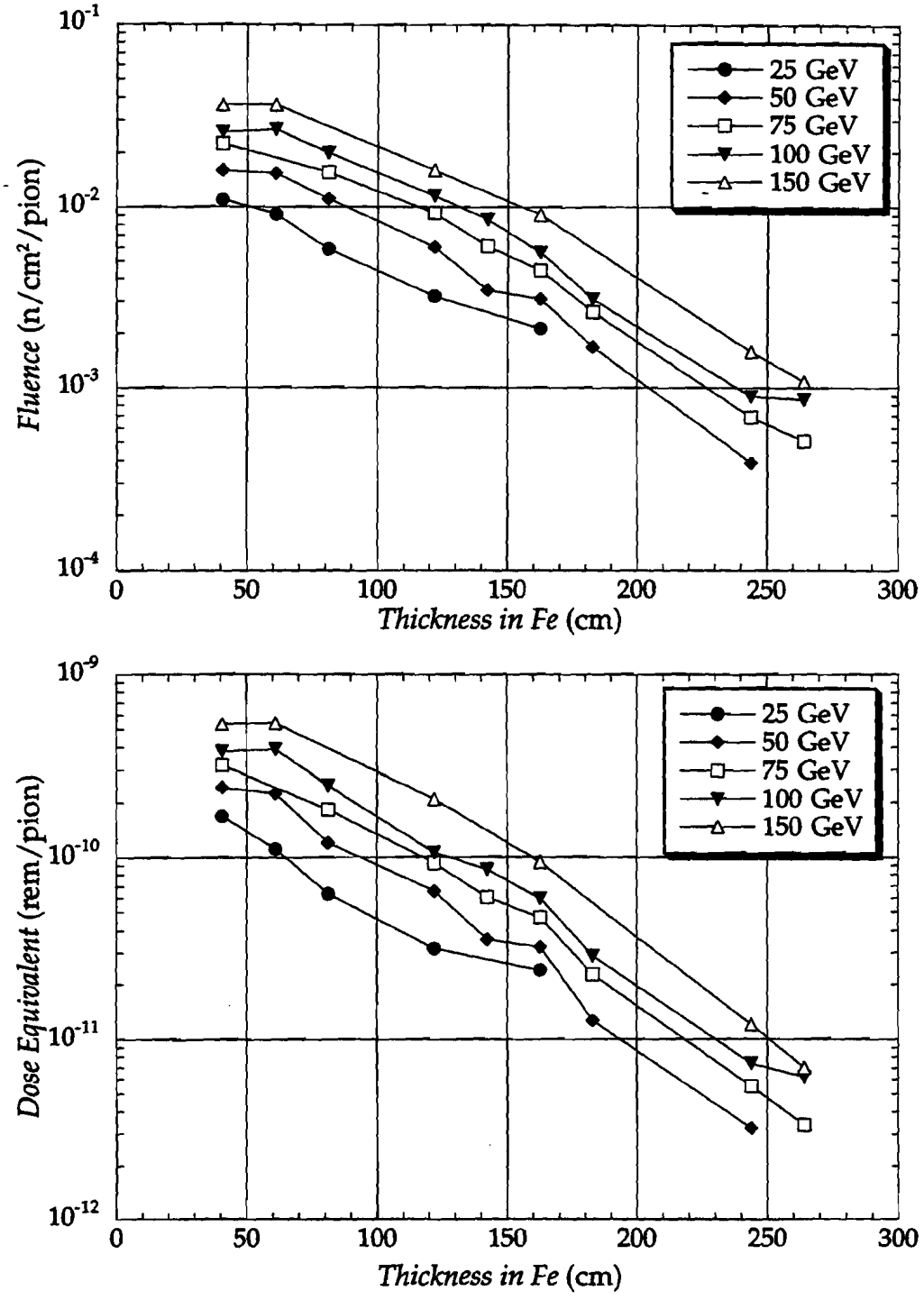

Figure 4.10. Fluence and Dose Equivalent vs. Thickness of Iron. Shown are fluence and dose equivalent plotted as a function of thickness in the longitudinal direction for incident pions at five energies. The fluence and dose equivalent decrease as a function of thickness at a specific energy.

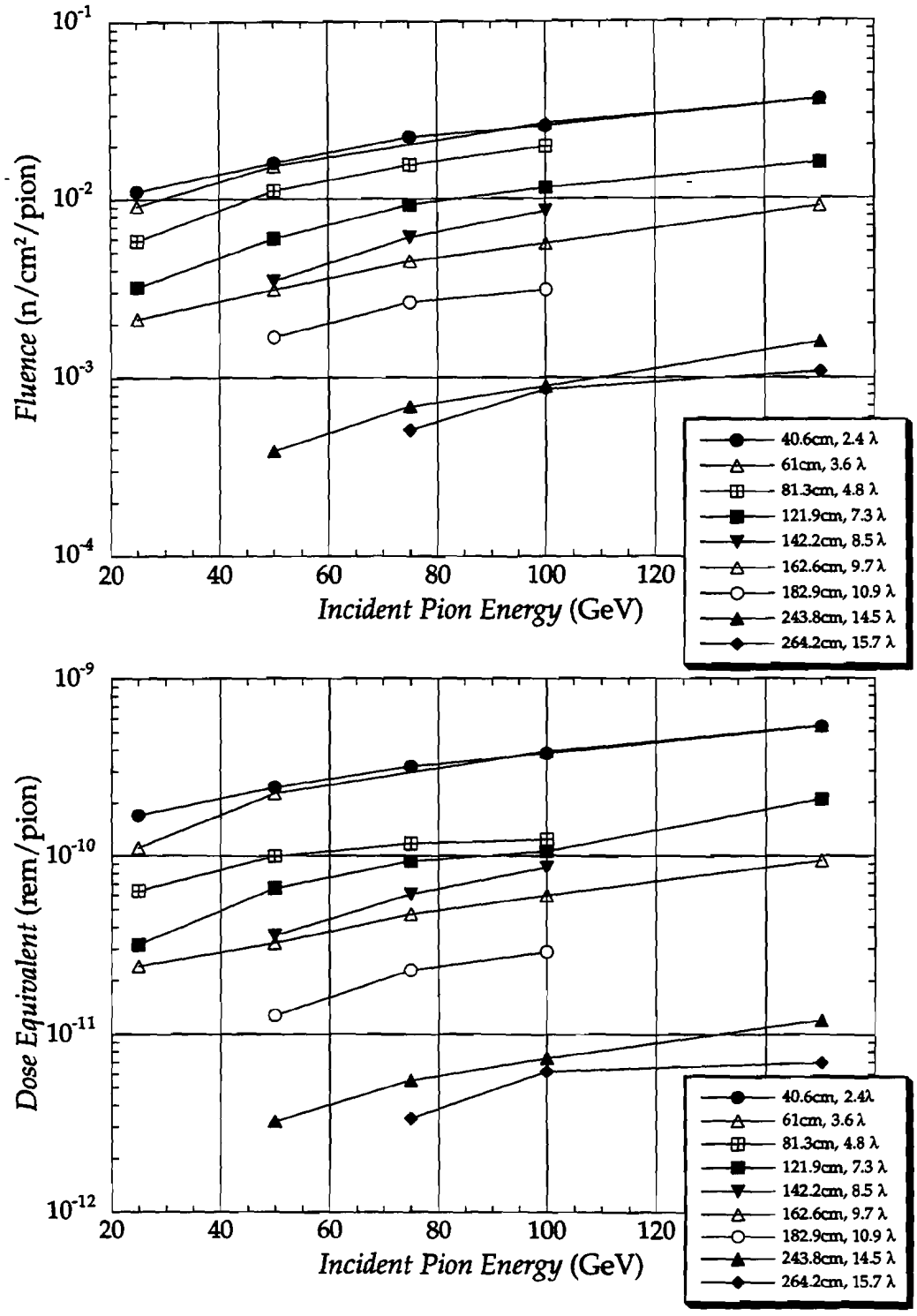

Figure 4.11. Fluence and Dose Equivalent vs. Incident Pion Energy. Shown are fluence and dose equivalent plotted as a function of incident pion energy in the longitudinal direction The fluence and dose equivalent increase as a function of incident energy at a specific thickness.

$$\Phi_o = \Phi_o' E^m$$

The exponential term $e^{-r/\lambda}$ represents the transmission of incident hadrons through the Fe shielding. Exponential attenuation as described by Equation 4.2, will only occur after secondary particle equilibrium has been reached. For high energy radiation effective equilibrium will be established after the radiation has penetrated about three mean free paths through the shielding (about 51 cm for iron) when 95% of the incident pions will have interacted [Sullivan 1992]. Particularly after equilibrium has been reached, it is neutrons that play the largest part in the propagation of the hadronic cascade

Figure 4.12 shows the results of fitting the expression 4.1 and 4.2 to lateral measurements of both fluence and dose equivalent at three pion energies (75, 100 and 150 GeV) and at the single shield thickness of 60.9 cm, with lambda (λ) fixed at 21.6 cm, a value based on previous analyses [Thomas et al. 1988]. Present results for Φ_o', and H_o' taken from the plots of Figure 4.12, are shown in Table 4.1. Taking both values of the exponent m from the plots of Figure 4.12 for fluence (0.83±0.10) and dose equivalent (0.86±0.02), which are the same within the errors, a weighted average of the exponent in energy can be found of:

$$\langle m \rangle = 0.86 \pm 0.02.$$

This result is consistent with the value 0.80±0.10 quoted by Thomas et al. [1984]. Cossairt et al. [1985] has predicted a value for the exponent m=0.84±0.02 based on Monte Carlo calculations with the code CASIM [Van Ginneken 1975] for incident protons ($200 \leq E \leq 800$ GeV) on an iron block (91cm X 91 cm X 366 cm). Mokhov et al. [1986], on the other hand, for the same geometry, has predicted a value of m= 0.74, based on calculations with the Monte Carlo code MARS10 [Kalinovsky et al. 1984], for incident protons with energies between 70 and 20000 GeV.

From the ratio of the source term strengths (H_o'/Φ_o'), found in the analyses, one calculates a conversion factor from dose equivalent to fluence of:

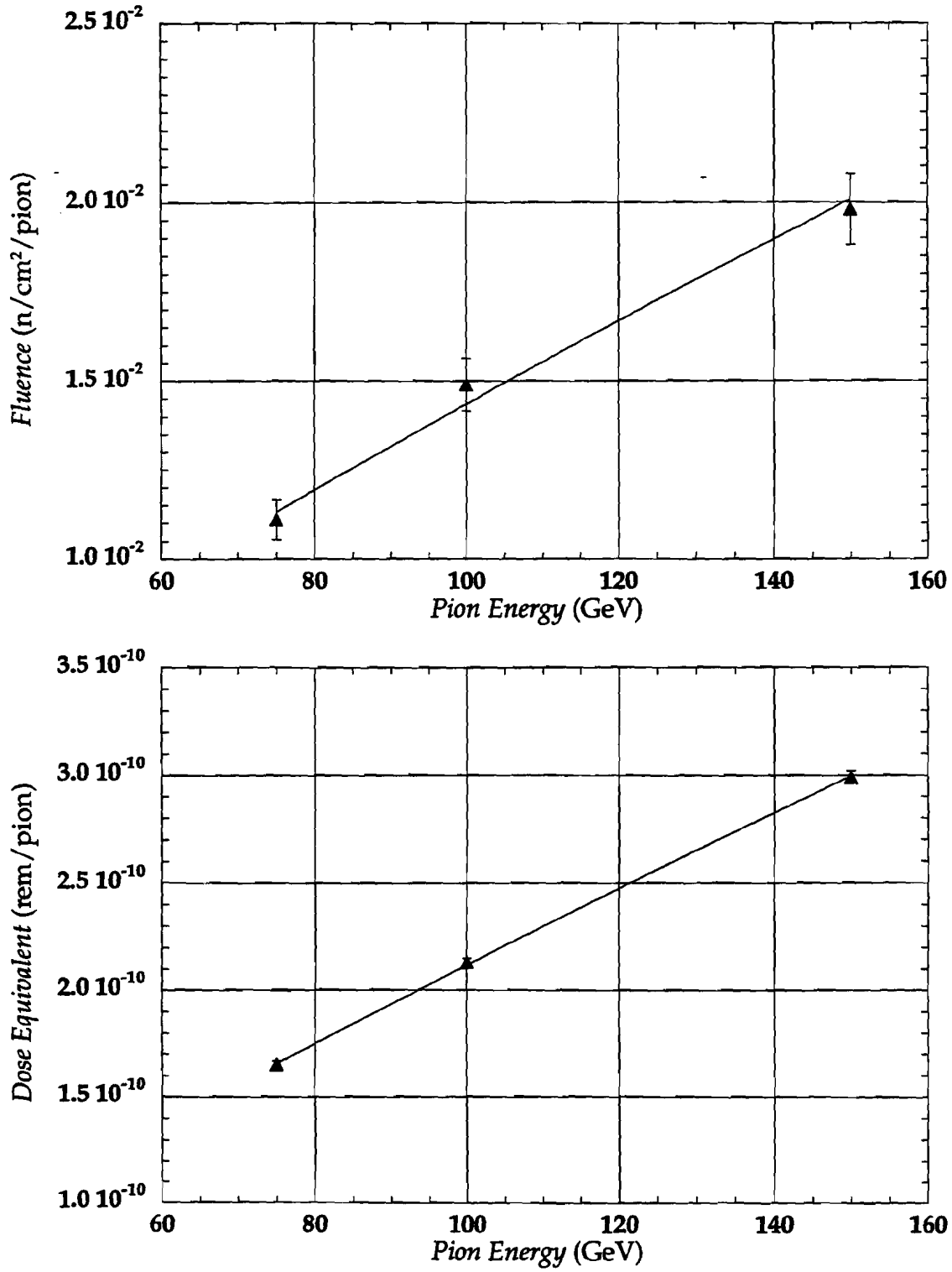

Figure 4.12. Fits to Fluence and Dose Equivalent vs Pion Energy. Shown are the fits of expression 4.1 and 4.2 to lateral measurements of both fluence and dose equivalent at three pion energies (75, 100 and 150 GeV) at a single shield thickness of 60.9 cm in iron. Results of the fits are shown in Table 4.1.

Table 4.1
Summary of Results on Lateral Shielding

	BUNKI [Data]	Stevenson [1984]	Stevenson [1986]	Van Ginneken [1975]	Cossairt et al. [1985]	Mokhov et al. [1986]
Source term Fluence(Φ_0') n/cm^2/pion	(19.9±1.5)	N/A	N/A	N/A	N/A	N/A
Source Term Dose Equivalent. (H_0') rem/pion	(2.57±0.39)x10^{-7}	N/A	N/A	N/A	N/A	N/A
Conversion Factor (D.E/Fluence) rem/n/cm^2	(1.29±0.62)x10^{-8}	2.80x10^{-8}	(0.76±0.04)x10^{-8}	0.44x10^{-8}	N/A	N/A
E^m	$E^{(0.86\pm0.02)}$	N/A	$E^{(0.80\pm0.10)}$	N/A	$E^{(0.84\pm0.02)}$	$E^{(0.74)}$
Comments	Neutrons outside end stop Fe shield due to beam directly hitting the end stop	Neutrons with energies greater than 20 MeV outside general accelerator shield	Moyer Model: Beam hitting thick target in shielded tunnel; at 90 degrees	CASIM calculation for neutrons outside of thick Fe shield	Fits to Monte Carlo cascade calculation at 90 degrees for beam hitting an iron block. (200 ≤ E ≤ 800 GeV)	Fits to Monte Carlo cascade calculation at 90 degrees for beam hitting an iron block. (70≤ E≤ 20000 GeV)

Table 4.1. Summary of Results on Lateral Shielding. Shown are the results of the fit at a single lateral depth of 60.9 cm in Fe and three pion energies. Also shown are the exponent in energy, source terms for fluence and dose equivalent and the conversion factor from fluence to dose equivalent. Comparison with Stevenson's, Van Ginneken's, Cossairt's and Mohkov's calculations are also presented. (See text for further discussion).

$$\frac{\text{Dose Equivalent}}{\text{Fluence}} = 1.29 \times 10^{-8} \text{ rem/n/cm}^2.$$

Therefore an expression to calculate the source term outside of a thick transverse Fe shield can be written:

$$H_o(E) = (1.29 \pm 0.62) \times 10^{-8} E^{(0.86 \pm 0.02)} \text{ rem/n/cm}^2.$$

Our knowledge of the source term to be associated with the dose equivalent outside of a lateral shield is, based on the current literature, somewhat confusing. This arises because it is not always clear to what experimental situation or model the quoted values refer. Table 4.1 summarizes the situation. While some of the situations represented by these references refer to all radiation that result from hadronic cascades, the most likely radition to leak through shielding at 90 degrees to the beam will be neutrons.

4.4 Forward (Longitudinal) Shielding at NWA

Unlike the lateral shielding case there is no similarly simple analytical expression (as, e.g., Equation 4.1) that can be used to describe the on-axis longitudinal cascade development. An one-dimensional model described by Lindenbaum [1961] suggests that if n collisions are necessary to degrade the energy of the incident particle so that no secondaries are produced in this n'th interaction, then the total number of particles reaching a depth z is given by the expression:

$$N(z) = N_o B_n(z/\lambda) e^{-z/\lambda} \quad , \qquad 4.3$$

where λ is the mean free path taken to be independent of energy and particle type, z is the thickness of the shielding, and $B_n(z/\lambda)$ is the build up term defined in this one dimensional description as :

$$B_n = 1 + p_1(z/\lambda) + p_1 p_2 (z/\lambda)^2/2! + \ldots + \prod_n p_i \left\{ (z/\lambda)^n / n! \right\},$$

where p_i is the multiplicity in the i'th interaction, also assumed to be independent of both energy and particle type. If the multiplicities are taken to be constant, the build up factor does not saturate but instead is a monotonically increasing function

of z, and under certain conditions approximates exponential absorption.

Following a suggestion by Thomas and Stevenson [1988] an attempt was made to describe the observed dependence of both fluence and dose equivalent in the forward direction on shield thickness and energy by use of an expression similar to that given in Equation 4.3. Thus,

$$R(E,z) = R_o(E,z)e^{-z/\lambda} \qquad 4.4$$

where $R(E,z)$ represents either dose equivalent or fluence and will depend on the energy of the incident particle and depth in the shield, λ is the mean free path (which is taken in the present analysis to have the same value 21.6 cm as in the lateral shielding case) and z is the thickness of the shielding. $R_o(E,z)$ can be separated into both depth and energy dependent terms:

$$R_o(E,z) = R_o(E)B(z) \qquad 4.5$$

where $B(z)$ is a build up term dependent on depth. This build up term can be approximated as an exponential in the form:

$$B(z) = e^{az} \qquad 4.6$$

Again, assuming a power law dependence on energy, as in the lateral case :

$$R_o(E) = R_0' E^m \qquad 4.7$$

where R_0' is the so called source term strength and E is the incident pion energy. Substituting Equations 4.6 and 4.7 into Equation 4.5, and then into Equation 4.4, one gets:

$$R = R_0' E^m e^{az} e^{-z/\lambda} \qquad 4.8$$

To determine the dependence on thickness, both the fluence and dose equivalent unfolded from the data were fit, at each energy, to the expression:

$$f(z) = m_1 e^{m_2 z} \qquad 4.9$$

Figures 4.13 and 4.14 show as an example the resultant fit at the pion energy of 100 GeV. The results for the coefficients m_1 and m_2 from fits at all energies are shown in Table 4.2.

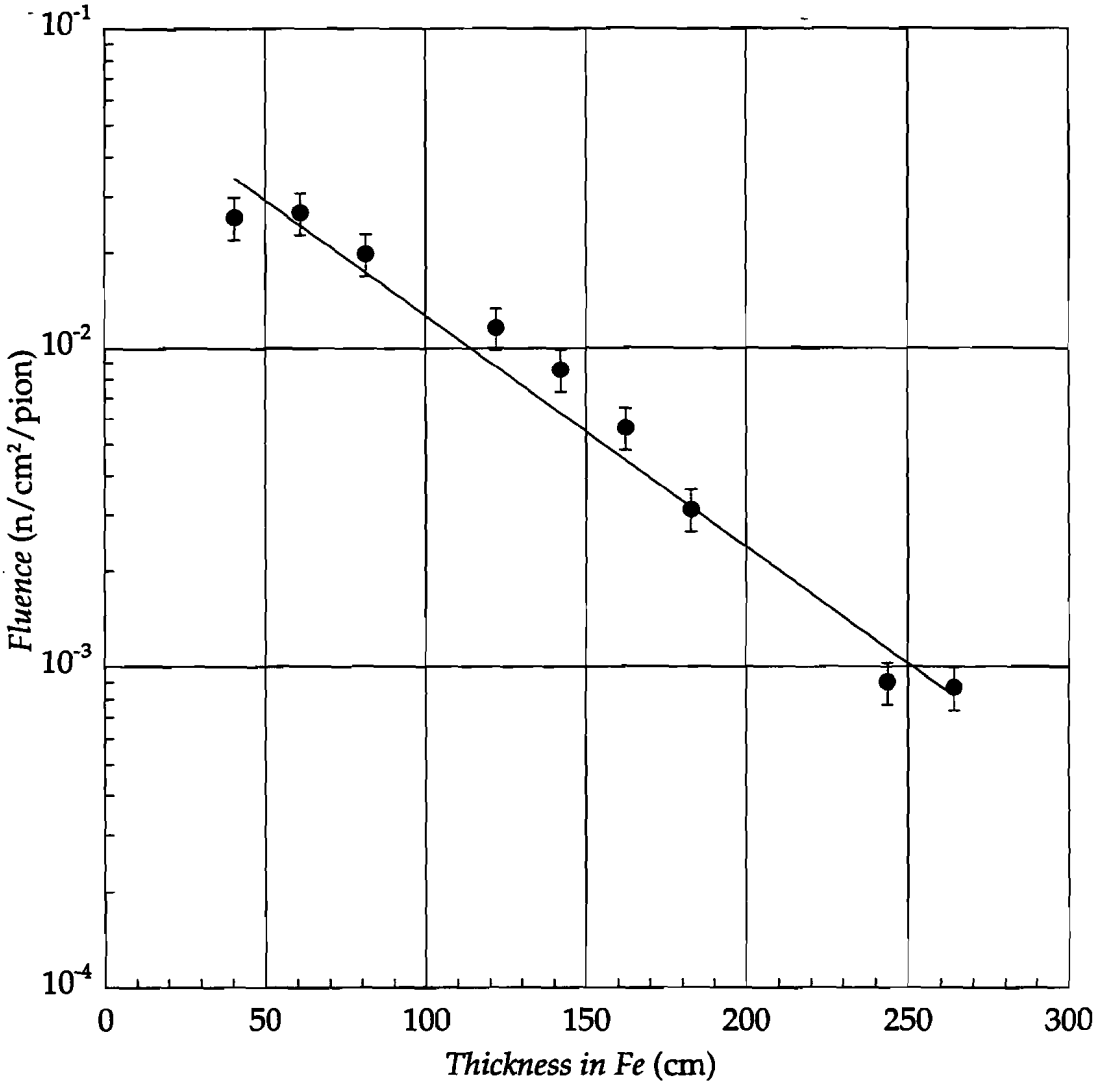

Figure 4.13. Neutron Fluence at 100 GeV. Plotted is neutron fluence as a function of thickness for 100 GeV incident pions in the longitudinal direction. Also shown is the fit of the data to expression 4.9. Results of the fit are given in Table 4.2.

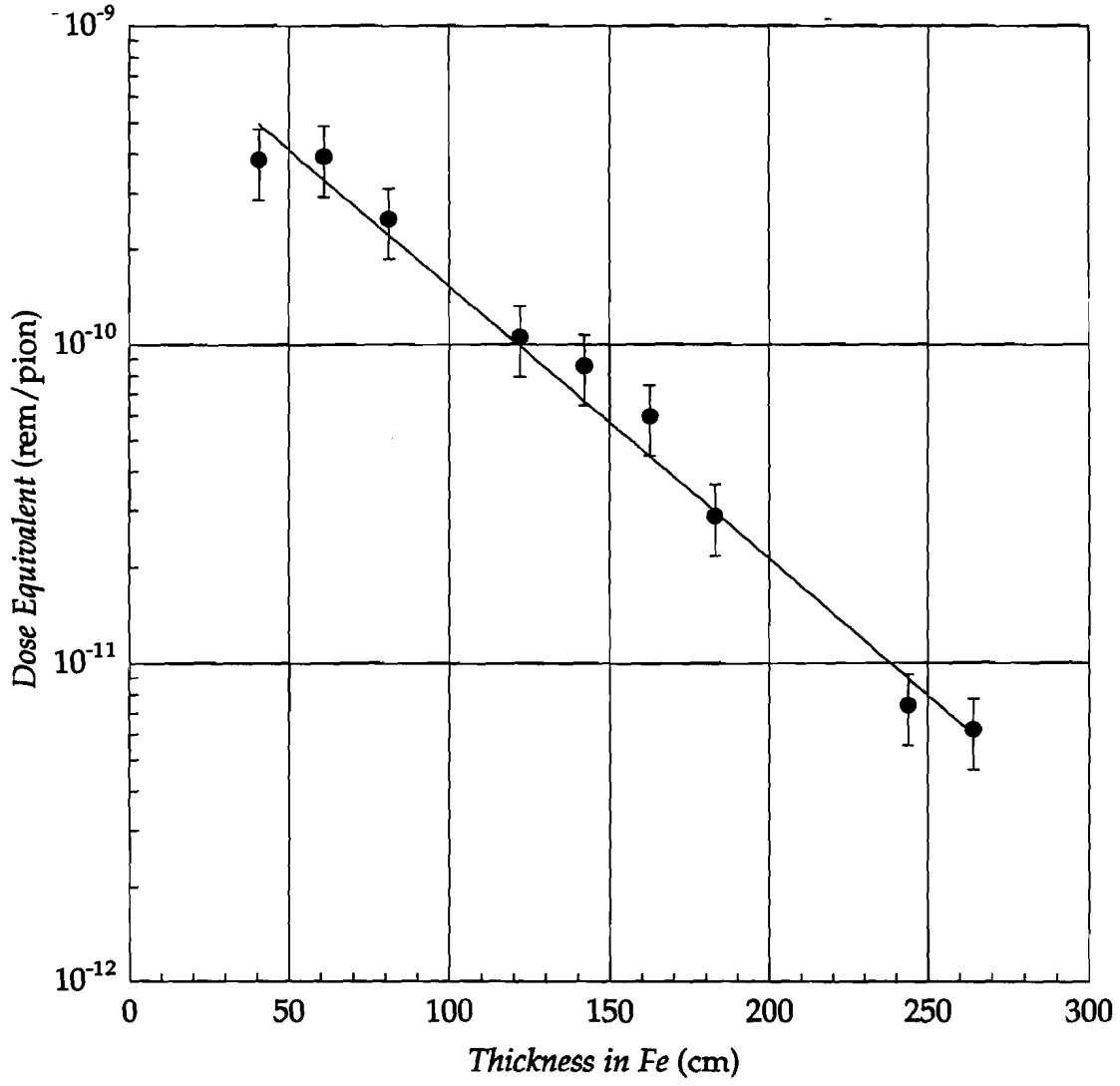

Figure 4.14. Dose Equivalent at 100 GeV. Plotted is dose equivalent as a function of thickness for 100 GeV incident pions in the longitudinal direction. Also shown is the fit of the data to expression 4.9. Results of the fit are given in Table 4.2.

Table 4.2
Summary of Fits to Eq. 4.9 for Fluence and Dose Equivalence vs Incident Pion Energy

	Fluence		Dose Equivalent	
Energy(GeV)	m_1	m_2	m_1 ($\times 10^{-10}$)	m_2
25	0.0196±0.0032	–0.0141±0.0016	2.876±0.856	–0.0169±0.0030
50	0.0441±0.0048	–0.0185±0.0007	7.188±1.344	–0.0216±0.0013
75	0.0591±0.0068	–0.0176±0.0006	9.435±1.807	–0.0207±0.0011
100	0.0675±0.0070	–0.0167±0.0006	11.01±1.92	–0.0197±0.0011
150	0.0870±0.0102	–0.0162±0.0007	15.53±3.03	–0.0199±0.0018
Average	N/A	–0.0166±0.0016	N/A	–0.0198±0.0018

Table 4.2 Summary of Fits of Fluence and Dose Equivalent as a Function of Incident Pion Energy for the Longitudinal Shielding. Shown are the results of the fit at five pion energies for the coefficients m_1 and m_2 Also shown is the average of the exponential coefficient (m_2) for fluence and dose equivalent.

The coefficient m_2, the exponential coefficient, is plotted as a function of energy in Figure 4.15. For fluence, an average over the incident pion energies gives,

$$\overline{m}_2 = -0.0166 \pm 0.0016$$

as shown in Table 4.2 ; for dose equivalent, averaging gives,

$$\overline{m}_2 = -0.0198 \pm 0.0018.$$

Since these values are approximately the same within the errors, an average yields an exponent of:

$$\langle m_2 \rangle = -0.0180 \pm 0.0012.$$

The energy dependence is obtained by fitting the coefficients m_1, shown in Table 4.2, to a power law in energy(E^m). The results for both fluence and dose equivalent are shown in Figure 4.16. The coefficient m is now the exponent of incident hadron energy E. Taking an average of the values of the coefficient m (0.79±0.09 for fluence and 0.87±0.16 for dose equivalent) from the fits, since they are the same within errors, one finds $\langle m \rangle$ = 0.83±0.08.

It appears, therefore, from these results that both the fluence and dose equivalent associated with neutrons that leak through iron shielding in the forward direction with respect to the incident beam, can be represented by the same dependence on thickness and hadron energy. Thus, if $R(E,z)$ represents either fluence or dose equivalent,

$$R(E,z) = R_o' E^{(0.83\pm0.08)} e^{-(0.018\pm0.001)z} \qquad 4.10$$

or alternatively,

$$R(E,z) = R_o' E^{(0.83\pm0.08)} e^{-z/(55.5\pm7.5)} \qquad 4.11$$

Equation 4.11 is in the form of exponential attenuation with a "generalized" mean free path of 55.5±7.5 cm for Fe. This should be compared with the "standard" value λ=21.6 cm which was used in the case of lateral Fe shielding.

From the fits in Figure 4.16, the source term strength R_o' for fluence is $(1.79 \pm 0.71) \times 10^{-3}$ n/cm^2-pion, while for dose equivalent it is $(2.02 \pm 1.42) \times 10^{-11}$

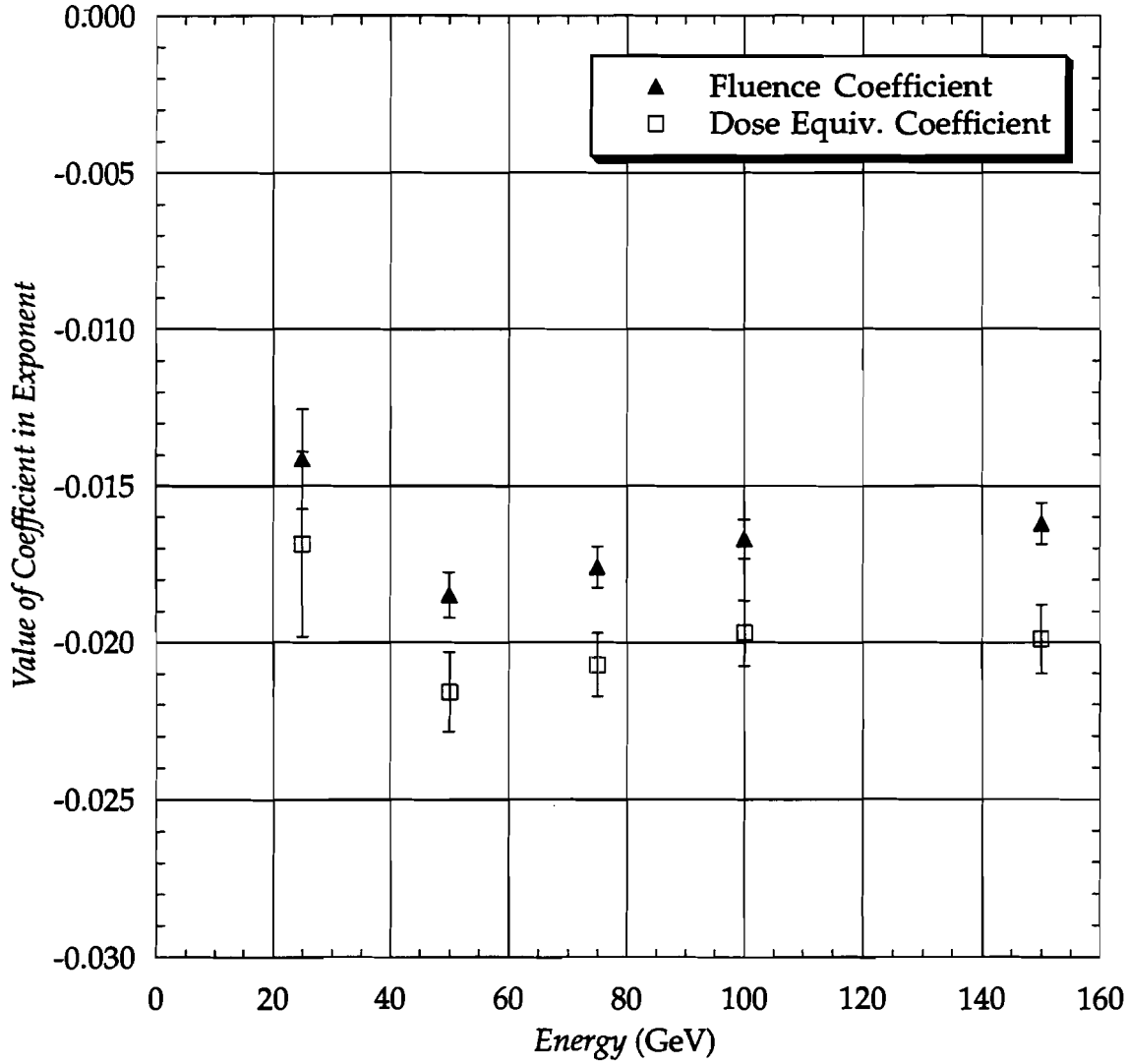

Figure 4.15. Exponents from the Fits. Plotted are the exponential coefficients for fluence and dose equivalent as a function of incident pion energy. These values (m_2) are also given in Table 4.2.

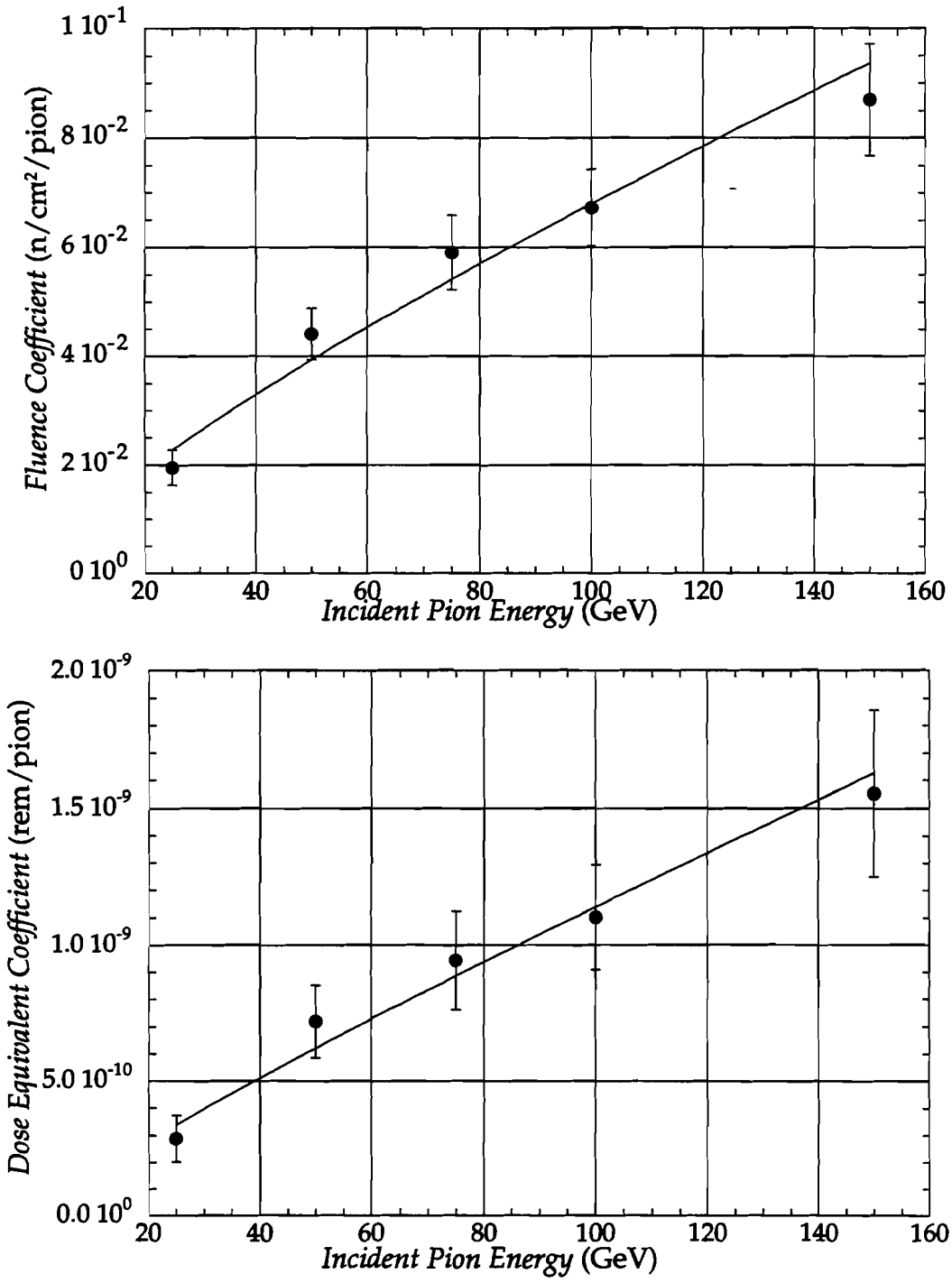

Figure 4.16. Energy Dependence Fit. Plotted are the coefficients (m_1) for fluence and dose equivalent as a function of incident pion energy. The energy dependence is obtained by fitting the coefficients (m_1) to a power law in energy. Values of the coefficients (m_1) are also given in Table 4.2.

rem/pion. The ratio of dose equivalent to fluence leads to a conversion factor or overall source term strength, outside of longitudinal Fe shielding of $(1.13 \pm 0.91) \times 10^{-8}$ rem/n/cm^2.

The exponential dependence on thickness given in Equation 4.11 can be written, as in Equation 4.8, in a form representing both a build-up and an attenuation term. Thus, from Equations 4.8 and 4.9,

$$m_2 = a - 1/\lambda \ . \qquad 4.12$$

Substituting the values of λ =21.6 cm as in the lateral case and m_2 =–0.018±0.001 that results from the fittings into Equation 4.12, the value of a for the longitudinal shielding case is found to be a=0.028. Thus, writing Equation 4.10 in the form of Equation 4.8 one finds:

$$R(E,z) = R_o' E^{(0.83 \pm 0.08)} e^{0.028z} e^{-z/21.6} \qquad 4.13$$

where $e^{0.028z}$ represents the build up term and $e^{-z/21.6}$ is the "standard" attenuation term.

In summary, both fluence and dose equivalent in the hadron energy range 25-150 GeV, can be represented by a dependence on both depth and energy as shown in Equation 4.13. The average conversion factor for longitudinal shielding is observed to be 10% smaller in absolute value than for the lateral shielding case. Unlike the lateral case, there is nothing in the literature for comparison with the present results.

4.5 FLUKA Monte Carlo Calculations

The Monte Carlo code FLUKA was used to simulate the measurements performed at the NWA enclosure for the on-axis (longitudinal) iron shielding. The newest version available, FLUKA92 [Fasso et al. 1993], simulates the development of hadron-induced cascades and includes the production and transport of neutrons down to the thermal energy range. This made it possible to run a single code and compare the results with the measurements performed. In the past FLUKA would

follow the neutrons down to 20 MeV, and then require a specially created file as input into another code, for example MORSE [Emmet 1975], in order to propagate the neutrons to thermal energies. In the current modeling of the experimental geometry, neutrons were scored when crossing a plane boundary in either direction at the detector position. In our case these positions (the Z-direction) range from 40.6 cm to 264 cm, the total thickness of iron shielding. For example, at a depth of 40 cm neutrons were scored when crossing the Z = 40 cm plane in both directions. The scoring surface was taken as an annulus centered on the beam axis and of radial width equal to the diameter of an arbitrary detector. In this case the radius of the detector was taken to be 30 cm to improve statistics. Inverse cosine weighting was applied to the number of trajectories passing through the annulus. The fluence in neutrons per cm^2 was determined from the neutrons passing through the annulus and its area. FLUKA92 does not (in the version used) calculate the dose equivalent.

Figures 4.17, 4.18 and 4.19 show the measured neutron spectra unfolded from the data by use of BUNKI compared to those generated in the FLUKA simulation. The agreement is generally very good at energies near the peak in the measured spectra (in the keV region) and, frequently, FLUKA is an adequate representation of the data at lower energies as well. However, the FLUKA simulation exhibits the presence of neutrons with energies that peak near 100 MeV which is not observed in the data. As discussed previously in Chapter 2, attempts to investigate the neutron region above 20 MeV experimentally were not successful, although preliminary studies suggested that the number of neutrons with energies above that value was small.

The relatively small size of the contribution of high energy neutrons suggested by the preliminary measurements is in fact corroborated by the FLUKA prediction in that the fluence of neutrons with energies above 9 MeV represent only 15% or less of the total fluence predicted at each pion energy and shield thickness.

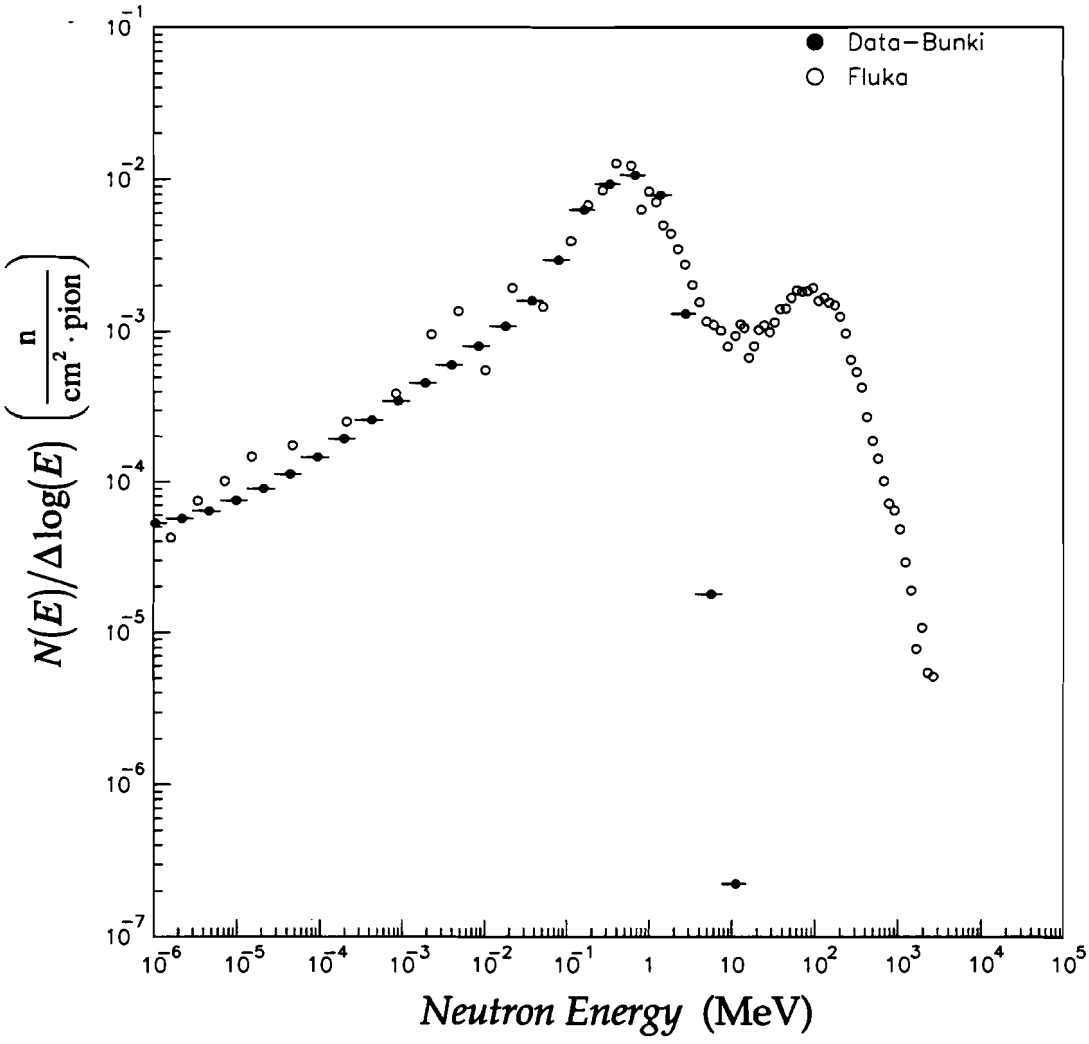

Figure 4.17. Neutron Spectra for Incident Pions on 40.6 cm of Iron. Shown is the neutron spectrum unfolded from the data by use of BUNKI compared to that generated by the FLUKA simulation, for 50 GeV incident pions on 40.6 cm (16 in, 2.4 λ) of iron in the longitudinal direction. The fluence per unit lethargy per pion is plotted as a function of neutron energy.

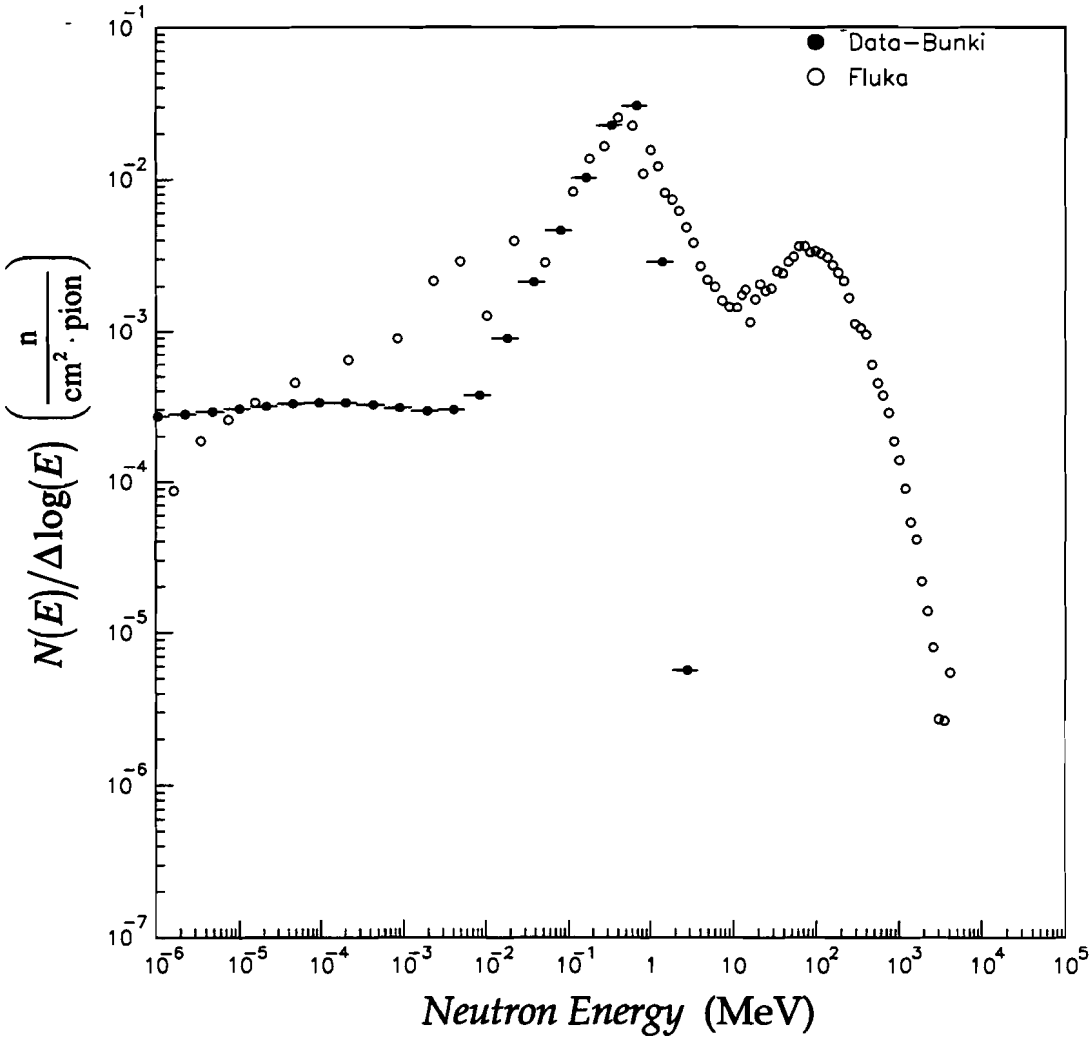

Figure 4.18. Neutron Spectra for Incident Pions on 61 cm of Iron. Shown is the neutron spectrum unfolded from the data by use of BUNKI compared to that generated by the FLUKA simulation, for 100 GeV incident pions on 61 cm (24 in, 3.6 λ) of iron in the longitudinal direction. The fluence per unit lethargy per pion is plotted as a function of neutron energy.

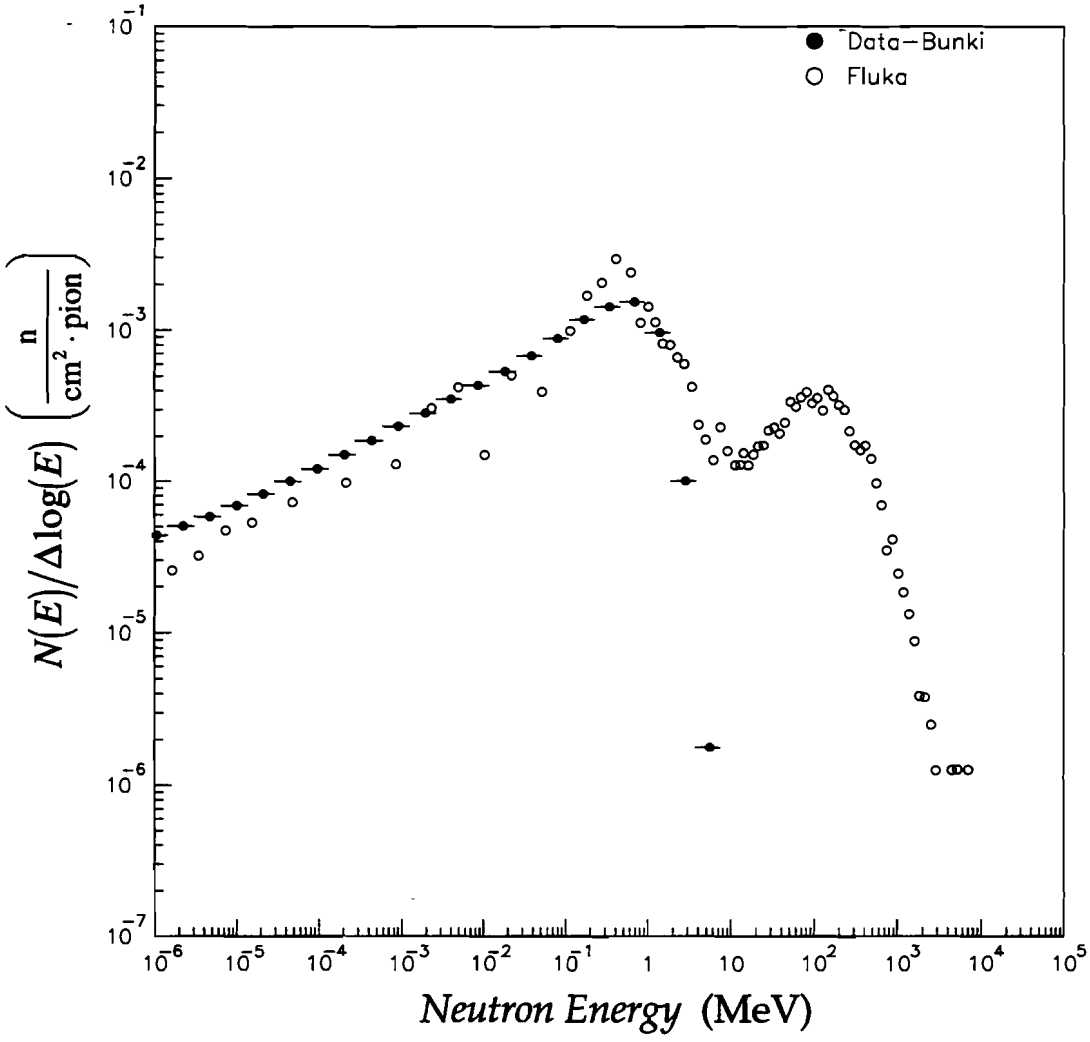

Figure 4.19. Unfolded Neutron Spectra for Incident Pions on 142.2 cm of Iron. Shown is the neutron spectrum unfolded from the data by use of BUNKI compared to that generated by the FLUKA simulation, for 50 GeV incident pions on 142.2 cm (56 in, 8.5 λ) of iron in the longitudinal direction. The fluence per unit lethargy per pion is plotted as a function of neutron energy.

Thus, the energy and thickness dependence exhibited by FLUKA is still a good representation of the majority of the data. The dependence on thickness calculated by FLUKA is compared in Figures 4.20, 4.21 and 4.22 with that unfolded from the data with BUNKI. Except for the thickest shield at each energy, the agreement is quite good for both the full FLUKA calculation as well as that truncated to energies below 9 MeV to match the upper energy limit observed for the data, even to the prediction by FLUKA of buildup at thicknesses between 40 and 50 cm. For the two thickest shields, where the agreement is less good, the FLUKA predictions are only two to three times smaller than the data.

The thickness and energy dependence of the fluence calculated by FLUKA was analyzed in the same way as was the data, described in the last section. As in the previous case, the same expression was used to describe the fluence in the forward direction. That is,

$$R = R_0' E^m e^{az} e^{-z/\lambda},$$

where $R_0' E^m$ is the source term or fluence at zero depth, E is the energy of the incident particle, z is the thickness of the shielding material (Fe), and λ is the mean free path in Fe (21.6 cm).

Figure 4.23 shows the neutron fluence at 100 GeV fitted to an exponential function,

$$y = m_1 e^{m_2 z}.$$

Table 4.3 shows the complete results of such fits of neutron fluence at all energies as a function of thickness; as seen, values of the exponent m_2 are constant to a few percent as a function of pion energy. The average value is equal to -0.0218 ± 0.0015. Recall that the data gave a value for the same exponent of -0.0180 ± 0.0012, about 17% lower in absolute value but almost within the stated accuracy of the data. Also the results of the FLUKA simulation truncated to neutron energies below 9 MeV show the same dependence on energy as does the full calculation, although absolute val-

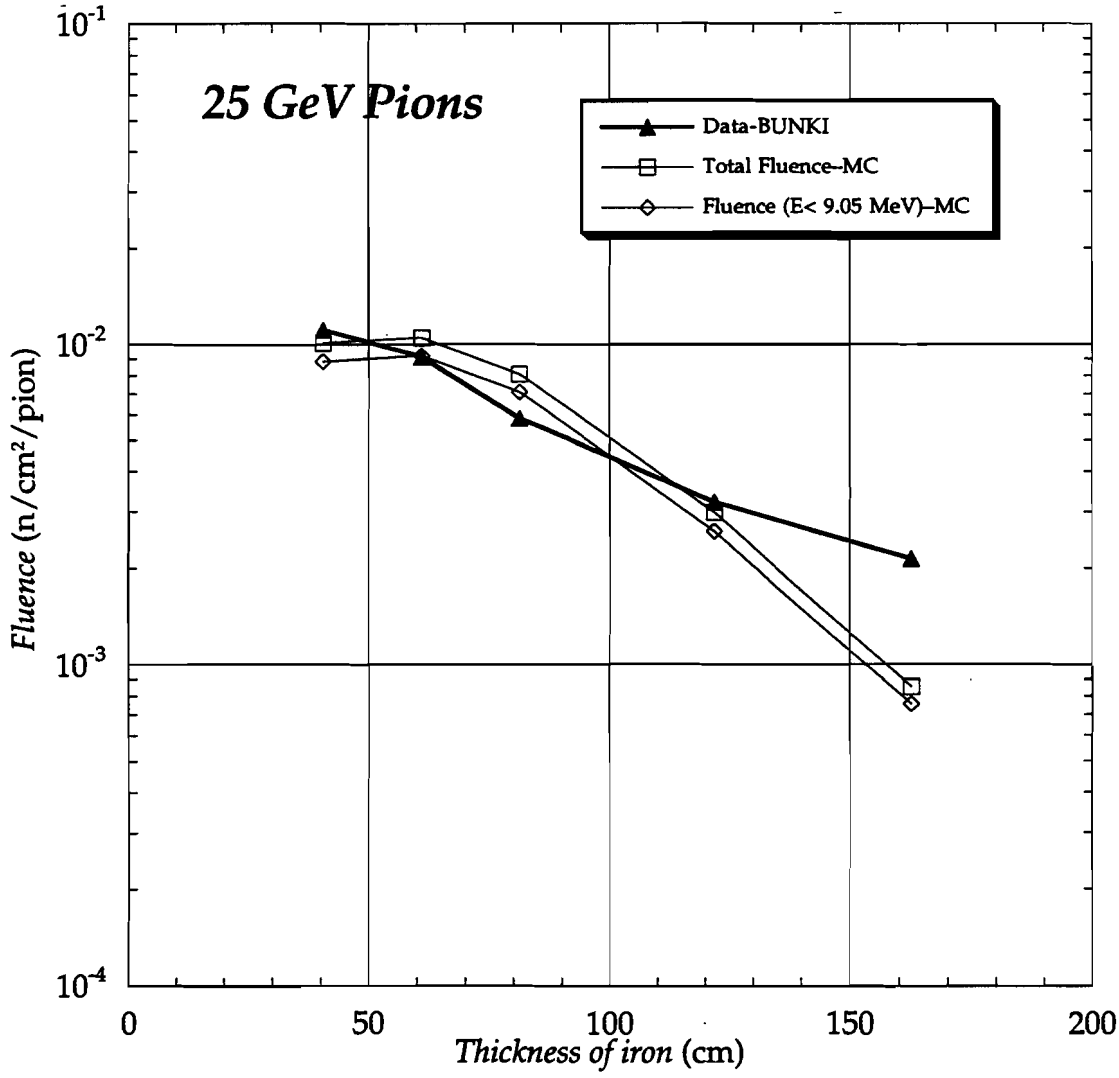

Figure 4.20. Thickness Dependence Comparison Between FLUKA and BUNKI at 25 GeV. The dependence on thickness calculated by FLUKA (labelled MC) both for total fluence and for fluence at neutron energies below 9 MeV is compared with that unfolded from the data by use of BUNKI. Plotted is the neutron fluence as a function of thickness for incident pions at 25 GeV.

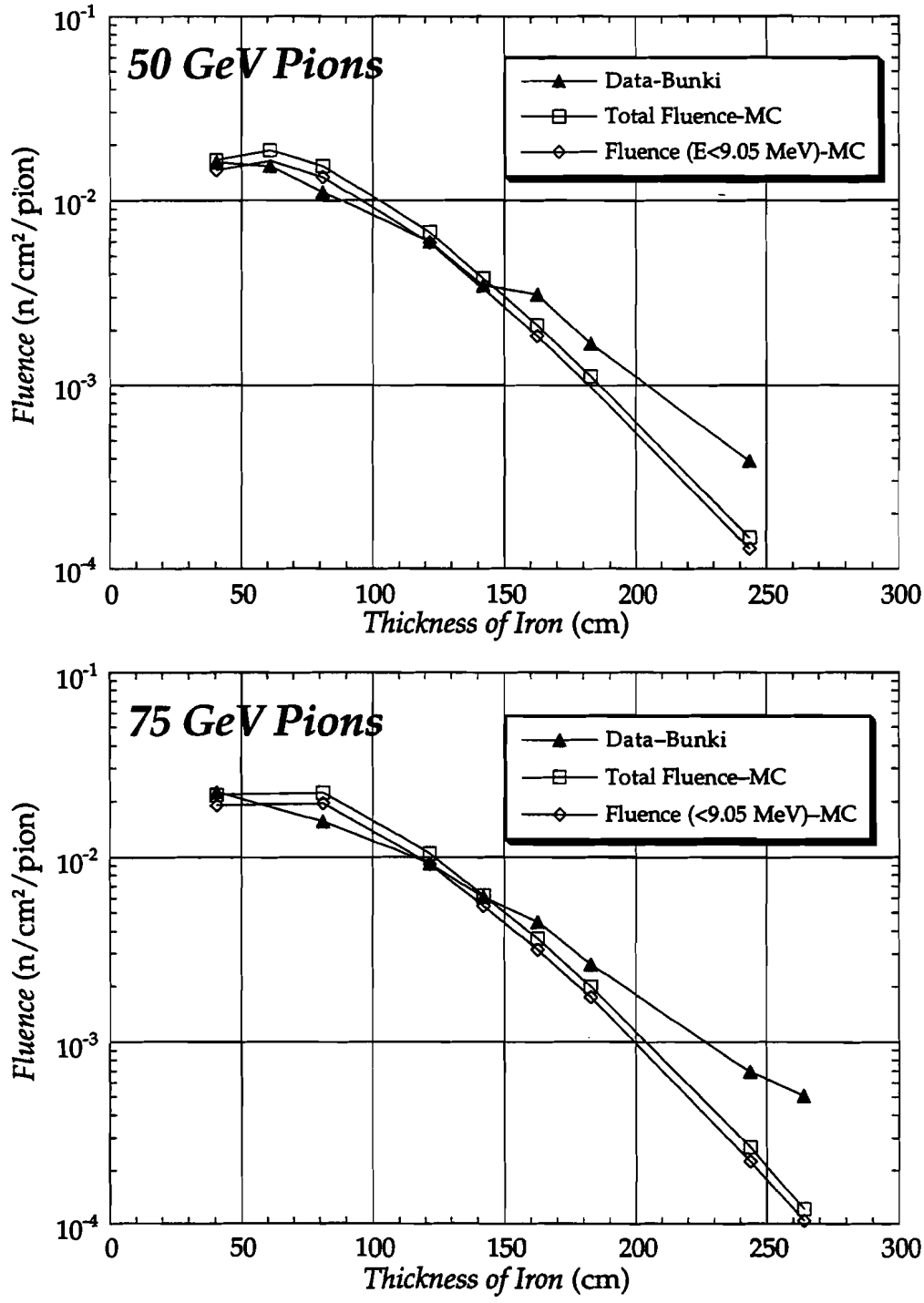

Figure 4.21. Thickness Dependence Comparison Between FLUKA and BUNKI at 50 and 75 GeV. The dependence on thickness calculated by FLUKA (labelled MC) both for total fluence and for fluence at neutron energies below 9 MeV is compared with that unfolded from the data by use of BUNKI. Plotted is the neutron fluence as a function of thickness for incident pions at 50 and 75 GeV.

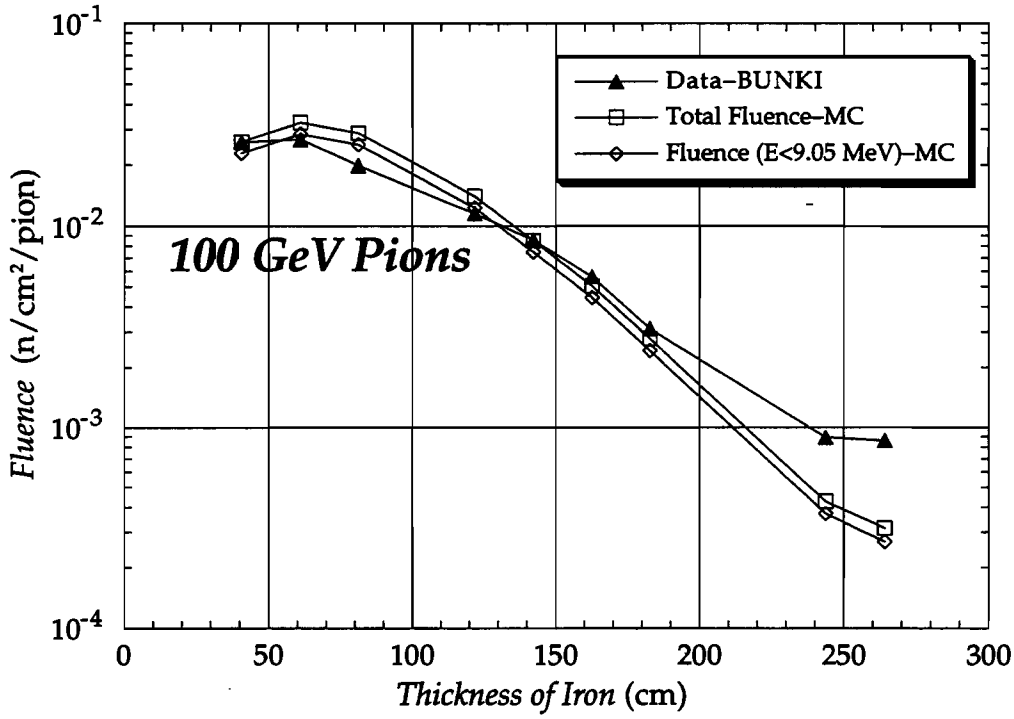

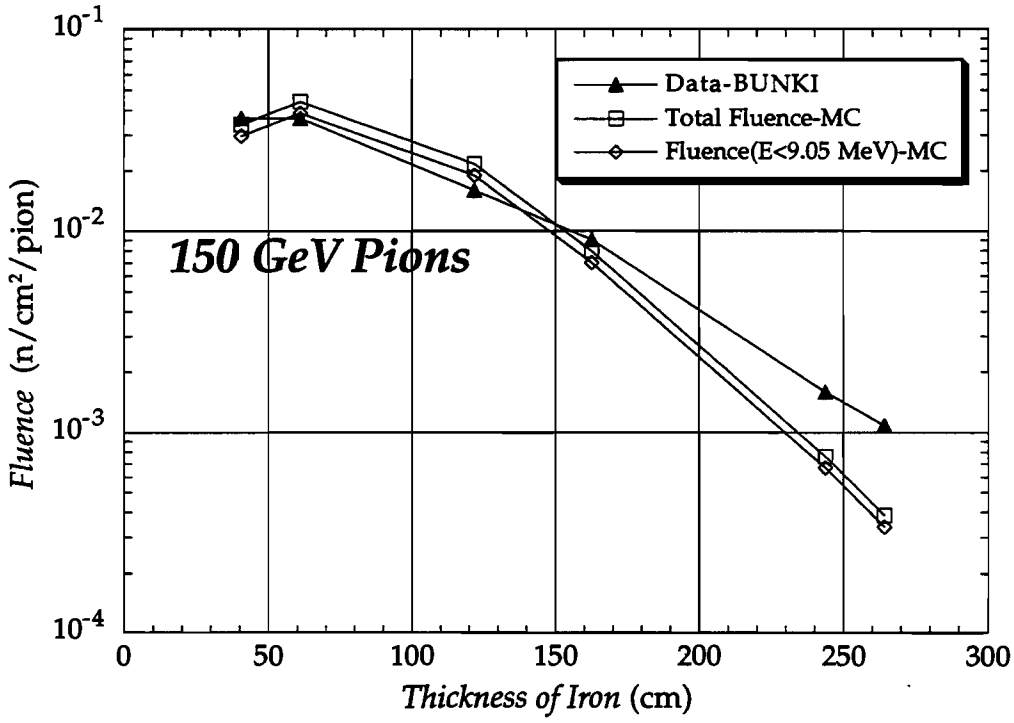

Figure 4.22. Thickness Dependence Comparison Between FLUKA and BUNKI at 100 and 150 GeV. The dependence on thickness calculated by FLUKA (labelled MC) both for total fluence and for fluence at neutron energies below 9 MeV is compared with that unfolded from the data by use of BUNKI. Plotted is the neutron fluence as a function of thickness for incident pions at 100 and 150 GeV.

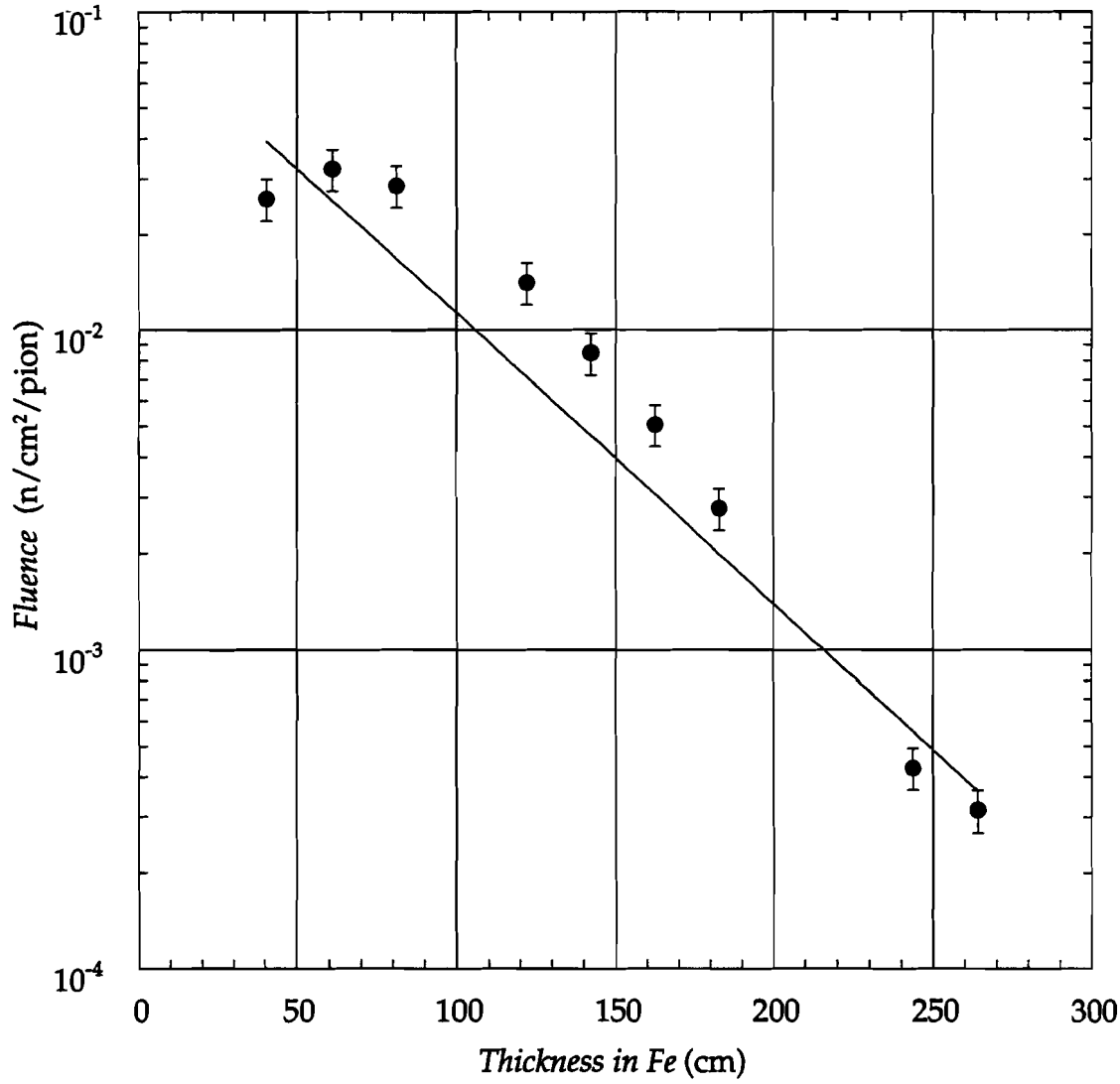

Figure 4.23. Calculations of Neutron Fluence at 100 GeV (FLUKA). Plotted is fluence as a function of thickness for 100 GeV incident pions in the longitudinal direction as simulated by FLUKA. Also shown is the fit of the data to expression 4.9. Results of the fit are given in Table 4.3.

Table 4.3
Summary of Fits of Fluence as a Function of Incident Pion Energy for the Longitudinal Shielding Generated by FLUKA

	Fluence		Fluence (E< 9.05 MeV)	
Energy (GeV)	m_1	m_2	m_1	m_2
25	0.0298±0.0043	–0.0208±0.0013	0.0260±0.0038	–0.0208±0.001
50	0.0642±0.0068	–0.0236±0.0007	0.0565±0.0059	–0.0236±0.0007
75	0.0830±0.0094	–0.0235±0.0007	0.0730±0.0082	–0.0236±0.0006
100	0.0922±0.0094	–0.0210±0.0006	0.0811±0.0082	–0.0210±0.0006
150	0.1045±0.0125	–0.0204±0.0006	0.0913±0.0109	–0.0204±0.0006
Average	N/A	–0.0218±0.0015	N/A	–0.0219±0.0016

Table 4.3. Summary of Fits of Fluence as a Function of Incident Pion Energy for the Longitudinal Shielding Generated by FLUKA. Shown are the results of the fit at five pion energies with the coefficients m_1 and m_2 Also shown is the average of the exponential coefficient (m_2) for total fluence and for fluence with energies lower than 9.05 MeV.

ues (as indicated by the coefficient m_1 in Table 4.3) are 10-15% lower.

After removing the depth dependence, Figure 4.24 shows that the dependence on energy can be represented by a power series in energy and the value of the exponent m is 0.68 ± 0.08 which is lower by 18% from the absolute value of 0.83 ± 0.08 given by BUNKI for the data, but is in agreement within the errors. The source term strength R_0' can be obtained from that same plot and is $(3.90 \pm 1.42) \times 10^{-3}$ n/cm^2/pion which is roughly twice the value in absolute terms found for the data, although they are almost in agreement within the rather sizeable errors. Similar fits to the m_1 coefficients from the truncated FLUKA simulation gives (3.43±1.25) x10^{-3} n/cm^2/pion, 12.5 % less.

In summary, from the FLUKA simulation, fluence can be written as:

$$R = (3.90 \pm 1.42) \times 10^{-3} \text{ n/cm}^2\text{/pion } \times E^{(0.68 \pm 0.08)} e^{(-z/45.9 \pm 3.2)}$$

or, alternatively,

$$R = (3.90 \pm 1.42) \times 10^{-3} \text{ n/cm}^2\text{/pion } \times E^{(0.68 \pm 0.08)} e^{(0.024z)} e^{(-z/21.6)}.$$

Table 4.4 shows a summary of the results for the on-axis longitudinal shielding where the measurements are compared to FLUKA results.

Even though the Monte Carlo simulation predicts that about 15% of the total fluence at each pion energy represents neutrons with energies greater than 9 MeV (which were, as discussed previously, not observed in the measurements) the energy and thickness dependence of the calculated results, are in good agreement within the stated accuracies with the actual data. Furthermore, the FLUKA calculation truncated to 9 MeV, gives results that are in excellent agreement with those from the full FLUKA calculation. This suggests that any additional fluence associated with high energy neutrons will not modify the dependence on thickness and energy.

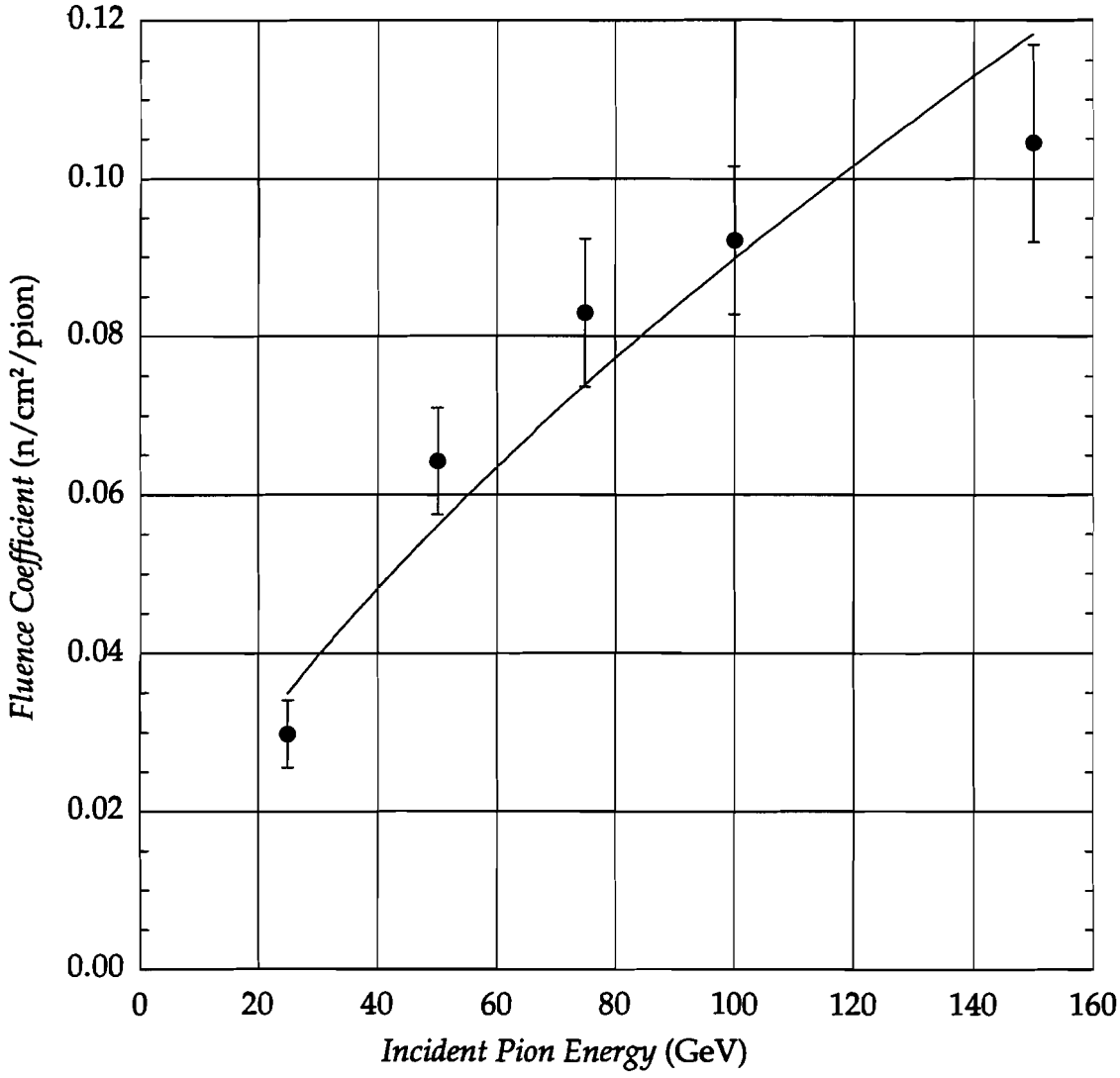

Figure 4.24. Energy Dependence Fit (FLUKA). Plotted are the coefficients (m_1) for fluence as a function of incident pion energy. The energy dependence is obtained by fitting the coefficients (m_1) to a power law in energy. Values of the coefficients (m_1) are given in Table 4.3.

Table 4.4
Summary Table for the On-Axis Longitudinal Shielding

	BUNKI (Data)	FLUKA	FLUKA (E<9.05 MeV)
Source term (R_0') n/cm^2/pion	$(1.79 \pm 0.71) \times 10^{-3}$	$(3.90 \pm 1.42) \times 10^{-3}$	$(3.43 \pm 1.25) \times 10^{-3}$
Source Term (R_0') rem/pion	$(2.02 \pm 1.42) \times 10^{-11}$	N/A	N/A
Conversion Factor rem/n/cm^2	$(1.13 \pm 0.91) \times 10^{-8}$	N/A	N/A
E^m	$E^{(0.83 \pm 0.08)}$	$E^{(0.68 \pm 0.08)}$	$E^{(0.68 \pm 0.08)}$
Generalized m.f.p (cm)	55	46	46

Table 4.4 Summary of Results for the On-Axis Longitudinal Shielding. Shown are source terms for fluence and dose equivalent, the exponent in energy, the conversion factor from fluence to dose equivalent and the generalized mean free path.

4.6 Proton Center PC-4 Results

4.6.1 The Roofs

Figures 4.25 and 4.26 show the neutron spectra, based on the BUNKI unfolding code, on the first and fourth roofs at the PC beamline enclosure PC-4 at different beam targeting angles. The peak between 0.1 and 1 MeV probably represents those neutrons that leak through iron (the large electromagnet in the targeting enclosure (see Fig. 2.4)) because of the small nuclear inelastic cross section for iron at such energies. Thermal neutrons and those with energies up to 1 keV contribute sizeably to the observed spectra because there was sufficient concrete in the vicinity to act as a moderator, but not enough to shield the neutrons from leaking out.

Tables 4.5 and 4.6 show the relative distribution in energy of both fluence and dose equivalent as obtained from BUNKI. On the roofs, even though roughly 90% of the fluence comes from neutrons with energies below 100 keV, 50% of the dose equivalent arises from neutrons with energies greater than 100 keV. Another 30% of the dose equivalent arises from neutrons with energies between 1.5 eV and 100 keV, while the other 20% arises from neutrons with energies below 1.5 eV. The preponderance of low energy neutrons is reflected in the fairly low value of the quality factor QF ≅ 3.8. It is seen in Tables 4.5 and 4.6 that targeting the beam at different angles does not affect the distribution of fluence or dose equivalent on the roofs.

4.6.2 Downstream Hyperon Extension Enclosure

Figure 4.27 shows the neutron spectra, based on the unfolding code BUNKI, for the upstream and downstream hyperon extension enclosures.

The downstream measurements for all targeting angles +3, 0, –3 mradians showed (see Tables 4.5 and 4.6) that although only about 25% of the fluence arises from neutrons with energies between 2 and 25 MeV, almost 70% of the dose equivalent comes from such neutrons. And while 60% of the fluence arises from neutrons

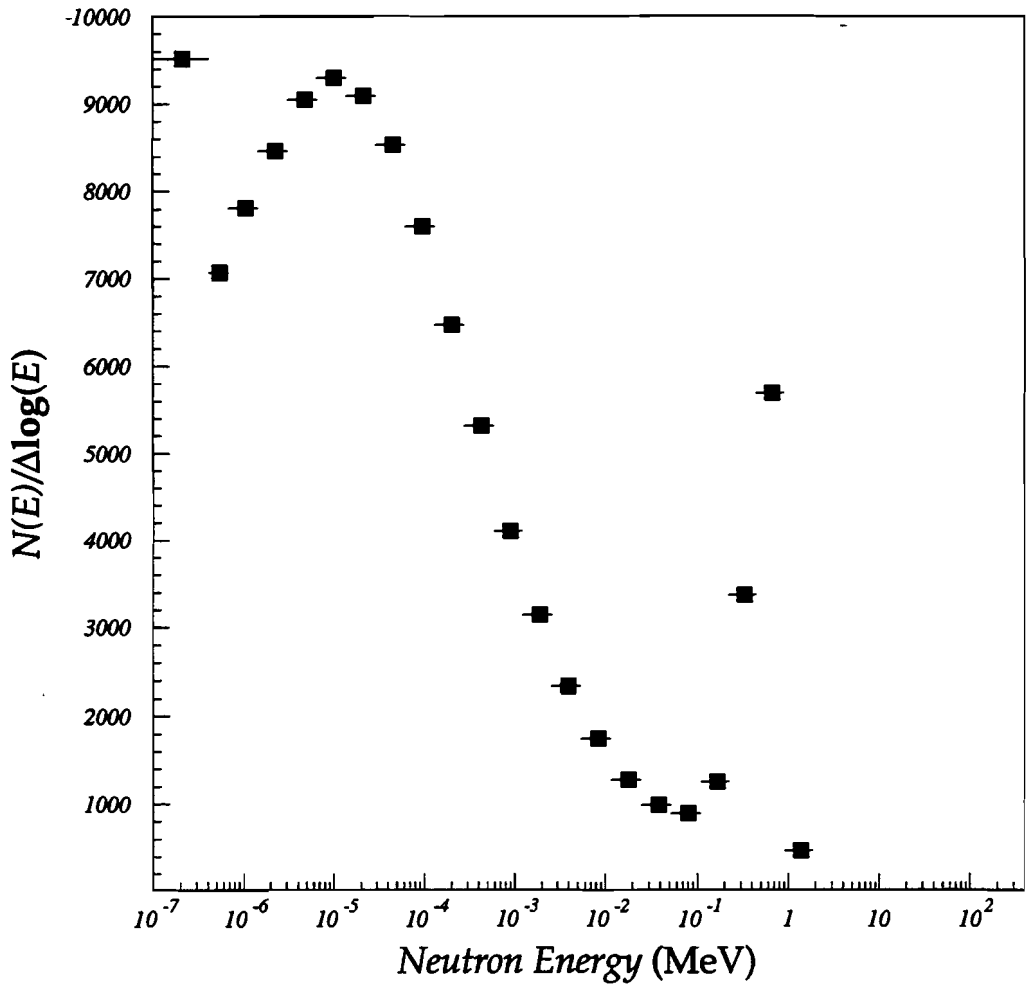

Figure 4.25. PC-4 First Roof Neutron Spectrum. Shown is the neutron spectrum unfolded using BUNKI from the data, for incident protons at 800 GeV. Plotted is fluence per unit lethargy as a function of neutron energy.

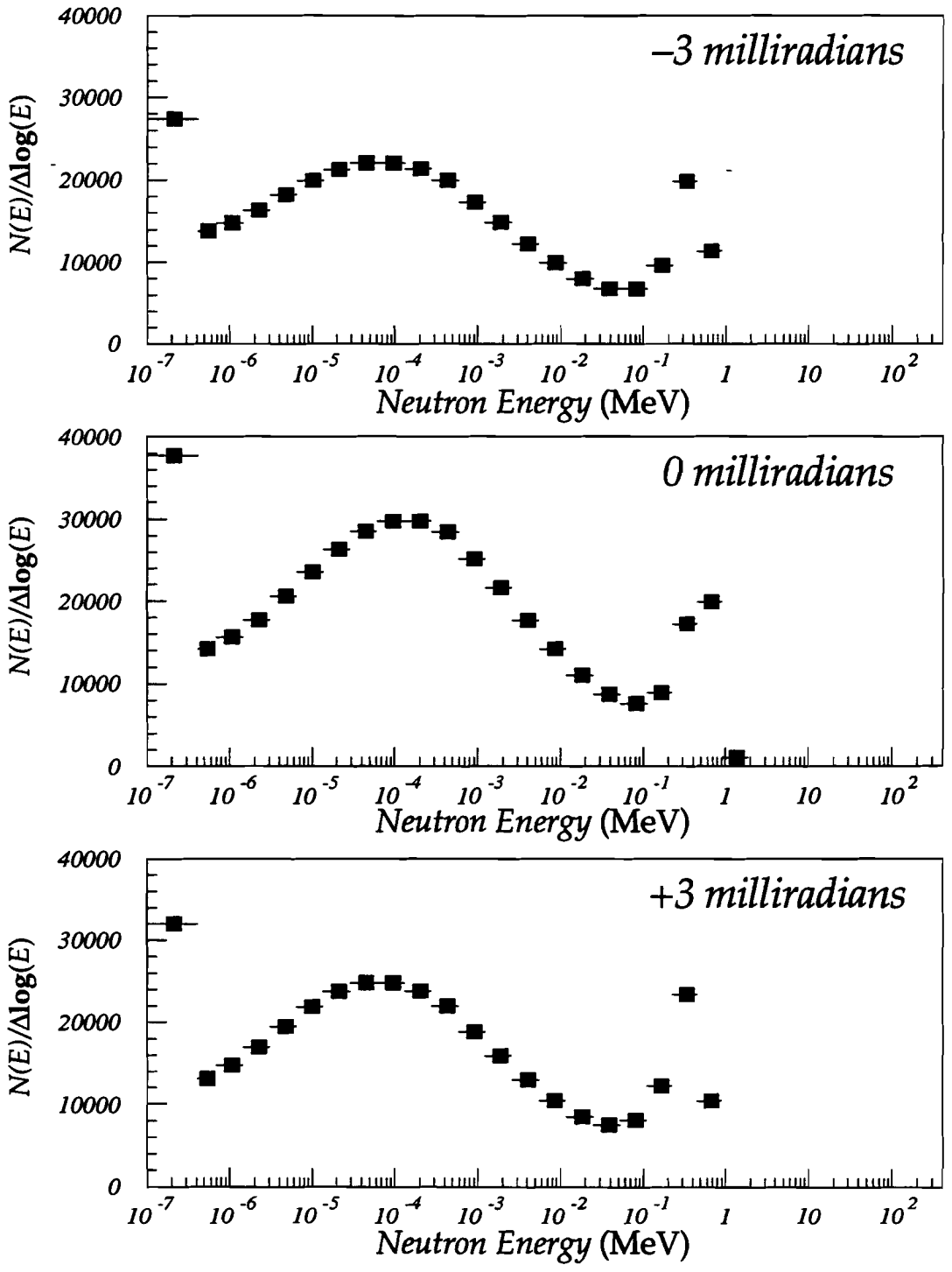

Figure 4.26. PC-4 Fourth Roof Neutron Spectra. Shown are the neutron spectra unfolded from the data,using BUNKI, for incident protons of 800 GeV at three beam targeting angles. Plotted is fluence per unit lethargy as a function of neutron energy.

Table 4.5
PC4 Fluence in Specific Energy Bins for Unfolded Neutron Spectra

Bin Range	1st roof	4th roof 0 mradians	4th roof +3 mradians	4th roof –3 mradians	Downstream 0 mradians	Downstream 3 mradians	Downstream –3 mradians	Upstream 0 mradians	Upstream +3 mradians	Upstream –3 mradians
< 1.5 eV	35.0	34.8	34.9	33.4	21.8	23.3	21.3	34.8	40.4	32.8
1.5 eV – 0.1 MeV	58.2	58.1	57.5	57.8	38.0	45.0	37.8	24.7	52.3	54.9
0.1 MeV – 2.0 MeV	6.7	7.4	7.6	8.8	14.3	10.7	15.8	1.6	0.4	11.4
2 MeV – 25 MeV	—	—	—	—	25.8	21.0	24.9	38.9	6.9	0.9
> 25 MeV	—	—	—	—	0.1	—	—	—	—	—

Table 4.5. PC-4 Fluence in Specific Energy Bins for Unfolded Neutron Spectra. Shown is the percentage of total fluence in specific energy bins at a given position. For the fourth roof, the downstream and upstream hyperon extensions, there are three beam targeting angles as shown in the table above.

Table 4.6
PC4 Dose Equivalent in Specific Energy Bins for Unfolded Neutron Spectra

Bin Range	1st roof	4th roof 0 mradians	4th roof 3 mradians	4th roof –3 mradians	Downstream 0 mradians	Downstream +3 mradians	Downstream –3 mradians	Upstream 0 mradians	Upstream +3 mradians	Upstream –3 mradians
< 1.5 eV	16.7	16.5	17	15.5	1.89	2.09	1.71	6.9	11.6	9.1
1.5 eV – 0.1 MeV	29.6	30.8	32.1	30	4.6	5.4	5.7	12.5	15.8	17.3
0.1 MeV – 2.0 MeV	53.6	52.7	50.9	54.5	20.7	23.0	21.6	3.9	2.2	64.9
2 MeV – 25 MeV	0.11	—	—	—	72.5	69.5	71	76.7	70.4	8.72
> 25 MeV	—	—	—	—	0.3	—	—	—	—	—
Quality Factor	3.7	3.8	3.7	3.8	6.5	7.4	6.4	5	4.5	5.2

Table 4.6. PC-4 Dose Equivalent in Specific Energy Bins for Unfolded Neutron Spectra. Shown is percentage of total dose equivalent in specific energy bins at a given position. For the fourth roof, the downstream and upstream hyperon extensions, there are three beam targeting angles as shown in the table above.

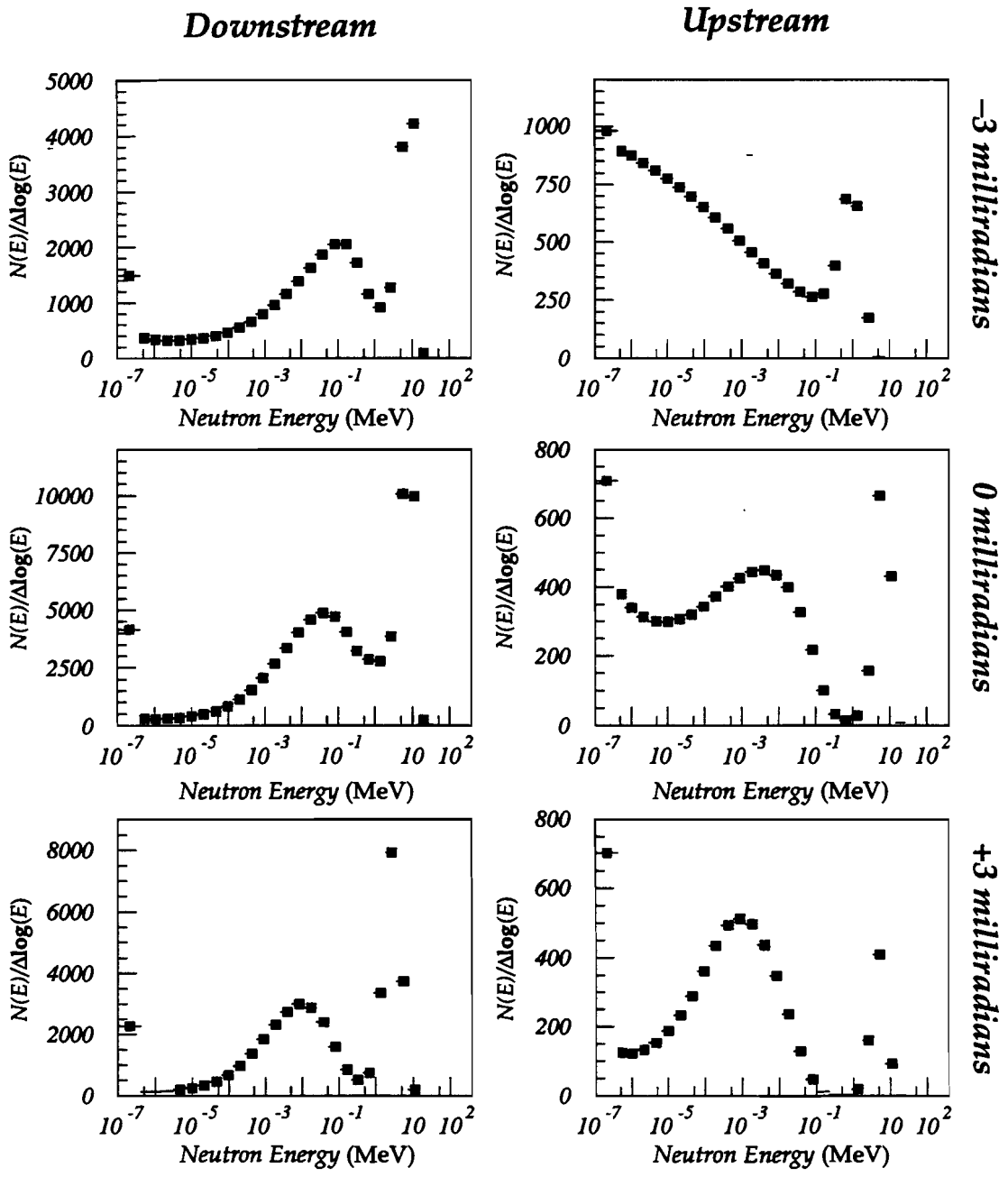

Figure 4.27. PC-4 Downstream and Upstream of the Hyperon Extension Enclosures Neutron Spectra. Shown are the neutron spectra unfolded using BUNKI from the data, for incident protons at 800 GeV at three different beam targeting angles. The plots on the left and right of the page represent respectively the downstream and upstream hyperon extension enclosure measurements. Plotted is fluence per unit lethargy as a function of neutron energy.

with energies below 0.1 MeV, only about 7% of the dose equivalent is contributed by such neutrons. The average quality factor is around 6.8 indicating the presence of neutrons with higher energies contributing to the dose equivalent and to a much harder spectra than those in the roof area.

Figure 4.28 shows neutron spectra, based on both unfolding codes BUNKI and LOUHI, for the downstream hyperon extension enclosure at +3 mradians. It can be seen from this figure that while there is some disagreement in the details, the spectra unfolded by both codes have the same general shape. Table 4.7 shows a comparison of the results of the unfolding done by the two different codes. The total fluence and dose equivalent agrees very well while the agreement for the average energy and quality factor is reasonably good.

4.6.3 Upstream Hyperon Extension Enclosure

The results of the upstream hyperon extension measurements show a dependence on the targeting angle. The upstream measurement at a +3 mradians targeting angle showed (see Tables 4.5 and 4.6) that 90% of the fluence comes from neutrons with energies below 0.1 MeV while only 27% of the dose equivalent comes from neutrons in that energy range. On the other hand neutrons with energies between 2 and 25 MeV contribute only 6.9% to the fluence but 70% to the dose equivalent.

At –3 mradians beam targeting angle, the measurement showed that 86% of the fluence comes from neutrons with energies below 0.1 MeV whereas only 16% of the dose equivalent comes from neutrons in that energy interval. Neutrons with energies between 0.1 and 2.0 MeV contribute 11% to the fluence while 65% of the dose equivalent comes from neutrons in that same energy interval.

At 0 mradians beam targeting angle, the neutrons with energies below 0.1 MeV contribute 69% to the fluence while neutrons in that same energy range contribute 19% to the dose equivalent. Furthermore, neutrons between 2 and 25 MeV

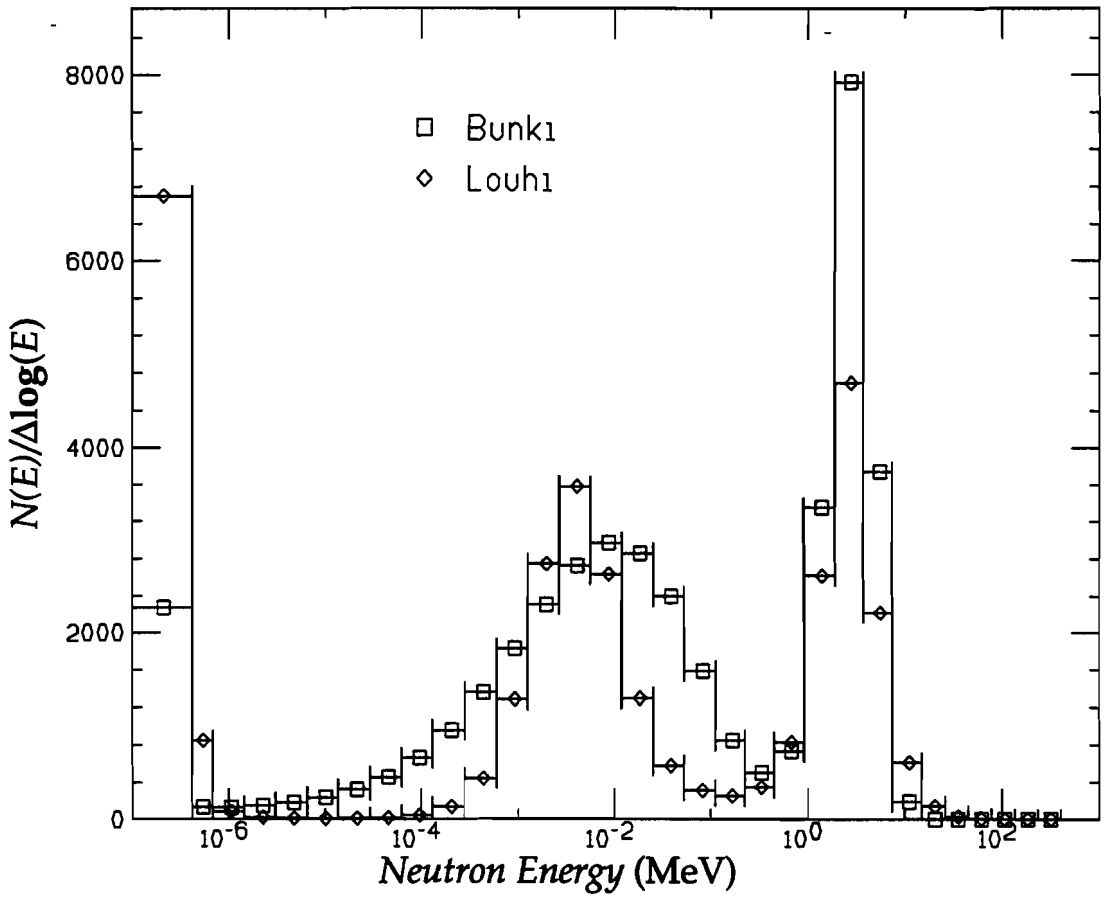

Figure 4.28. PC-4 Downstream Hyperon Extension Enclosure Neutron Spectra at +3 Milliradians. Shown are the neutron spectra using unfolding codes BUNKI and LOUHI from the data, for incident protons at 800 GeV and +3 milliradians targeting angle. Plotted is fluence per unit lethargy as a function of neutron energy.

Table 4.7

PC-4 Comparison of Results Obtained Using BUNKI and LOUHI Unfolding Codes

	BUNKI	LOUHI
Total Fluence (N/cm^2)	15790	15900
Total Dose Equivalent (mrem)	0.203	0.208
Average Energy (MeV)	1.18	1.41
Quality Factor	7.5	8.0

Table 4.7. PC-4 Comparison of the Unfolded Data by use of BUNKI and LOUHI. Shown are the results at the downstream hyperon extension at +3 miliradians of fluence, total dose equivalent, average energy and quality factor.

contribute 39% to the fluence but almost 77% to the dose equivalent. The average quality factor is significantly lower than that measured in the downstream extension, demonstrating a much softer neutron spectra.

4.7 Monte Carlo Calculations at PC-4

CASIM [Van Ginneken 1975] is a Monte Carlo code that was used to estimate the dose equivalent for the PC-4 data set. This program is based on the development of intranuclear cascades when high energy particles strike large shields of arbitrary shape and composition. The program can treat particles with incident momentum in the range 20–20000 GeV/c. It has a cut off at 0.3 GeV/c, which corresponds to a kinetic energy of 46.8 MeV for a nucleon; it does not follow particles with momentum lower than this cut off. In contrast to the FLUKA code, CASIM uses directly inclusive distributions, i.e., particle yields as function of angle and momentum from inelastic interactions, in order to produce the particles to follow in the cascade simulation. It is a weighted Monte Carlo program; this means that only one or two high energy particles are allowed to be created in each collision, but these particles carry a weight related to their probability of production for the energy carried with them. The program calculates star densities, that is, the density of inelastic interactions as a function of location and particle type crossing the region of interest. From star densities, conversion to dose equivalent is possible. Unlike FLUKA92, CASIM does not estimate neutron fluence.

The dose equivalent calculated by CASIM agrees within a factor of two with measurements made on the roofs. Table 4.8 shows the comparison between the measurement and CASIM for the dose equivalent at the first roof. In addition a comparison with CASIM of the measured averaged dose equivalent at three different targeting angles on the fourth roof is presented in the same table.

Table 4.8
Comparison of Measurements and CASIM Calculations

	Dose Equivalent (mrem)	
	1st Roof	4th Roof
Measurements	0.118	0.369
Monte Carlo (CASIM)	0.178±0.121	0.570±0.433

Table 4.8 PC-4 Comparison of Dose Equivalent Unfolded from the Data by BUNKI with CASIM Simulations. Shown are the results at the first and fourth roofs of the dose equivalent obtained from the data by use of BUNKi and the simulation generated by CASIM. The CASIM results are presented for the same number of incident protons as the measurements. The agreement is roughly within the errors associated with the simulation.

Chapter 5

Conclusions

In this chapter the major conclusions are summarized. They are based on the analyses discussed in the previous chapter. The conclusions are related to the dosimetric quantities of fluence and dose equivalent for neutrons. The results summarized below should be applicable at all accelerator laboratories at which neutrons that arise from the interaction of high energy hadrons with matter must be shielded.

5.1 Dependence on Shielding Thickness

From the study of shielding in the forward direction, the shape of the spectrum for those neutrons that leak through an Fe absorber is roughly independent of beam energy and absorber thickness. This holds even for shield thicknesses as small as 40.6 cm (16"), and suggests, therefore, that the hadronic cascade within the iron is well-developed and secondary-particle equilibrium is achieved at absorber thickness of less than 3 mean free paths (i.e, about 51 cm).

In the transverse (lateral) shielding direction, measurements were performed at only one shield thickness, so that the thickness dependence associated with neutron fluence and dose equivalent could not be determined. Even so, the results are consistent with the empirical expressions, Equations 4.1 and 4.2, with an effective mean free path of 21.6 cm, the so-called " standard" value, in agreement with the value for the mean free path obtained in a least-squares analysis of the results from Monte Carlo calculations [Fasso et al. 1990]

In the longitudinal shielding direction, the dependence on thickness of both total fluence and dose equivalent can be represented by the product of a build-up

factor ($e^{0.028z}$) and an attenuation term ($e^{-z/21.6}$); or, alternatively, as an attenuation term with a generalized mean free path λ=55.5±7.7 cm, larger by a factor of 2.5 than the "standard" lateral shielding value, λ=21.6 cm.

In Figure 5.1 the average quality factor obtained from the unfolded data is plotted as a function of absorber thickness. The observed decrease with increasing shield thickness is consistent with an overall "softening" (that is, a lowering) of the average neutron energy with increasing depth.

5.2 Dependence on Energy

The dependence of both fluence and dose equivalent on incident hadron energy E is given by a power law expression E^m, and is essentially the same for both lateral (m=0.86±0.02) and longitudinal (m=0.83±0.08) shielding directions. The "standard" value for lateral shielding is 0.80±0.10.

The "standard" result (0.80±0.10) quoted by Thomas [1988] actually arises from a statistical analysis [Thomas et al. 1984, Liu et al. 1984] of a fairly large data base of experimental attempts to determine the source strength parameter associated with the semi-empirical Moyer Model developed in 1961 [Moyer, 1961, 1962], before the widespread use of Monte Carlo techniques, to determine the transverse shielding requirements for high energy accelerators. This model, even now, has proved to be a reasonable method for the estimation of the shielding needed at high energy accelerator facilities. The present results verify the detailed energy dependence given by the Moyer Model for the case of lateral shielding, and even suggests the same energy dependence for the forward-direction shielding for which the Moyer Model is not meant to apply.

5.3 Conversion Factor

The source strength, or conversion factor between dose equivalent and fluence, is very closely the same for both lateral and longitudinal shielding directions. This is somewhat surprising in view of the Moyer Model representation

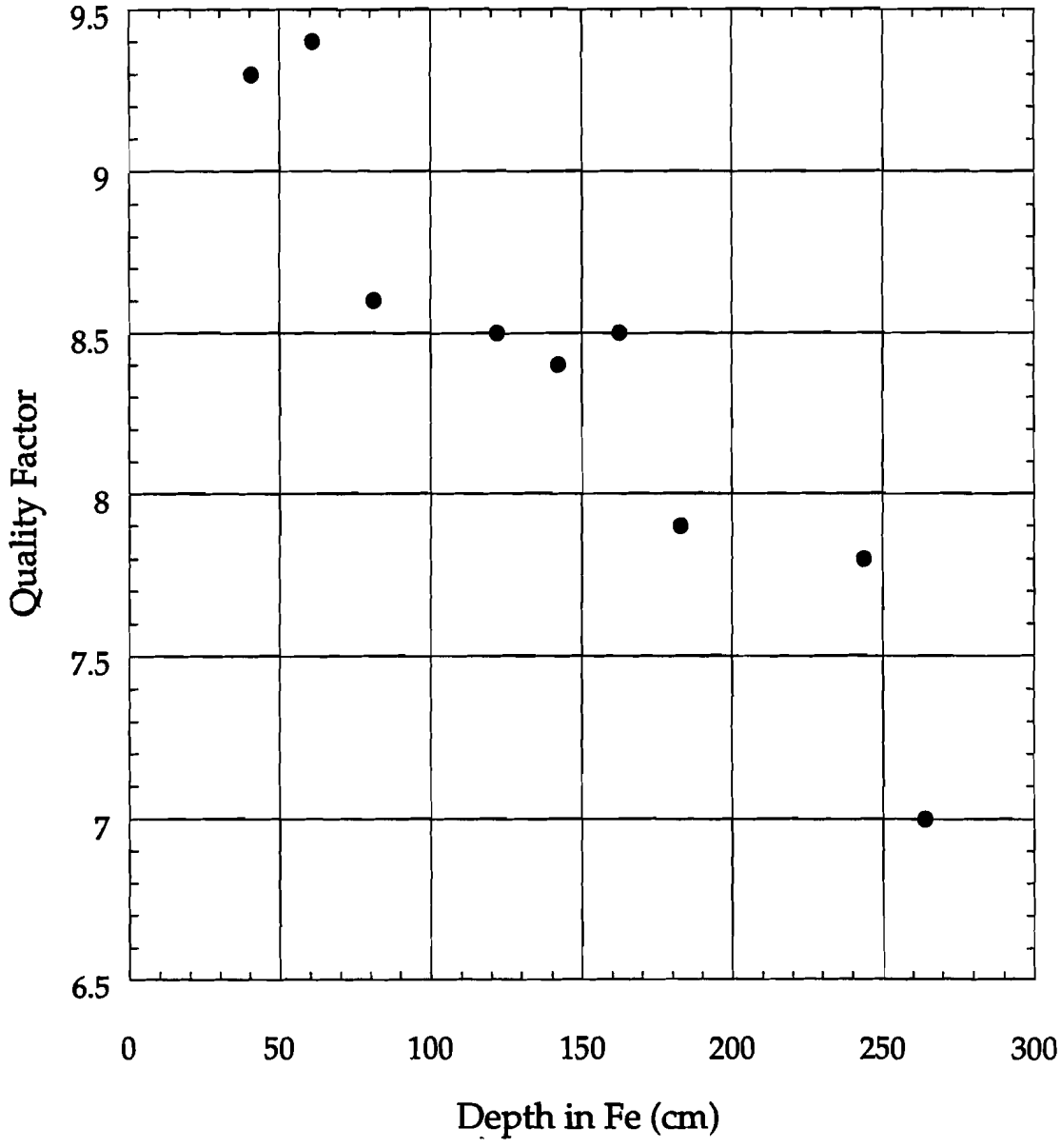

Figure 5.1. Average Quality Factor at NWA. Plotted is the average quality factor as a function of thickness in Fe in the longitudinal direction at NWA. Note that the QF decreases slightly with increasing Fe depth.

[McCaslin, 1982] which would predict different values dependent on the angle of observation. The value at 90 degrees is $(0.76\pm0.10) \times 10^{-8}$ rem/n/cm^2 for the Moyer Model, based on the source term value $(2.84\pm0.14) \times 10^{-7}$ rem/n/cm^2 from the analysis of Thomas et al [1984], and would be larger at smaller angles. Based on the present measurements and analysis it was found to be $(1.29\pm0.62) \times 10^{-8}$ rem/n/cm^2 for the lateral case and $(1.13\pm0.91) \times 10^{-8}$ rem/n/cm^2 for the longitudinal shielding.

It should however be mentioned again that the Moyer Model was first formulated for a beam striking a target or a beam stop of limited radial extent within a tunnel. This is rather different from the experimental situation studied in the present work.

5.4 Comparison with Monte Carlo Calculations

The agreement of the spectral data with the predictions of the Monte Carlo code FLUKA is generally excellent, particularly at neutron energies between 10 keV and 5-10 MeV, and frequently down to very low energies as well. On the other hand, Monte Carlo (FLUKA) simulation showed that neutrons with energies higher than 10 MeV should contribute between 10-15 % to the total fluence at each pion energy and shield thickness. As mentioned and discussed in Chapters 3 and 4, there is little evidence in the data for the existence of such neutrons.

Even so, the dependence of fluence on energy and thickness, from the FLUKA calculation is in agreement within the rather large errors of the analysis with that determined from the data. This is true for the full FLUKA predictions as well as for the FLUKA simulation truncated to neutrons energies below 9 MeV. Therefore, assuming that the Monte Carlo calculation is a reasonable representation of the data that exists, it appears that the expression which represents the energy and thickness dependence (e.g., Equation 4.13) obtained from the analysis of the actual data will remain valid even though the small fraction of higher energy neutrons pre-

dicted by FLUKA were not seen experimentally.

5.5 Properties of the Neutron Fields

Based on the spectral measurements taken outside of the shielding at the experimental beam line enclosure at PC-4, it was found that on the roofs at least 50 % of the dose equivalent comes from neutrons with energies above 0.1 MeV. At both downstream and upstream enclosures 60-70 % of the dose equivalent arises from such neutrons. This occurs in spite of the fact that over 60 % of the fluence is from neutrons with energies less than 0.1 MeV at all locations. The average quality factor at all locations is about 5 although the roofs show smaller values (softer spectra) and the downstream extension larger values (harder spectra).

The results summarized above generally reflect the conclusions of Elwyn [1991, Cossairt et al. 1988] who has reported on the average properties of neutron radiation fields outside shielded enclosures at Fermilab. Based on a series of measurements at about 14 locations around the laboratory, 23 % of the fluence and 77 % of the dose equivalent arises from neutrons with energies above 0.1 MeV; and the quality factor of the neutron field is about 5. Thus, the PC-4 area is fairly typical of shielded accelerator-generated neutron radiation areas.

Finally, the present results suggest that what happens within an experimental enclosure can sometimes affect the properties of the neutron field at locations outside shielding. For example, targeting of primary proton beam at different angles within the beam line enclosure can affect the shape of the neutron spectra as well as the distribution of fluence and dose equivalent at specific locations outside of shielding, and must be considered in the design of the shielding for high energy experiments.

Appendices

Appendices A, B and C represent a compilation of the entire data ensemble collected at NWA.

Appendix A

In Appendix A, Tables A.1 through A.10 present all the data unfolded by use of BUNKI and LOUHI (total fluence, dose equivalent, average quality factor etc.) collected at NWA.

Depth 40.6 cm of Fe Data Taken at NWA

	BUNKI					LOUHI				
Energy (GeV)	25	50	75	100	150	25	50	75	100	150
Total Fluence ($N/cm^2 \cdot 10^7 \cdot$Pions)	110600	160000	224000	257800	364000	112000	158000	220700	253400	361400
Total Dose Eqv. (Rem/10^7 Pions)	1.69×10^{-3}	2.44×10^{-3}	3.22×10^{-3}	3.82×10^{-3}	5.41×10^{-3}	1.89×10^{-3}	2.81×10^{-3}	3.70×10^{-3}	4.28×10^{-3}	6.06×10^{-3}
Rem/Fluence	1.53×10^{-8}	1.53×10^{-8}	1.44×10^{-8}	1.48×10^{-8}	1.48×10^{-8}	1.69×10^{-8}	1.79×10^{-8}	1.68×10^{-8}	1.69×10^{-8}	1.68×10^{-8}
Average Energy(MeV)	0.55	0.56	0.52	0.47	0.48	1.2	1.0	0.92	0.71	0.82
Quality Factor(QF)	9.2	9.3	9.2	9.4	9.3	9.2	9.5	9.4	9.6	10.3

Table A.1. Results of the Unfolding are Shown. The total fluence as unfolded by use of BUNKI and LOUHI is shown. Total dose equivalent, conversion factors fluence to dose equivalent and quality factors calculated by the two codes are shown.

Depth 61 cm of Fe Data Taken at NWA

	BUNKI					LOUHI				
Energy (GeV)	25	50	50	100	150	25	50	50	100	150
Total Fluence ($N/cm^2 . 10^7$.Pions)	91300	153000	154000	267000	363800	89840	152400	152700	266300	360700
Total Dose Eqv. (rem/10^7 Pions)	1.11×10^{-3}	2.25×10^{-3}	2.23×10^{-3}	3.91×10^{-3}	5.45×10^{-3}	1.42×10^{-3}	2.76×10^{-3}	2.75×10^{-3}	4.81×10^{-3}	6.76×10^{-3}
Rem/Fluence	1.22×10^{-8}	1.50×10^{-8}	1.45×10^{-8}	1.56×10^{-8}	1.50×10^{-8}	1.58×10^{-8}	1.81×10^{-8}	1.80×10^{-8}	1.80×10^{-8}	1.87×10^{-8}
Average Energy(MeV)	0.33	0.41	0.40	0.41	0.41	.40	0.54	0.52	0.53	0.53
Quality Factor(QF)	9.1	9.5	9.5	9.5	9.5	9.4	10.3	10.2	10.3	

Table A.2. Results of the Unfolding are Shown. The total fluence as unfolded by use of BUNKI and LOUHI is shown. Total dose equivalent, conversion factors fluence to dose equivalent and quality factors calculated by the two codes are shown.

Depth 81.3 cm of Fe Data Taken at NWA

	BUNKI				LOUHI			
Energy (GeV)	25	40	50	50	25	40	50	50
Total Fluence ($N/cm^2 \cdot 10^7$ Pions)	58500	90100	111000	111000	45490	68220	81270	84670
Total Dose Eqv. (rem/10^7 Pions)	6.37×10^{-4}	9.97×10^{-4}	1.17×10^{-3}	1.24×10^{-3}	7.07×10^{-4}	1.20×10^{-3}	1.48×10^{-3}	1.53×10^{-3}
Rem/Fluence	1.10×10^{-8}	1.10×10^{-8}	1.05×10^{-8}	1.12×10^{-8}	1.55×10^{-8}	1.76×10^{-8}	1.83×10^{-8}	1.81×10^{-8}
Average Energy (MeV)	0.32	0.35	0.44	0.36	0.32	2.3	2.0	2.0
Quality Factor (QF)	8.5	8.5	8.0	8.5	8.1	9.1	9.4	9.4

	BUNKI			LOUHI		
Energy (GeV)	75	100	100	75	100	100
Total Fluence ($N/cm^2 \cdot 10^7 \cdot$Pions)	156000	201000	196000	120100	164700	159000
Total Dose Eqv. (rem/10^7 Pions)	1.84×10^{-3}	2.43×10^{-3}	2.55×10^{-3}	2.29×10^{-3}	2.97×10^{-3}	2.96×10^{-3}
Rem/Fluence	1.10×10^{-8}	1.21×10^{-8}	1.30×10^{-8}	1.91×10^{-8}	1.80×10^{-8}	1.86×10^{-8}
Average Energy (MeV)	0.36	0.36	0.36	1.7	1.22	1.28
Quality Factor (QF)	8.7	8.8	9.1	9.9	9.7	9.9

Table A.3. Results of the Unfolding are Shown. The total fluence as unfolded by use of BUNKI and LOUHI is shown. Total dose equivalent, conversion factors fluence to dose equivalent and quality factors calculated by the two codes are shown.

Depth 121.9 cm of Fe Data Taken at NWA

	BUNKI				LOUHI			
Energy (GeV)	25	50	50	150	25	50	50	150
Total Fluence ($N/cm^2.10^7$ Pions)	32100	60400	63600	160100	32570	60480	63540	185100
Total Dose Eqv. ($rem/10^7$ Pions)	3.16×10^{-4}	6.57×10^{-4}	6.98×10^{-4}	2.09×10^{-3}	3.74×10^{-4}	8.0×10^{-4}	8.48×10^{-4}	2.74×10^{-3}
Rem/Fluence	0.98×10^{-8}	1.08×10^{-8}	1.10×10^{-8}	1.09×10^{-8}	1.15×10^{-8}	1.32×10^{-8}	1.33×10^{-8}	1.48×10^{-8}
Average Energy (MeV)	0.36	0.30	0.32	0.30	0.52	0.36	0.40	0.38
Quality Factor (QF)	8.1	8.7	8.6	8.7	8.1	9.0	9.0	9.3

	BUNKI			LOUHI		
Energy (GeV)	50	75	100	50	75	100
Total Fluence ($N/cm^2 .10^7$ Pions)	55600	92400	116000	54970	91720	113700
Total Dose Eqv. ($rem/10^7$ Pions)	6.18×10^{-4}	9.33×10^{-4}	1.06×10^{-3}	7.79×10^{-4}	1.17×10^{-3}	1.36×10^{-3}
Rem/Fluence	1.11×10^{-8}	1.01×10^{-8}	0.91×10^{-8}	1.42×10^{-8}	1.28×10^{-8}	1.20×10^{-8}
Average Energy (MeV)	0.28	0.25	0.23	0.36	0.32	0.28
Quality Factor (QF)	8.9	8.6	8.2	9.0	8.6	8.2

Table A.4. Results of the Unfolding are Shown. The total fluence as unfolded by use of BUNKI and LOUHI is shown. Total dose equivalent, conversion factors fluence to dose equivalent and quality factors calculated by the two codes are shown.

Depth 142.2 cm of Fe Data Taken at NWA

	BUNKI			LOUHI		
Energy (GeV)	40	50	75	40	50	75
Total Fluence ($N/cm^2 \cdot 10^7$ .Pions)	39400	34700	60800	39720	34890	61320
Total Dose Eqv. (rem/10^7 Pions)	4.18×10^{-4}	3.57×10^{-4}	6.06×10^{-4}	4.78×10^{-4}	3.50×10^{-4}	6.61×10^{-4}
Rem/Fluence	1.06×10^{-8}	1.03×10^{-8}	9.92×10^{-9}	1.20×10^{-8}	1.17×10^{-8}	1.08×10^{-8}
Average Energy (MeV)	0.40	0.34	0.27	0.96	0.85	0..37
Quality Factor (QF)	8.0	8.2	8.4	8.1	8.0	8.1

	BUNKI			LOUHI		
Energy (GeV)	100	100	100	100	100	100
Total Fluence ($N/cm^2.10^7$Pions)	84300	88260	84650	84680	89110	84670
Total Dose Eqv. (rem/10^7 Pions)	7.95×10^{-4}	9.08×10^{-4}	8.78×10^{-4}	1.03×10^{-3}	0.99×10^{-3}	0.99×10^{-3}
Rem/Fluence	1.10×10^{-8}	1.02×10^{-8}	1.03×10^{-8}	1.22×10^{-8}	1.11×10^{-8}	1.17×10^{-8}
Average Energy (MeV)	0.33	0.27	0.31	0.55	0.37	0..52
Quality Factor (QF)	8.5	8.5	8.3	8.4	8.2	8.3

Table A.5. Results of the Unfolding are Shown. The total fluence as unfolded by use of BUNKI and LOUHI is shown. Total dose equivalent, conversion factors fluence to dose equivalent and quality factors calculated by the two codes are shown.

Depth 162.6 cm of Fe Data Taken at NWA

	BUNKI					LOUHI				
Energy (GeV)	25	50	75	100	150	25	50	75	100	150
Total Fluence ($N/cm^2.10^7$Pions)	21300	31100	44700	56100	90700	22460	31100	44460	56020	90200
Total Dose Eqv. (rem/10^7 Pions)	$2.40x10^{-4}$	$3.24x10^{-4}$	$4.69x10^{-4}$	$5.98x10^{-4}$	$9.45x10^{-4}$	$2.45x10^{-4}$	$4.0x10^{-4}$	$5.78x10^{-4}$	$7.30x10^{-4}$	$11.7x10^{-4}$
Rem/Fluence	$1.13x10^{-8}$	$1.04x10^{-8}$	$1.05x10^{-8}$	$1.07x10^{-8}$	$1.04x10^{-8}$	$1.09x10^{-8}$	$1.29x10^{-8}$	$1.30x10^{-8}$	$1.30x10^{-8}$	$1.30x10^{-8}$
Average Energy (MeV)	0.49	0.31	0.28	0.30	0.27	0.71	0.39	0.35	0.36	0.34
Quality Factor (QF)	8.2	8.4	8.6	8.6	8.6	8.1	9.5	9.1	9.2	8.9

Table A.6. Results of the Unfolding are Shown. The total fluence as unfolded by use of BUNKI and LOUHI is shown. Total dose equivalent, conversion factors fluence to dose equivalent and quality factors calculated by the two codes are shown.

Depth 182.9 cm of Fe Data Taken at NWA

	BUNKI			LOUHI		
Energy (GeV)	50	75	100	50	75	100
Total Fluence ($N/cm^2 .10^7$ Pions)	16800	26400	31100	16600	26320	31410
Total Dose Eqv. ($rem/10^7$ Pions)	1.27×10^{-4}	2.28×10^{-4}	2.89×10^{-4}	1.45×10^{-4}	2.54×10^{-4}	3.14×10^{-4}
Rem/Fluence	7.56×10^{-9}	8.64×10^{-9}	9.29×10^{-9}	8.73×10^{-9}	9.65×10^{-9}	10.0×10^{-9}
Average Energy (MeV)	0.19	0.22	0.23	0.25	0.30	0.31
Quality Factor (QF)	7.6	8.0	8.2	7.2	7.6	7.7

Table A.7. Results of the Unfolding are Shown. The total fluence as unfolded by use of BUNKI and LOUHI is shown. Total dose equivalent, conversion factors fluence to dose equivalent and quality factors calculated by the two codes are shown.

Depth 243.8 cm of Fe Data Taken at NWA

	BUNKI				LOUHI			
Energy (GeV)	50	75	100	150	50	75	100	150
Total Fluence ($N/cm^2 \cdot 10^7$ Pions)	3640	5970	7230	13900	3868	6009	7509	13640
Total Dose Eqv. (rem/10^7 Pions)	3.20×10^{-5}	4.61×10^{-5}	6.36×10^{-5}	1.10×10^{-4}	3.10×10^{-5}	5.37×10^{-4}	6.73×10^{-5}	1.41×10^{-4}
Rem/Fluence	8.79×10^{-9}	7.72×10^{-9}	8.80×10^{-9}	7.91×10^{-9}	8.01×10^{-9}	8.94×10^{-9}	8.96×10^{-9}	1.03×10^{-8}
Average Energy (MeV)	0.33	0.23	0.28	0.19	0.47	0.29	0.39	0.25
Quality Factor (QF)	8.2	9.2	8.0	7.6	7.4	7.9	7.8	8.0

	Bunki				Louhi			
Energy (GeV)	50	75	100	150	50	75	100	150
Total Fluence ($N/cm^2 .10^7$Pions)	4110	7781	10680	17800	4250	7917	10490	17450
Total Dose Eqv. (rem/10^7 Pions)	3.28×10^{-5}	6.41×10^{-5}	8.39×10^{-5}	1.31×10^{-4}	3.23×10^{-5}	7.17×10^{-5}	1.04×10^{-4}	1.65×10^{-4}
Rem/Fluence	7.98×10^{-9}	8.11×10^{-9}	7.84×10^{-9}	7.36×10^{-9}	1.32×10^{-8}	9.06×10^{-9}	9.91×10^{-9}	9.46×10^{-9}
Average Energy (MeV)	0.31	0.24	0.18	0.17	1.9	0.33	0.23	0.22
Quality Factor (QF)	7.0	7.5	7.6	7.4	6.8	7.8	7.8	7.5

Table A.8. Results of the Unfolding are Shown. The total fluence as unfolded by use of BUNKI and LOUHI is shown. Total dose equivalent, conversion factors fluence to dose equivalent and quality factors calculated by the two codes are shown.

Depth 264.2 cm of Fe Data Taken at NWA

	BUNKI				LOUHI			
Energy (GeV)	75	100*	125	150	75	100	125	150
Total Fluence ($N/cm^2 \cdot 10^7$ Pions)	5100	4900	8630	10800	5289	5133	8542	10790
Total Dose Eqv. (rem/10^7 Pions)	3.36×10^{-5}	1.71×10^{-5}	6.19×10^{-5}	6.97×10^{-5}	$.377 \times 10^{-4}$	0.15×10^{-4}	$.749 \times 10^{-4}$	$.847 \times 10^{-4}$
Rem/Fluence	6.59×10^{-9}	3.49×10^{-9}	7.17×10^{-9}	6.45×10^{-9}	7.13×10^{-9}	2.92×10^{-9}	8.77×10^{-9}	7.85×10^{-9}
Average Energy (MeV)	0.18	0.18	0.18	0.14	1.4	0.04	0.22	0.18
Quality Factor (QF)	6.9	4.9	7.3	6.9	6.0	3.7	7.4	6.9

* 100GeV Problems in the accelerator, very low intensity.

Table A.9. Results of the Unfolding are Shown. The total fluence as unfolded by use of BUNKI and LOUHI is shown. Total dose equivalent, conversion factors fluence to dose equivalent and quality factors calculated by the two codes are shown.

Depth 60.9 cm of Fe Data Taken at NWA in the Lateral Direction

	BUNKI			LOUHI		
Energy (GeV)	75	100	150	75	100	150
Total Fluence ($N/cm^2.10^7$ Pions)	111000	149000	198000	113000	155000	207000
Total Dose Eqv. ($rem/10^7$ Pions)	$1.65x10^{-3}$	$2.13x10^{-3}$	$2.99x10^{-3}$	$1.86x10^{-3}$	$2.26x10^{-3}$	$3.41x10^{-3}$
Rem/Fluence	$1.47x10^{-8}$	$1.43x10^{-8}$	$1.51x10^{-8}$	$1.65x10^{-8}$	$1.45x10^{-8}$	$1.65x10^{-8}$
Average Energy (MeV)	0.43	0.46	0.42	0.64	0.70	0.59
Quality Factor(QF)	9.4	9.0	9.5	9.3	8.9	9.4

Table A.10. Results of the Unfolding in the Lateral Direction. The unfolding from the data by use of BUNKI and LOUHI is shown with the values for fluence, dose equivalent and quality factors among other parameters.

Appendix B

In Appendix B, the neutron spectra unfolded from the data by use of BUNKI for incident pions up to five different energies and ten depths are presented. Those plots show the entire data set collected at NWA in the longitudinal direction while in Chapter 4 only three of those plots at depths of 40.6, 162.6 and 243.8 cm were included for purposes of illustration.

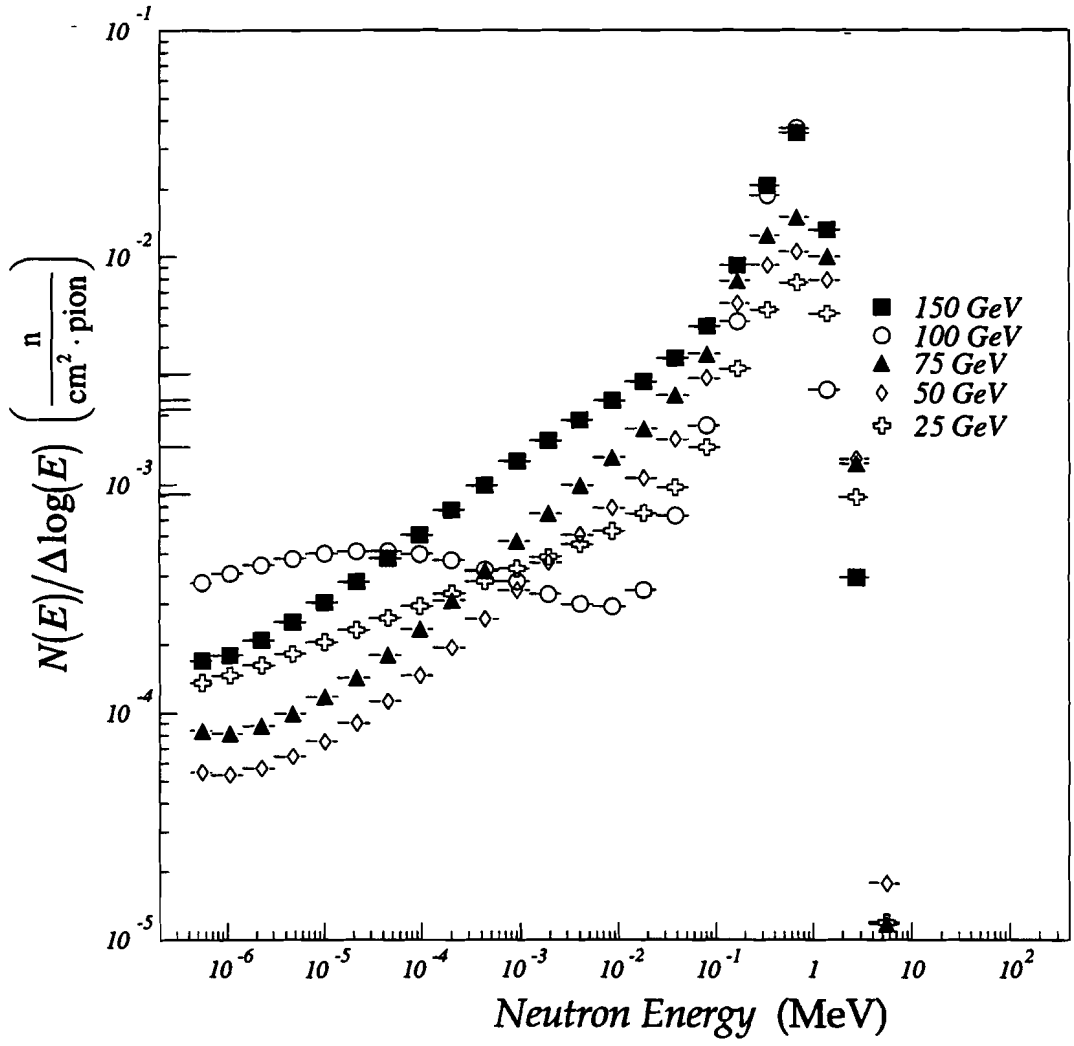

Figure B.1. Unfolded Neutron Spectra for Incident Pions on 40.6 cm of Iron. Shown are the neutron spectra obtained using BUNKI for incident pions at five different energies on 40.6 cm (16 in, 2.4 λ) of iron. For each energy, the fluence per unit lethargy per pion is plotted as a function of neutron energy.

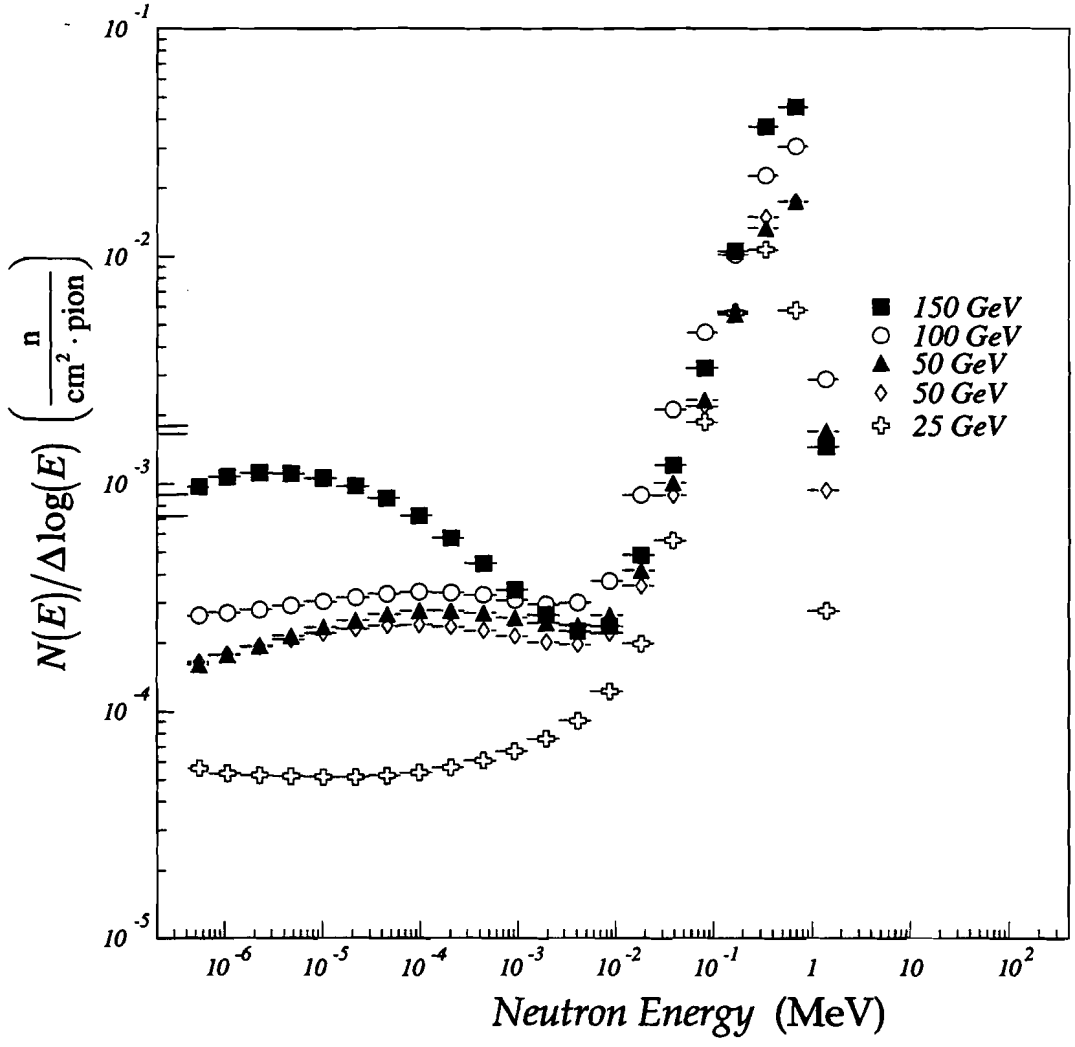

Figure B.2. Unfolded Neutron Spectra for Incident Pions on 61 cm of Iron. Shown are the neutron spectra obtained using BUNKI for incident pions at four different energies on 61 cm (24 in, 3.6 λ) of iron. For each energy, the fluence per unit lethargy per pion is plotted as a function of neutron energy.

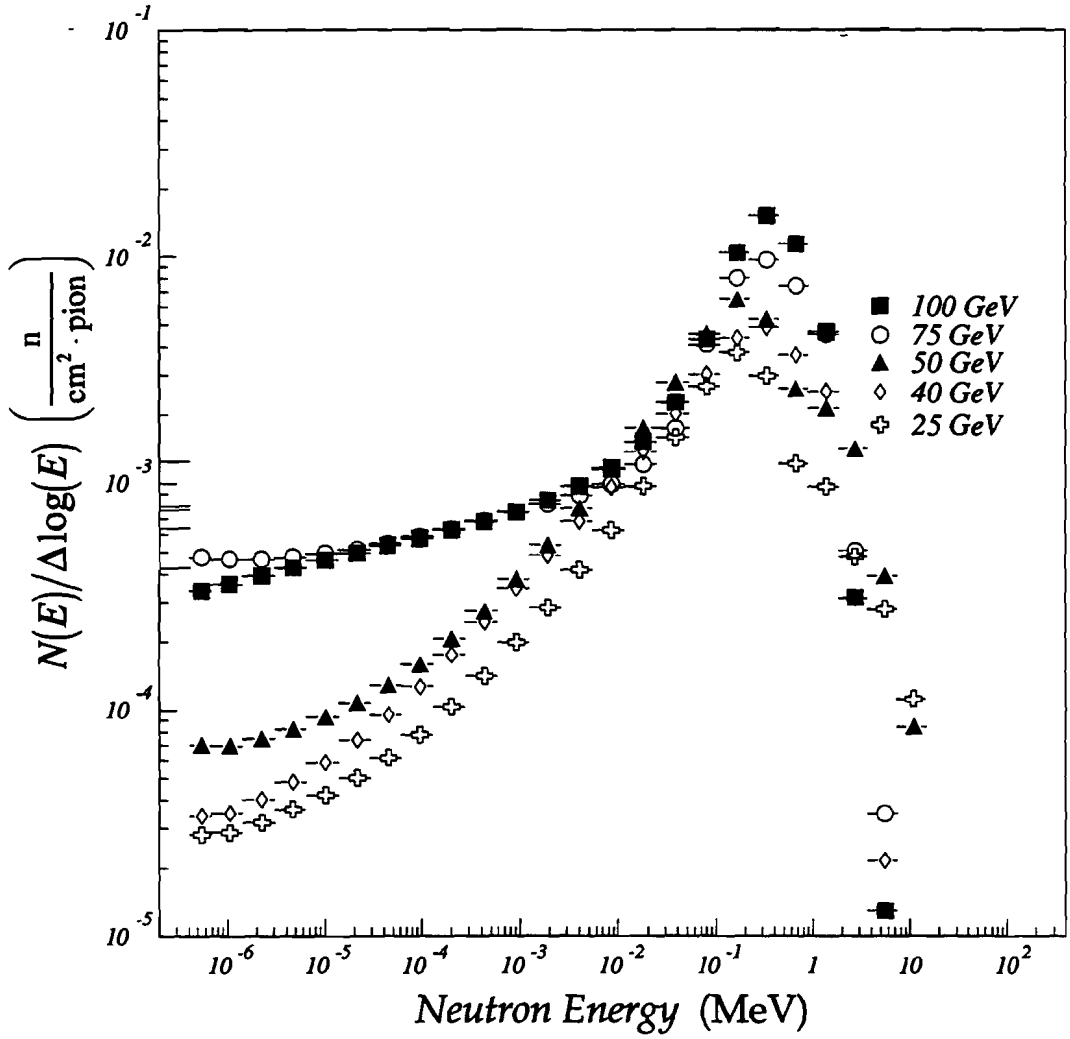

Figure B.3. Unfolded Neutron Spectra for Incident Pions on 81.3 cm of Iron. Shown are the neutron spectra obtained using BUNKI for incident pions at five different energies on 81.3 cm (32 in, 4.8 λ) of iron. For each energy, the fluence per unit lethargy per pion is plotted as a function of neutron energy.

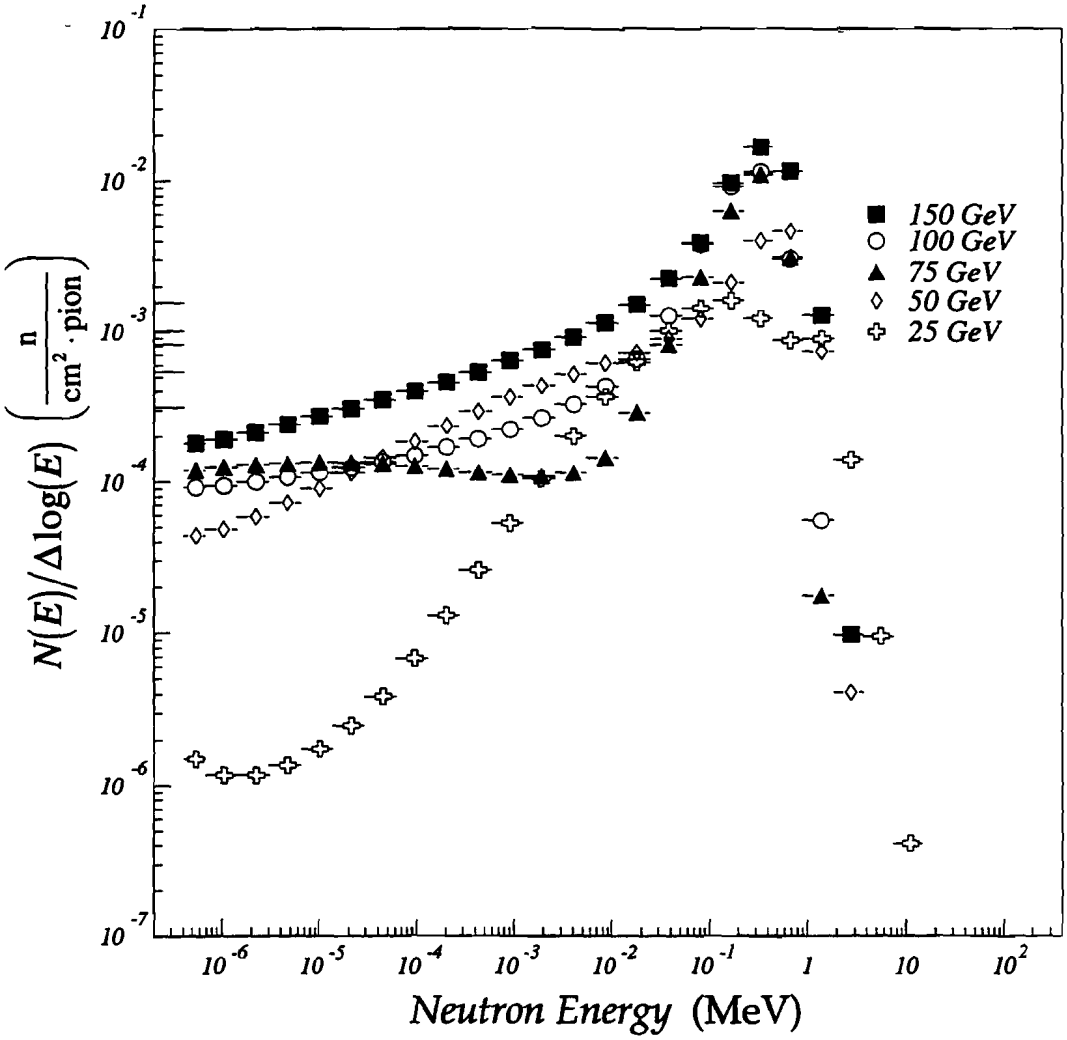

Figure B.4. Unfolded Neutron Spectra for Incident Pions on 121.9 cm of Iron. Shown are the neutron spectra obtained using BUNKI for incident pions at five different energies on 121.9 cm (48 in, 7.3λ) of iron. For each energy, the fluence per unit lethargy per pion is plotted as a function of neutron energy.

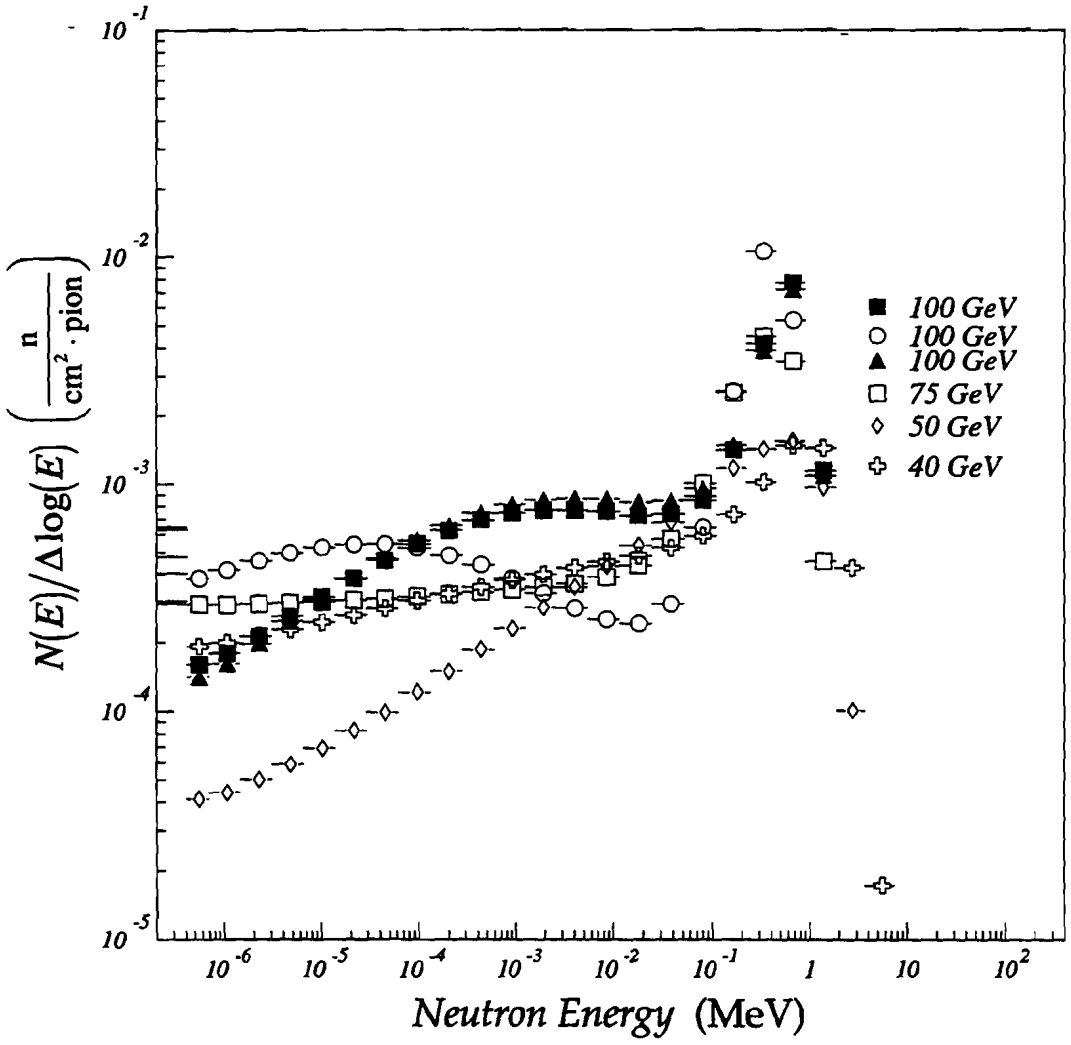

Figure B.5. Unfolded Neutron Spectra for Incident Pions on 142.2 cm of Iron. Shown are the neutron spectra obtained using BUNKI for incident pions at three different energies on 142.2 cm (56 in, 8.5 λ) of iron. For each energy, the fluence per unit lethargy per pion is plotted as a function of neutron energy.

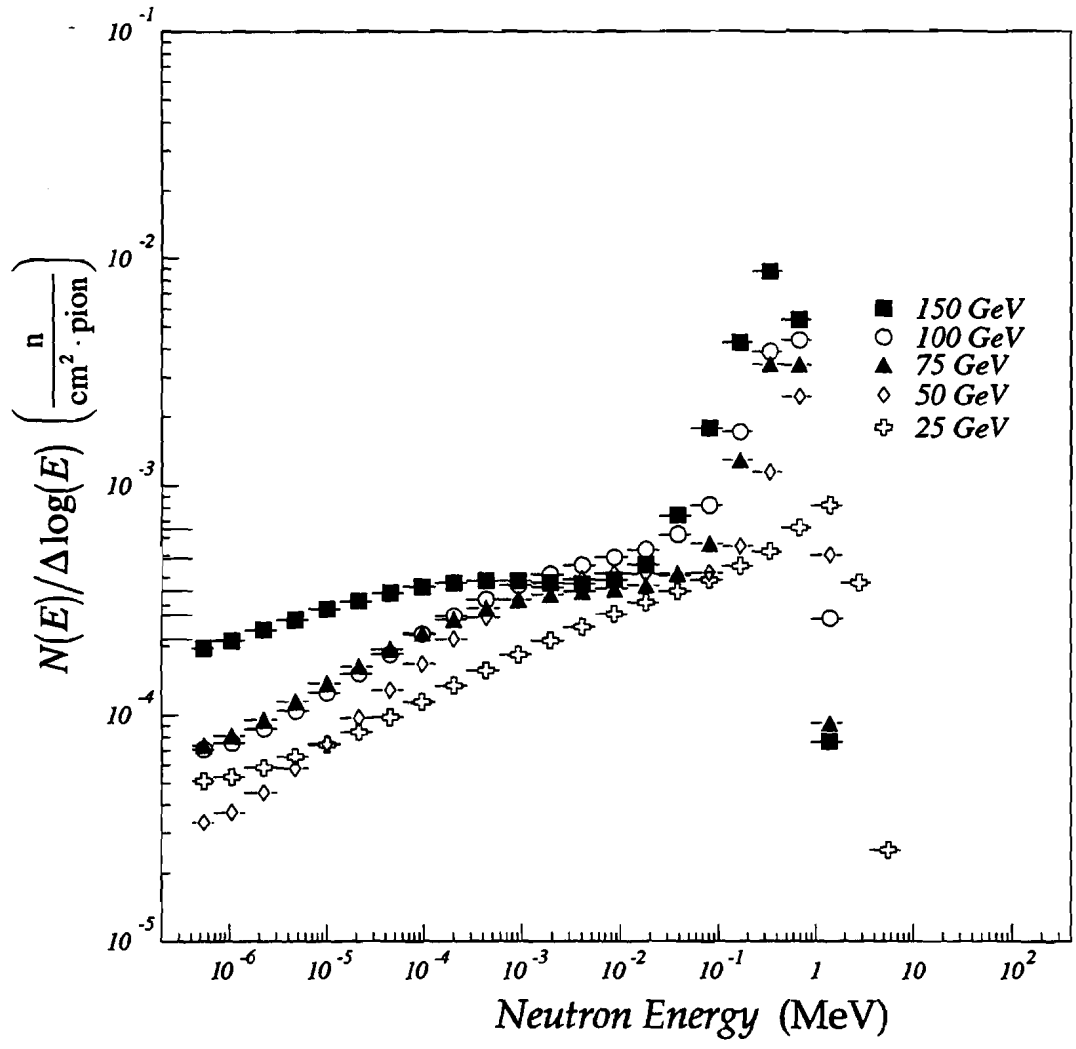

Figure B.6. Unfolded Neutron Spectra for Incident Pions on 162.6 cm of Iron. Shown are the neutron spectra obtained using BUNKI for incident pions at five different energies on 162.6 cm (64 in, 9.7 λ) of iron. For each energy, the fluence per unit lethargy per pion is plotted as a function of neutron energy.

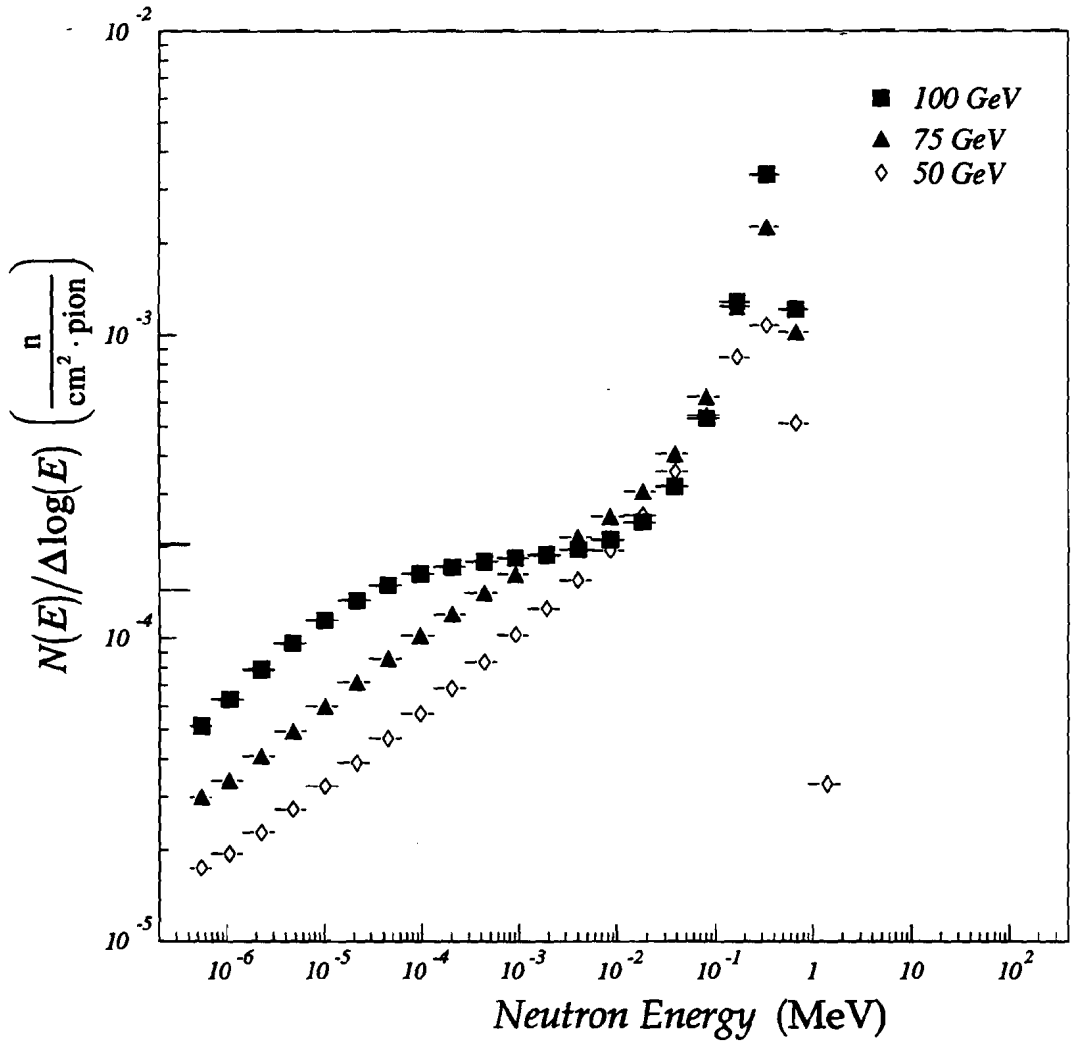

Figure B.7. Unfolded Neutron Spectra for Incident Pions on 182.9 cm of Iron. Shown are the neutron spectra obtained using BUNKI for incident pions at three different energies on 182.9 cm (72 in, 10.9 λ) of iron. For each energy, the fluence per unit lethargy per pion is plotted as a function of neutron energy.

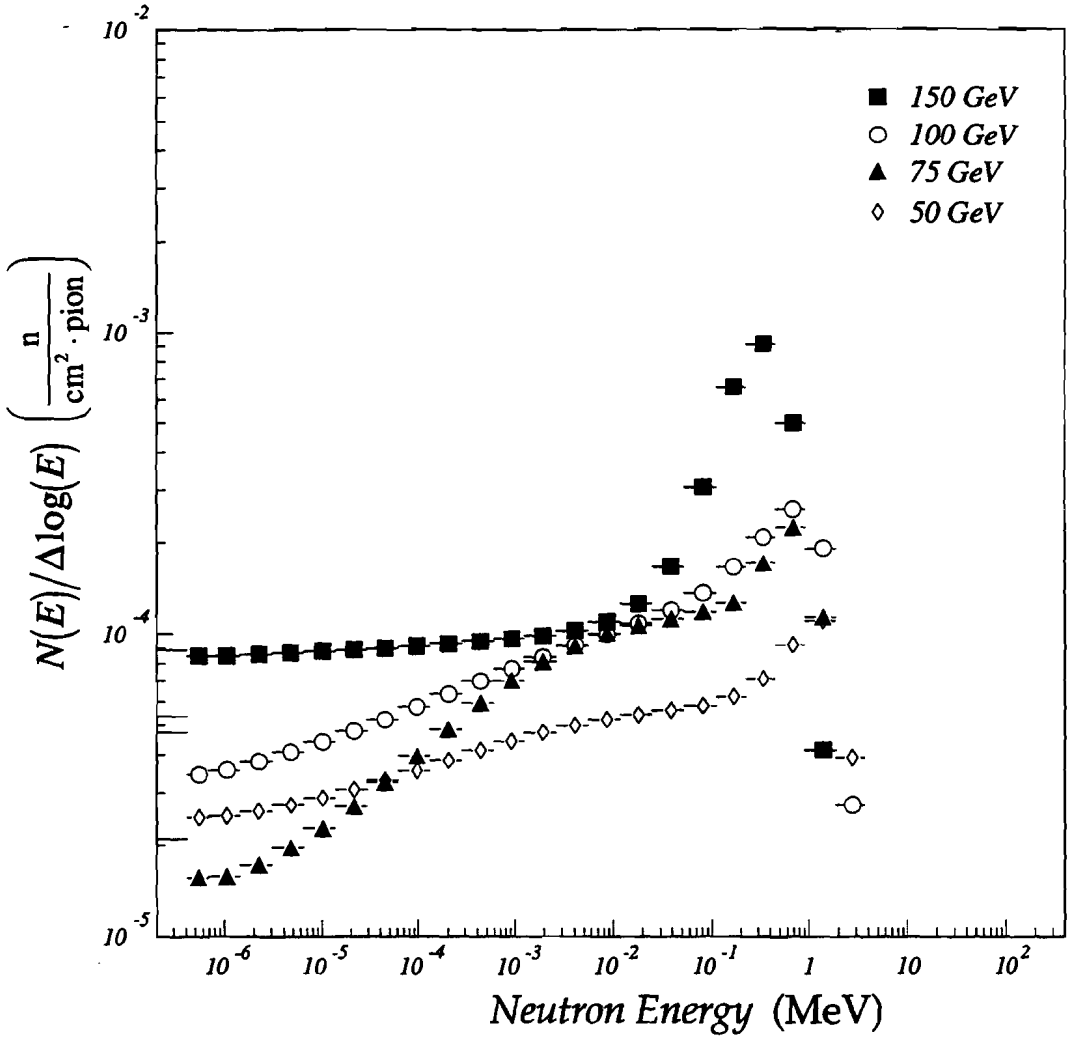

Figure B.8. Unfolded Neutron Spectra for Incident Pions on 243.8 cm of Iron. Shown are the neutron spectra obtained using BUNKI for incident pions at four different energies on 243.8 cm (96 in, 14.5 λ) of iron. For each energy, the fluence per unit lethargy per pion is plotted as a function of neutron energy. Data set taken on December 27, 1991.

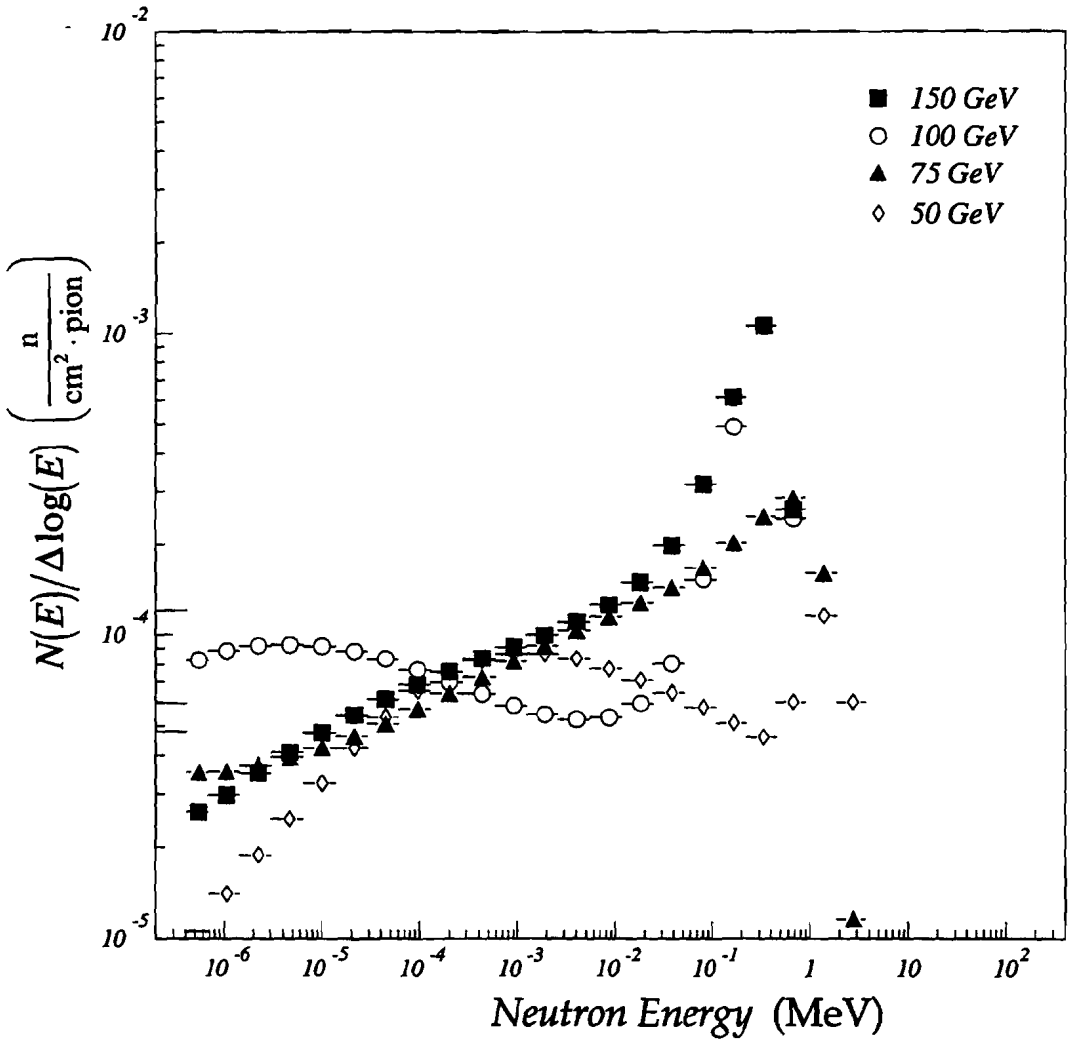

Figure B.9. Unfolded Neutron Spectra for Incident Pions on 243.8 cm of Iron. Shown are the neutron spectra obtained using BUNKI for incident pions at four different energies on 243.8 cm (96 in, 14.5 λ) of iron. For each energy, the fluence per unit lethargy per pion is plotted as a function of neutron energy. Data set taken on December 31, 1991.

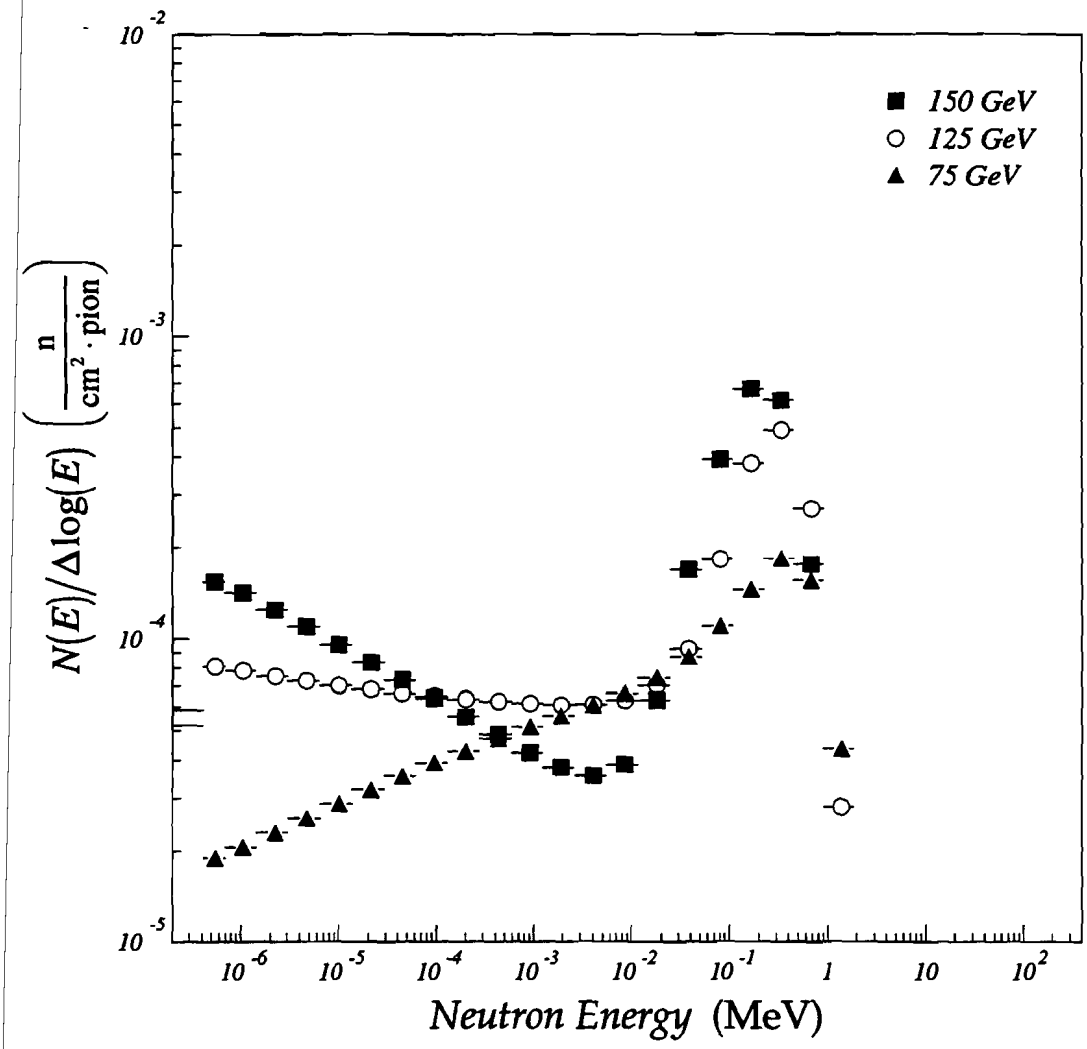

Figure B.10 Unfolded Neutron Spectra for Incident Pions on 264.2 cm of Iron. Shown are the neutron spectra obtained using BUNKI for incident pions at three different energies on 264.2 cm (104 in, 15.7 λ) of iron. For each energy, the fluence per unit lethargy per pion is plotted as a function of neutron energy.

Appendix C

In Appendix C, the neutron spectra unfolded from the data by use of BUNKI for incident pions at all energies and depths are compared to those generated by the FLUKA simulation in the longitudinal direction. Plotted is neutron fluence per unit lethargy per pion as function of neutron energy.

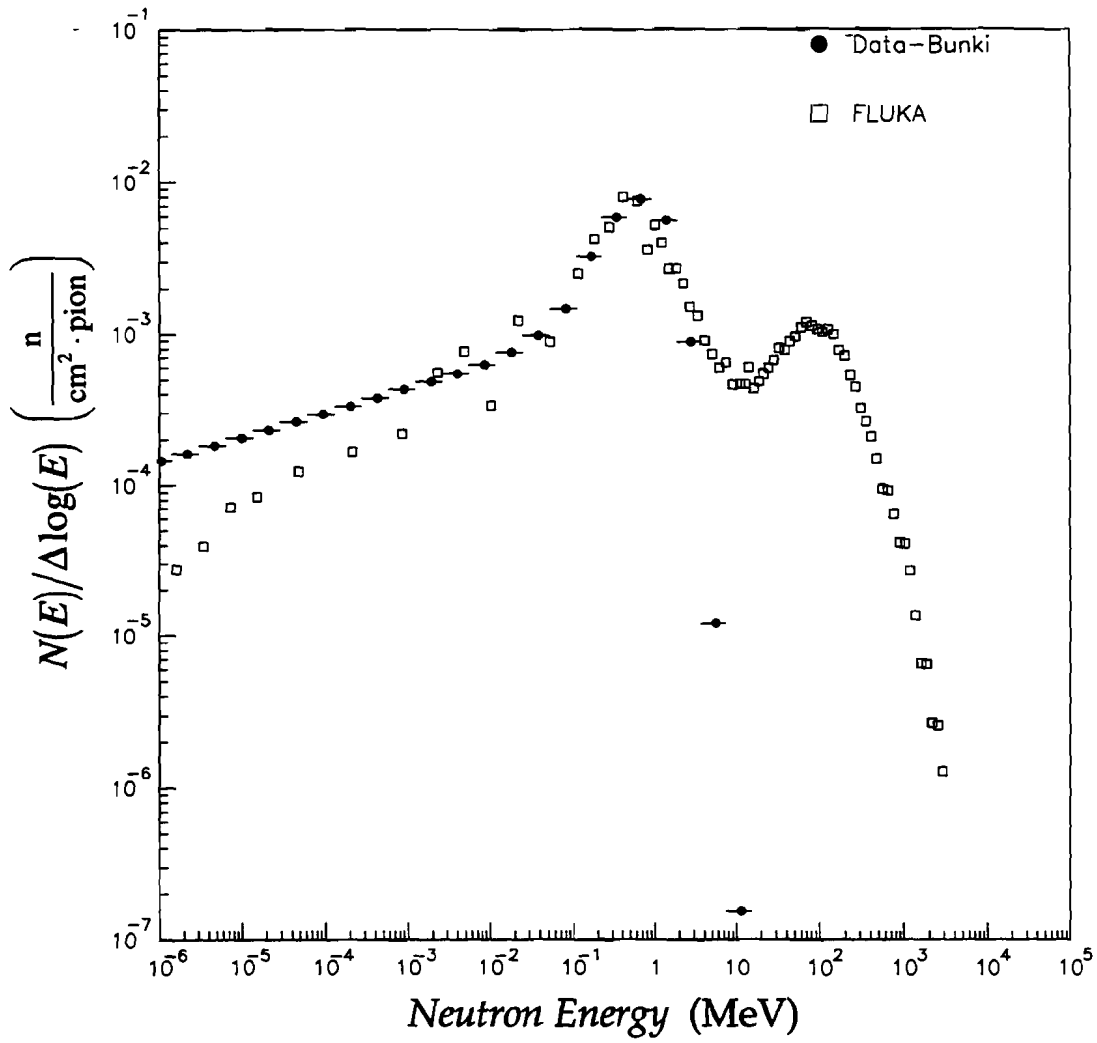

Figure C.1. Unfolded Neutron Spectra for Incident Pions on 40.6 cm of Iron. Shown is the neutron spectrum unfolded from the data by use of BUNKI compared to that generated by the FLUKA simulation, for 25 GeV incident pions on 40.6 cm (16 in, 2.4 λ) of iron in the longitudinal direction. The fluence per unit lethargy per pion is plotted as a function of neutron energy.

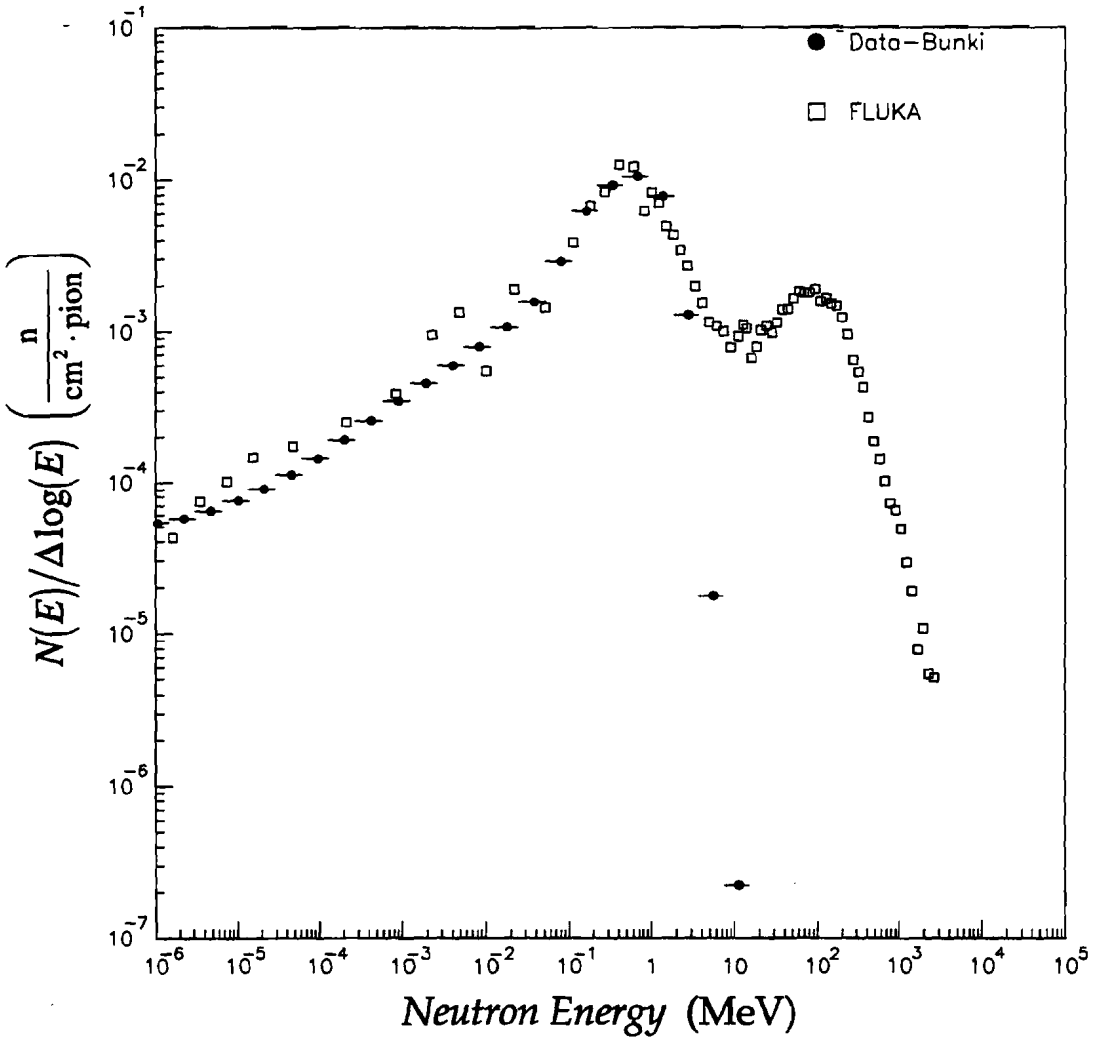

Figure C.2. Unfolded Neutron Spectra for Incident Pions on 40.6 cm cm of Iron. Shown is the neutron spectrum unfolded from the data by use of BUNKI compared to that generated by the FLUKA simulation, for 50 GeV incident pions on 40.6 cm (16 in, 2.4 λ) of iron in the longitudinal direction. The fluence per unit lethargy per pion is plotted as a function of neutron energy.

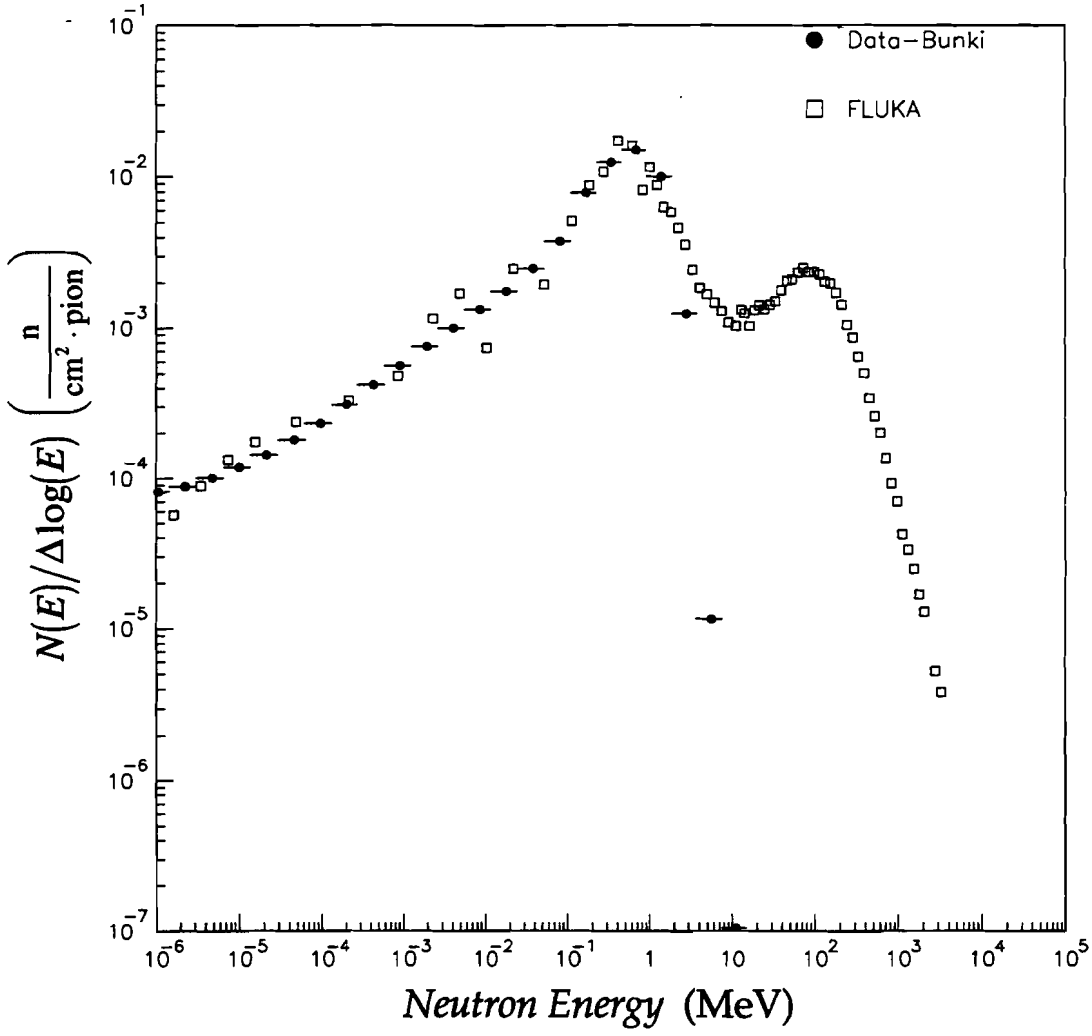

Figure C.3. Unfolded Neutron Spectra for Incident Pions on 40.6 cm of Iron. Shown is the neutron spectrum unfolded from the data by use of BUNKI compared to that generated by the FLUKA simulation, for 75 GeV incident pions on 40.6 cm (16 in, 2.4 λ) of iron in the longitudinal direction. The fluence per unit lethargy per pion is plotted as a function of neutron energy.

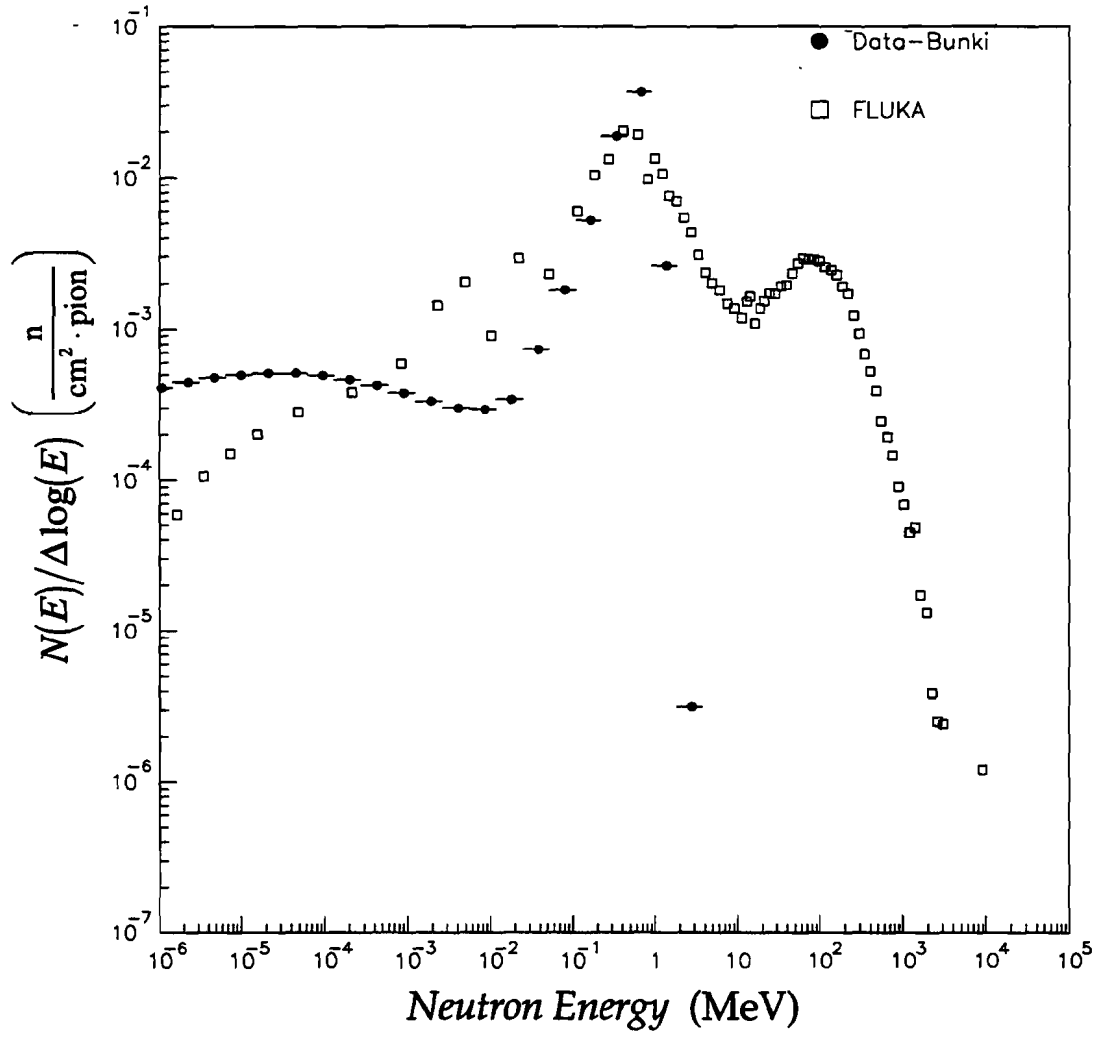

Figure C.4. Unfolded Neutron Spectra for Incident Pions on 40.6 cm of Iron. Shown is the neutron spectrum unfolded from the data by use of BUNKI compared to that generated by the FLUKA simulation, for 100 GeV incident pions on 40.6 cm (16 in, 2.4 λ) of iron in the longitudinal direction. The fluence per unit lethargy per pion is plotted as a function of neutron energy.

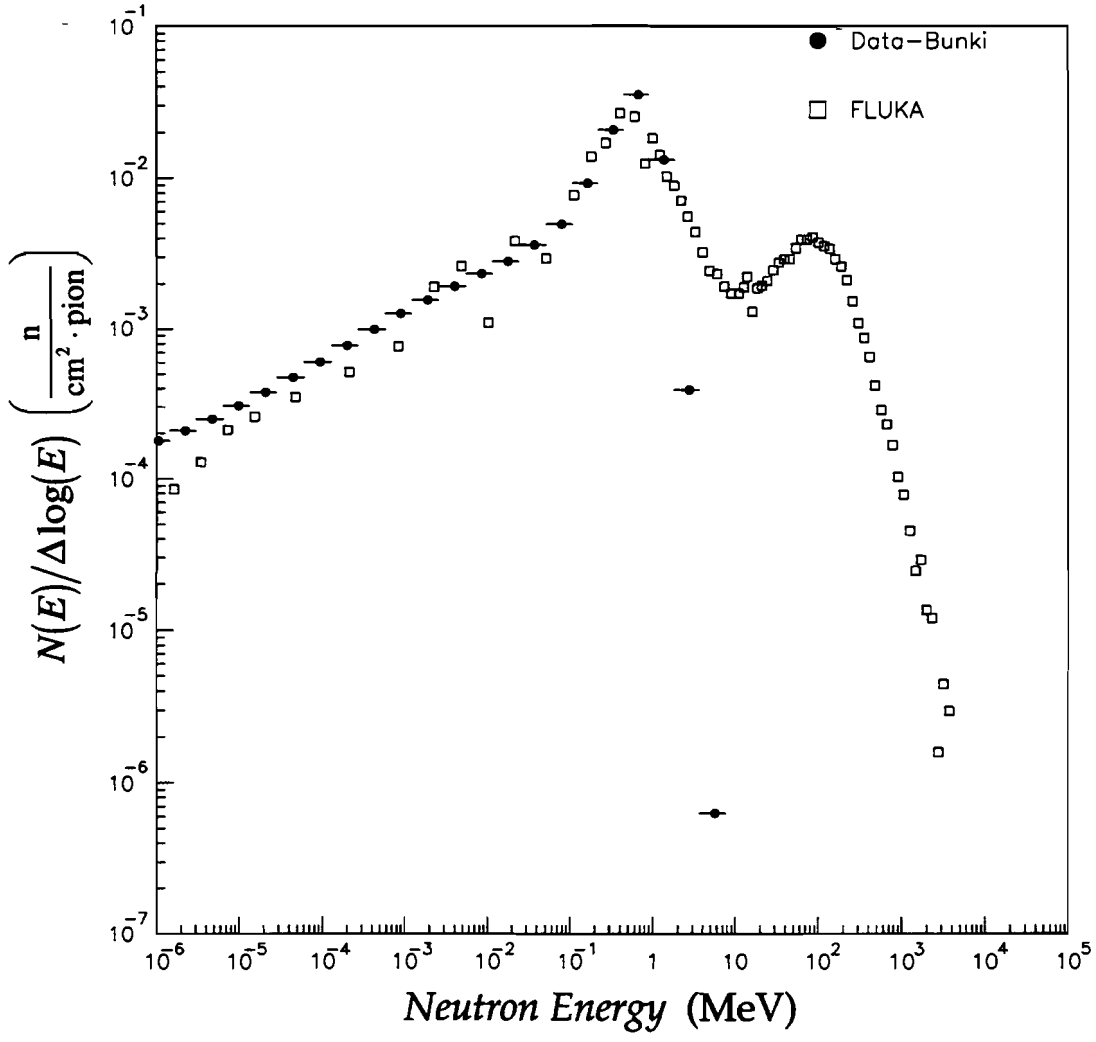

Figure C.5. Unfolded Neutron Spectra for Incident Pions on 40.6 cm of Iron. Shown is the neutron spectrum unfolded from the data by use of BUNKI compared to that generated by the FLUKA simulation, for 150 GeV incident pions on 40.6 cm (16 in, 2.4 λ) of iron in the longitudinal direction. The fluence per unit lethargy per pion is plotted as a function of neutron energy.

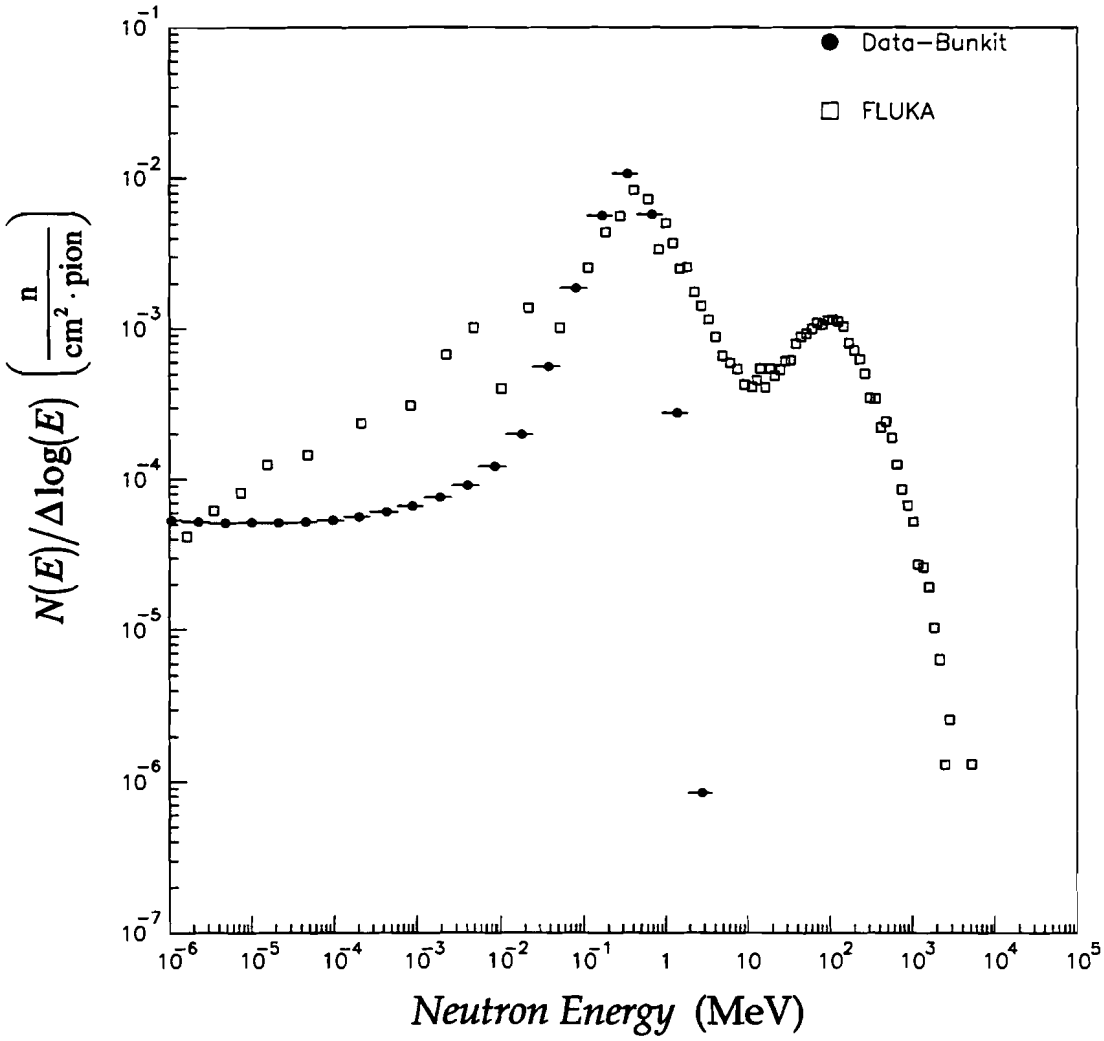

Figure C.6. Unfolded Neutron Spectra for Incident Pions on 61 cm of Iron. Shown is the neutron spectrum unfolded from the data by use of BUNKI compared to that generated by the FLUKA simulation, for 25 GeV incident pions on 61 cm (24 in, 3.6 λ) of iron in the longitudinal direction. The fluence per unit lethargy per pion is plotted as a function of neutron energy.

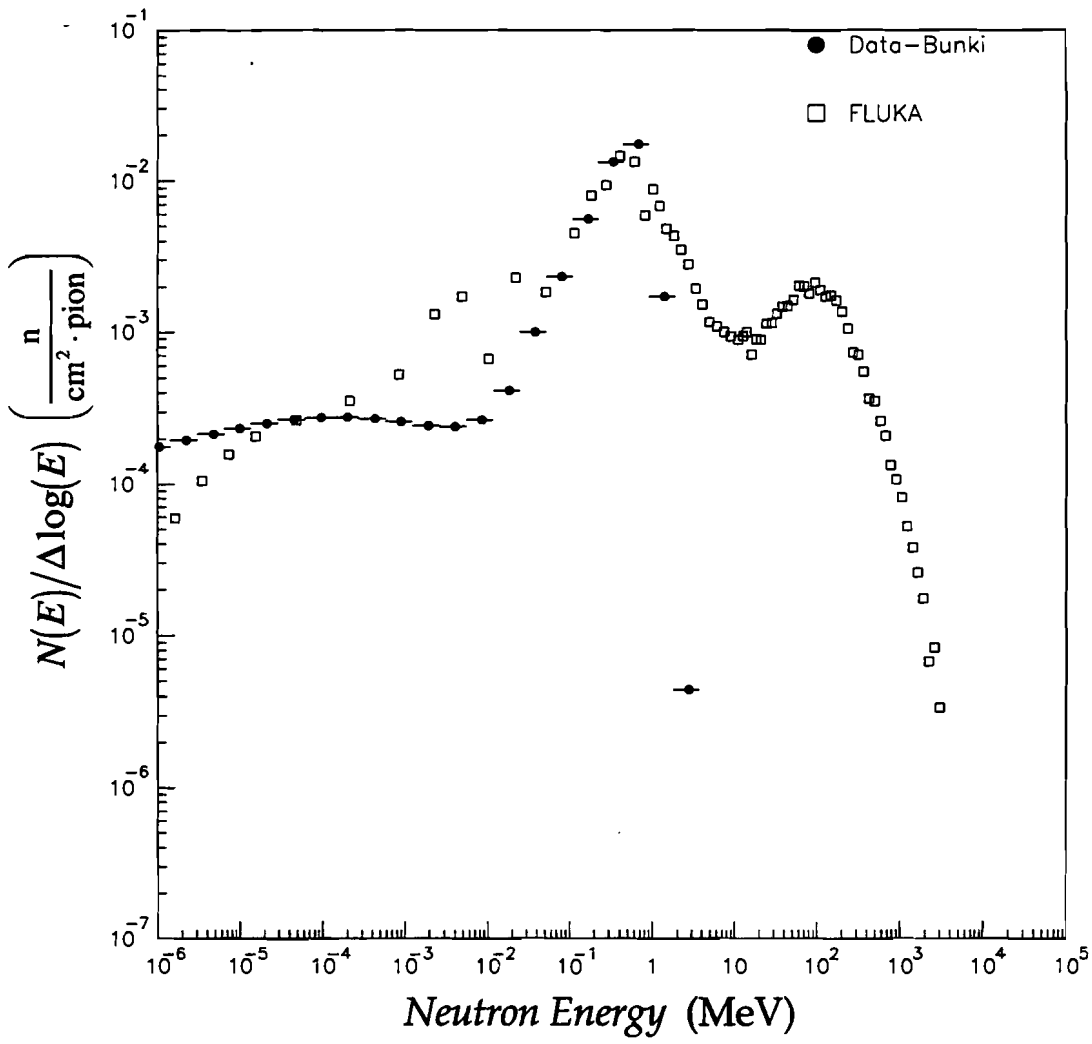

Figure C.7. Unfolded Neutron Spectra for Incident Pions on 61 cm of Iron. Shown is the neutron spectrum unfolded from the data by use of BUNKI compared to that generated by the FLUKA simulation, for 50 GeV incident pions on 61 cm (24 in, 3.6 λ) of iron in the longitudinal direction. The fluence per unit lethargy per pion is plotted as a function of neutron energy.

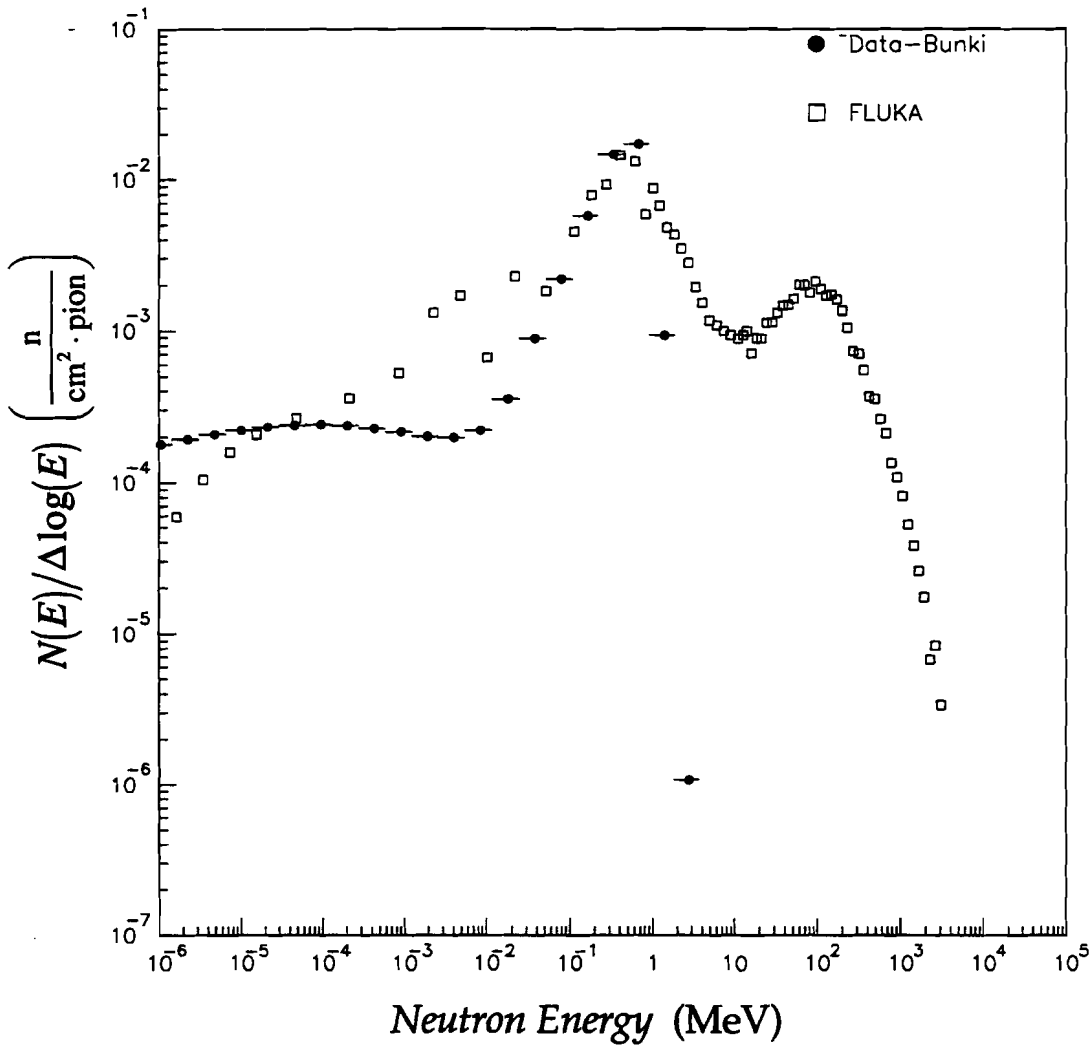

Figure C.8. Unfolded Neutron Spectra for Incident Pions on 61 cm of Iron. Shown is the neutron spectrum unfolded from the data by use of BUNKI compared to that generated by the FLUKA simulation, for 50 GeV incident pions on 61 cm (24 in, 3.6 λ) of iron in the longitudinal direction. The fluence per unit lethargy per pion is plotted as a function of neutron energy. This is the second set of data taken at 50 GeV at this depth.

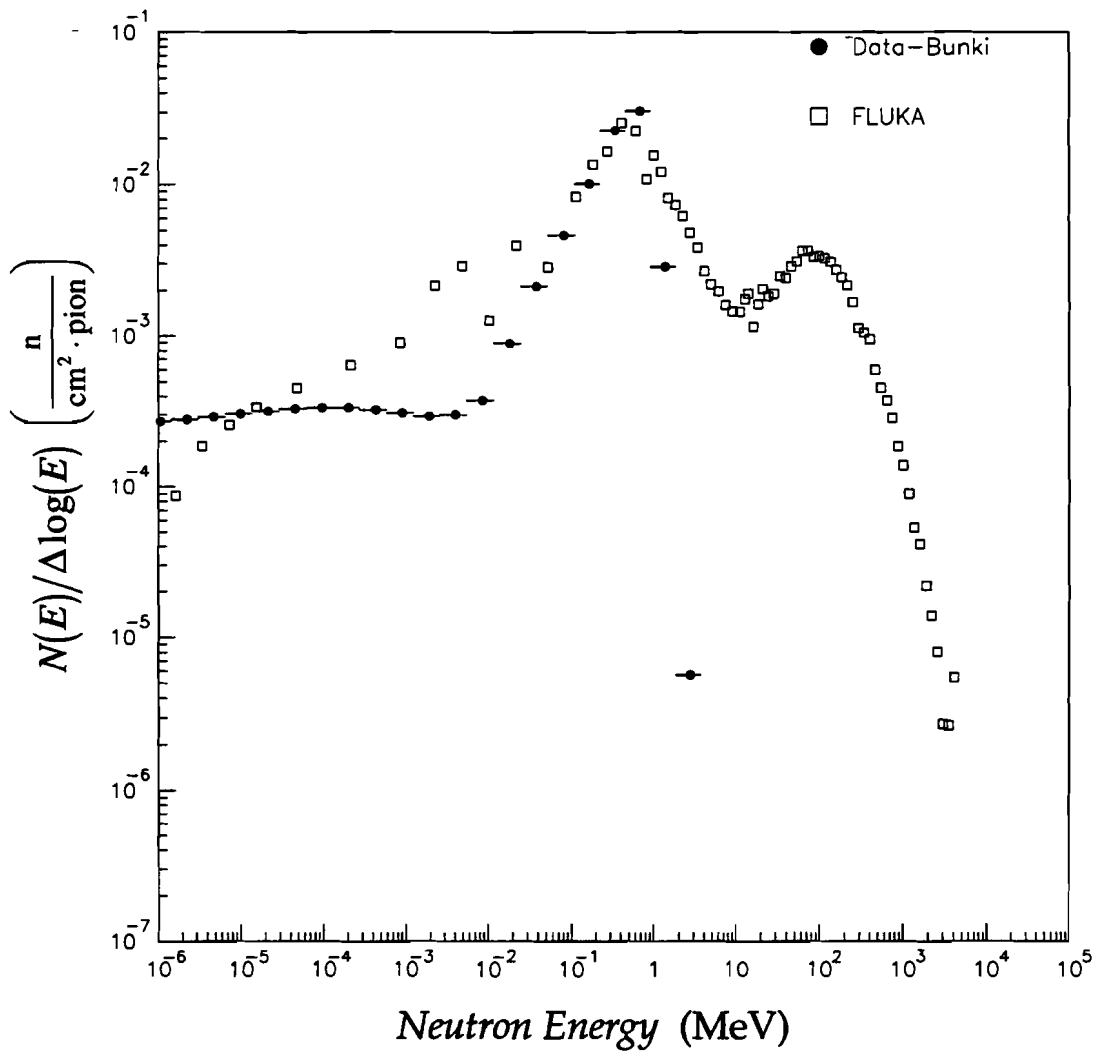

Figure C.9. Unfolded Neutron Spectra for Incident Pions on 61 cm of Iron. Shown is the neutron spectrum unfolded from the data by use of BUNKI compared to that generated by the FLUKA simulation, for 100 GeV incident pions on 61 cm (24 in, 3.6 λ) of iron in the longitudinal direction. The fluence per unit lethargy is plotted as a function of neutron energy.

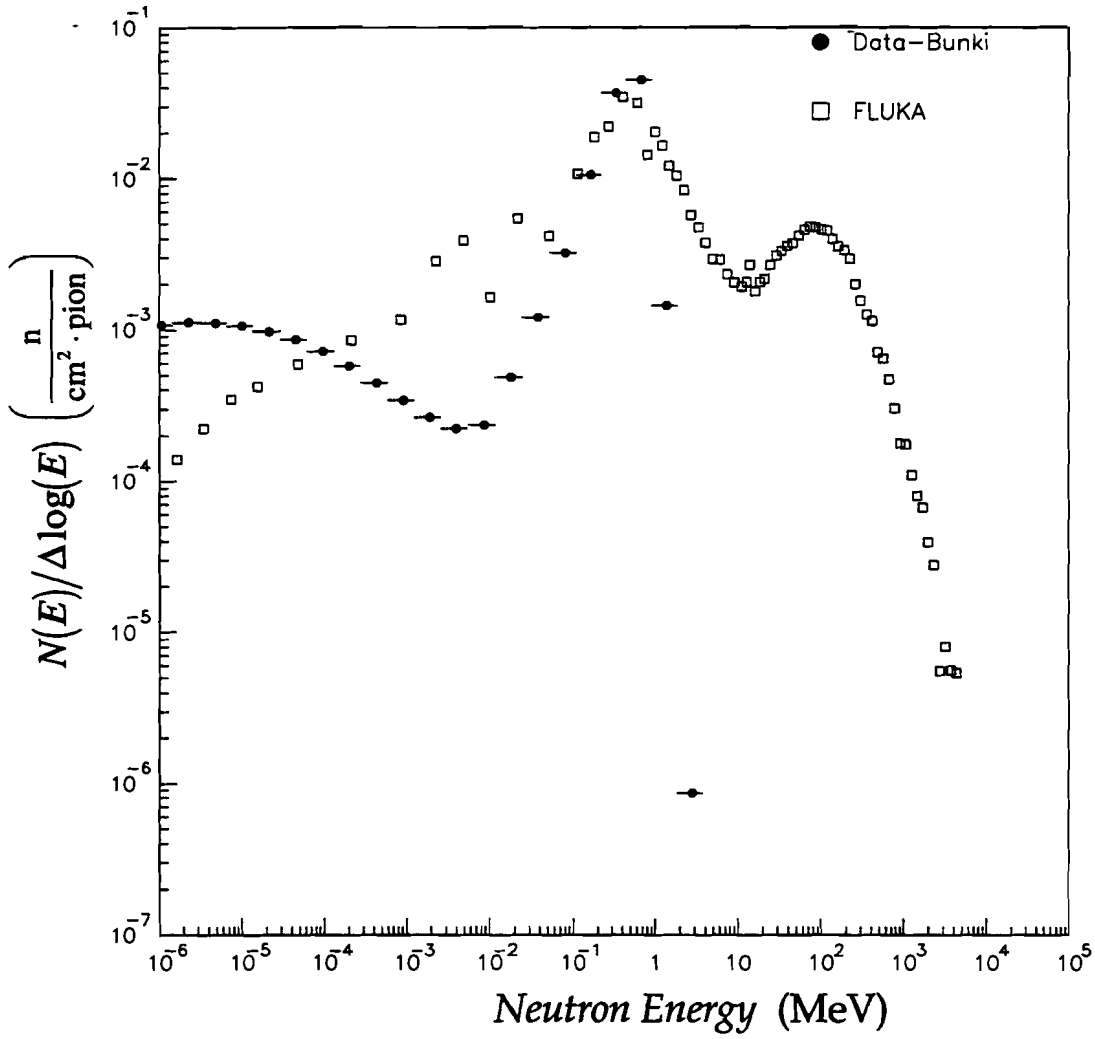

Figure C.10. Unfolded Neutron Spectra for Incident Pions on 61 cm of Iron. Shown is the neutron spectrum unfolded from the data by use of BUNKI compared to that generated by the FLUKA simulation, for 150 GeV incident pions on 61 cm (24 in, 3.6 λ) of iron in the longitudinal direction. The fluence per unit lethargy per pion is plotted as a function of neutron energy.

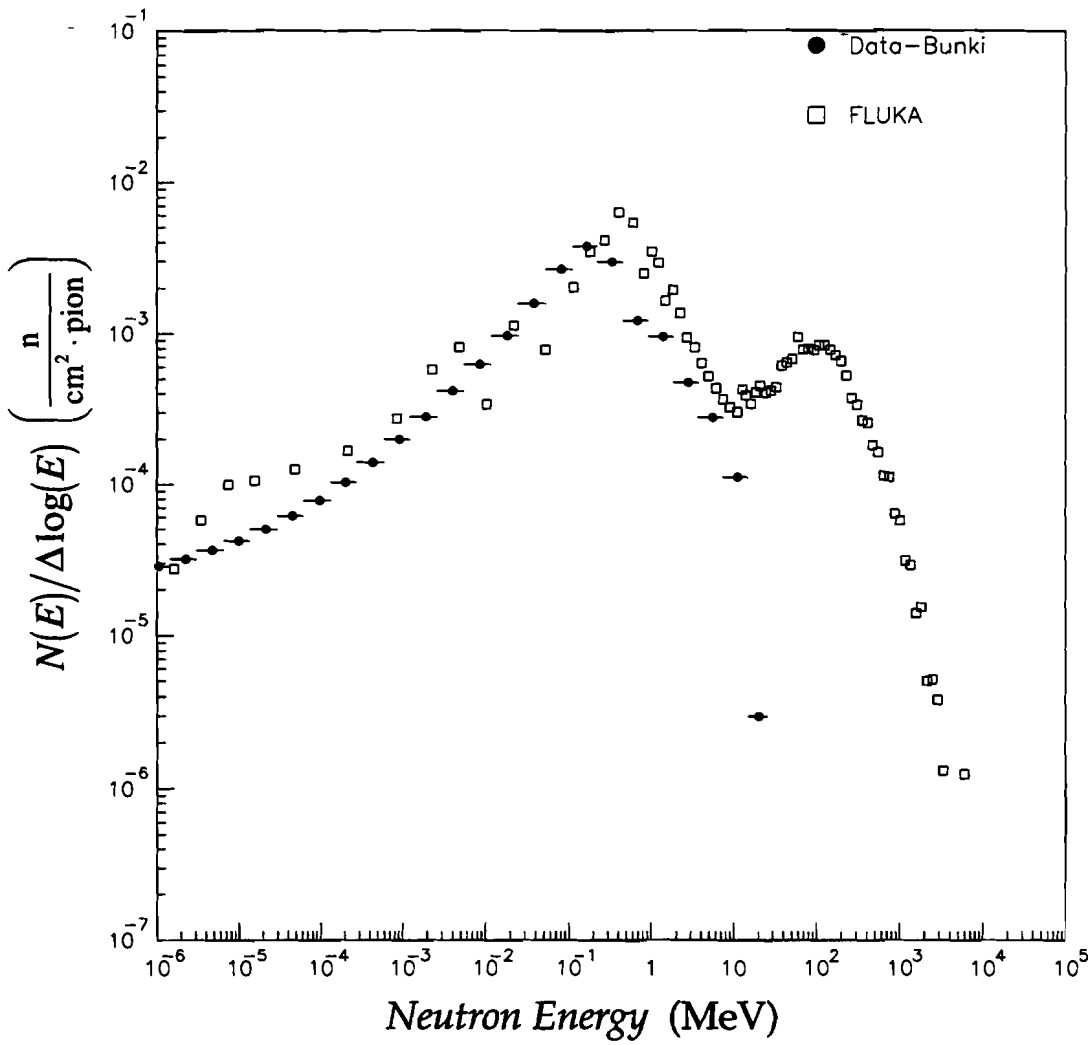

Figure C.11. Unfolded Neutron Spectra for Incident Pions on 81.3 cm of Iron. Shown is the neutron spectrum unfolded from the data by use of BUNKI compared to that generated by the FLUKA simulation, for 25 GeV incident pions on 81.3 cm (32 in, 4.8 λ) of iron in the longitudinal direction. The fluence per unit lethargy per pion is plotted as a function of neutron energy.

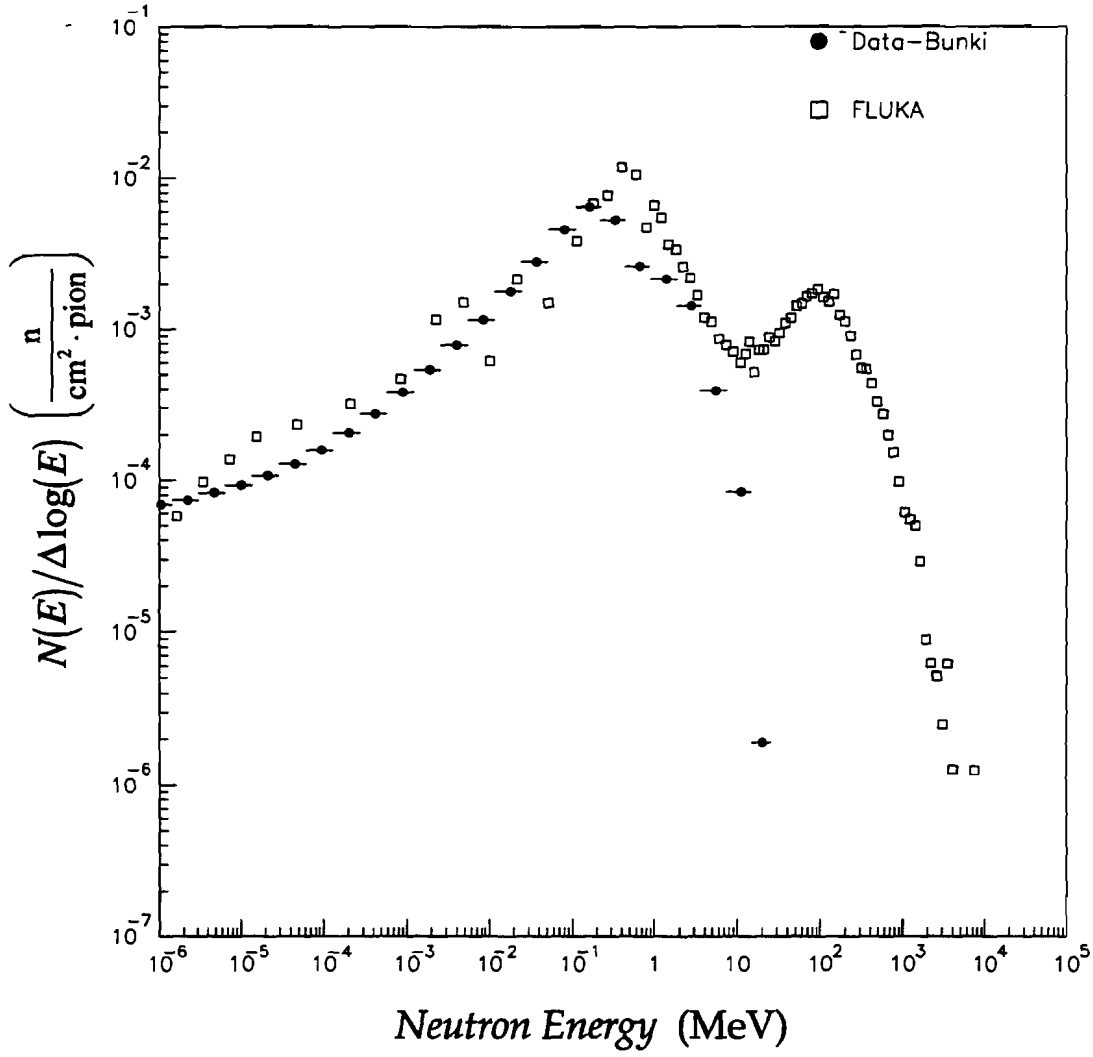

Figure C.12. Unfolded Neutron Spectra for Incident Pions on 81.3 cm of Iron. Shown is the neutron spectrum unfolded from the data by use of BUNKI compared to that generated by the FLUKA simulation, for 50 GeV incident pions on 81.3 cm (32 in, 4.8 λ) of iron in the longitudinal direction. The fluence per unit lethargy per pion is plotted as a function of neutron energy.

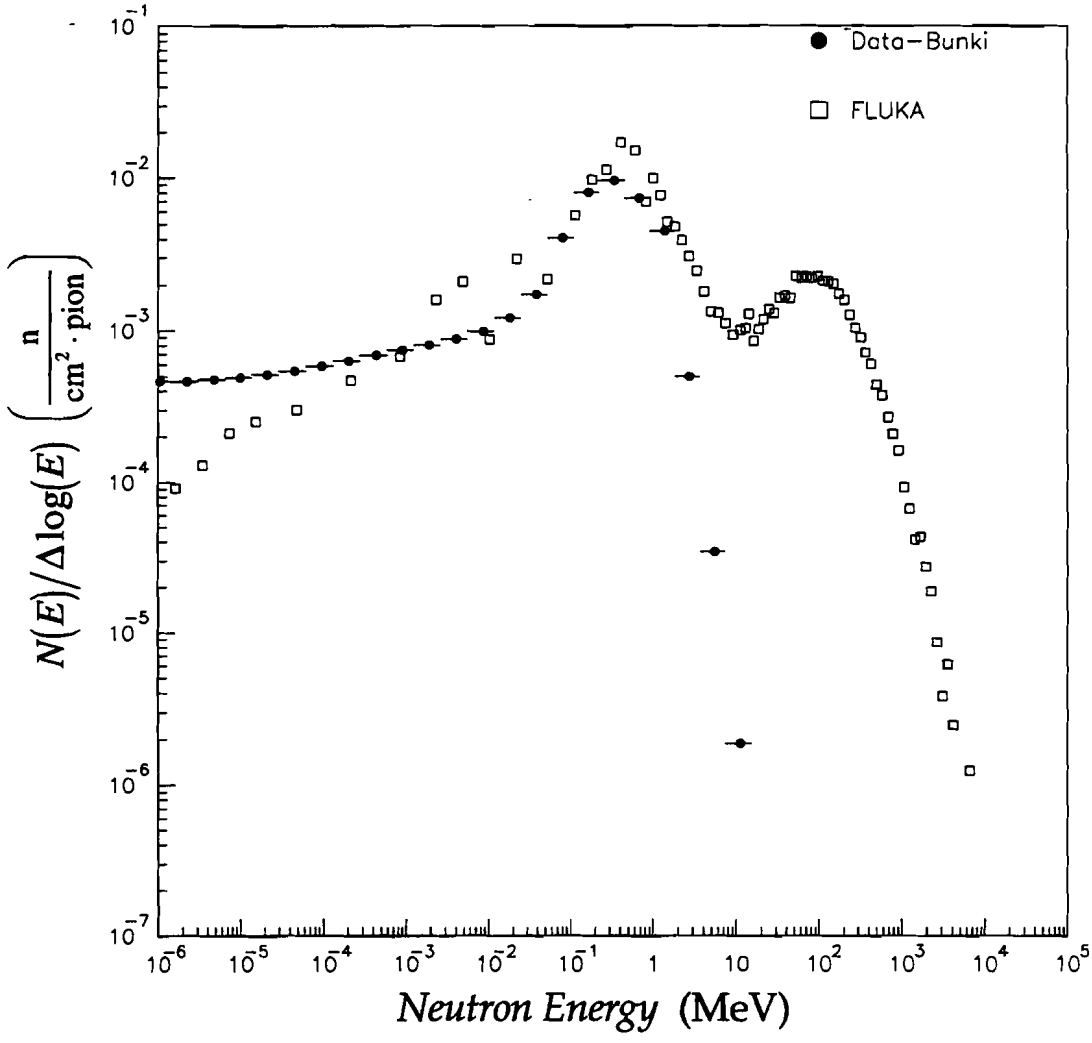

Figure C.13. Unfolded Neutron Spectra for Incident Pions on 81.3 cm of Iron. Shown is the neutron spectrum unfolded from the data by use of BUNKI compared to that generated by the FLUKA simulation, for 75 GeV incident pions on 81.3 cm (32 in, 4.8 λ) of iron in the longitudinal direction. The fluence per unit lethargy per pion is plotted as a function of neutron energy.

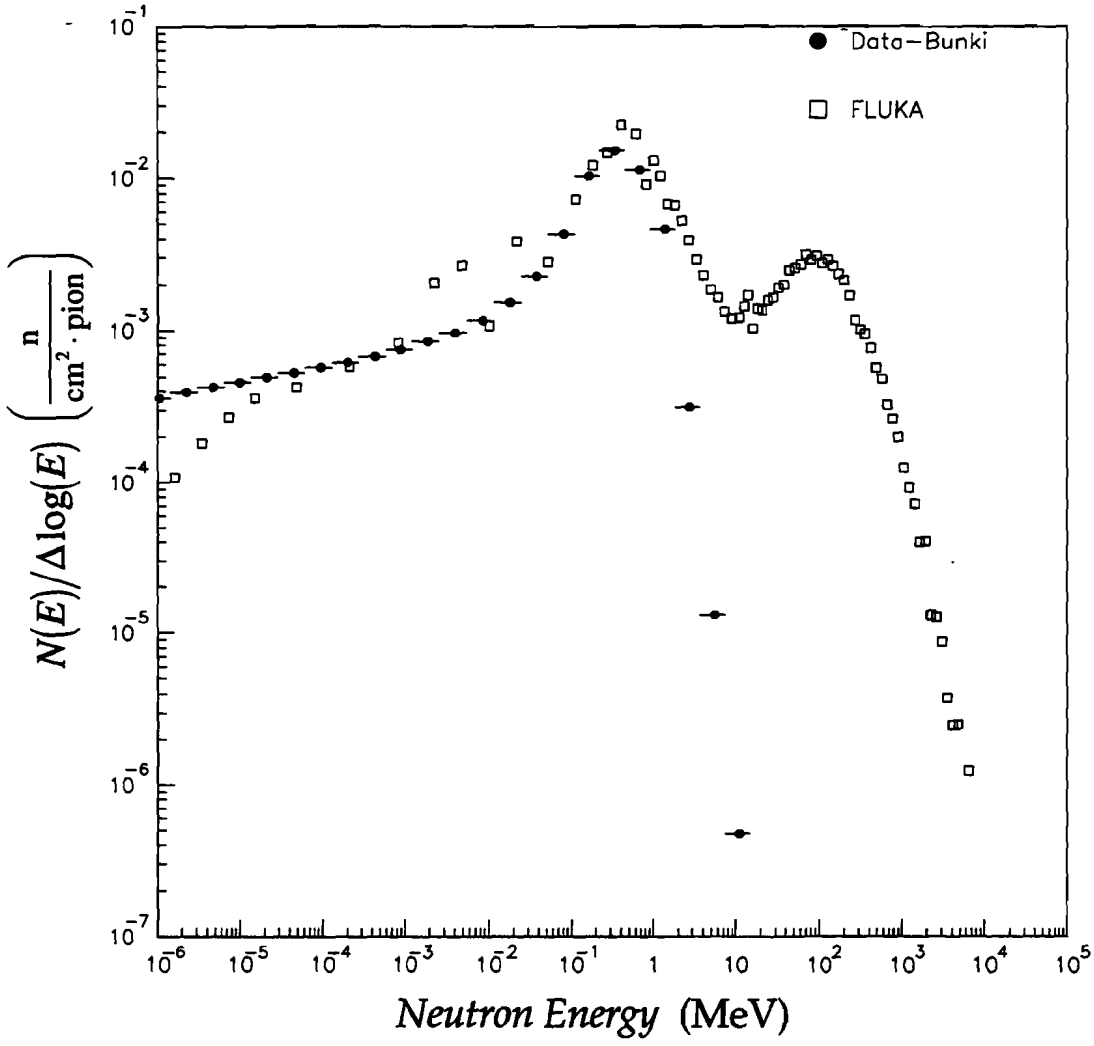

Figure C.14. Unfolded Neutron Spectra for Incident Pions on 81.3 cm of Iron. Shown is the neutron spectrum unfolded from the data by use of BUNKI compared to that generated by the FLUKA simulation, for 100 GeV incident pions on 81.3 cm (32 in, 4.8 λ) of iron in the longitudinal direction. The fluence per unit lethargy per pion is plotted as a function of neutron energy.

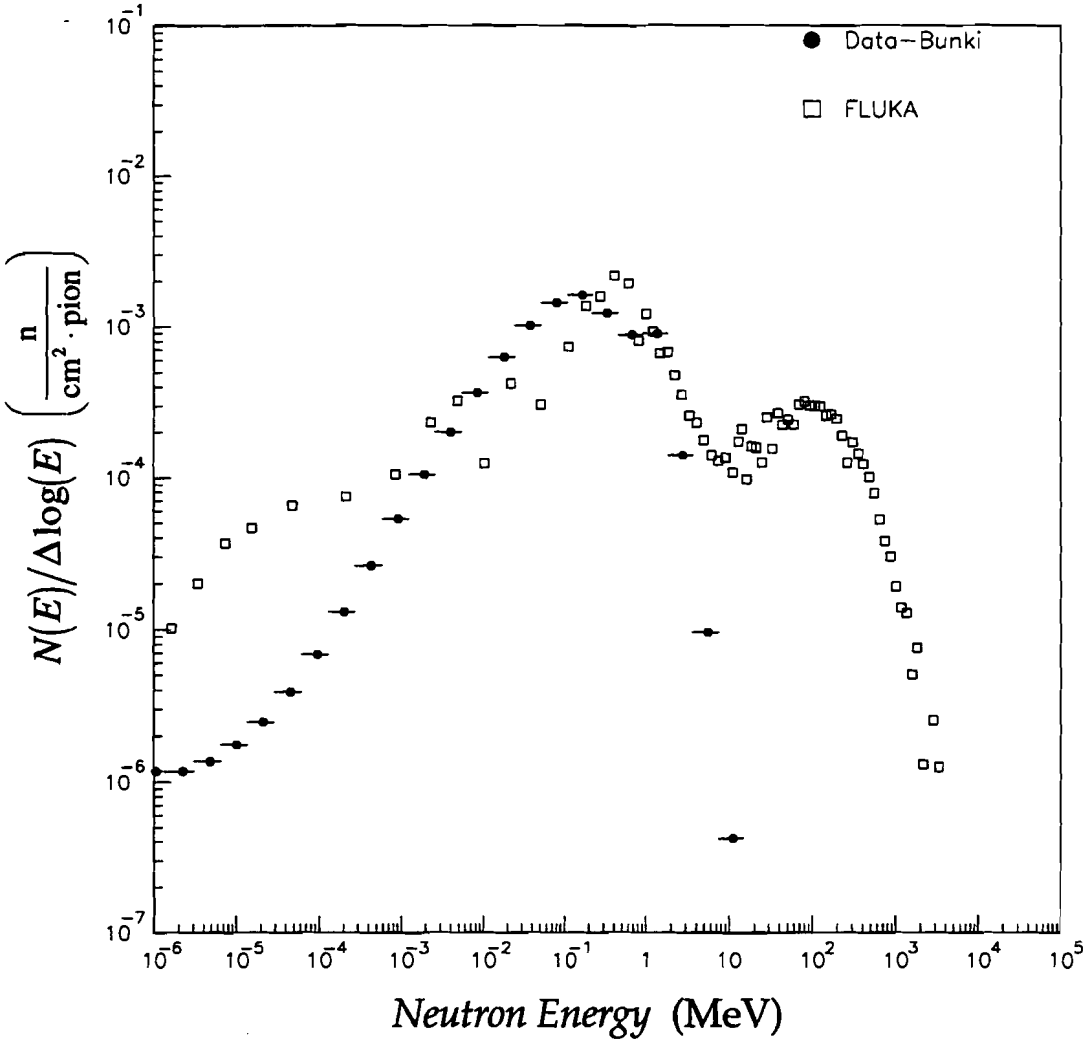

Figure C.15. Unfolded Neutron Spectra for Incident Pions on 121.9 cm of Iron. Shown is the neutron spectrum unfolded from the data by use of BUNKI compared to that generated by the FLUKA simulation, for 25 GeV incident pions on 121.9 cm (48 in, 7.3 λ) of iron in the longitudinal direction. The fluence per unit lethargy per pion is plotted as a function of neutron energy.

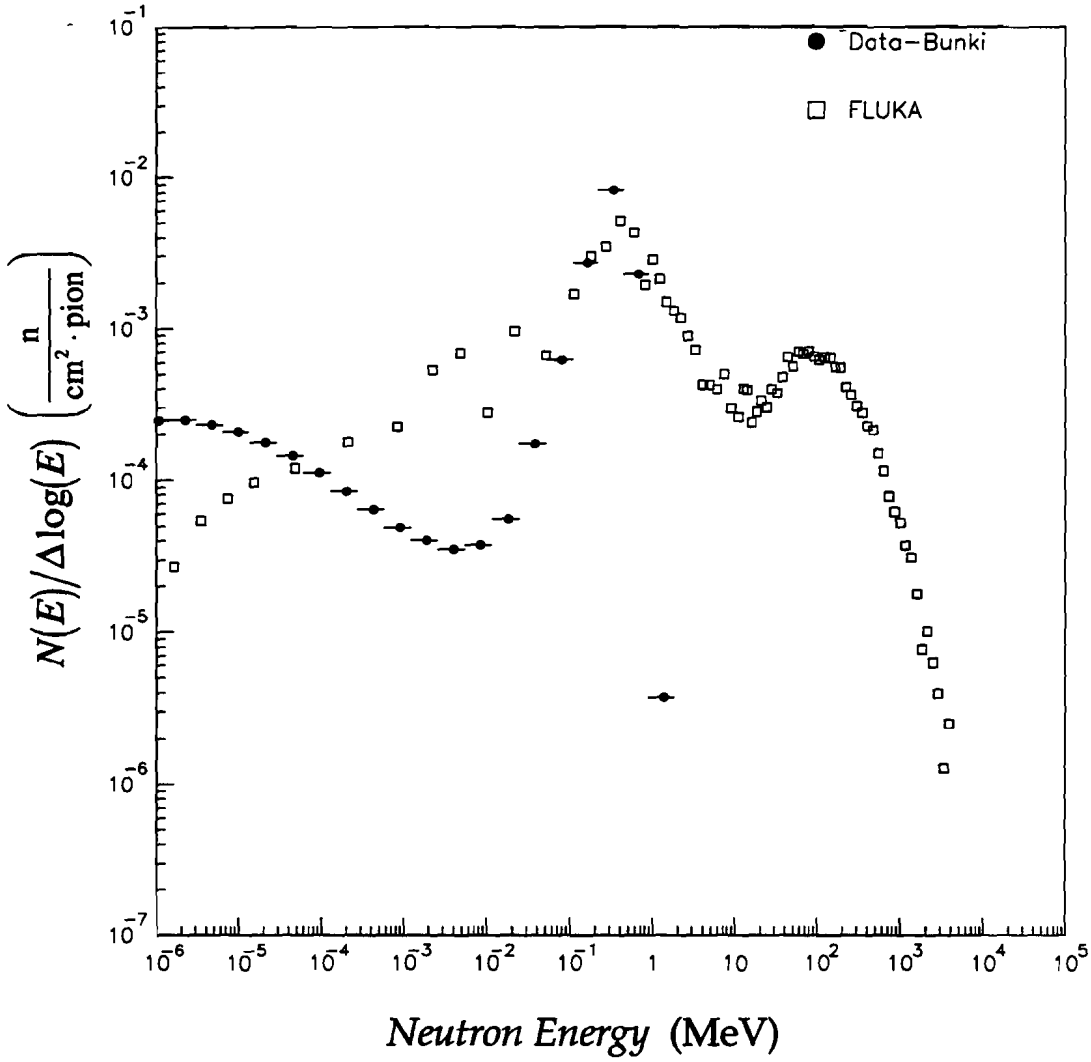

Figure C.16. Unfolded Neutron Spectra for Incident Pions on 121.9 cm of Iron. Shown is the neutron spectrum unfolded from the data by use of BUNKI compared to that generated by the FLUKA simulation, for 50 GeV incident pions on 121.9 cm (48 in, 7.3 λ) of iron in the longitudinal direction. The fluence per unit lethargy is plotted as a function of neutron energy. Data set taken on December 11, 1991.

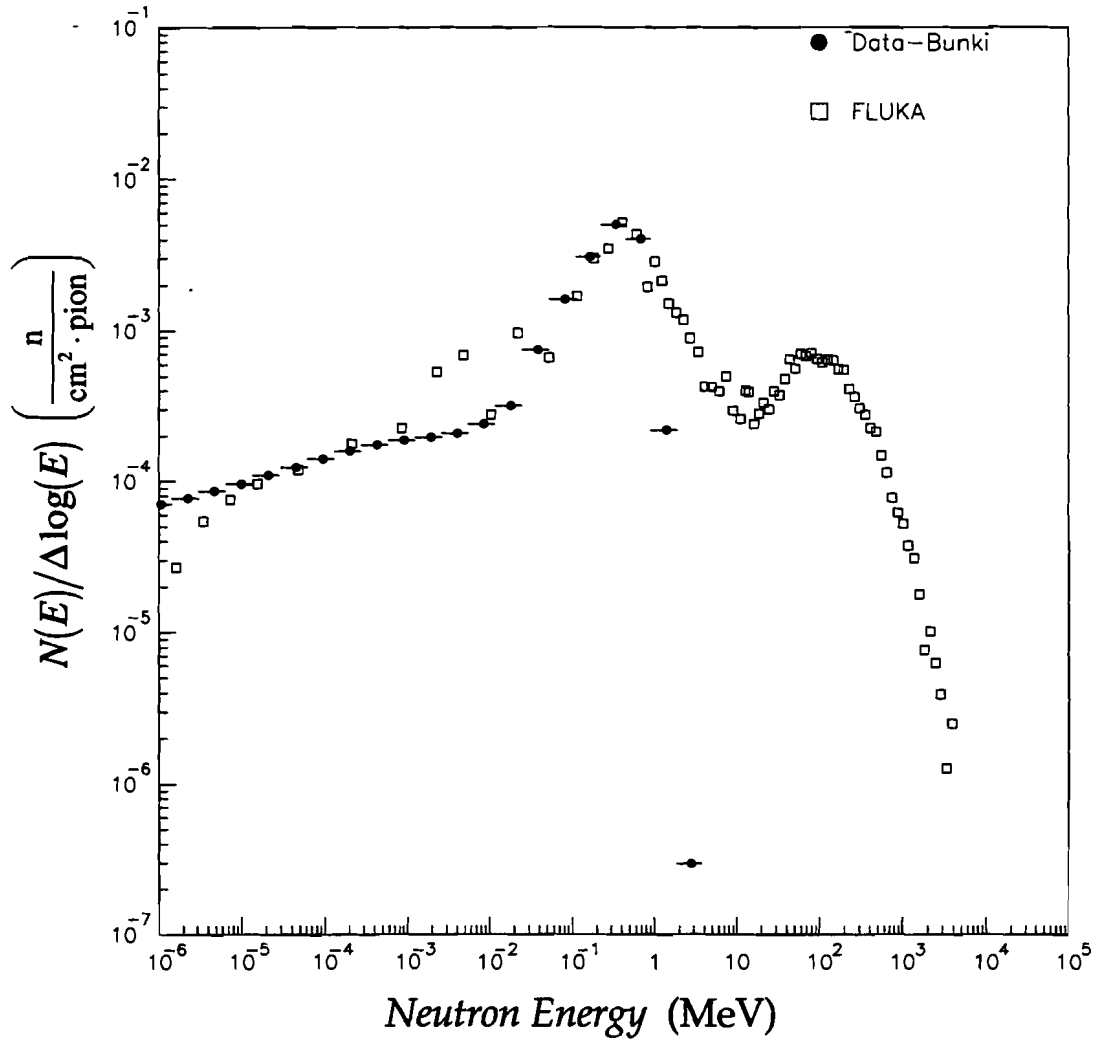

Figure C.17. Unfolded Neutron Spectra for Incident Pions on 121.9 cm of Iron. Shown is the neutron spectrum unfolded from the data by use of BUNKI compared to that generated by the FLUKA simulation, for 50 GeV incident pions on 121.9 cm (48 in, 7.3 λ) of iron in the longitudinal direction. The fluence per unit lethargy is plotted as a function of neutron energy. Data set taken on december 24, 1991.

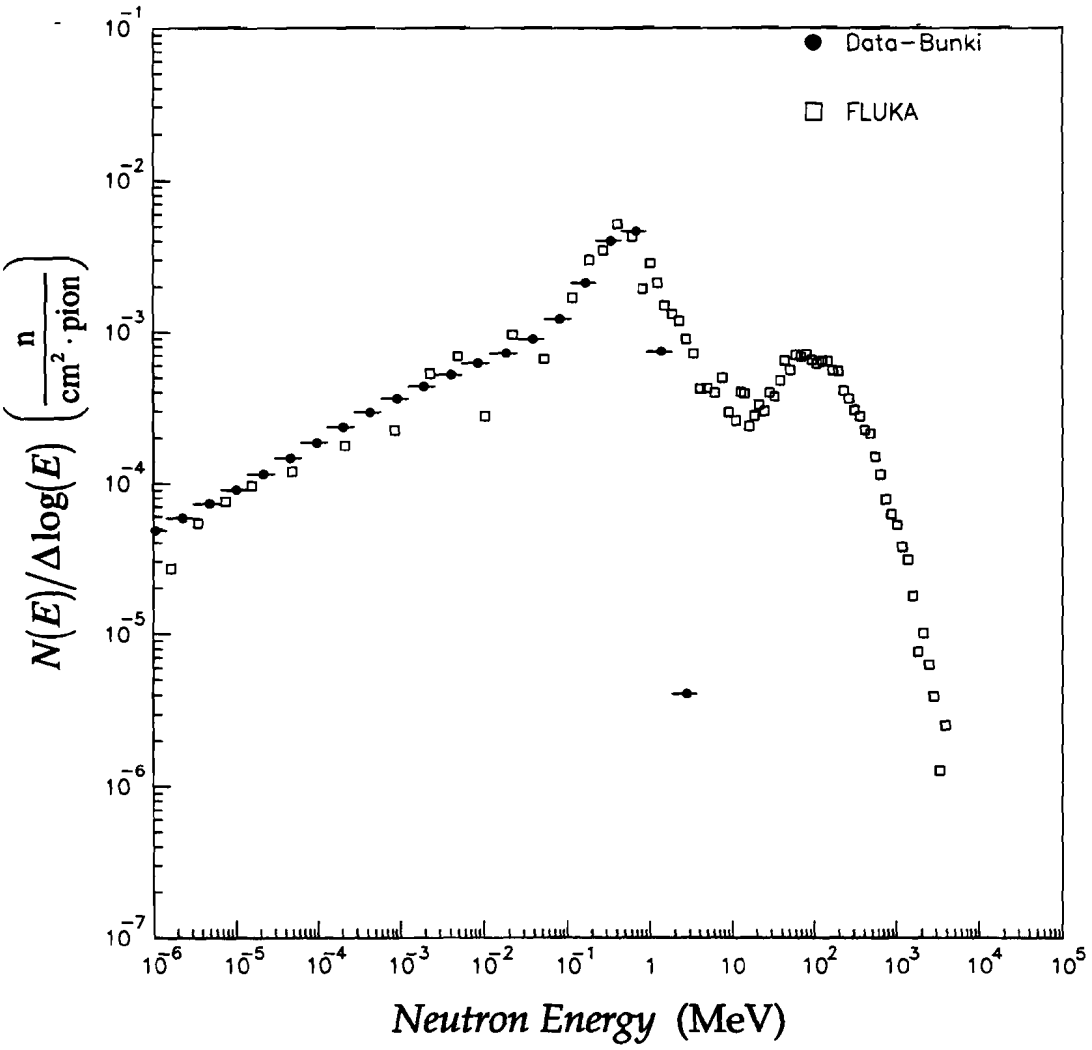

Figure C.18. Unfolded Neutron Spectra for Incident Pions on 121.9 cm of Iron. Shown is the neutron spectrum unfolded from the data by use of BUNKI compared to that generated by the FLUKA simulation, for 50 GeV incident pions on 121.9 cm (48 in, 7.3 λ) of iron in the longitudinal direction. The fluence per unit lethargy per pion is plotted as a function of neutron energy. Data set taken on December 25, 1991.

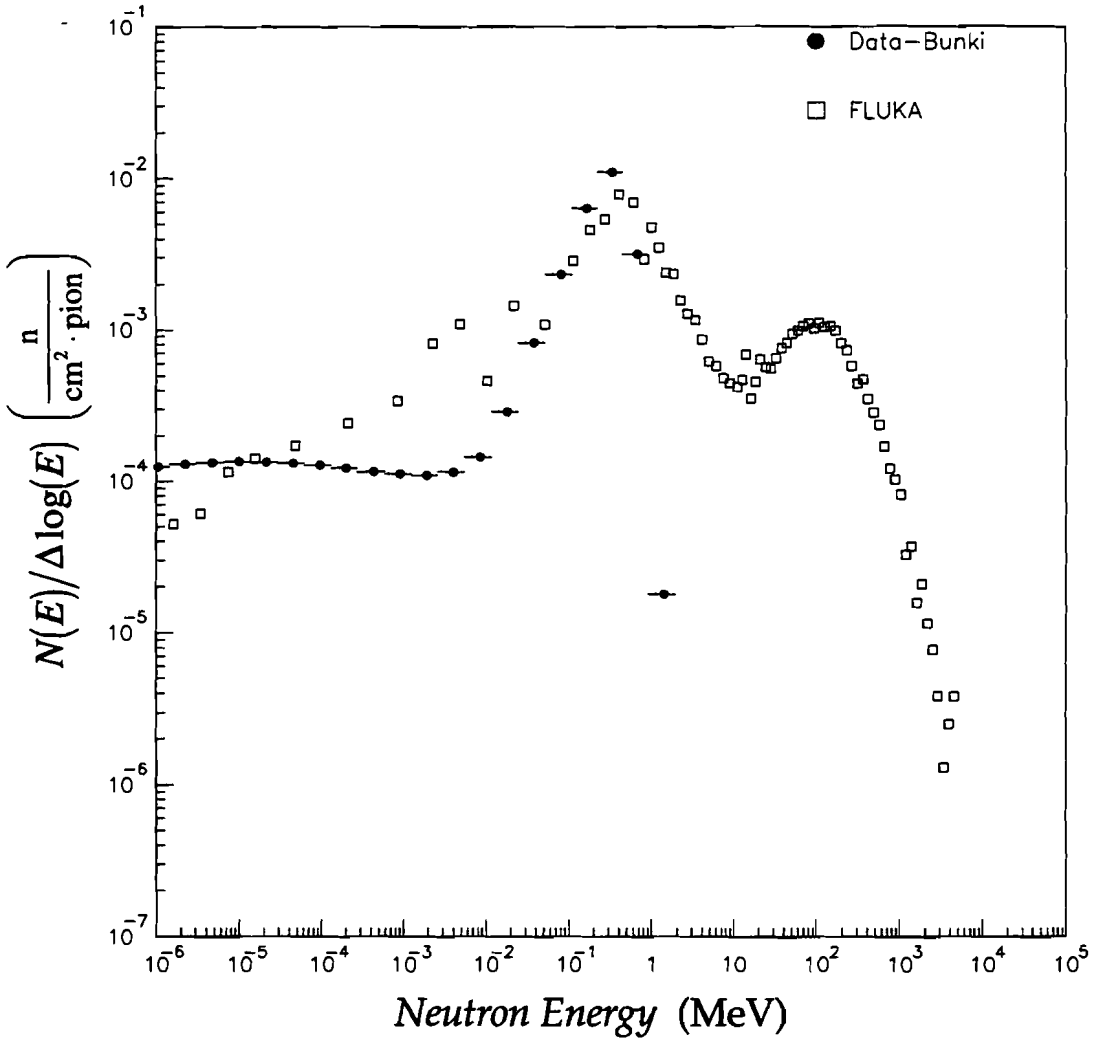

Figure C.19. Unfolded Neutron Spectra for Incident Pions on 121.9 cm of Iron. Shown is the neutron spectrum unfolded from the data by use of BUNKI compared to that generated by the FLUKA simulation, for 75 GeV incident pions on 121.9 cm (48 in, 7.3 λ) of iron in the longitudinal direction. The fluence per unit lethargy is plotted as a function of neutron energy.

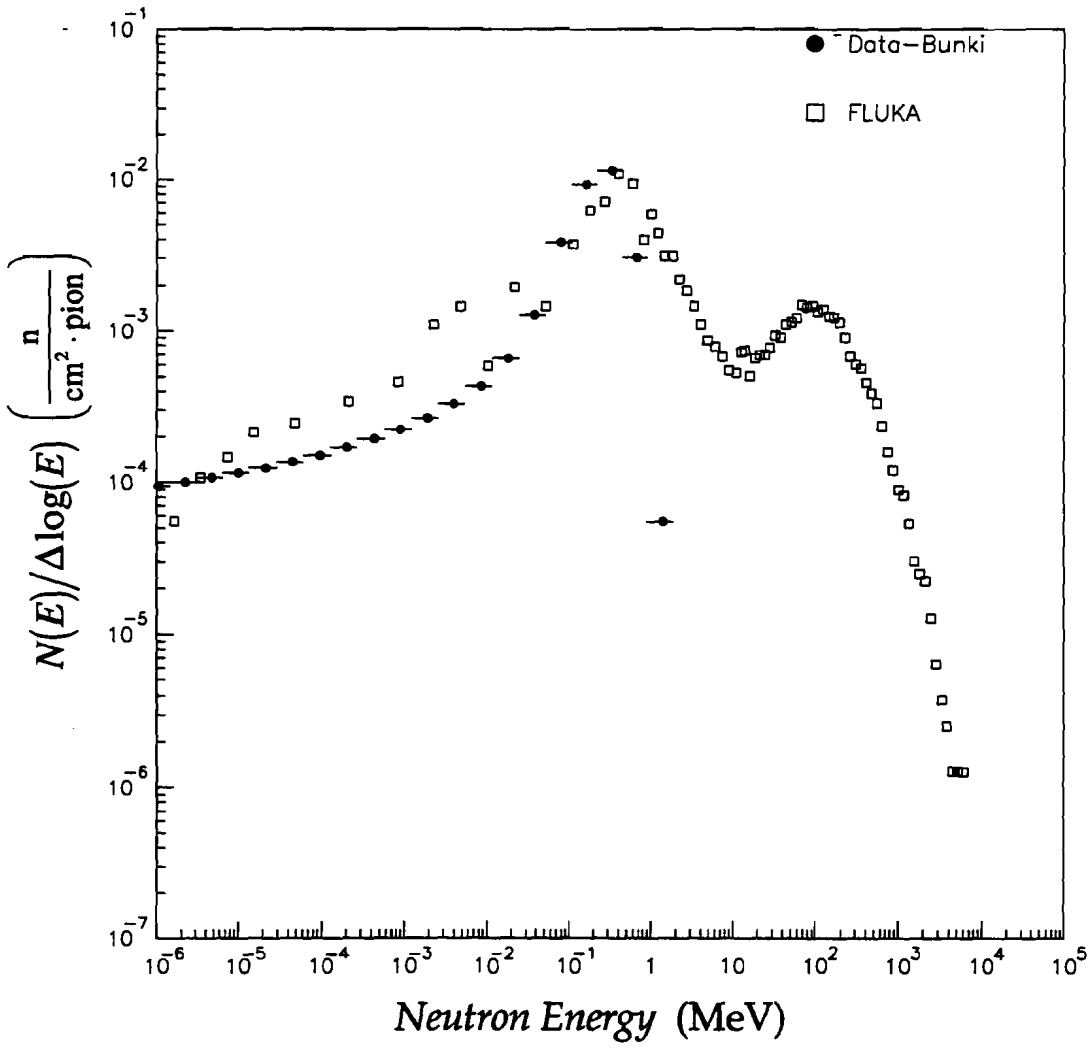

Figure C.20. Unfolded Neutron Spectra for Incident Pions on 121.9 cm of Iron. Shown is the neutron spectrum unfolded from the data by use of BUNKI compared to that generated by the FLUKA simulation, for 100 GeV incident pions on 121.9 cm (48 in, 7.3 λ) of iron in the longitudinal direction. The fluence per unit lethargy per pion is plotted as a function of neutron energy.

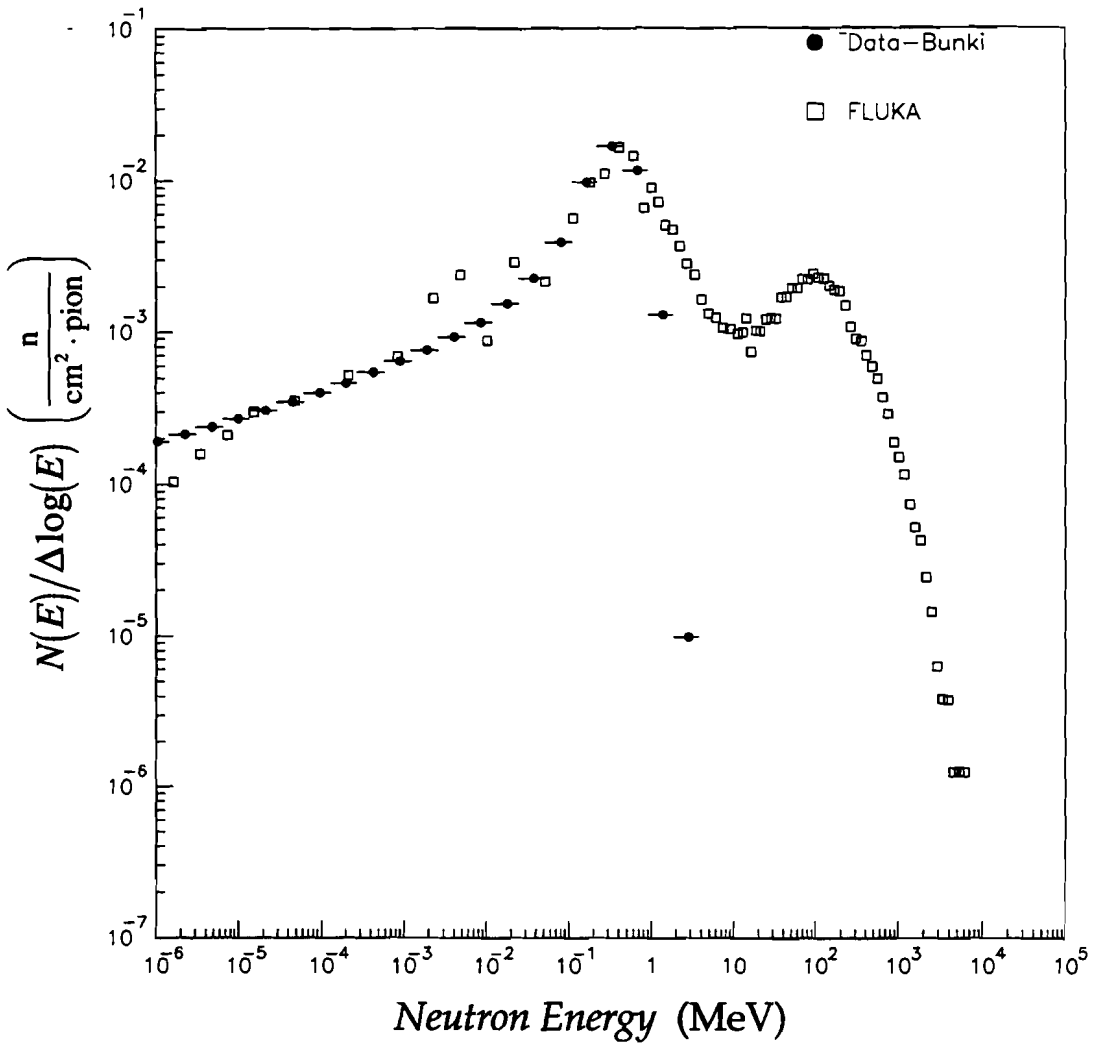

Figure C.21. Unfolded Neutron Spectra for Incident Pions on 121.9 cm of Iron. Shown is the neutron spectrum unfolded from the data by use of BUNKI compared to that generated by the FLUKA simulation, for 150 GeV incident pions on 121.9 cm (48 in, 7.3 λ) of iron in the longitudinal direction. The fluence per unit lethargy per pion is plotted as a function of neutron energy.

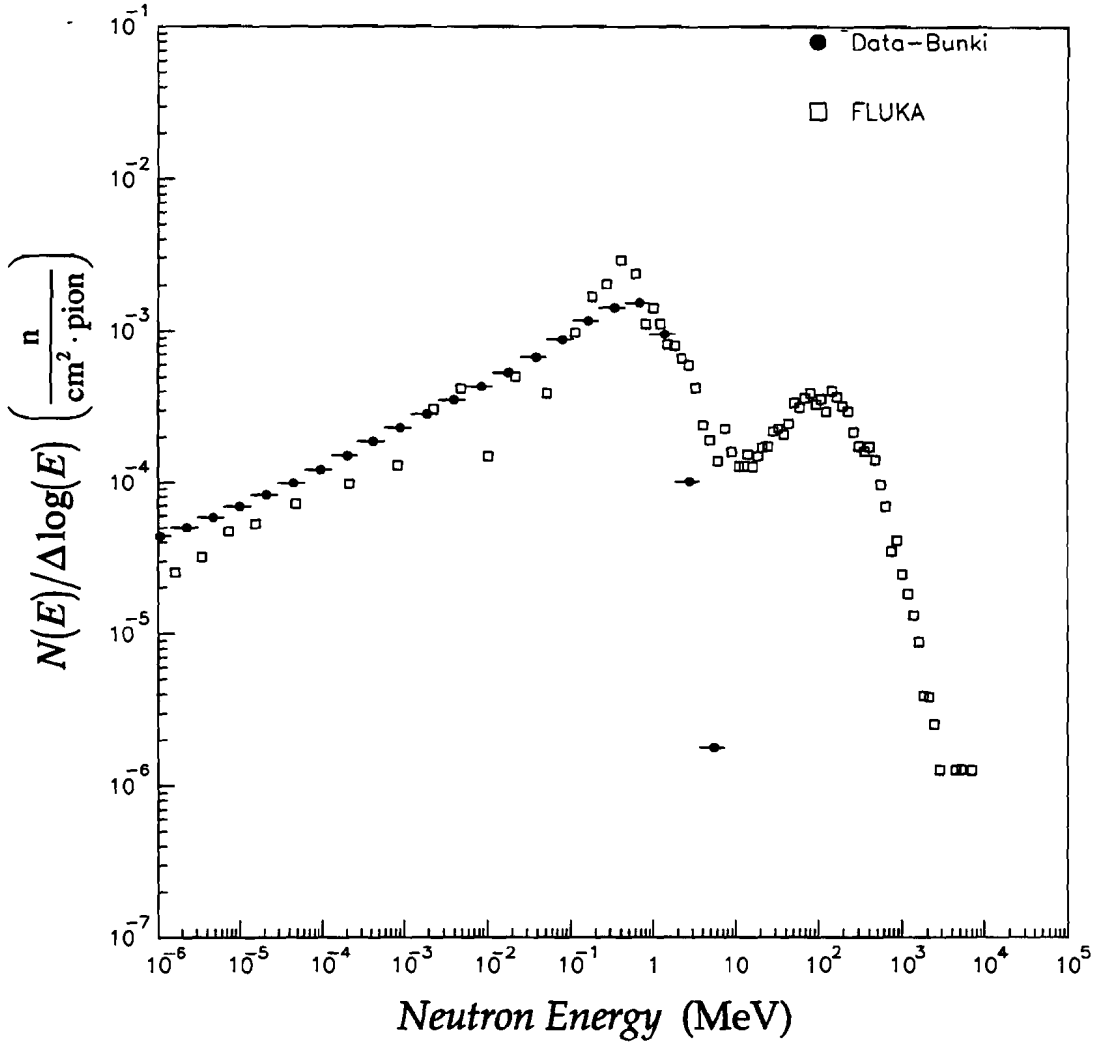

Figure C.22. Unfolded Neutron Spectra for Incident Pions on 142.2 cm of Iron. Shown is the neutron spectrum unfolded from the data by use of BUNKI compared to that generated by the FLUKA simulation, for 50 GeV incident pions on 142.2 cm (56 in, 8.5 λ) of iron in the longitudinal direction. The fluence per unit lethargy is plotted as a function of neutron energy.

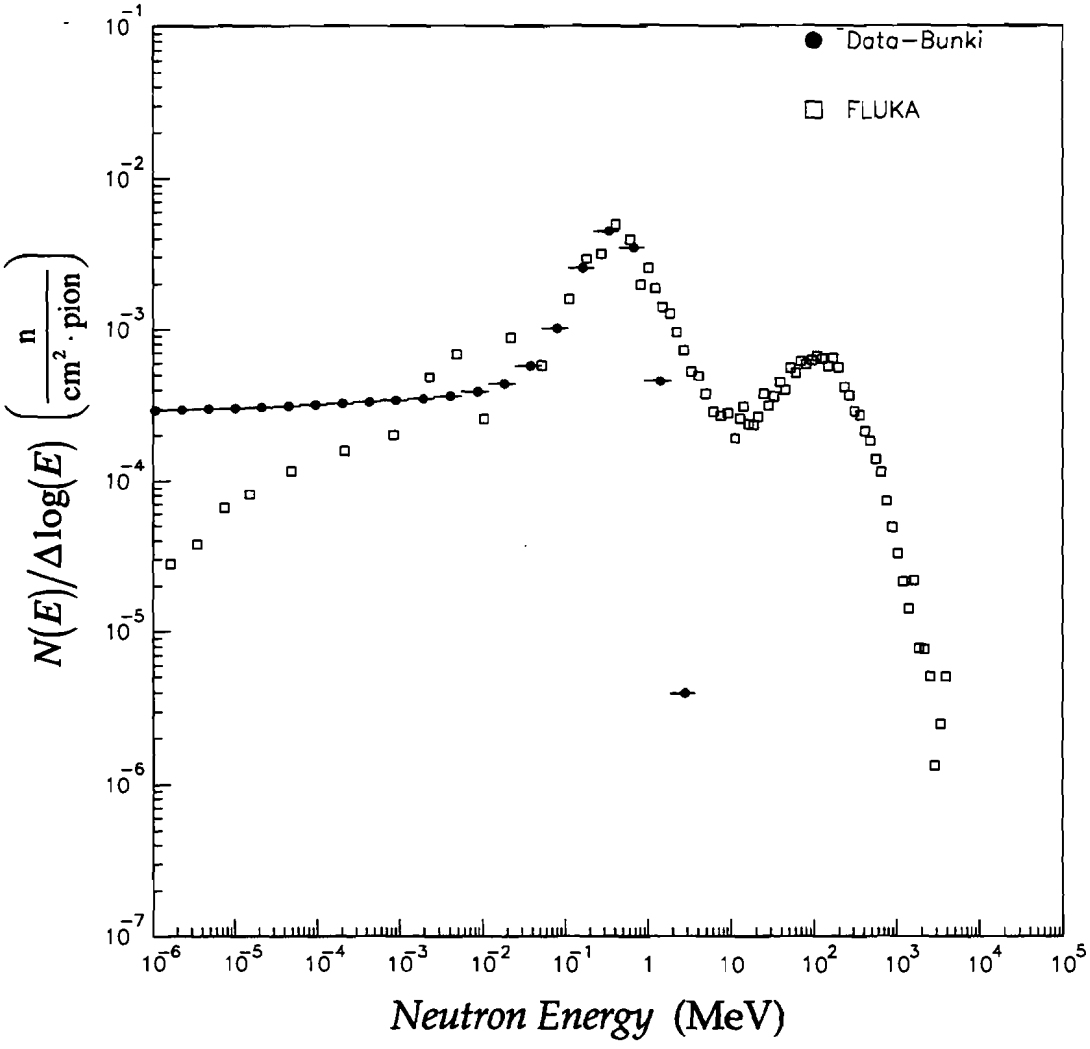

Figure C.23. Unfolded Neutron Spectra for Incident Pions on 142.2 cm of Iron. Shown is the neutron spectrum unfolded from the data by use of BUNKI compared to that generated by the FLUKA simulation, for 75 GeV incident pions on 142.2 cm (56 in, 8.5 λ) of iron in the longitudinal direction. The fluence per unit lethargy is plotted as a function of neutron energy.

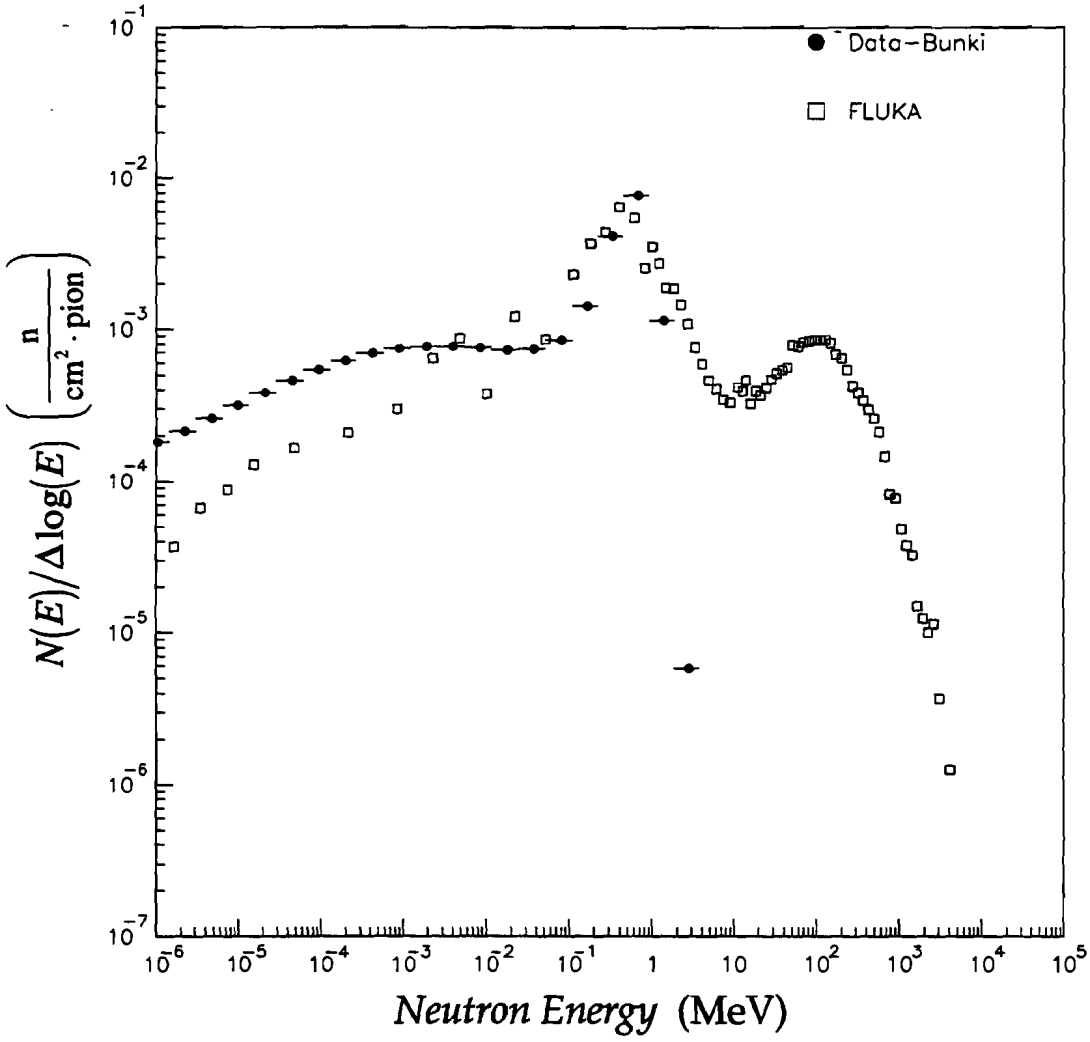

Figure C.24. Unfolded Neutron Spectra for Incident Pions on 142.2 cm of Iron. Shown is the neutron spectrum unfolded from the data by use of BUNKI compared to that generated by the FLUKA simulation, for 100 GeV incident pions on 142.2 cm (56 in, 8.5 λ) of iron in the longitudinal direction. The fluence per unit lethargy is plotted as a function of neutron energy.

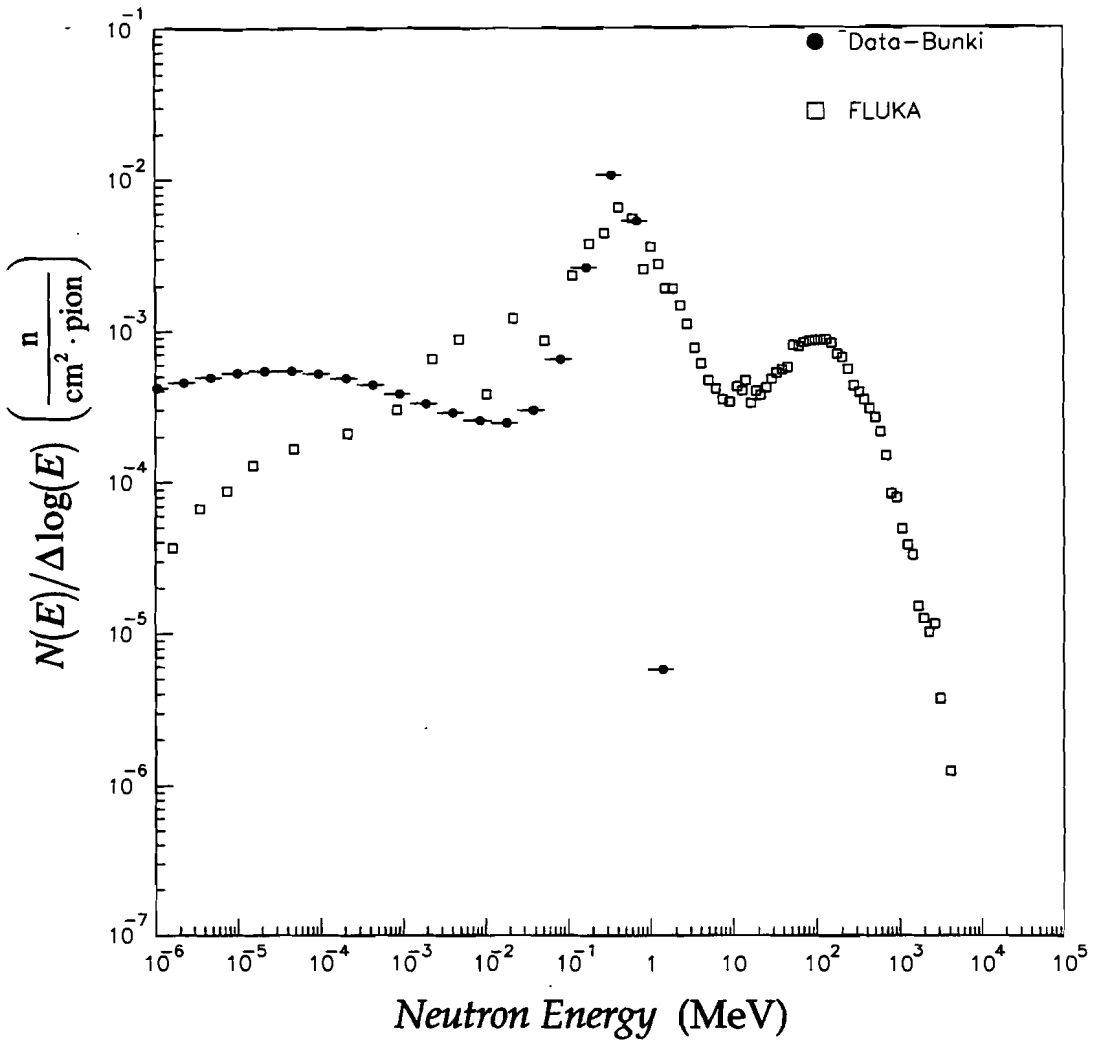

Figure C.25. Unfolded Neutron Spectra for Incident Pions on 142.2 cm of Iron. Shown is the neutron spectrum unfolded from the data by use of BUNKI compared to that generated by the FLUKA simulation, for 100 GeV incident pions on 142.2 cm (56 in, 8.5 λ) of iron in the longitudinal direction. The fluence per unit lethargy per pion is plotted as a function of neutron energy.

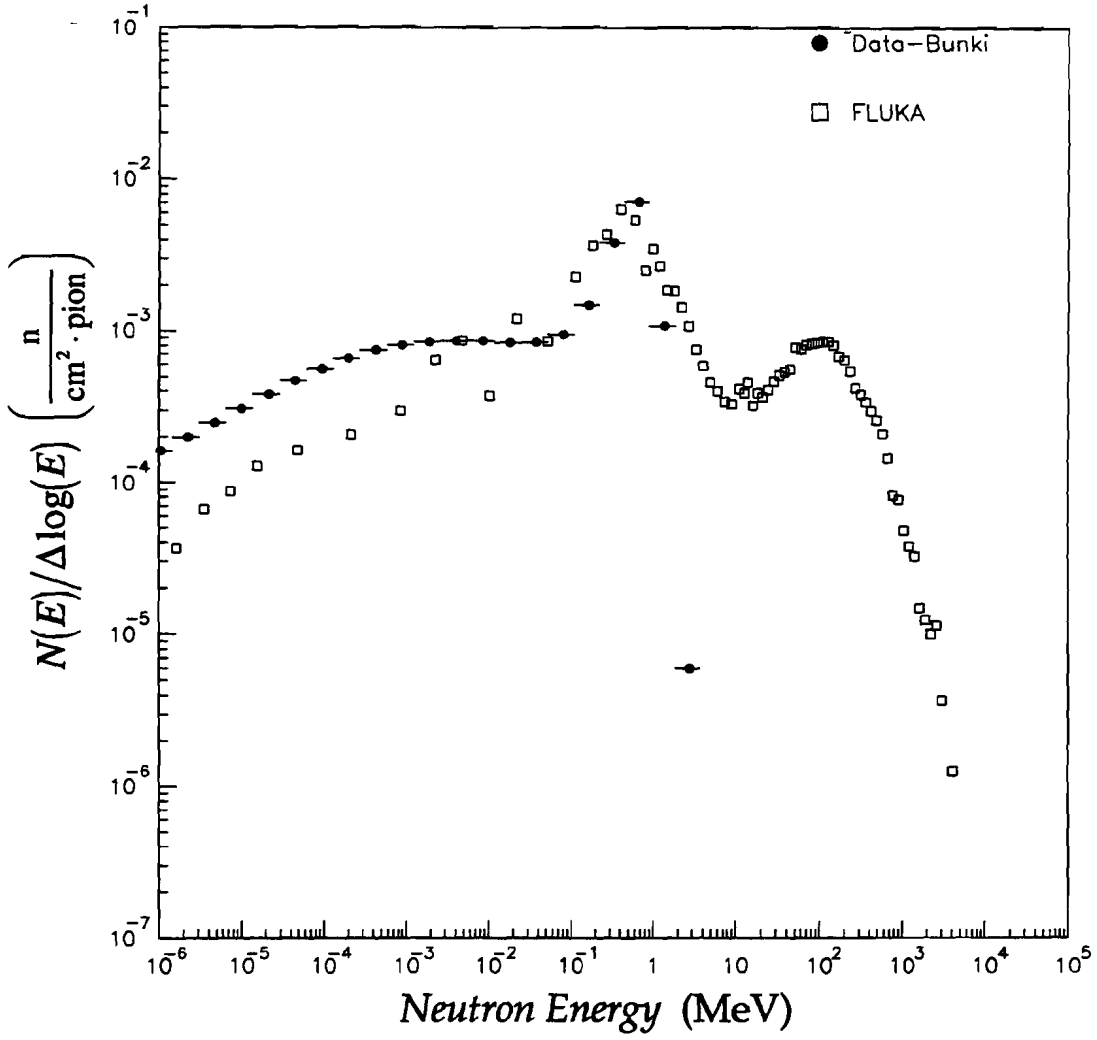

Figure C.26. Unfolded Neutron Spectra for Incident Pions on 142.2 cm of Iron. Shown is the neutron spectrum unfolded from the data by use of BUNKI compared to that generated by the FLUKA simulation, for 100 GeV incident pions on 142.2 cm (56 in, 8.5 λ) of iron in the longitudinal direction. The fluence per unit lethargy per pion is plotted as a function of neutron energy.

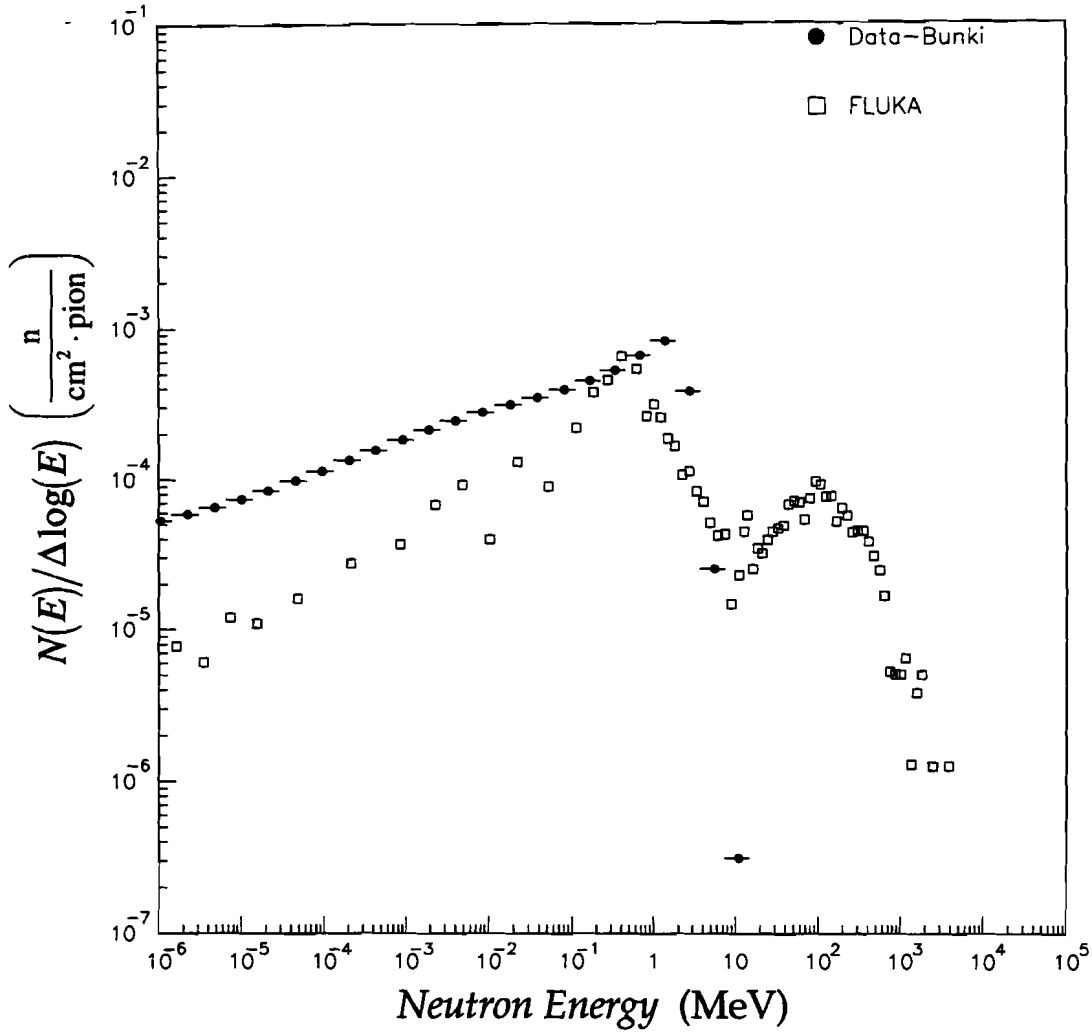

Figure C.27. Unfolded Neutron Spectra for Incident Pions on 162.6 cm of Iron. Shown is the neutron spectrum unfolded from the data by use of BUNKI compared to that generated by the FLUKA simulation, for 25 GeV incident pions on 162.6 cm (64 in, 9.7 λ) of iron in the longitudinal direction. The fluence per unit lethargy per pion is plotted as a function of neutron energy.

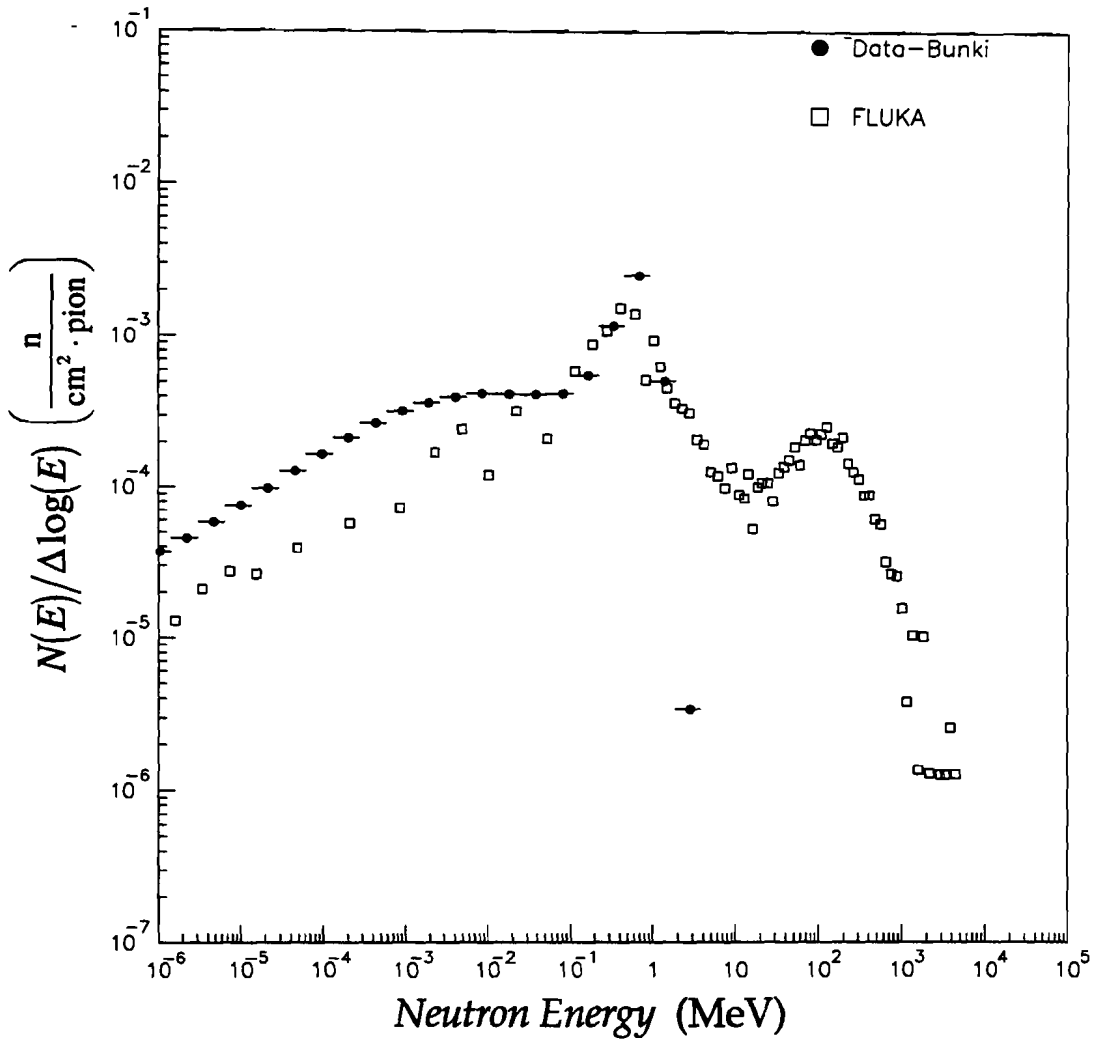

Figure C.28. Unfolded Neutron Spectra for Incident Pions on 162.6 cm of Iron. Shown is the neutron spectrum unfolded from the data by use of BUNKI compared to that generated by the FLUKA simulation, for 50 GeV incident pions on 162.6 cm (64 in, 9.7 λ) of iron in the longitudinal direction. The fluence per unit lethargy per pion is plotted as a function of neutron energy.

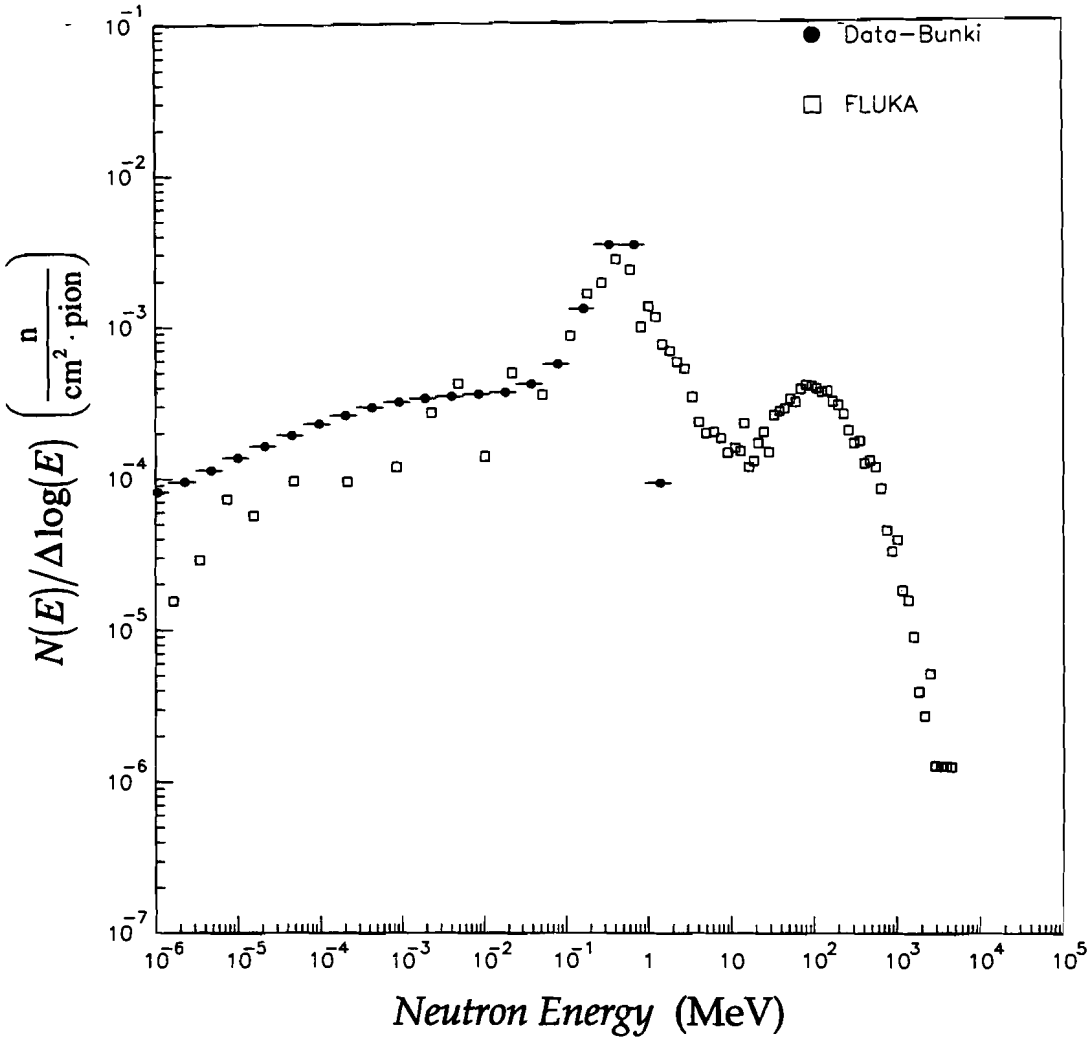

Figure C.29. Unfolded Neutron Spectra for Incident Pions on 162.6 cm of Iron. Shown is the neutron spectrum unfolded from the data by use of BUNKI compared to that generated by the FLUKA simulation, for 75 GeV incident pions on 162.6 cm (64 in, 9.7 λ) of iron in the longitudinal direction. The fluence per unit lethargy per pion is plotted as a function of neutron energy.

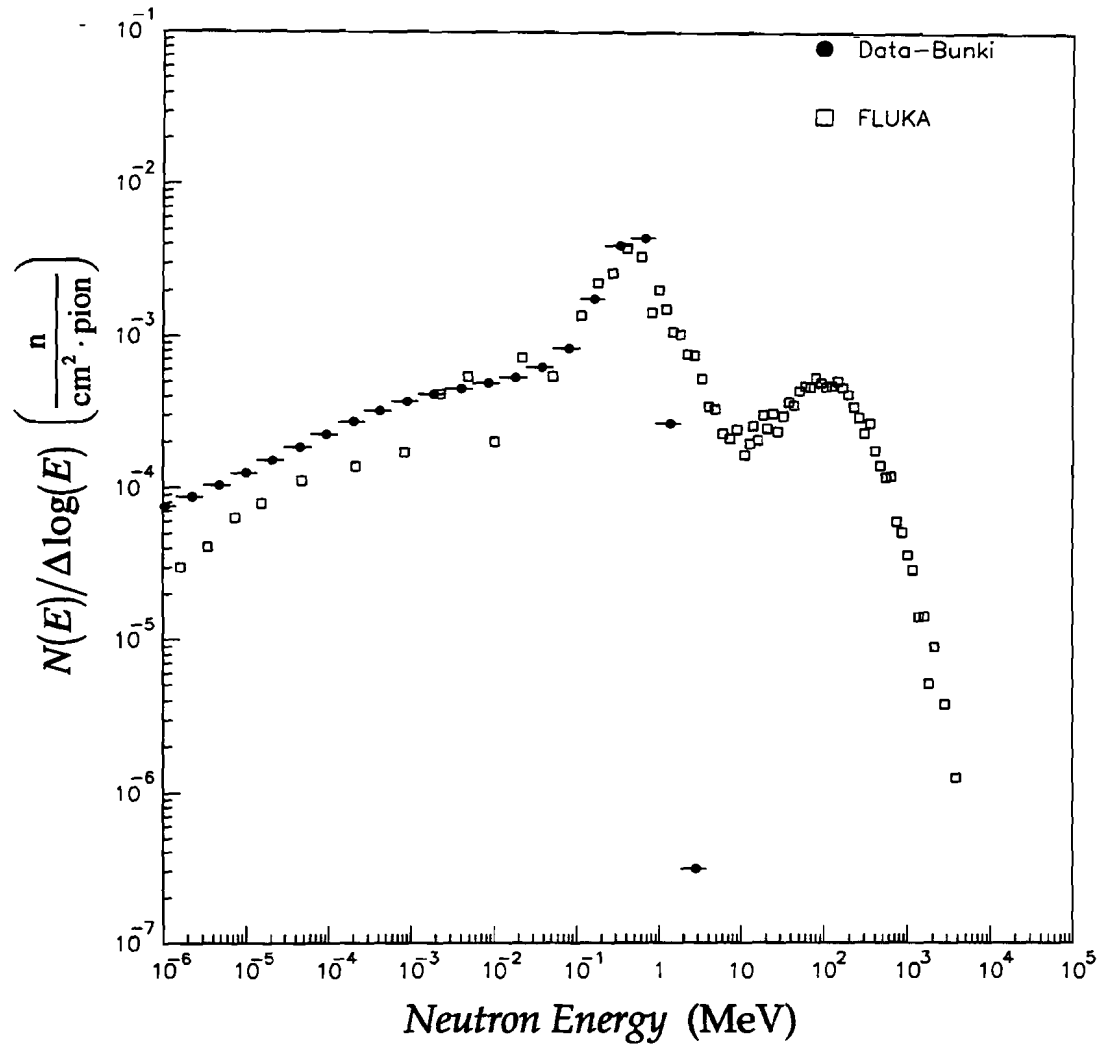

Figure C.30. Unfolded Neutron Spectra for Incident Pions on 162.6 cm of Iron. Shown is the neutron spectrum unfolded from the data by use of BUNKI compared to that generated by the FLUKA simulation, for 100 GeV incident pions on 162.6 cm (64 in, 9.7 λ) of iron in the longitudinal direction. The fluence per unit lethargy per pion is plotted as a function of neutron energy.

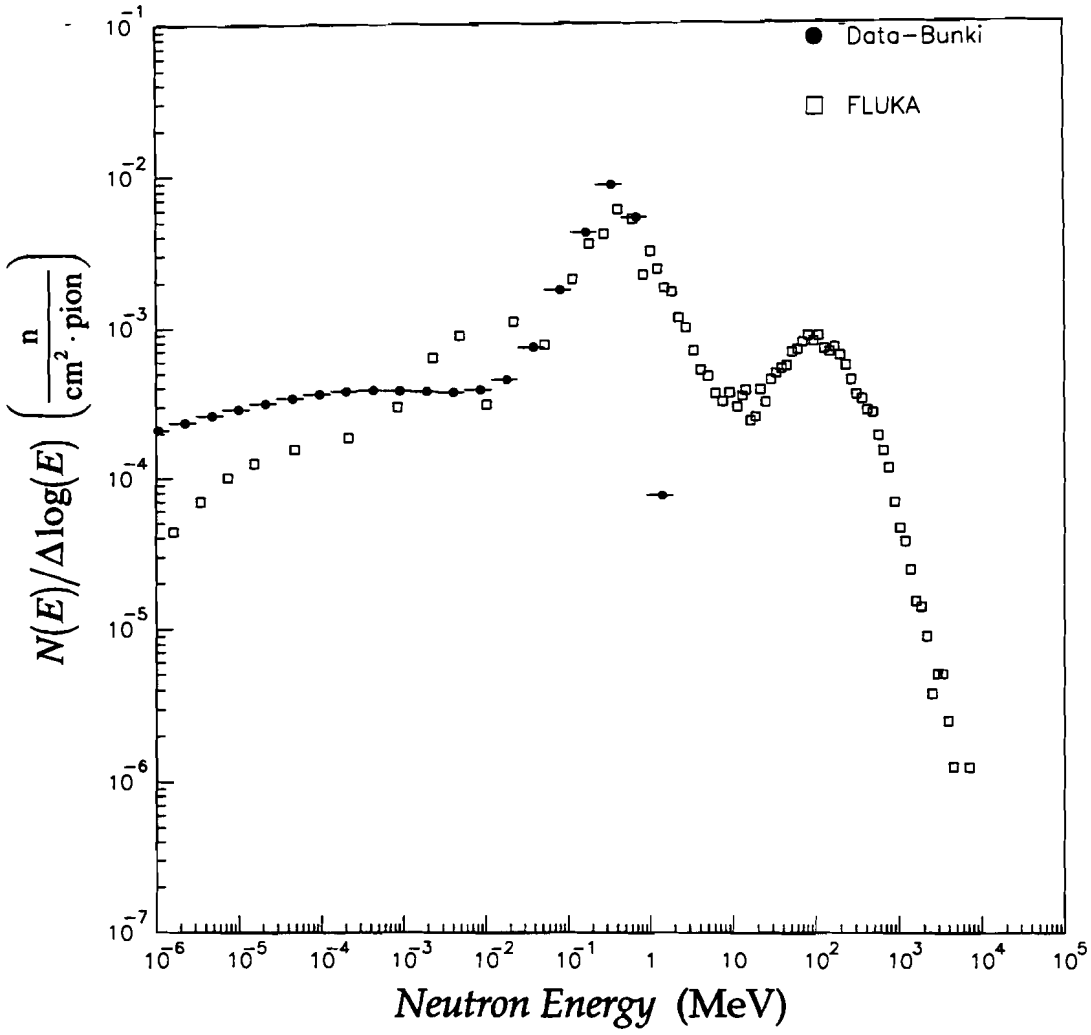

Figure C.31. Unfolded Neutron Spectra for Incident Pions on 162.6 cm of Iron. Shown is the neutron spectrum unfolded from the data by use of BUNKI compared to that generated by the FLUKA simulation, for 150 GeV incident pions on 162.6 cm (64 in, 9.7 λ) of iron in the longitudinal direction. The fluence per unit lethargy per pion is plotted as a function of neutron energy.

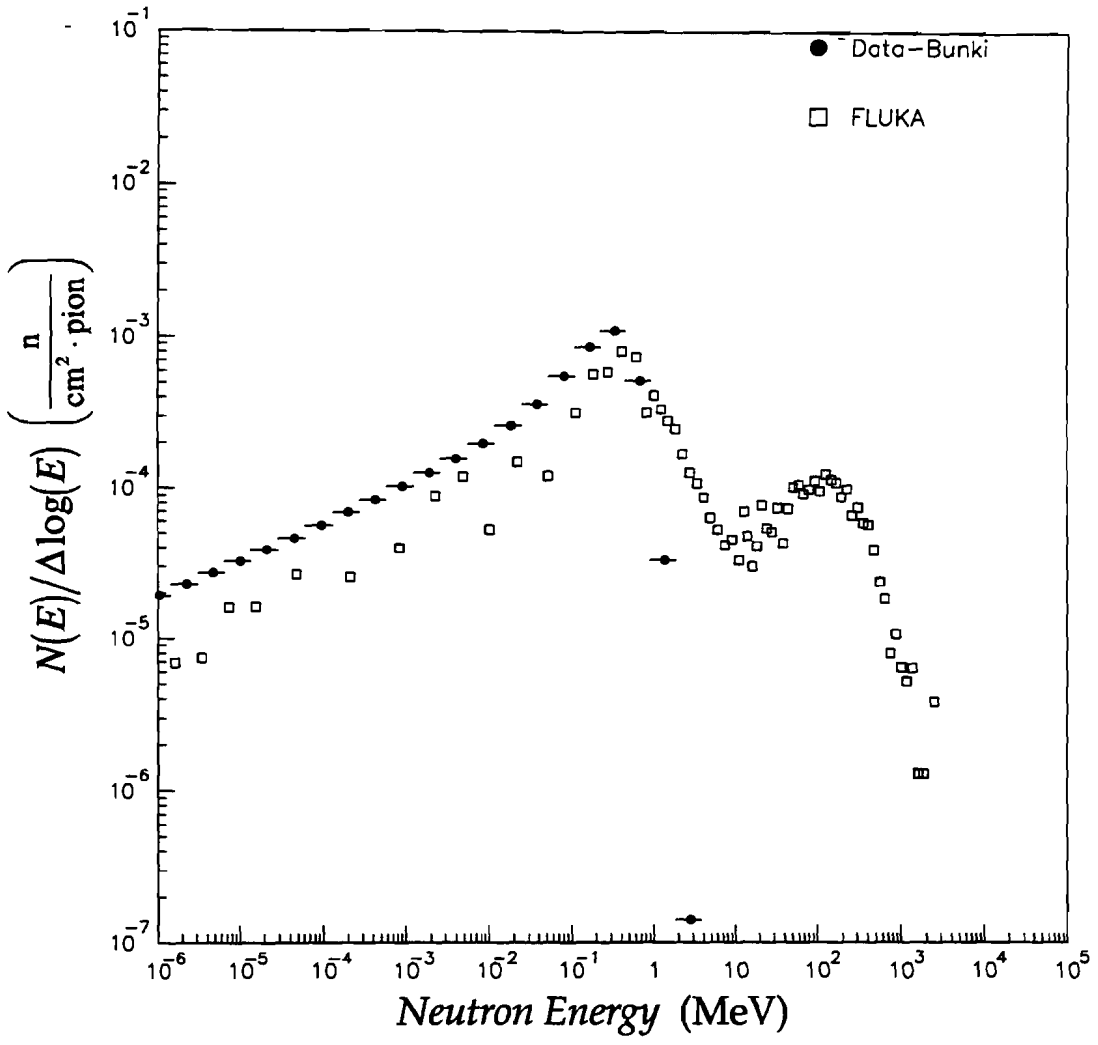

Figure C.32. Unfolded Neutron Spectra for Incident Pions on 182.9 cm of Iron. Shown is the neutron spectrum unfolded from the data by use of BUNKI compared to that generated by the FLUKA simulation, for 50 GeV incident pions on 182.9 cm (72 in, 10.9 λ) of iron in the longitudinal direction. The fluence per unit lethargy per pion is plotted as a function of neutron energy.

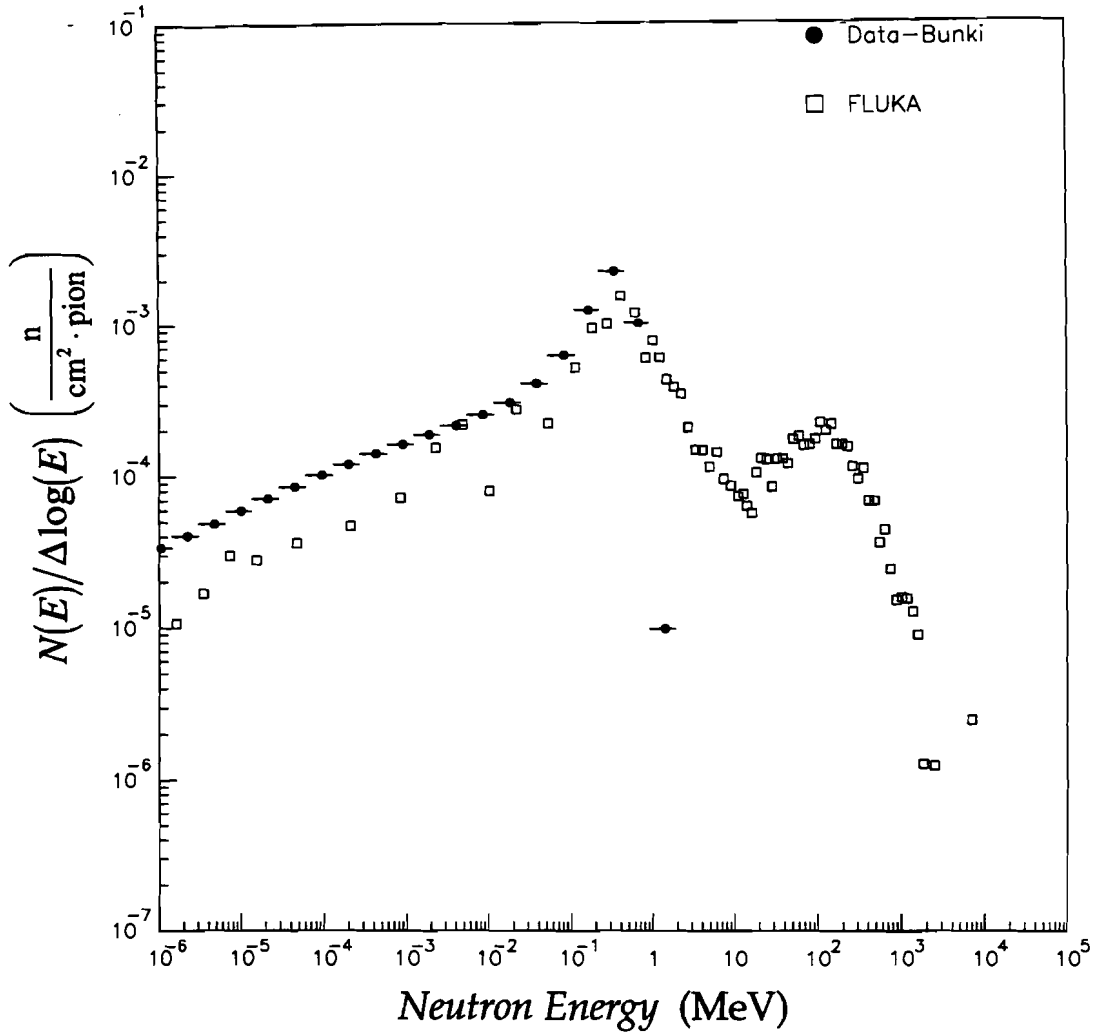

Figure C.33. Unfolded Neutron Spectra for Incident Pions on 182.9 cm of Iron. Shown is the neutron spectrum unfolded from the data by use of BUNKI compared to that generated by the FLUKA simulation, for 75 GeV incident pions on 182.9 cm (72 in, 10.9 λ) of iron in the longitudinal direction. The fluence per unit lethargy per pion is plotted as a function of neutron energy.

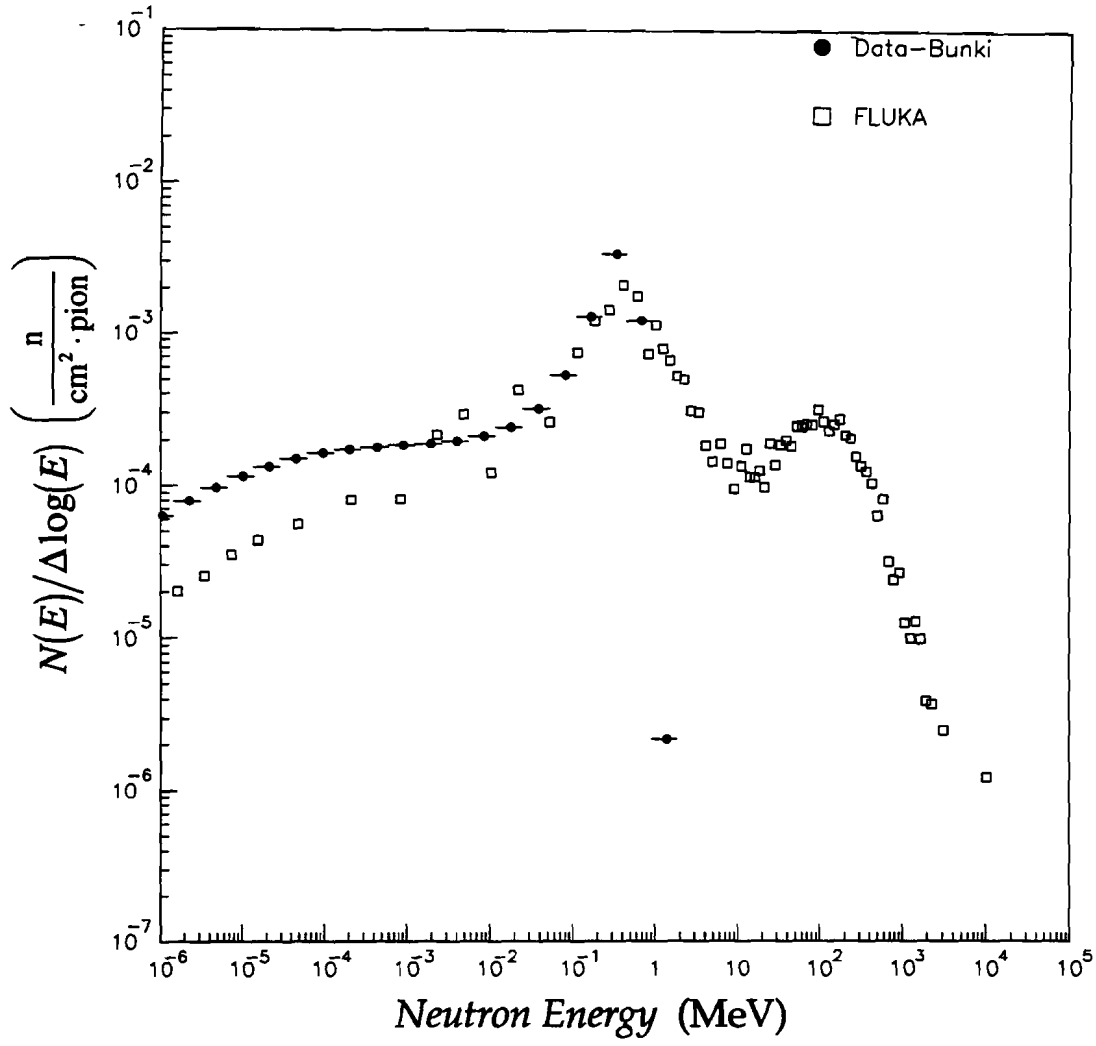

Figure C.34. Unfolded Neutron Spectra for Incident Pions on 182.9 cm of Iron. Shown is the neutron spectrum unfolded from the data by use of BUNKI compared to that generated by the FLUKA simulation, for 100 GeV incident pions on 182.9 cm (72 in, 10.9 λ) of iron in the longitudinal direction. The fluence per unit lethargy is plotted as a function of neutron energy.

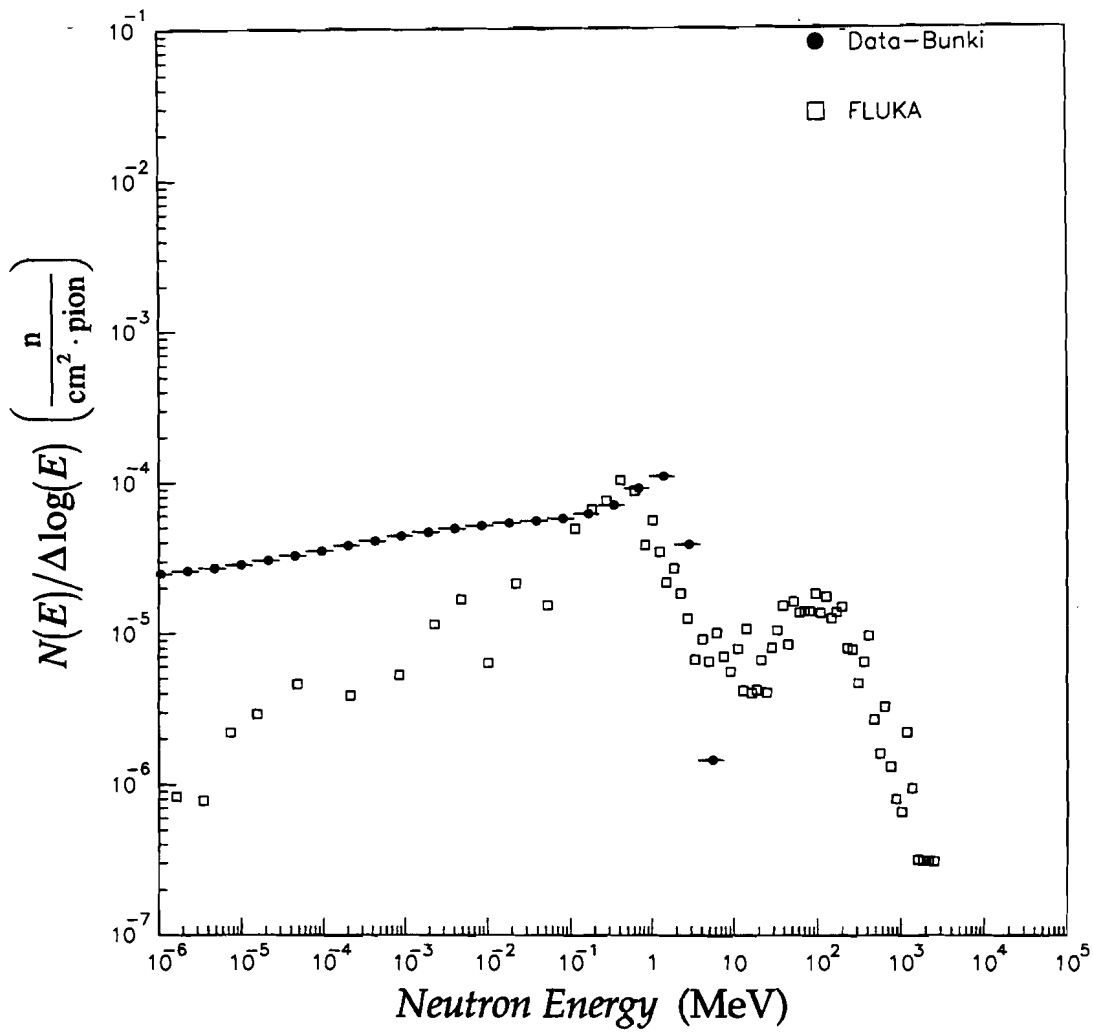

Figure C.35. Unfolded Neutron Spectra for Incident Pions on 243.8 cm of Iron. Shown is the neutron spectrum unfolded from the data by use of BUNKI compared to that generated by the FLUKA simulation, for 50 GeV incident pions on 243.8 cm (96 in, 14.5 λ) of iron in the longitudinal direction. The fluence per unit lethargy per pion is plotted as a function of neutron energy.

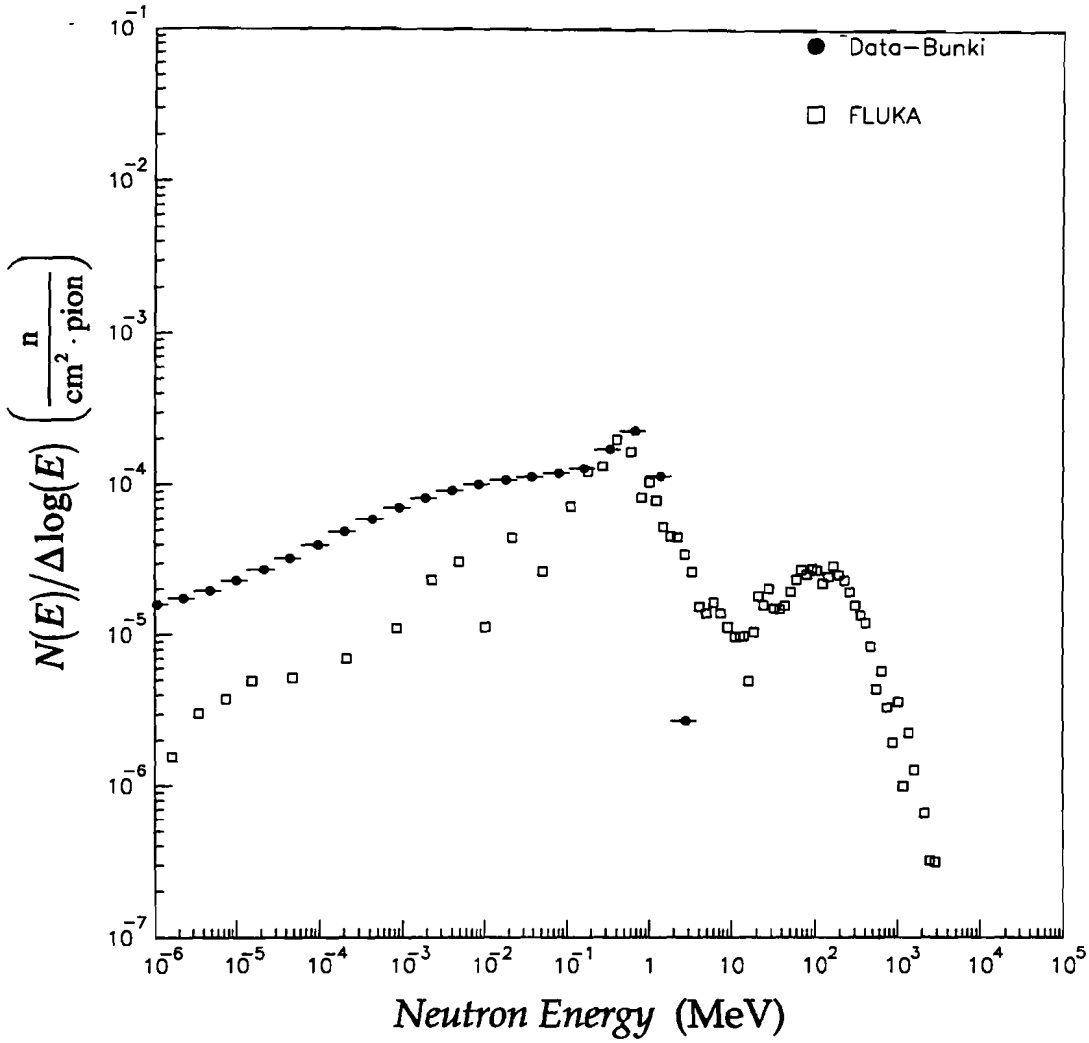

Figure C.36. Unfolded Neutron Spectra for Incident Pions on 243.8 cm of Iron. Shown is the neutron spectrum unfolded from the data by use of BUNKI compared to that generated by the FLUKA simulation, for 75 GeV incident pions on 243.8 cm (96 in, 14.5 λ) of iron in the longitudinal direction. The fluence per unit lethargy per pion is plotted as a function of neutron energy.

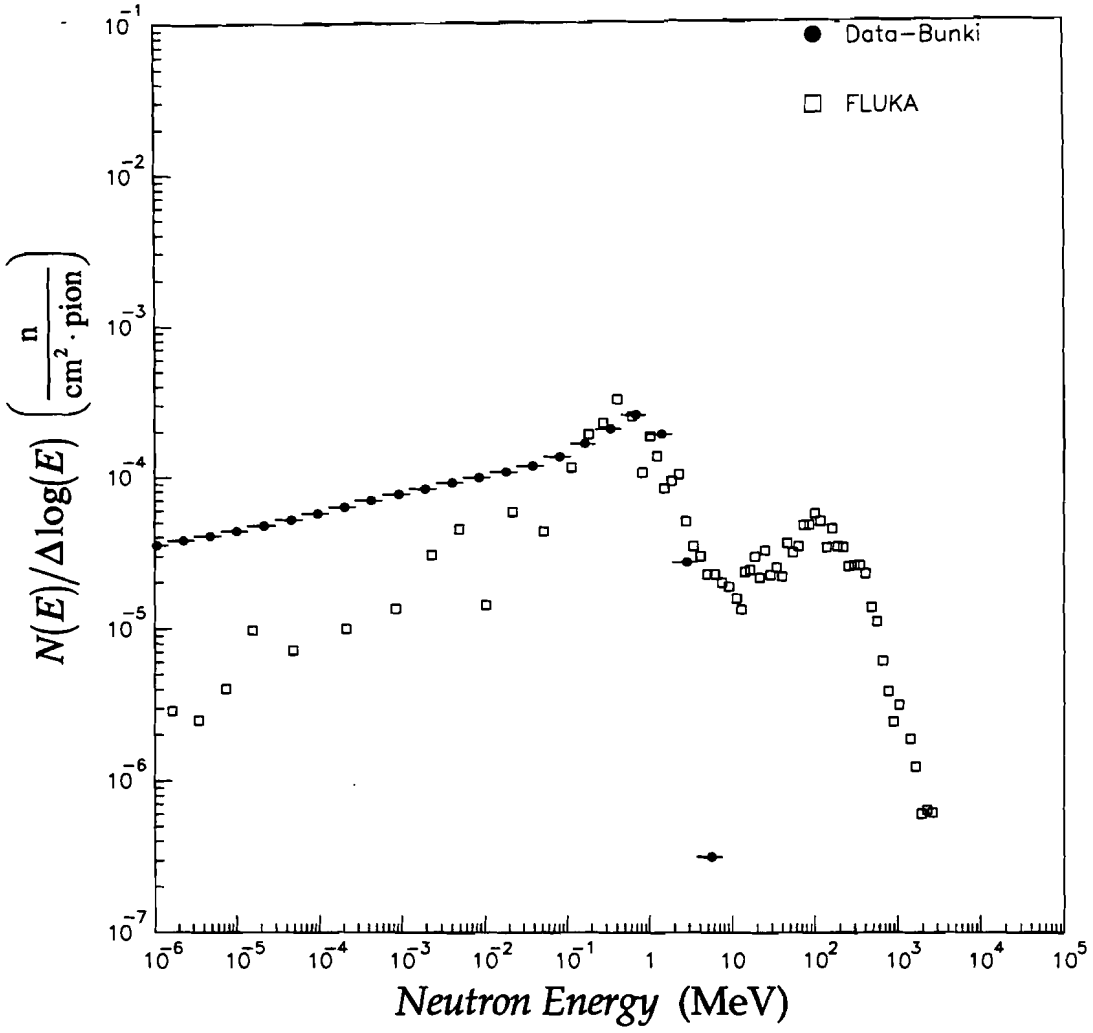

Figure C.37. Unfolded Neutron Spectra for Incident Pions on 243.8 cm of Iron. Shown is the neutron spectrum unfolded from the data by use of BUNKI compared to that generated by the FLUKA simulation, for 100 GeV incident pions on 243.8 cm (96 in, 14.5 λ) of iron in the longitudinal direction. The fluence per unit lethargy per pion is plotted as a function of neutron energy.

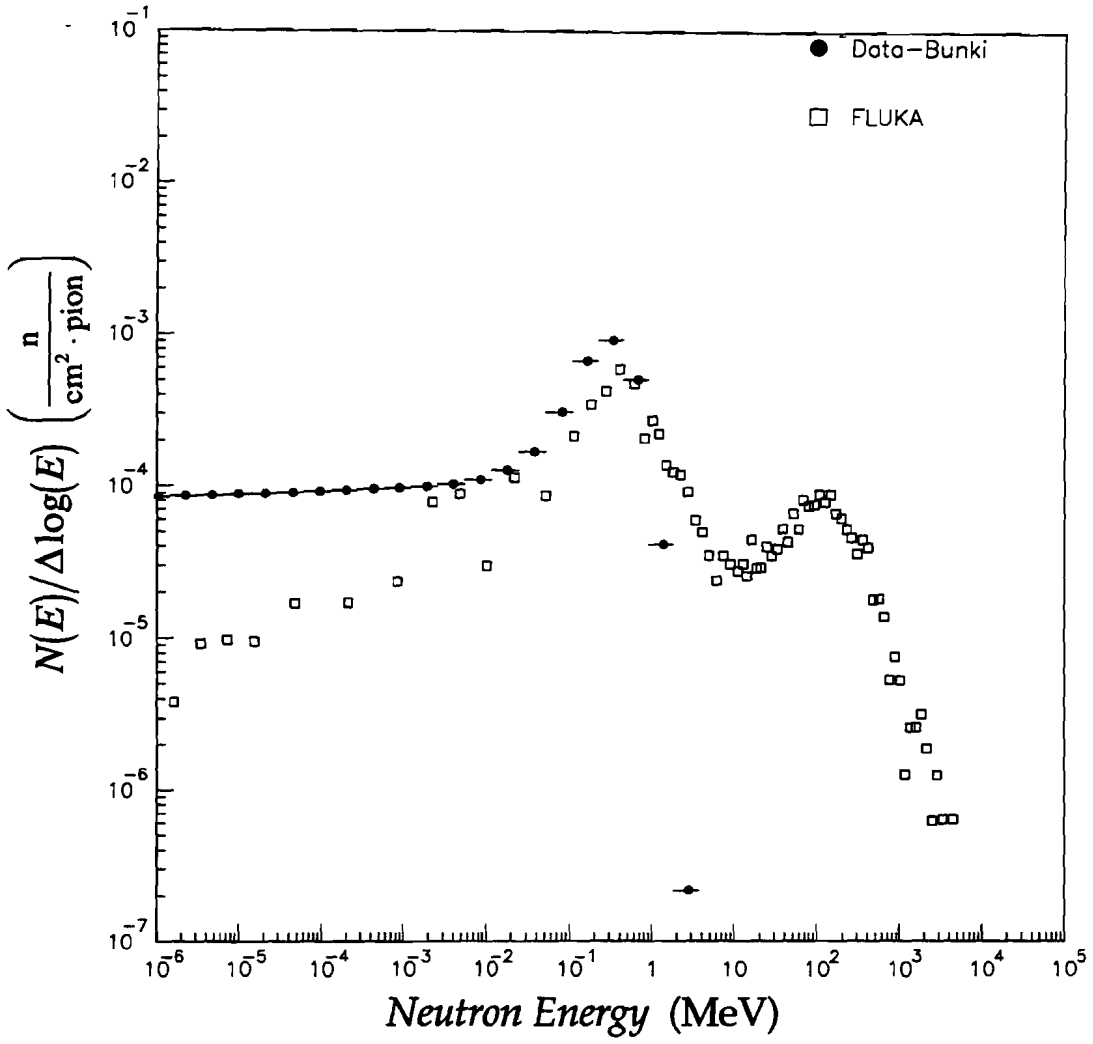

Figure C.38. Unfolded Neutron Spectra for Incident Pions on 243.8 cm of Iron. Shown is the neutron spectrum unfolded from the data by use of BUNKI compared to that generated by the FLUKA simulation, for 150 GeV incident pions on 243.8 cm (96 in, 14.5 λ) of iron in the longitudinal direction. The fluence per unit lethargy per pion is plotted as a function of neutron energy.

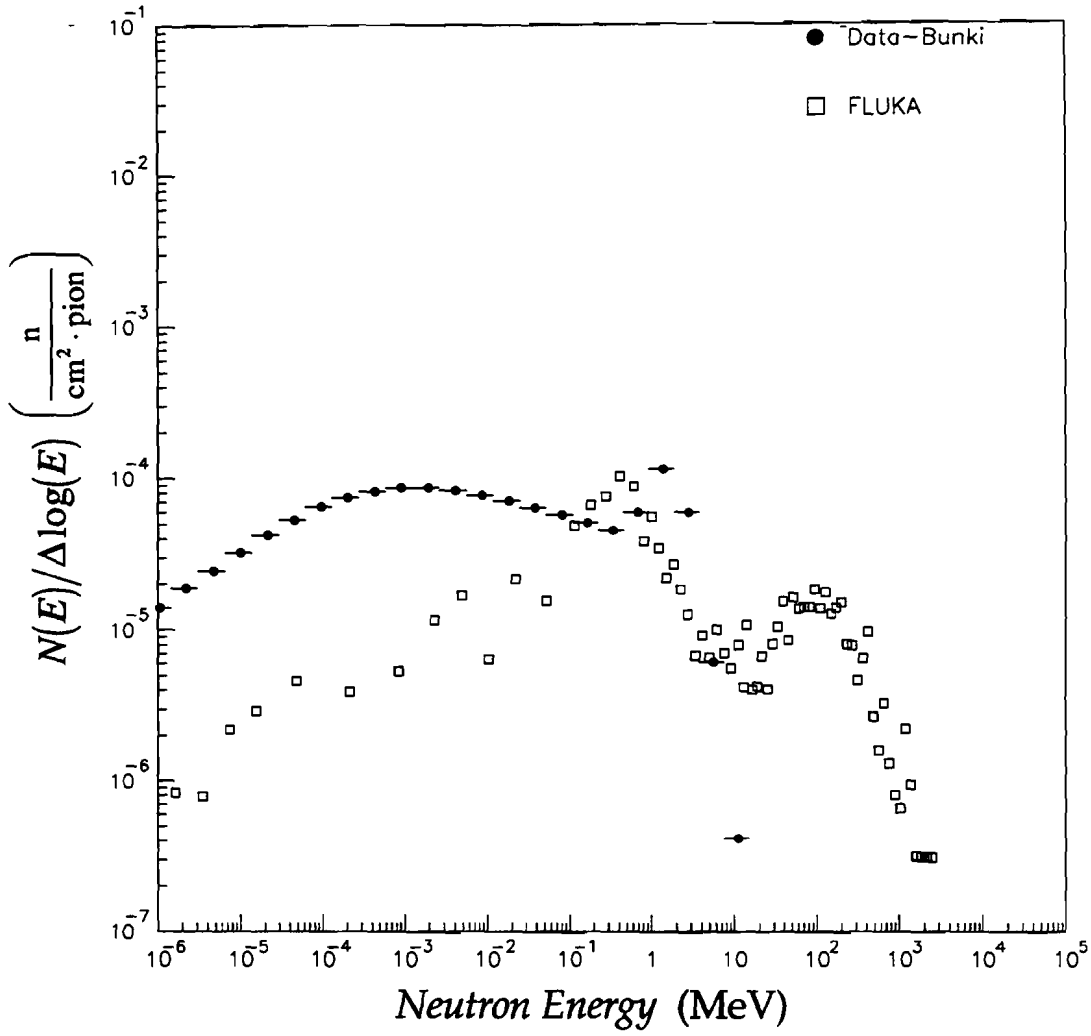

Figure C.39. Unfolded Neutron Spectra for Incident Pions on 243.8 cm of Iron. Shown is the neutron spectrum unfolded from the data by use of BUNKI compared to that generated by the FLUKA simulation, for 50 GeV incident pions on 243.8 cm (96 in, 14.5 λ) of iron in the longitudinal direction. The fluence per unit lethargy per pion is plotted as a function of neutron energy. This set of data was taken on December 31.

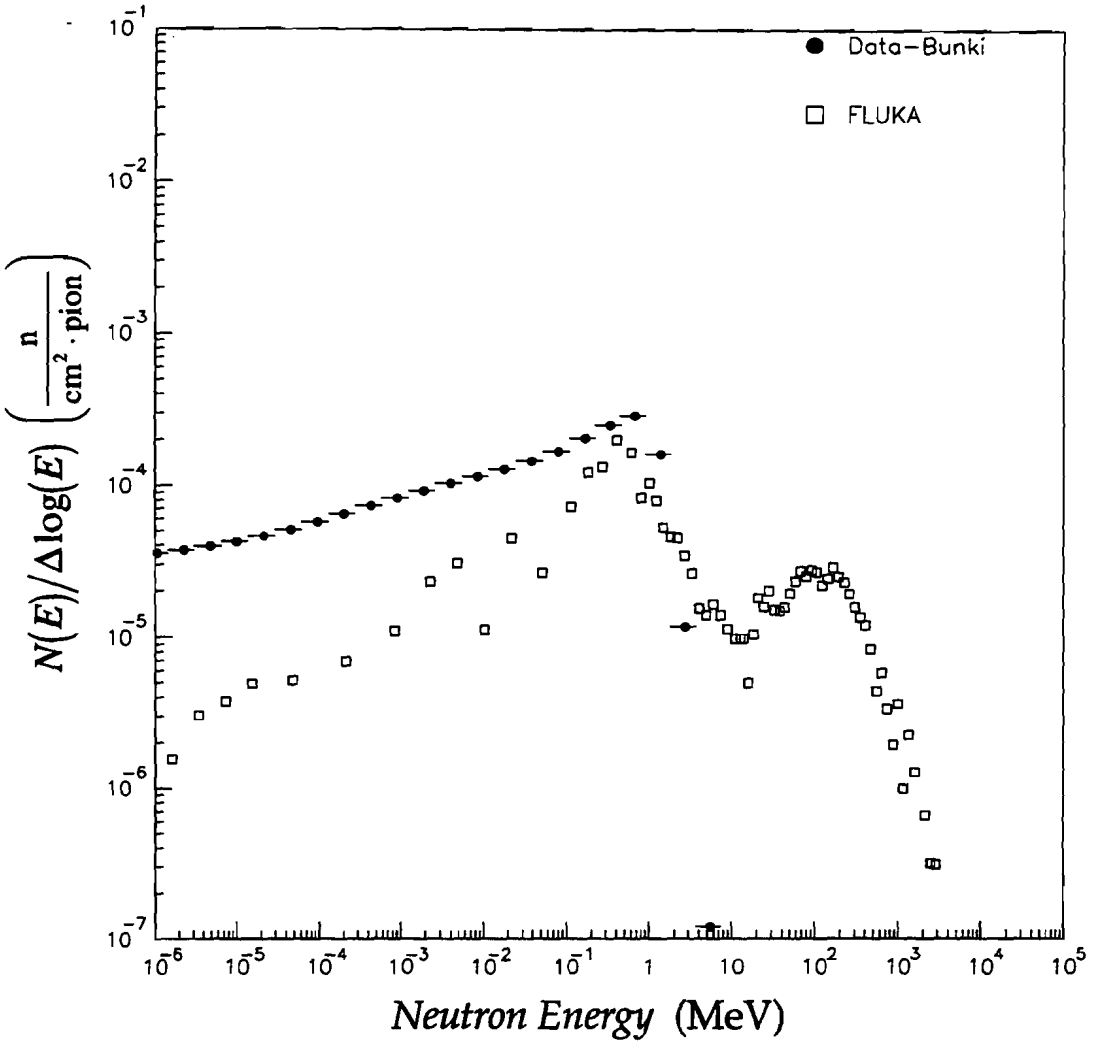

Figure C.40. Unfolded Neutron Spectra for Incident Pions on 243.8 cm of Iron. Shown is the neutron spectrum unfolded from the data by use of BUNKI compared to that generated by the FLUKA simulation, for 75 GeV incident pions on 243.8 cm (96 in, 14.5 λ) of iron in the longitudinal direction. The fluence per unit lethargy per pion is plotted as a function of neutron energy. This set of data was taken on December 31.

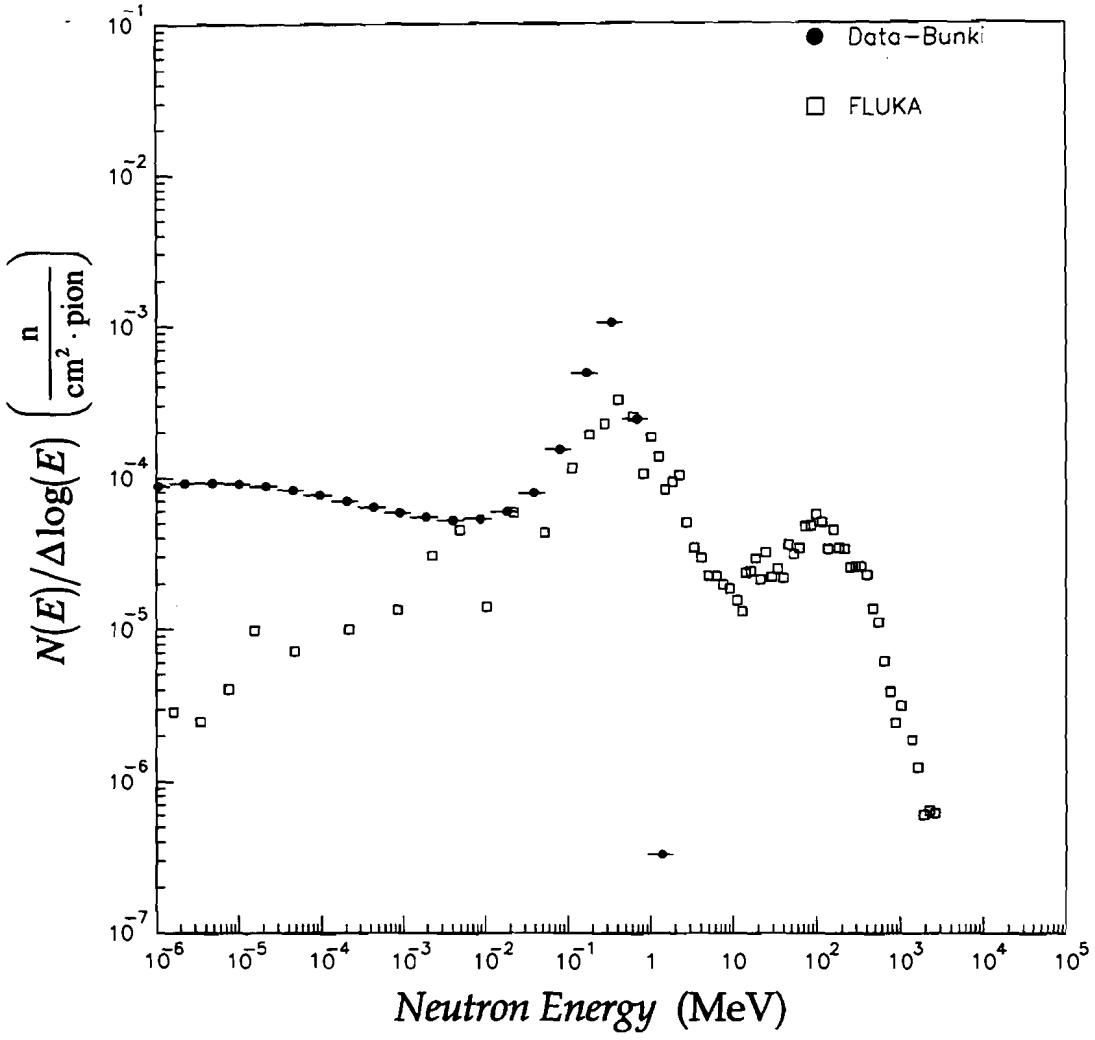

Figure C.41. Unfolded Neutron Spectra for Incident Pions on 243.8 cm of Iron. Shown is the neutron spectrum unfolded from the data by use of BUNKI compared to that generated by the FLUKA simulation, for 100 GeV incident pions on 243.8 cm (96 in, 14.5 λ) of iron in the longitudinal direction. The fluence per unit lethargy per pion is plotted as a function of neutron energy. This set of data was taken on December 31.

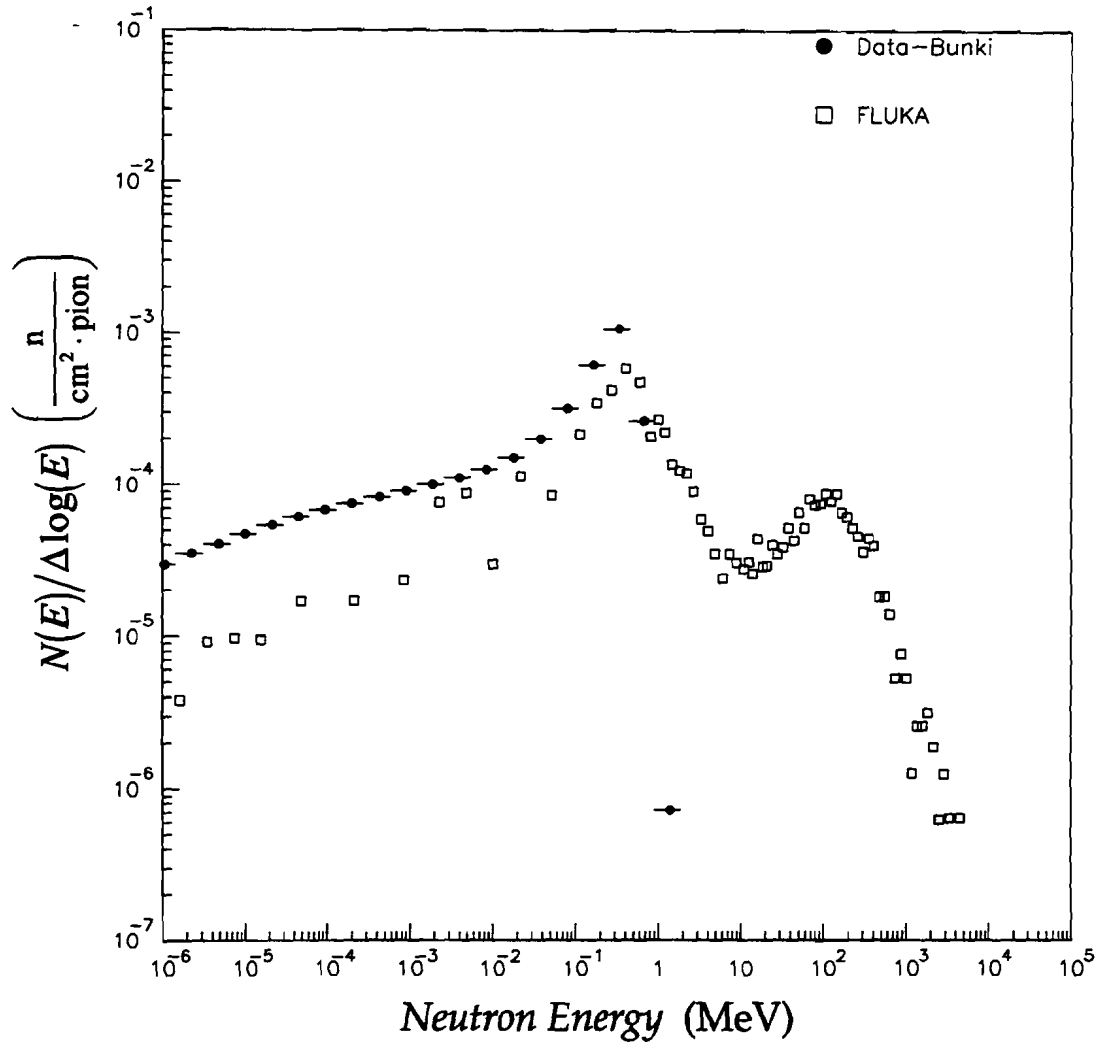

Figure C.42. Unfolded Neutron Spectra for Incident Pions on 243.8 cm of Iron. Shown is the neutron spectrum unfolded from the data by use of BUNKI compared to that generated by the FLUKA simulation, for 150 GeV incident pions on 243.8 cm (96 in, 14.5 λ) of iron in the longitudinal direction. The fluence per unit lethargy per pion is plotted as a function of neutron energy. This set of data was taken on December 31.

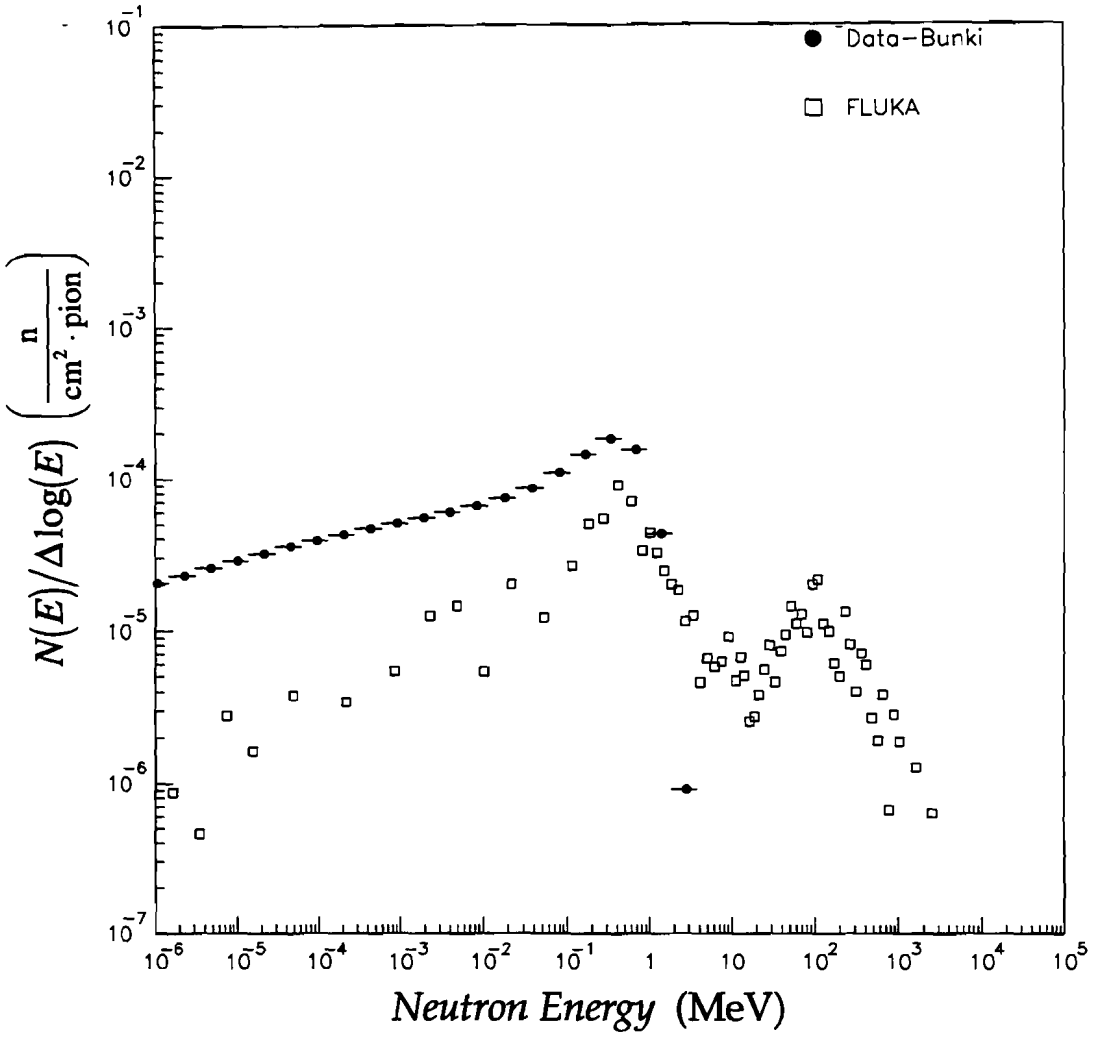

Figure C.43. Unfolded Neutron Spectra for Incident Pions on 264.2 cm of Iron. Shown is the neutron spectrum unfolded from the data by use of BUNKI compared to that generated by the FLUKA simulation, for 75 GeV incident pions on 264.2 cm (104 in, 15.7 λ) of iron in the longitudinal direction. The fluence per unit lethargy per pion is plotted as a function of neutron energy.

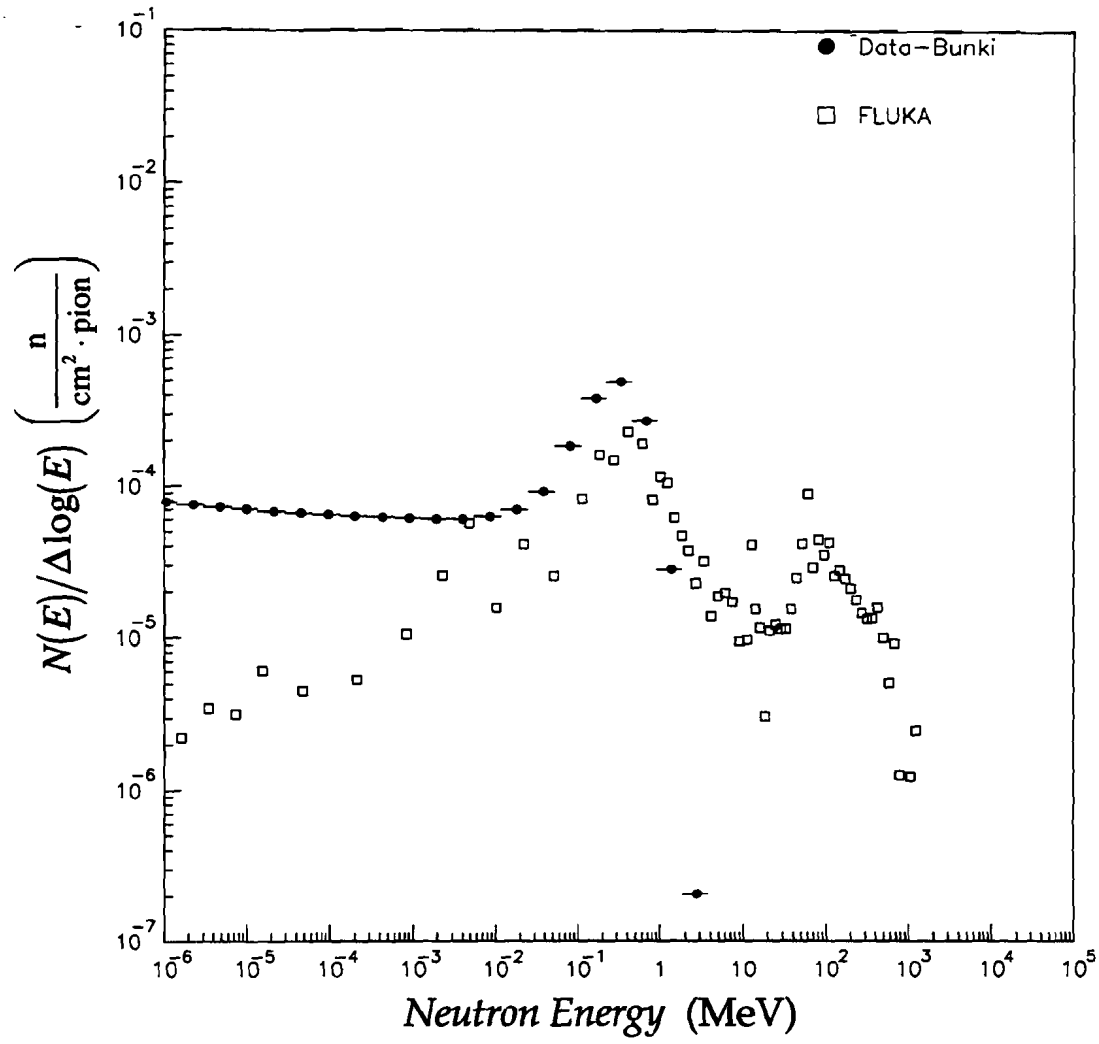

Figure C.44. Unfolded Neutron Spectra for Incident Pions on 264.2 cm of Iron. Shown is the neutron spectrum unfolded from the data by use of BUNKI compared to that generated by the FLUKA simulation, for 125 GeV incident pions on 264.2 cm (104 in, 15.7 λ) of iron in the longitudinal direction. The fluence per unit lethargy per pion is plotted as a function of neutron energy.

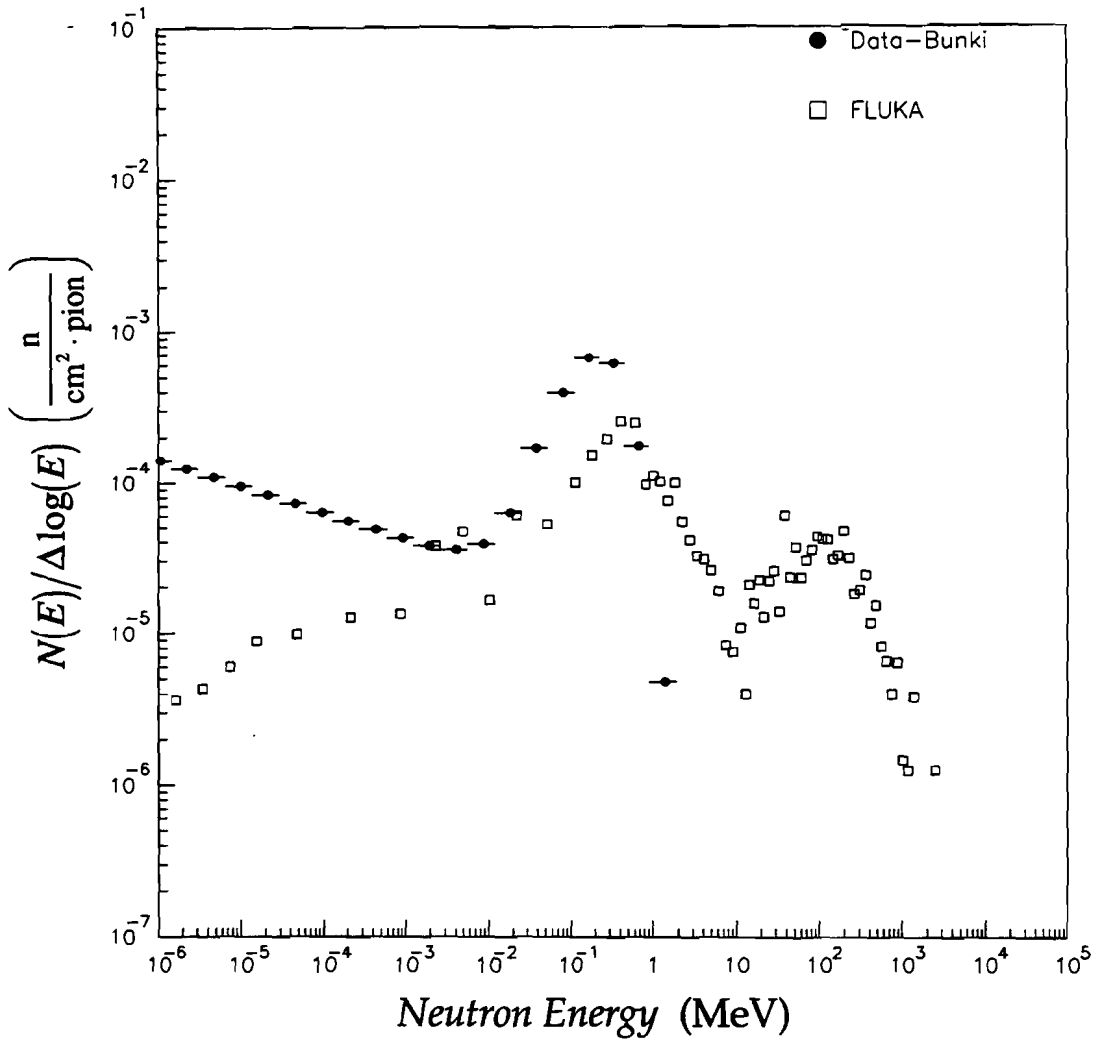

Figure C.45. Unfolded Neutron Spectra for Incident Pions on 264.2 cm of Iron. Shown is the neutron spectrum unfolded from the data by use of BUNKI compared to that generated by the FLUKA simulation, for 150 GeV incident pions on 264.2 cm (104 in, 15.7 λ) of iron in the longitudinal direction. The fluence per unit lethargy per pion is plotted as a function of neutron energy.

References

References

Awschalom, M. Bonner Spheres and Tissue-Equivalent Chambers for Extensive Radiation Area Monitoring around a 1/2 TeV Proton Synchrotron. Procedings IAEA Symp. on Neutron Monitoring for Radiation Protection Purposes. Vienna. 1:297; 1972.

Awschalom, M., Sanna, R.S. Applications of Bonner Sphere Detectors in Neutron Field Dosimetry. Radiat. Prot. Dosim. 10: 89-101; 1985.

Bramblett, R.L., Ewing, R.I., Bonner, T.W. A New Type of Spectrometer. Nuclear Instruments and Methods 9:1-12; 1960.

Canberra Software, S100- System 100 Version 2.0 1988. Canberra Industries, Inc. One State Street, Meridien, CT 06450 USA.

Cossairt, J.D., Butala, S.W., Gerardi, M.A. Absorbed Dose Meaurements at an 800 GeV Proton Accelerator; Comparison with Monte Carlo Calculations. Nucl. Instr. and Meth. in Phys. Res. A 238:504-508; 1985.

Cossairt, J.D., Elwyn, A.J. Personal dosimetry in a Mixed Field of High Energy Muons and Neutrons, Health Phys. 52:813-818; 1987.

Cossairt, J.D., Elwyn, A.J., Freeman, W.S, Salsbury, W.C., Yurista, P.M. Measurements of Neutrons in Enclosures and Outside of Shielding at the Tevatron. Fermilab-Conf-88/106, 1988.

Elwyn, A.J., Cossairt, J.D. A Study of Neutron Leakage through an Fe Shield at an Accelerator. Health Phys. 51:723-735; 1986.

Elwyn, A.J. Characteristics of Neutron Fields Outside Shielding. Radiation Physics Notes #93, Fermilab, 1991.

Emmet, M.B. ORNL Report 4972; 1975.

Fasso, A., Goebel, K., Hofert, M., Ranft, J., Stevenson, G. R., Shielding Against High Energy Radiation. Landolt-Bornstein Numerical Data and Functional Relationships in Science and Tecnology, Group I: Nuclear and Particle Physics, Springer-Verlag, Vol. 11, 1990.

Fasso, A., Ferrari, A., Ranft, J., Sala, P.R., Stevenson, G.R., Zazula, J.M. A Comparison of FLUKA Simulations with Measurements of Fluence and Dose in Calorim-

eter Structures. Nucl. Instr. and Meth. in Phys. Res. A 322:459-468; 1993.

Gollon, P.J. Comments on Bonner Sphere Unfolding. Brookhaven National Laboratory, Memorandum Jan 17,1983.

Hertel, N.E., Davidson, J.W. The Response of Bonner Spheres to Neutrons from Thermal Energies to 17.3 MeV. Nucl. Instr. and Meth. in Phys. Res. A 238:509-516; 1985.

Hess, W.N., Patterson, H.W., Wallace, R.W., Chupp, E.L. Cosmic Ray Neutron Energy Spectrum. Phy. Rev. 116:445-457; 1959.

International Atomic Energy Agency. Compendium of Neutron Sources and Detector Responses for Radiation Protection Purposes. Vienna,Technical Reports Series 28; 1990.

International Commission on Radiation Units and Measurements. Basic Aspects of High Energy Particle Interactions and Radiation Dosimetry. Bethesda, MD: ICRU Publications; ICRU Report 28; 1978.

Ing, H., Cross, W.G., Bunge, P.J. Spectrometers for Radiation Protection at Chalk River Nuclear Laboratories. Radiat. Prot. Dosim. 10:137-145; 1985.

Lindenbaum, S.J. Shielding of High Energy Accelerators. Ann. Rev. Nucl. Sci 11:213; 1961.

Liu, K., Stevenson, G.R., Thomas, R.H., Thomas, S.V. Variance and Regression Analyses of Moyer Model Parameter Data and their Variation with Primary Proton Energy. Health Phys. 46:674-681; 1984.

Lowry, K.A., Johnson, T.L. Modification to Iterative Recursion Unfolding Algorithms and Computer Codes to Find More Appropriate Neutron Spectra. U.S. Naval Research Laboratory, Report NRL-5340, Washigton, D.C.1984.

McCaslin, J.B. A High-Energy Neutron-Flux Detector. Health Phys. 2: 339-407; 1959.

McCaslin, J.B., Smith, A.R., Stephens, L.D., Thomas, R.H. An Intercomparison of Dosimetric Techniques in Radiation Fields at two High-Energy Accelerators. Health Phys. 33: 611-620; 1977.

McCaslin, J.B., Sun, R.S., Swanson,W.P., Elwyn, A.J., Freeman,W.S., Yurista,P.M. Measurements of Neutron spectra and Doses in the Tevatron Tunnel for 800 GeV

Circulating Proton Beams, SSC-58 1986.

McCaslin, J.B., Swanson, W.P. Moyer Model Approximations for Point and Extended Beam Losses. Nucl. Instr. and Meth. in Phys. Res .A 256:418-426; 1987.

Mokhov, N.V., Cossairt, J.D. A Short Review of Monte Carlo Hadronic Cascade Calculations in the Multi-TeV Energy Region. Nucl. Instr. and Meth. in Phys. Res. A 244:349-355; 1986.

Moritz, L.E. Measurement of Neutron Leakage Spectra at a 500-MeV Proton Accelerator. Health Phys. 56: 287-296; 1989.

Moritz, L.E., Suzuki,T., Noguchi, M., Oki, Y., Miura, T., Miura, S., Iawara, H., Barn, S., Hirayama, H., Kondo, K. Characteristics of the Neutron Field in the KEK Counter Hall. Health Phys. 58: 487-492; 1990.

Kalinovsky, A.N., Mokhov, N.V., Nikitin,Y.P. Penetration of High Energy Particles Through Matter. Energoatomizdat, USSR; 1984.

Patterson, H.W., Hess, W.N., Moyer,B.J., Wallace, R.W. The Flux and Spectrum of Cosmic Ray Produced Neutrons as a Function of Altitude. Health Phys. 2: 69 - 72;1959.

Rohrig, N. Plotting Neutron Fluence Spectra. Health Phys. 45:817-818;1983.

Routti, J.T., Sandeberg, J.V. General Purpose Unfolding LOUHI78 with Linear and Non-Linear Regularization. Comp. Phy. Commun. 21:119-144;1980.

Sanna, R.S. Thirty One Group Response Matrices for the Multisphere Neutron Spectrometer over the Energy Range Thermal to 400 MeV. USAEC, HASL-267 March 1973.

Shaw, K.B., Stevenson, G.R. Thomas, R.H., Evaluation of Dose Equivalent from Neutron Energy Spectra. Health Phys. 17:459-469; 1969.

Solon, L.E. (Ed), Report. TID-7545, USAEC 1957.

Stevenson, G.R. The Estimation of Dose Equivalent from Activation of Plastic Scintillators. Health Phys. 47: 837-847; 1984.

Stevenson, G.R. Shielding of Extended Targets at Proton Energies Greater than 3 GeV. CERN Internal Report TIS-RP/IR/86-04; 1986.

Sullivan, A.H. A Guide to the Radiation and Radioactivity Levels near High Energy Accelerators. Nuclear Technology Publishing, Asford, Kent TN 23 15W, England; 1992.

Thomas, R.H., Thomas, S. V. Variance and Regression Analyses of Moyer Model Parameters Data- a Sequel. Health Phys. 46:954-956; 1984.

Thomas, R.H., Stevenson, G.R. Radiation Protection Around High Energy Accelerators. Radiat. Prot. Dosim. 10: 283-301; 1985.

Thomas, R.H., Stevenson, G.R. Radiological Safety Aspects of the Operation Proton Accelerators, Technical Reports series No. 283, IAEA, Vienna, 1988.

Thorngate, J.H. Griffith, R.V. Neutron Spectrometers for Radiation Monitoring at Lawrence Livermore National Laboratory. Radiat. Prot. Dosim. 10:125-135; 1985.

Van Ginneken, A. Casim, Program to Simulate Hadronic Cascade in Bulk Matter. Fermilab Report FN-272; 1975.